THE UNIVERSITY OF HULL

Automated lithological mapping using airborne hyperspectral thermal infrared data

Anchorage Island, Antarctica

BEING A THESIS SUBMITTED FOR THE DEGREE OF
DOCTOR OF PHILOSOPHY
IN THE UNIVERSITY OF HULL

BY

Martin Black
BSc (Hons), MScR

APRIL 2016

British Antarctic Survey
NATURAL ENVIRONMENT RESEARCH COUNCIL

NERC SCIENCE OF THE ENVIRONMENT

UNIVERSITY OF Hull
Faculty of Science

Abstract

The thermal infrared portion of the electromagnetic spectrum has considerable potential for mineral and lithological mapping of the most abundant rock-forming silicates that do not display diagnostic features at visible and shortwave infrared wavelengths. Lithological mapping using visible and shortwave infrared hyperspectral data is well developed and established processing chains are available; however, there is a paucity of such methodologies for hyperspectral thermal infrared data. Here, a new fully automated processing chain for deriving lithological maps from hyperspectral thermal infrared data is presented; the processing chain is developed through testing of existing algorithms on synthetic hyperspectral data. The processing chain is then applied to the first ever airborne hyperspectral thermal data collected in the Antarctic. A combined airborne hyperspectral survey, targeted geological field mapping campaign and detailed mineralogical and geochemical datasets are applied to a small test site in West Antarctica where the geological relationships are typical of continental margin arcs. The challenging environmental conditions and cold temperatures in the Antarctic meant that the data have a significantly lower signal to noise ratio than is usually attained from airborne hyperspectral sensors. Preprocessing techniques were applied to improve the signal to noise ratio and convert the radiance images to ground leaving emissivity. Following preprocessing, the fully automated processing chain was applied to the hyperspectral imagery to generate a lithological map. The results show that the image processing chain was successful, despite the low signal to noise ratio of the imagery; the results are encouraging with the thermal imagery allowing clear distinction between granitoid types.

Acknowledgements

I would like to firstly thank my supervisors, Teal Riley and Andrew Fleming at the British Antarctic Survey (BAS) and Graham Ferrier and Tim Bellerby at the University of Hull, for their intellectual support and guidance throughout the PhD. I would also like to thank Peter Fretwell at BAS for his important input to the project.

I would also like to acknowledge: Alasdair Mac Arthur and Chris MacLellen at the NERC Field Spectroscopy Facility for support with spectral analysis; David Neave, Iris Buisman and Nick Marsh for their assistance, guidance and input with geochemical analyses; Stephen Achal, Eldon Puckrin and Alex Shipp for their help and support during fieldwork; Daniel Schaepfer, Rudolf Richter, John McFee and Alejandra Umana Diaz for answering my atmospheric correction queries; and Alex Burton-Johnson and Joe Gilbert for their geological assistance and help with thin section work. I would also like to thank all of my fellow students throughout my time at BAS for their help over many cups of tea and table tennis games.

Most of all I would like thank my wife Jayne and my family for their encouragement, support, proof-reading and putting up with me thinking out loud about hyperspectral data over the last few years.

This PhD was funded by a NERC PhD studentship in conjunction with BAS and the University of Hull (NERC Grant: NE/K50094X/1). Fieldwork in the 2014 austral summer was supported through a BAS Antarctic Funding Initiative (AFI) Collaborative Gearing Scheme Grant (CGS-86) and supported by a NERC FSF spectrometer loan (No. 675.0613). A full spectrum reflectometer was kindly provided during the field campaign through collaborators Eldon Puckrin (DRDC Valcartier) and Stephen Achal (ITRES Research Ltd.).

Declaration and Statement of Copyright

I confirm that no part of the material presented in this thesis has previously been submitted by me or any other person for a degree in this or any other university. In all cases, where it is relevant, material from the work of others has been acknowledged.

Martin Black

Table of Contents

List of Figures

List of Tables

1 Introduction

Remote sensing in the solar reflective spectral range has been widely demonstrated to be an invaluable methodology to assist geological analysis (van der Meer *et al.*, 2012). Hyperspectral data collected at visible and near infrared (VNIR; 0.4–1 μm) and shortwave infrared (SWIR; 1–2.5 μm) wavelengths has been widely reported in the literature for mapping mineral absorption features occurring within transition metals (i.e. Fe, Mn, Cu, Ni, Cr etc.), alteration minerals that display absorption features associated with Mg-OH and Al-OH bonds, as well as carbonates, sulphates, oxides and hydroxides (e.g. Abrams *et al.*, 1977; Kruse *et al.*, 1990; Hook and Rast, 1990; Hook *et al.*, 1991; Clark *et al.*, 1993a; Kruse *et al.*, 1993; Abrams and Hook, 1995; Clark and Swayze, 1996; Resmini *et al.*, 1997; Rowan *et al.*, 2003).

Although these reflectance-based datasets have been successful for mapping of minerals associated with alteration, from a geological mapping perspective, mapping of rock forming silicates is critical; particularly relevant to this study which considers igneous lithologies. When considering only VNIR/SWIR data there are significant limitations in the range and quality of the geological parameters that can be retrieved, as many important rock-forming minerals do not display diagnostic absorption features at VNIR/SWIR wavelengths (e.g. Drury, 2001; Gupta, 2003; van der Meer *et al.*, 2012).

The longwave or thermal infrared (TIR; 8–14 μm) wavelength range has the capability of retrieving additional physical parameters and more accurately resolving the composition (e.g. minerals and their abundance) and physical condition (e.g. particle size, sorting) of a material than solar reflected radiation (Hook *et al.*, 1998, 2005; Hecker *et al.*, 2012). Many common rock-forming minerals such as quartz, feldspars, olivines, pyroxenes, micas and clay minerals have clearer spectral features in the 8-14 μm wavelength region (van der Meer *et al.*, 2012). The majority of geological mapping studies using thermal infrared remote sensing data have utilised multispectral data; multispectral sensors measure a small number (< 20) of broadly spaced, often non-contiguous bands (Kramer, 2002). The Advanced Spaceborne Thermal

Emission and Reflection Radiometer (ASTER) and the Thermal Infrared Multispectral Scanner (TIMS) sensors have demonstrated the utility of TIR data to discriminate a wide range of minerals, especially silicates, as well as proving useful for lithological mapping (e.g. Rowan and Mars, 2003; Chen *et al.*, 2007; Rogge *et al.*, 2009; Haselwimmer *et al.*, 2010, 2011; Salvatore *et al.*, 2014); however, these satellite platforms are limited by their coarse spatial and spectral resolution.

The development of airborne hyperspectral TIR sensors producing images with tens to hundreds of contiguous spectral channels provided the potential for a step-change in the range of mineralogical information and accuracy available from the surface. Currently, there are a number of operational airborne hyperspectral TIR instruments, including the Spatially Enhanced Broadband Array Spectrograph System (SEBASS), the Airborne Hyperspectral Scanner (AHS), the ITRES Thermal Airborne Spectrographic Imager (TASI), and the Specim AisaOWL (van der Meer *et al.*, 2012). Previous studies using airborne hyperspectral TIR data have illustrated the exceptional potential of these types of sensors for mapping silicates, carbonates, sulphates, and clays (e.g. Hewson *et al.*, 2000; Cudahy *et al.*, 2001; Calvin *et al.*, 2001; Vaughan *et al.*, 2003b, 2005; Aslett *et al.*, 2008; Riley and Hecker, 2013).

However, a number of issues relating to processing of the imagery remain, which significantly affects the accuracy of the temperature-emissivity separation and subsequently the quality of the interpretation of the generated mineralogical and lithological maps. These issues include the coarser spectral resolution and poorer spectral calibration of currently available instruments (compared to VNIR/SWIR instruments), inaccurate correction of the effects of the atmosphere, low signal to noise ratios and a lack of understanding of the influence of a wide range of compositional, morphological, topographical and environmental factors on the spectral emissivity signal received at-sensor (Salvaggio and Miller, 2001; Shimoni *et al.*, 2007; Feng *et al.*, 2012). The complexity of the processing chain (atmospheric correction and the underdetermined nature of temperature emissivity separation; Gillespie *et al.*, 1998) and lack of defined methodologies for processing of hyperspectral airborne

TIR datasets relative to the processing of VNIR and SWIR hyperspectral datasets is an additional factor in limiting the usefulness of the data and the quality of geological interpretation (van der Meer *et al.*, 2012).

The main aim of this study was to develop a fully automated processing chain, robust to noise, in order to produce a lithological map from airborne hyperspectral TIR data. The processing chain, with minimal inputs and parameters, is designed to assist geologists in processing, analysing and interpreting hyperspectral TIR datasets; established techniques which are routinely applied to VNIR/SWIR datasets are integrated into a fully automated processing chain applied to hyperspectral TIR data. The automated processing chain could specifically benefit geologists working in the Antarctic where remote sensing data is increasingly becoming an important tool for planning and conducting preliminary analysis to aid in targeting key areas to visit in the field.

Additionally, this thesis also presents the first known analysis of airborne hyperspectral TIR data from the Antarctic. The significant challenges presented by the extreme environment in the Antarctic which produced a dataset with a very low signal to noise ratio are tackled. The results are validated and interpreted in the context of the study area in conjunction with a full suite of ancillary data: detailed high quality ground reference spectral data collected using a new, high resolution field portable spectrometer, thin section and scanning electron microscope analysis, electron microprobe analysis, whole rock geochemical data and mineral modal analysis.

1.1 Aims

The research aims to:

- Develop an automated and repeatable processing chain to produce a lithological map using airborne hyperspectral thermal infrared data
- Understand the potential of airborne hyperspectral thermal infrared data for characterising igneous lithologies

Both aims are tackled in the context of the Antarctic environment; a uniquely challenging environment which has not previously been studied using airborne hyperspectral data for lithological mapping purposes. Detailed reasons for these aims are given in Chapter 2 with respect to the published literature and the current research gaps.

1.2 Thesis structure

This thesis is broken down into seven chapters, including this introduction. **Chapter 2** presents the background to the research including the physical principles, an explanation of thermal hyperspectral remote sensing, the spectral properties of rocks and minerals, a review of existing and state-of-the-art methods for geological mapping using TIR data and a review of geological remote sensing in the polar regions. **Chapter 3** describes the study area (Anchorage Island) that forms the basis for this research, including the airborne data acquisition as well as the field campaign. **Chapter 4** sets out the methodology, describing: 1) the theoretical basis, 2) the use of synthetic hyperspectral data, 3) the investigation of processing techniques and algorithms applied to synthetic data, and 4) the geochemical analysis followed by the development of an automated processing chain to produce a lithological map (utilising the Anchorage Island hyperspectral data). **Chapter 5** presents the results of processing of the synthetic data and the real hyperspectral data from Anchorage Island along with the produced lithological map. **Chapter 6** contains a discussion of the findings and recommendations for future studies. **Chapter 7** provides concluding remarks for the thesis.

1.3 Context

This research was carried out in the context of the Geology and Geophysics team and the Mapping and Geographic Information Centre at the British Antarctic Survey (BAS). The hyperspectral data was collected during an airborne survey funded by the UK Foreign and Commonwealth Office (FCO) and conducted by the British Antarctic Survey, ITRES Research Ltd. and Defence Research & Development (DRDC) Suffield, Canada in February 2011.

This PhD was funded by a NERC PhD studentship in conjunction with BAS and the University of Hull (NERC Grant: NE/K50094X/1). Fieldwork in the 2014 austral summer was supported through a BAS Antarctic Funding Initiative (AFI) Collaborative Gearing Scheme Grant (CGS-86) and supported by a NERC FSF spectrometer loan (No. 675.0613). A full spectrum reflectometer was kindly provided during the field campaign through collaborators Eldon Puckrin (DRDC) and Stephen Achal (ITRES).

1.4 Publications

A number of papers were produced as part of this research and are included in Appendix A. The main findings of the thesis and development of the automated processing chain and its applicability in the Antarctic are presented in:

- **Black, M.**, Riley, T., Ferrier, G., Fleming, A., Fretwell, P. (2016). Automated lithological mapping using airborne hyperspectral thermal infrared data: A case study from Anchorage Island, Antarctica. *Remote Sensing of Environment*, **176**, 225-241. doi: 10.1016/j.rse.2016.01.022.

Early work on the atmospheric correction investigation and the use of radiative transfer models to produce surface reflectance imagery using VNIR and SWIR data are presented in:

- **Black, M.**, Fleming, A., Riley, T., Ferrier, G., Fretwell, P., McFee, J., Achal, S., Diaz, A. U. (2014). On the Atmospheric Correction of

Antarctic Airborne Hyperspectral Data. *Remote Sensing*, **6**(5), 4498-4514. doi: 10.3390/rs6054498

The VNIR/SWIR data was also investigated for mapping of lichen through collaboration with a visiting researcher Paula Casanovas. I was heavily involved in the development of a new technique for mapping lichen coverage using the hyperspectral data. The technique was subsequently modified for application to satellite data and applied to produce a new map of lichen coverage for the whole of the Antarctic Peninsula; findings are presented in two papers:

- **Black, M.**, Casanovas, P., Convey, P., Fretwell, P. (2015) High resolution mapping of Antarctic vegetation communities using airborne hyperspectral data. *Proceedings of Remote Sensing and Photogrammetry Society Annual Conference*, Aberystwyth, Wales, UK. September 3-5. doi: 10.13140/2.1.5189.6648
- Casanovas, P., **Black, M.**, Convey, P., Fretwell, P. (2015) Mapping lichen distribution on the Antarctic Peninsula using remote sensing, lichen spectra and photographic documentation by citizen scientists. *Polar Research*, **34**, 25633. doi: 10.3402/polar.v34.25633

A detailed laboratory spectral investigation into rare earth element (REE) deposits was carried out and yielded promising results. I was involved to help understand the feasibility of remote sensing for detecting REEs through investigations to understand the signal-to-noise ratio, atmospheric conditions and sensor characteristics; the results are presented in:

- Neave, D.A., **Black, M.**, Riley, T.R., Gibson, S.A., Ferrier, G., Wall, F., Broom-Fendley, S. (2016). On the feasibility of imaging carbonatite-hosted rare earth element (REE) deposits using remote sensing. *Economic Geology*, **111**(3), 641-665. doi 10.2113/econgeo.111.3.641

I collaborated with Dr. Alex Burton-Johnson to aid in the planning of fieldwork in the Antarctic. Initial analysis using satellite data led to the development of a new technique for extracting rock outcrop. I aided in expanding the study by applying the technique automatically to a large number of Landsat

tiles covering the entire continent. We produced a new rock outcrop extent dataset for the whole continent and revised the estimate of total exposed rock to 0.18%, half of the previous estimate. The results are presented in:

- Burton-Johnson, A., **Black, M.**, Fretwell, P., Kaluza-Gilbert, J. (2015). A fully automated methodology for differentiating rock and ice in Antarctica from Landsat imagery: A new rock outcrop map and area estimation for the entire Antarctic continent.
  The Cyrosphere Discuss., 2016, 1-16. doi: 10.5194/tc-2016-56.

2 Background and review

2.1 Introduction

Remote Sensing is a general term for the science of obtaining information about an object or area though analysis of data collected by a sensor that is not in direct contact with the object or area of investigation (Lillesand *et al.*, 2004). Here optical remote sensing is considered, using sensors which form images of the Earth's surface by measuring the solar radiation reflected or emitted from the ground. Specifically this thesis focuses on the thermal infrared domain (TIR; 8 – 14 μm) and considers surface emitted radiance; however, the solar spectral region which includes the visible near-infrared (VNIR; 0.4 – 1.0 μm) and short wave infrared (SWIR; 1.0 – 2.5 μm) domains which utilise surface reflected radiance, is also briefly discussed. Optical remote sensing is a form of *passive* remote sensing as the sensors are using external energy generated by the Sun (in the form of electromagnetic radiation) in contrast to *active* sensors which provide their own energy source (e.g. techniques such LiDAR and radar; Campbell and Wynne, 2012).

Passive optical remote sensing is based on the interaction of electromagnetic radiation as it travels from the Sun, through the Earth's atmosphere, interacts with the ground surface and is subsequently measured by a sensor (from an airborne or spaceborne platform). The compositional variations and changes in physical properties of surface materials leads to emission minima and maxima (spectral features) in the retrieved electromagnetic at-sensor signal; these spectral features can be interpreted to analyse surface materials. Sensors which are used to measure this signal across the electromagnetic spectrum are either multispectral or hyperspectral sensors. Here hyperspectral sensors are considered and are defined by their high number of narrow, contiguous spectral bands where for each picture element (pixel) a continuous spectrum over the sensor's defined wavelength interval is measured (Goetz *et al.*, 1985); this is in comparison to multispectral sensors which measure fewer (< 20), broadly spaced, non-contiguous bands (Kramer, 2002).

Hyperspectral sensors were initially developed at the National Aeronautics and Space Administration (NASA) Jet Propulsion Laboratory (JPL) in the early 1980s, with a primary focus on geological applications (Goetz *et al.*, 1985) and have since been widely demonstrated to be an invaluable tool to assist geological analysis (van der Meer *et al.*, 2012). The solar range (VNIR and SWIR) has been widely reported in the literature for mapping mineral absorption features occurring within transition metals and alteration minerals. However, for geologists the TIR domain has great potential; many common rock-forming minerals such as quartz, feldspars, olivines, pyroxenes, micas and clay minerals have spectral features in the TIR wavelength region (van der Meer *et al.*, 2012).

Comprehensive reviews of the principles and applications of remote sensing have been presented (e.g. Lillesand *et al.*, 2004; Sabins, 2007; Rees, 2012) along with applied works on applications as diverse as forestry (Wulder and Franklin, 2003), urban studies (Weng and Quattrochi, 2006) and the ocean (Martin, 2014). With specific relevance to this thesis, the interested reader is referred to reviews of polar remote sensing (Maslanik and Barry, 1990; Rees, 2005; Lubin and Massom, 2006; Massom and Lubin, 2006) and geological remote sensing (Rencz, 1999; Drury, 2001; Gupta, 2003; van der Meer *et al.*, 2012).

This section presents an overview of the physical principles of electromagnetic radiation and its interaction with the Earth's surface and atmosphere in the TIR domain, followed by the properties of minerals which give the signal its spectral features. This is followed by a discussion on geological remote sensing and review of case studies from both the Antarctic and the Arctic regions. Whilst a discussion on the engineering principles behind hyperspectral sensors is briefly outlined in Section 2.3, a comprehensive review is beyond the scope of this thesis and the interested reader is referred to reviews given by others (e.g. Kramer, 2002; Borengasser *et al.*, 2007; Ben-Dor *et al.*, 2013).

2.2 Physical principles

Any object which has a kinetic temperature above absolute zero (0 K, —273° C) will emit electromagnetic radiation. The Earth absorbs incoming solar radiation and a proportion is re-emitted at longer wavelengths. Sensors can detect this emitted radiance in the TIR domain and form images of the thermal radiance emitted by the Earth's surface.

Planck's blackbody radiation law describes the electromagnetic radiance emitted by a blackbody at a given wavelength as a function of the blackbody's temperature; a blackbody is an idealised (or perfect) emitter where the spectral radiance, L_{bb} ($W\ sr^{-1}\ m^{-2}\ m$) is related to its kinetic temperature, T (K) and wavelength, λ (μm) through

$$L_{bb}(\lambda, T) = \frac{2hc^2}{\lambda^5}\left(\frac{1}{e^{\frac{hc}{\lambda bT}} - 1}\right) \tag{1}$$

where h is Planck's constant (6.626×10^{-34} J s), b is Boltzmann's constant (1.3806×10^{-23} J K^{-1}) and c is the speed of light in a vacuum (2.9979246×10^8 ms^{-1}). The total amount of energy radiated by a blackbody and the wavelength of maximum emittance depends on the temperature of the blackbody and can be described by the Stefan-Boltzmann law and Wien's law (Figure 2.1).

The Stefan-Boltzmann law describes the total amount of emitted electromagnetic radiation by a blackbody as a function of its absolute temperature, where the emitted radiation corresponds to the integral of the radiation curve, through

$$T_{rad} = \sigma T^4 \tag{2}$$

where T_{rad} is the radiant flux of a blackbody (W m^{-2}), T is the kinetic temperature (K) and σ is the Stefan-Boltzmann constant (5.6697×10^{-8} W m^{-2} K^{-4}). Equation 2 shows that higher temperature blackbodies will emit a larger total amount of radiation, however the relation is proportional to the fourth power of the blackbody's temperature (Figure 2.1).

Wein's law describes the wavelength at which the maximum spectral exitance occurs

$$\lambda_{max} = \frac{A}{T} \tag{3}$$

where λ_{max} is the wavelength of maximum spectral exitance (μm), A is Wein's constant (2897.8 μm K), and T is kinetic temperature (K). Wein's law explains that, as an objects temperature increases, the wavelength of its maximum exitance shifts to shorter wavelengths (compare Figure 2.1). The average temperature of the sun is ~5800 K and its peak emission is in the visible domain at approximate 0.55 μm, while a much colder object, such as the Earth, at approximately 293 K has its maximum emission in the TIR at around 9.7 μm.

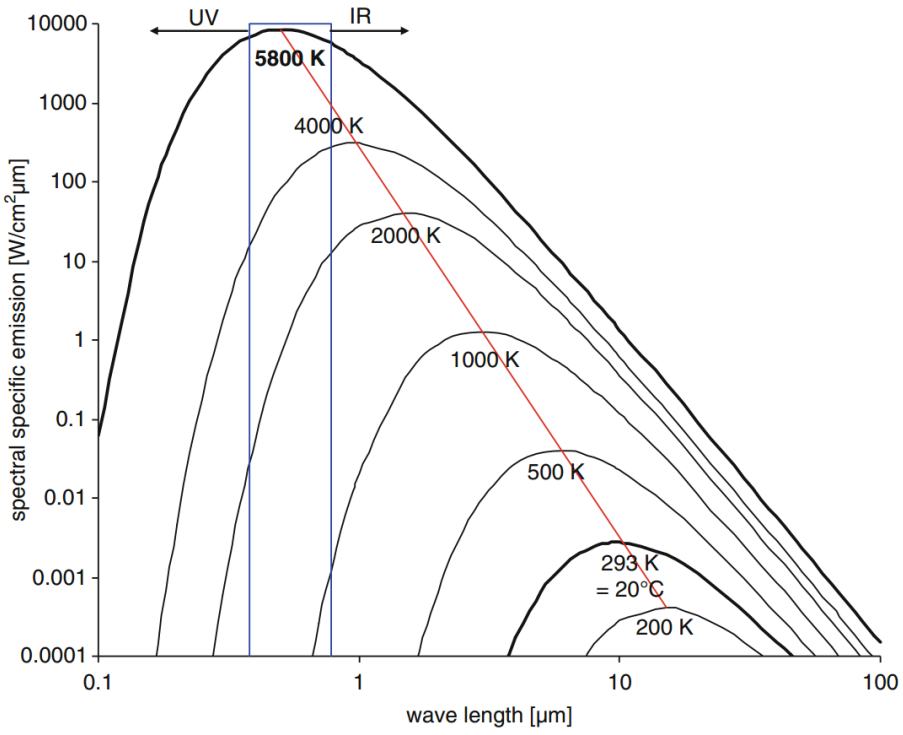

Figure 2.1: *Blackbody radiation curves at different temperatures, as derived from Equation 1. The laws of Planck (black curves) and Wien (red line) are depicted in this figure. The area under a particular curve indicates the Stefan-Boltzmann law. The bold lines at 5800 K and 293 K indicate the electromagnetic curves of the Sun and Earth respectively. The blue box indicates the region of visible light (the solar spectral domain). Abbreviated terms: UV, ultraviolet; IR, infrared. Modified after Kuenzer and Dech (2013).*

Whilst Planck's law defines blackbody radiation (where a blockbody is a perfect emitter of radiance), in reality very few objects are blackbodies as they emit less than their predicted radiation. This is taken into account through the emissivity coefficient (ϵ); ϵ is the radiant flux of an object at given temperature, calculated through the ratio of thermal radiation from the object to the radiation from a blackbody of the same temperature (as given by the Stefan-Boltzmann law). Kirchoff's law states that for a material in thermal equilibrium, all absorbed energy, α, is re-emitted, ϵ, as a function of wavelength, λ, as

$$\epsilon = \alpha \tag{4}$$

Following from this, the material specific spectral properties of transmittance, τ, absorption, α and reflectance, ρ are the ratio of incoming and outgoing radiance of each process; as governed by the law of energy conservation, their relation as a function of wavelength, λ, is given by

$$\tau + \alpha + \rho = 1 \tag{5}$$

where the macroscale transmittance, τ, is assumed to be negligible for sufficiently thick and dense materials, such as rock surfaces. Following Kirchoff's law the conversion between reflectance and emissivity as a function of wavelength, λ, is given as

$$\epsilon = 1 - \rho \tag{6}$$

Emissivity varies depending on surface material and wavelength but is not temperature dependent (Flynn *et al.*, 2001). For passive optical remote sensing there are two domains of interest; in the solar domain (VNIR and SWIR), the Sun illuminates the Earth (neglecting solar atmospheric effects) with an intensity spectrum of approximately 5800 K, whilst in the thermal domain (TIR) the Earth's surface emits long wave electromagnetic radiation with an intensity spectrum of around 293 K. The radiative distributions of the solar and thermal domains show little overlap, hence they can be used independently to derive complementary information on surface features (c.f. Figure 2.1 and Section 2.4).

2.3 Thermal hyperspectral remote sensing

When acquiring hyperspectral imagery there are three important 'resolutions' to consider; spatial, spectral, and radiometric. Brief definitions for these are outlined below.

- *Spatial:* the size of the smallest resolvable detail. Established primarily by the sensor aperture and the flying height. Commonly the spatial size of pixels (pixel resolution) is quoted, but the smallest resolvable detail may less than this value (i.e. subpixel).
- *Spectral:* two factors make up spectral resolution; the number of spectral bands and the width of the spectral bands. Hyperspectral sensors are commonly referred to as high spectral resolution due to their large number of narrow width spectral bands.
- *Radiometric:* the sensitivity at which differences in radiation intensity can be resolved; finer radiometric resolution increases the ability to detect small changes in radiation intensity.

A related concept to consider, but perhaps slightly less important for lithological mapping, is that of temporal resolution. Temporal resolution is the process of collecting multiple images of the same scene separated in time and

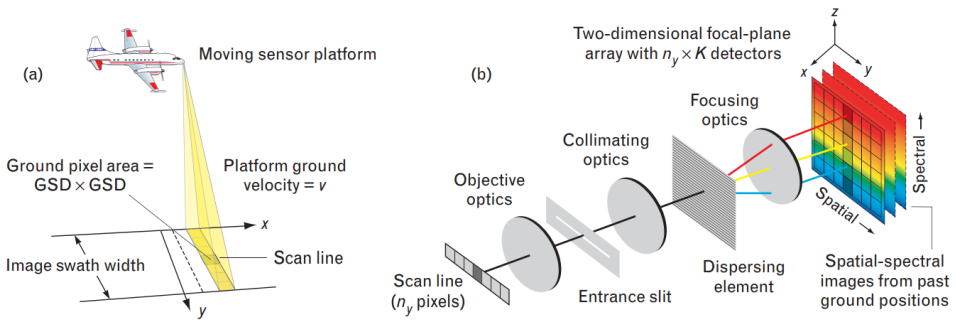

Figure 2.2: *(a) Geometry of a push-broom hyperspectral imaging system. The area coverage rate is the swatch width times the platform ground velocity v. The area of one pixel on the ground is the square of the ground sample distance (GSD). (b) Schematic of an imaging spectrometer which disperses light onto a 2D array of detectors with n_y elements in the cross-track (spatial) dimension and K elements in the spectral dimension for a total of $N = K \times n_y$ detectors. From Shaw and Burke (2003).*

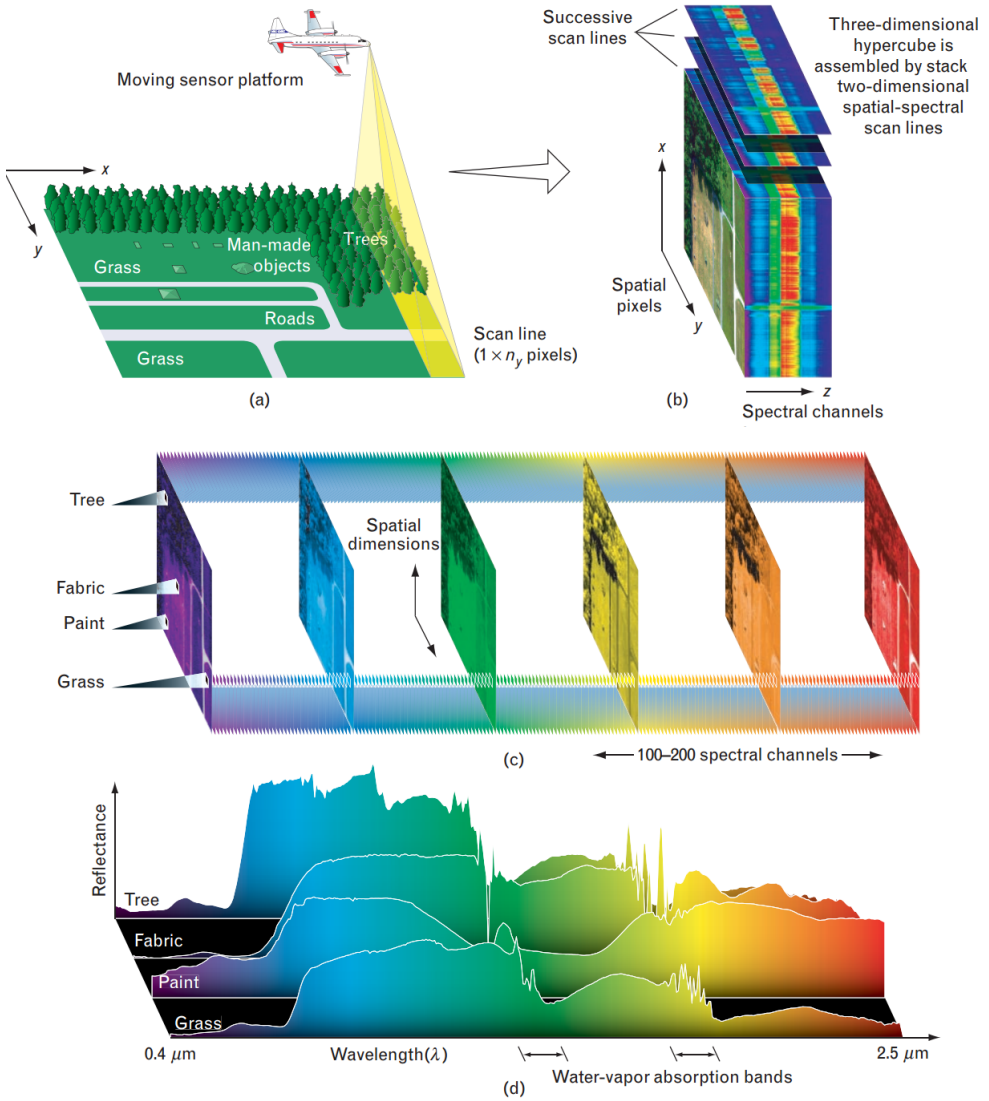

Figure 2.3: *Structure of the hyperspectral data cube. (a) A push-broom sensor on an airborne or spaceborne platform collects spectral information for a one-dimensional row of cross-track pixels, called a scan line. (b) Successive scan lines comprised of the spectra for each row of cross-track pixels are stacked to obtain a three-dimensional hyperspectral data cube. In this illustration the spatial information of a scene is represented by the x and y dimensions of the cube, while the amplitude spectra of the pixels are projected into the z dimension. (c) The assembled three-dimensional hyperspectral data cube can be treated as a stack of two-dimensional spatial images, each corresponding to a particular narrow waveband. A hyperspectral data cube typically consists of hundreds of such stacked images. (d) Alternately, the spectral samples can be plotted for each pixel or for each class of material in the hyperspectral image. Distinguishing features in the spectra provide the primary mechanism for detection and classification of materials in a scene. From Shaw and Burke (2003).*

is important for studying change over time (Shaw and Burke, 2003). These resolutions are involved in the acquisition of spectral image data. A common format for hyperspectral data collection involves the use of a 'push-broom' sensor. A cross-track line of spatial pixels is decomposed into K spectral bands, often through the use of a dispersing element or diffraction grating (Shaw and Burke, 2003); these concepts are illustrated in detail in Figures 2.2 and 2.3.

The overall concept of hyperspectral imagery (or imaging spectroscopy) is shown in Figure 2.4. Following the removal of atmospheric effects (Section 2.3.1), each pixel contains a complete reflectance (in the solar domain) or emittance (in the thermal domain) spectrum of the underlying material(s) within the pixel. It is then desirable to interpret these features (usually in a quantitative manner) with respect to the spectral characteristics of the materials of interest to the end-user (e.g. Section 2.4). However, the unique characteristics of a hyperspectral dataset present a number of processing problems (Chang, 2003) which must be considered when carrying out image analysis using techniques such as classification, segmentation or spectral mixture analysis (Landgrebe, 2005).

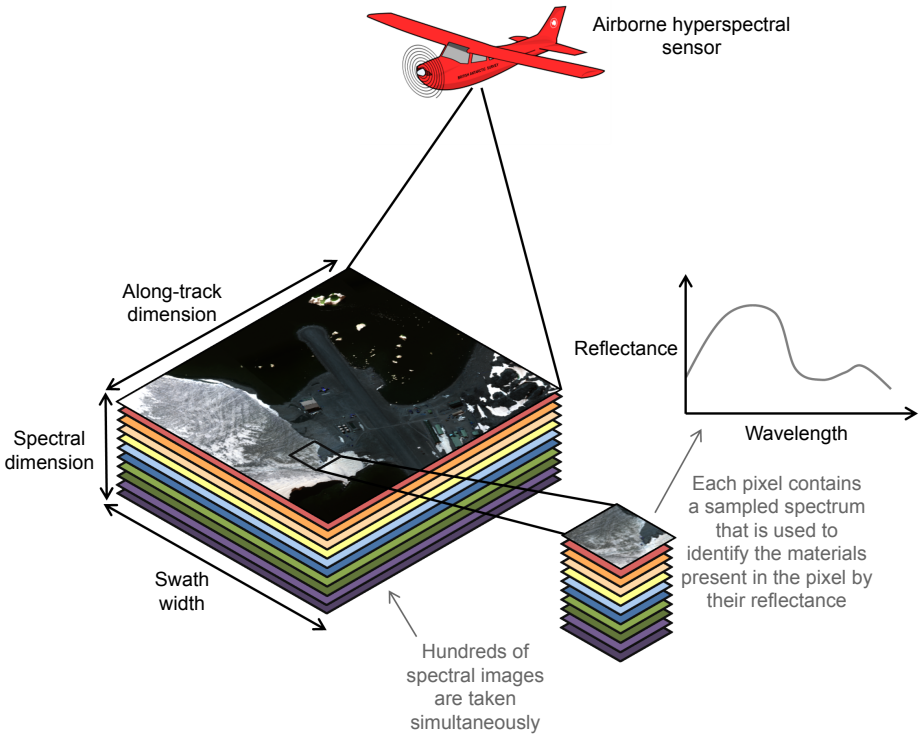

Figure 2.4: *The concept of imaging spectroscopy. An airborne imaging spectrometer simultaneously samples spectral wavebands over a large area, producing a hyperspectral image. After appropriate processing, reflectance spectra from the image can be interpreted to identify materials present in the scene; examples show the spectral variations of different surface materials. Adapted from Shaw and Burke (2003).*

2.3.1 Atmospheric influence

The electromagnetic radiation is modified through interactions with gaseous, liquid or solid constituents in the Earth's atmosphere. The main processes are (a) selective and non-selective scattering by aerosols and dust, (b) selective absorption by water vapour (H_2O), carbon dioxide (CO_2), ozone (O_3) and other gases, and (c) atmospheric emission due to the thermal state and water vapour content in the atmosphere itself (Gupta, 2003). For these reasons, the Earth's atmosphere has a number of 'atmospheric windows', areas of high transmissivity and low emissivity, with the solar and thermal domains positioned within these atmospheric windows.

Despite passive optical remote sensing techniques operating within atmospheric windows, there is still atmospheric influence which needs to be compensated for, especially for quantitative applications (Liang *et al.*, 2002).

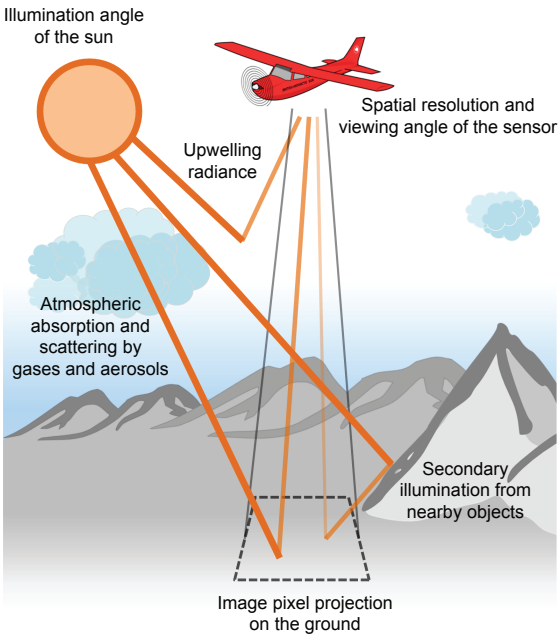

Figure 2.5: *Atmospheric and scene-related factors that can contribute to degradations in the imaging process. The spatial resolution of the sensor and the degree of atmospheric scattering and absorption are the most significant contributors to diminished image quality. Adapted from Shaw and Burke (2003).*

Whilst sensors measure the 'radiance' spectrum (the total amount of energy radiated from the ground, including atmospheric effects), it is desirable to recover the surface reflectance or emittance spectrum (the proportion of incoming radiance reflected from the ground) as this affords the best opportunity to identify the surface materials because it is, in theory, independent of the illumination and atmospheric parameters (Shaw and Burke, 2003; Black *et al.*, 2014b). In principle, the reflectance or emittance spectrum can be recovered from the observed radiance spectrum over regions in which the illumination is non-zero (Shaw and Burke, 2003). The reflectance/emittance spectrum provides the best opportunity to identify materials by comparison to reference libraries (Shaw and Burke, 2003), laboratory measurements or field measurements (Rogge *et al.*, 2009). There are numerous practical considerations (Figure 2.5) when analysing hyperspectral data; perhaps the most important of which is the degree of scattering and absorption due to atmospheric effects. These atmospheric effects complicate the process of convolving reflectance/emittance spectra from the measured radiance; therefore atmospheric correction such as radiative transfer models are required (Shaw and Burke, 2003).

The electromagnetic radiation emitted by the Earth's surface in the TIR domain undergoes a single pass through the Earth's atmosphere. The basic radiative transfer equation in the TIR domain as given by Dash *et al.* (2002) is (where each term is a function of wavelength, λ, omitted for clarity)

$$L^e_{as} = L^e_{path} + \tau \cdot L^e_{ag} + \tau \cdot [1 - \epsilon] \cdot \frac{F}{\pi} \tag{7}$$

where L^e_{as} is the total thermal radiance received at-sensor, L^e_{path} the thermal path radiance emitted by the atmosphere between the ground and the sensor, τ the ground-to-sensor transmittance, L^e_{ag} the ground emitted radiance, ϵ the ground surface emissivity and F the downwelling thermal sky flux at the ground (Richter and Coll, 2002). This basic radiative transfer equation assumes that the Earth's surface is a Lambertian reflector and that the local atmosphere is in thermal equilibrium with no scattering. The thermal path radiance, L_p is highly dependant on the temperature and water vapour profile

of the atmosphere, whilst the ground-to-sensor transmittance, τ, is least affected, as the ground surface is warmer than the atmosphere. The reflected downwelling radiance, F, is typically small due to the high (0.95 – 0.99) emissivity, ϵ, of natural materials. The TIR emitted radiance signal is subject to selective absorption due to particular atomic processes (*e.g.* rotational and vibrational modes) which characterise the material the signal interacts with (Gupta, 2003).

To remove the effect of the single atmospheric pass on the thermal emitted signal from the Earth's surface, the atmospheric influence can be calculated using the the radiative transfer model as given in Equation 7, which yields the ground emitted radiance, L^{e}_{ag}. Methods which apply the radiative transfer model approach require measurements of atmospheric parameters where the most important parameters are temperature and water vapour content (Wan and Li, 1997; Sobrino *et al.*, 1993). There can be provided by a contemporaneous launch of a radiosonde, however this is often not available to most studies. Therefore, assumptions are made about the atmospheric conditions at the time of data acquisition, with standard climatologically developed atmospheric profiles provided in radiative transfer models often used instead.

A number of approaches have been developed to convert at-sensor measured radiance to ground emitted radiance, the most notable of which are the Emissive Empirical Line Method (EELM; Distasio Jr. and Resmini, 2010), In-Scene Atmospheric Compensation (ISAC; Young *et al.*, 2002), Autonomous Atmospheric Compensation (AAC; Gu *et al.*, 2000) and radiative transfer look-up-tables (LUTs; e.g. Richter and Schläpfer, 2002, 2014).

The EELM and ISAC approaches require the presence of reference pixels within the scene and from these pixels a solution is generated to scale the remaining pixels in the scene; these techniques hold the radiative transfer parameters constant for the whole scene and neglect the effects of sensor view angle and topography, which can lead to unfeasible measures of surface emittance. The performance of the AAC approach is strongly dependant on the spectral and spatial resolution of the sensor along with requiring

robust calibration of the sensor. AAC requires narrow spectral bandwidth as the approach derives the radiative transfer parameters from the ratio of two bands, one within an atmospheric absorption band and one outside of the atmospheric absorption band, where the recommended band is around 11.7 μm (Gu *et al.*, 2000). Despite some shortcomings, these techniques offer a number of key advantages. They are computationally easy to implement and can be rapidly applied to the whole scene, they require no assumptions about the scene or atmospheric content and require limited ancillary data input.

The radiative transfer LUTs approach of Richter and Schläpfer (2002, 2014) interpolates the required atmospheric parameters from each pixel based on their individual viewing geometry, using few inputs (visibility and total water vapour) to select the radiative transfer parameters from the LUTs; this approach still assumes an atmosphere which approximates the actual *in-situ* conditions and residual atmospheric effects may remain. This approach was successfully applied to VNIR and SWIR data in the Antarctic, through the application of the the ATCOR radiative transfer model (Black *et al.*, 2014b; Appendix A).

2.3.2 Temperature emissivity separation

Following the calculation of ground leaving emitted radiance, L_g, isolation of the surface emissivity spectrum, ϵ, (and also surface kinetic temperature, T) can be derived through

$$L_g(\lambda) = \epsilon(\lambda) \cdot L_{bb}(\lambda, T) \tag{8}$$

however the blackbody radiance, L_{bb}, is spatially and temporally variable and the surface's actual energy budget as given by the kinetic temperature, T, is governed by a variety of environmental factors including heat capacity, heat conductance, evaporation and so on. This therefore leads to an underdetermined problem, where for each n measurement of surface radiance, there are $n+1$ unknowns (spectral emissivity and temperature).

A number of algorithms have been presented in the literature for temperature emissivity separation, including the reference channel method (Kahle *et al.*, 1980), normalised emissivity method (Gillespie, 1985), alpha residuals (Kealy and Gabell, 1990), thermal spectral indices (Becker and Li, 1990), spectral ratio (Watson, 1992), temperature–emissivity separation (TES) using the maximum-minimum difference of emissivity (Gillespie *et al.*, 1998), and iterative spectral smooth temperature and emissivity separation (Borel, 1998, 2008). The wide variety of algorithm development stems from the underdetermined nature of TES (n knowns, and $n + 1$ unknowns). Comprehensive reviews are given by Dash *et al.* (2002) and Quattrochi and Luvall (2004), and comparison studies between TES methods by others (Hook *et al.*, 1992; Kealy and Hook, 1993; Li *et al.*, 1999); a brief outline of common TES approaches follows.

The simplest approach to TES is to assume that emissivity is equal to that of a blackbody at one or more wavelengths within the measured TIR spectrum. The wavelength itself can be decided during the analysis or can be determined by the highest temperature when the measured spectral radiance is used in the inverse of Equation 1. The sample radiance and its emissivity are then known and the surface kinetic temperature and emissivity spectrum are calculated. This method can also be modified so that maximum assumed emissivity can be less than unity (Kahle *et al.*, 1980).

The normalised emissivity method (NEM) calculates the surface temperature for all channels with a constant user-defined emissivity, and for each pixel, the channel with the highest temperature is selected and emissivity values estimated (Gillespie, 1985). The alpha residual method (Kealy and Gabell, 1990) utilises an empirical relationship between the standard deviation and mean emissivity to restore amplitude to the alpha-residual spectrum, thereby recovering the surface temperature. The alpha-residual method relies on Wien's approximation which introduces slope errors into the spectrum (Gillespie *et al.*, 1998).

The iterative spectral smooth temperature and emissivity separation (Borel, 1998, 2008) approach is based on a revised version of the ISAC algorithm for atmospheric correction, which seeks to minimise the residuals by using a LUT

of atmospheres and determines temperature and emissivity automatically. However, the technique is dependant on a large database of atmospheric LUTs and begins to breakdown as atmospheric water vapour values exceed 3 g cm^2 (Borel, 2008).

The maximum-minimum difference (MMD) of emissivity method (Gillespie *et al.*, 1998) calculates relative emissivity based on a regression of laboratory emissivity values onto the maximum-minimum apparent emissivity difference, similar to the alpha residuals method. However, it avoids Wien's approximation and therefore has lesser slope errors (Gillespie *et al.*, 1998). The MMD method was also combined with the NEM technique to develop a TES algorithm suitable for TIR sensors with many bands, originally developed for the Advanced Spaceborne Thermal Emission and Reflection Radiometer (ASTER) (Gillespie *et al.*, 1998). The MMD technique has been widely applied in the published literature and due to its development for sensors with many bands, it is ideally suited for performing TES using hyperspectral TIR data.

2.4 Spectral properties of rocks and minerals

The spectral properties of rocks represent the composite spectral response of the minerals of which they are composed (Drury, 2001). Mineral spectral reflectance and emission properties are a function of their chemistry and structure and record the interaction of photons with the particles and chemical bonds within a mineral. Wavelength-specific spectral (absorption or emission) features represent particular photon-mineral interactions that can be electronic or vibrational in nature (Clark, 1999).

Electronic processes occur when isolated atoms or ions absorb photons resulting in a change from one energy state to another and encompass crystal field effects, charge transfer absorptions, conduction-bands, and colour centre effects. Electronic processes occur at VNIR wavelengths due primarily to transition metals (i.e. Fe, Mn, Cu, Ni, Cr etc.) of which the most important is iron (Gupta, 2003). Iron-bearing minerals display spectral features at wave-

lengths less than ~0.55 μm associated with Fe-O charge transfer and between 0.85 and 0.92 μm associated with crystal field effects.

The vibrational energy state, which yields specific features at TIR and SWIR wavelengths is the primary focus here. The atomic-molecular vibrational processes are the result of bending and stretching molecular motions where the fundamental tones occur in the TIR, and overtones and combinations in the SWIR. In the SWIR domain mineral spectral features are associated with the presence of hydroxyl (OH^-) ions or water molecules (Drury, 2001). Water bound in minerals produces diagnostic spectral features associated with overtones and their combinations at 1.9, 1.4, 1.14, and 0.94 μm. These spectral features are only useful in a laboratory setting as in remotely sensed spectra they are swamped by the identical effects of atmospheric water absorption. Minerals containing OH^- ions, including many silicates and alteration minerals, display important spectral features associated with Mg-OH and Al-OH bonds near 2.3 and 2.2 μm. These features are prominent in micas, clays, and magnesium bearing hydroxylated minerals such as chlorite and amphibole and provide an important basis for the discrimination of chemically different rocks (Drury, 2001). In the SWIR region vibrational transitions and their overtones are also associated with carbonate minerals of which the most important is that located ~2.3 μm.

The TIR domain has the capability of retrieving additional physical parameters (e.g. mineral abundance) and resolving significantly more accurately the composition and physical condition (e.g. particle size, weathering) of a material than solar reflected radiation at VNIR/SWIR wavelengths (Hook *et al.*, 1998, 2005; Hecker *et al.*, 2012). Many common rock-forming minerals such as quartz, feldspars, olivines, pyroxenes, micas and clay minerals have spectral features in the 8-14 μm wavelength region (Figure 2.6; van der Meer *et al.*, 2012). Physical properties such as particle size and packing can produce changes in the emission spectra in terms of relative depth of spectral features or 'smoothing' spectral features, though the position of features is not changed (Gupta, 2003). In the TIR, the spectra of minerals are additive in nature; therefore rock spectra in the TIR region are readily interpretable

in terms of relative mineral abundances (Gupta, 2003). However, in the VNIR/SWIR, processes such as volume scattering, (intimate) mixing of constituent minerals and textural properties (grain size, packing) can complicate mineral identification (Gupta, 2003).

For silicate minerals, a pronounced emittance minimum cause by fundamental Si-O stretching vibrations occurs near 10 μm (Hunt and Salisbury, 1975; Salisbury, 1991). The vibrational frequency, and thus the wavelength of the minimum, depends on the degree of coordination among the silicon-oxygen tetrahedral in the crystal lattice. The framework silicates, quartz and feldspar, have emittance minima at shorter wavelengths (9.3 and 10 μm, respectively) than sheet silicates such as muscovite (10.3 μm) and chain silicates such as the amphibole minerals (10.7 μm) (Hunt, 1980). Emission Fourier transform infrared (FTIR) spectroscopy has been successfully used to predict feldspar amounts and their mineralogical composition in igneous rocks (Hecker *et al.*, 2010). Carbonates have strong absorption features associated with CO_3 internal vibrations both in the 6-8 μm region (Adler and Kerr, 1963; Hunt and Salisbury, 1975) and also at 11.4 and 14.3 μm due to C-O bending modes. Sulphate minerals have an intense feature near 8.7 μm caused by fundamental stretching motions (van der Meer, 1995; Lane and Christensen, 1997).

From a geological mapping perspective, mapping of rock forming silicates is critical. When considering only VNIR/SWIR data there are significant limitations in the range and quality of the geological parameters that can be retrieved, as many important rock forming minerals do not display diagnostic absorption features at VNIR/SWIR wavelengths (van der Meer *et al.*, 2012). Hence, the TIR domain offers huge potential for geological mapping (see also Section 2.5).

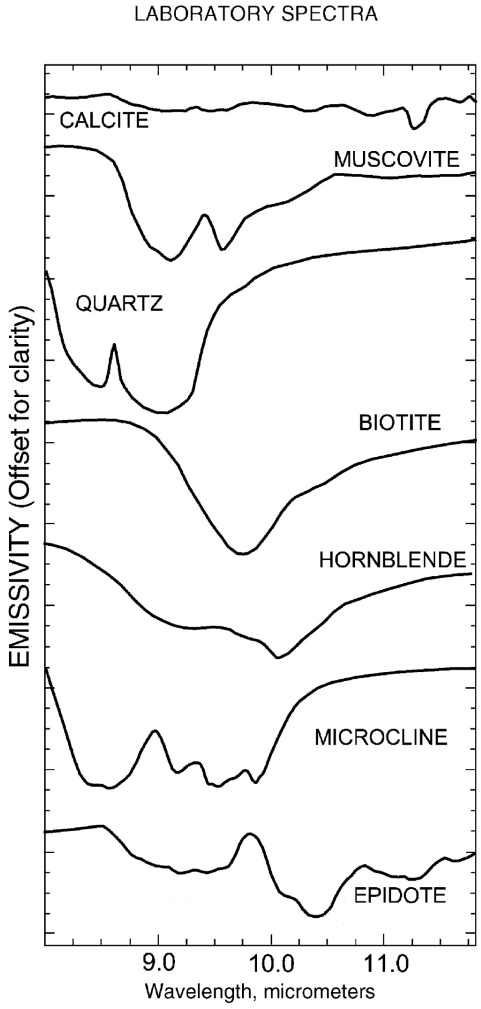

Figure 2.6: *Laboratory emissivity spectra of important rock forming minerals; adapted from Rowan and Mars (2003); hornblende is a generic type of amphibole and microcline is a type of feldspar.*

2.5 Geological remote sensing using thermal infrared data

Remote sensing in the solar reflective spectral range has been widely demonstrated to be an invaluable methodology to assist geological analysis (van der Meer *et al.*, 2012). Hyperspectral data collected at VNIR/SWIR wavelengths has been widely reported in the literature for mapping mineral absorption features occurring within transition metals and alteration minerals. Whilst VNIR/SWIR data have been successful for mapping of minerals associated with alteration, from a geological mapping perspective, mapping of rock forming silicates is critical. When considering only VNIR/SWIR data there are significant limitations, as many important rock forming minerals do not display diagnostic absorption features at VNIR/SWIR wavelengths, thus the TIR domain has great potential for geological studies (Section 2.4; van der Meer *et al.*, 2012).

Previous studies using airborne hyperspectral TIR data have illustrated the exceptional potential of these types of sensors for mapping silicates, carbonates, sulphates, and clays (Section 2.5.4). A brief discussion follows on the data analysis techniques commonly used in the processing of (hyper)spectral data followed by a review of thermal remote sensing case studies in the proceeding sections.

2.5.1 Overview and concepts

The overall concept of hyperspectral imagery (or imaging spectroscopy) was explained in Section 2.3 and illustrated in Figure 2.4 (page 16). Following the removal of atmospheric effects (Section 2.3.1), each pixel contains a complete reflectance (in the solar domain) or emittance (in the thermal domain) spectrum of the underlying material(s) within the pixel. It is then desirable to interpret these features (usually in a quantitative manner) with respect to the spectral characteristics of the materials of interest to the end-user (e.g. Section 2.4). The basic task when analysing hyperspectral data is to identify the material(s) present (in a pixel) from its reflectance/emittance spectrum. It is often helpful to consider the concept of a *spectral signature* which uniquely

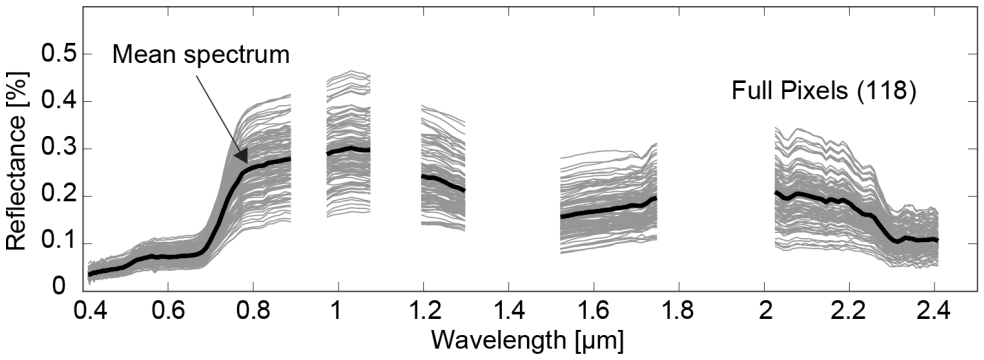

Figure 2.7: *Example of variability in reflectance spectra measured over multiple instances of a given material (in this case, vehicle paint) in a scene. The shapes of the spectra are fairly consistent, but the amplitudes vary considerably over the scene. To exploit this spectral shape invariance, some detection algorithms give more weight to the spectral shape than to the spectral amplitude in determining whether a given material is present in a pixel. The gaps correspond to water-vapour absorption bands where the data are unreliable and are discarded. From Shaw and Burke (2003).*

characterises a material; however, in reality this is often not the case as, even under laboratory conditions, repeated spectra of the same material can show significant variance due to variations in the material's surface (Figure 2.7; Manolakis and Shaw, 2002).

When considering a remotely sensed hyperspectral dataset, the variability is even more profound due to multiple factors such as the sensor noise, material composition, surrounding materials, variation in illumination conditions and changing atmospheric conditions (Manolakis and Shaw, 2002; Shaw and Burke, 2003). However, despite this, numerous remote sensing studies still use the spectral signature approach (assuming one spectrum exactly represents a material) and many well developed spectral libraries exist for carrying out analysis with this approach (e.g. Baldridge *et al.*, 2009). Perhaps the most challenging issue when analysing hyperspectral data is a result of spectral mixing, which leads to the two concepts of *pure* and *mixed* pixels.

The spectrum of each image pixel is the combined reflectance of the surface components within the sensors field of view (FOV), therefore, unless individual materials cover an area larger than the pixel size (or spatial resolution), the concept of *mixed* pixels arises (Figure 2.8). Mixed pixels can also occur

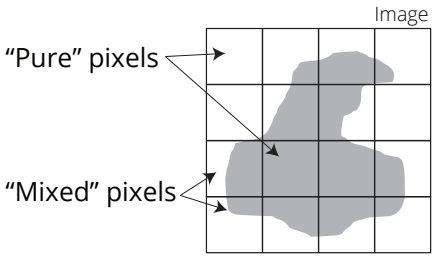

Figure 2.8: *The concept of mixed pixels within an image, where a specific material (grey) will only occupy a limited number of complete pixels (pure pixels) and the remaining pixels are mixed.*

independently of the spatial resolution of the sensor, as distinct materials can be combined into a homogeneous mixture resulting in a spectrum which is a composite of the individual spectra of the distinct materials (Plaza *et al.*, 2011). Hyperspectral imagery often contains few pixels which are considered pure, meaning that mixed pixels represent an additional challenge when processing hyperspectral data because their signals do not correspond to any single, well defined material (Rogge *et al.*, 2009; Manolakis and Shaw, 2002). Processing of the spectral signature variability and composition within mixed pixels remains one of the most challenging problems, practically and theoretically (Manolakis and Shaw, 2002).

In a geological context, the composition of materials within individual pixels is of interest, therefore, the processing applied differs from techniques such as target detection and classification. Target detection is useful for locating specific materials through diagnostic features in the spectra; it is often of particular interest in military applications for detecting military vehicles or objects, where target spectra are known *a priori*; a comprehensive view of target detection is given by Manolakis *et al.* (2003). Classification is similar to target detection, however, instead of detecting the presence of single features, classification aims to apply discrete 'labels' to pixels within a hyperspectral image. This classification then allows the end-user to characterise and identify these labels into meaningful land cover types within a scene (e.g. roads, forest, grassland and so on). A comprehensive review of hyperspectral classification is given by Camps-Valls *et al.* (2014).

The geological problem is posed somewhat differently from that considered in target detection and classification; using *a priori* spectra to find specific targets is not necessarily appropriate, as it is unlikely that all target spectra will be known in advance (though this technique can be applied in a geological context, e.g. Clark *et al.*, 2003). Classification is not effective as geological targets rarely, if ever, form distinct homogeneous regions which can be discretely labelled through classification techniques. Instead geological mapping (or bedrock mapping) considers the pixel spectrum in reference to the known reflectance of the mineral assemblages that make up individual rock units (Harris *et al.*, 2005; Rogge *et al.*, 2009). Units are mapped based on spatial continuity of surface composition and abundance using techniques such as endmember extraction and spectral mixture analysis (Rogge *et al.*, 2009), rather than using target detection or classification using individual minerals.

In a geological context, the hyperspectral processing chain (e.g. Rogge *et al.*, 2009; Plaza *et al.*, 2012) is as follows: (1) identify the number of endmembers to extract, (2) extract endmembers using an endmember extraction algorithm (EEA), (3) perform spectral mixture analysis (SMA) using the extracted endmembers to unmix the remaining pixels and (4) interpret endmembers and abundance images to produce geological maps. Step 3 follows the assumption that each pixel vector in the hyperspectral scene measures the response of multiple materials (Adams *et al.*, 1986) (i.e. each pixel in the image is formed from an arbitrary mixture of the extracted endmembers). This processing chain, also known as spectral unmixing, represents the state of the art in hyperspectral remote sensing; however, for completeness, a brief review of commonly applied spectral matching techniques is given in Section 2.5.2 followed by a review of the state of the art techniques of spectral unmixing in Section 2.5.3.

2.5.2 Spectral matching

Spectral matching techniques were developed in the pioneering days of hyperspectral image analysis in the 1980s (Gupta, 2003); the general approach involves the characterisation of absorption features, comparison to spectral libraries for identification and subsequent mapping. The most commonly applied techniques in this category of analysis are absorption band characterisation, spectral feature fitting and spectral angle mapping.

2.5.2.1 Absorption band characterisation This technique is based on quantifying the characteristics of an absorption band, such as the wavelength position, shape and strength (or depth) of a particular feature and was pioneered in the early days of hyperspectral data analysis (Kruse *et al.*, 1988, 1993). A comprehensive outline of the technique is given by van der Meer (2004). This technique is commonly achieved through fitting a continuum or hull (Figure 2.9), and following this, the normalised spectrum can be characterised by a number of features and compared to laboratory or field measurements (Kruse *et al.*, 1993). This technique is useful for rapidly analysing the large amounts of data in a hyperspectral scene by condensing the image spectral data into a small number of variables. However, the technique is limited by sensitivity to noise, the presence of mixing and subpixel mixtures, and ambiguity of defining (broad) absorption features (Gupta, 2003); nonetheless it performs well for materials with sharp, narrow absorption features.

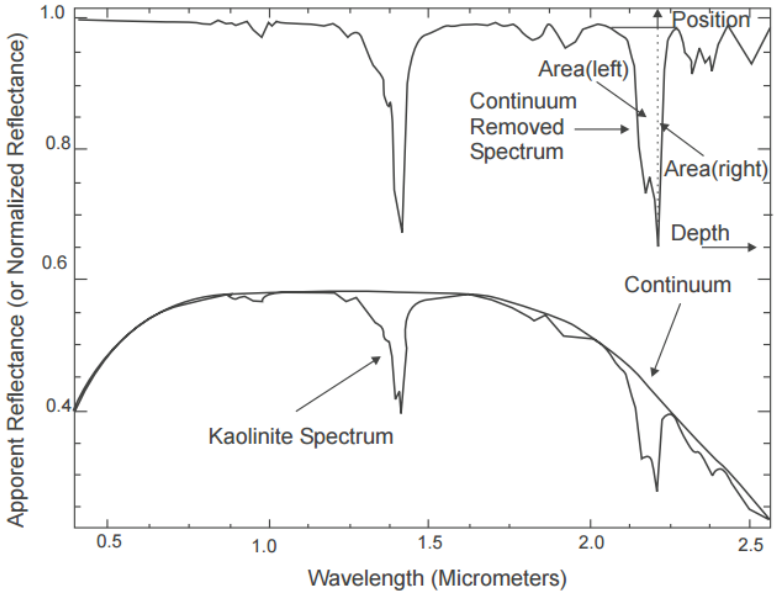

Figure 2.9: *Definition of the continuum and continuum removal and subsequent definition of absorption feature characteristics. From van der Meer (2004).*

2.5.2.2 Spectral feature fitting This technique involves matching the complete shape of a spectral feature and is a more rigorous approach than absorption band characterisation (Gupta, 2003). It is commonly achieved through the matching of image spectra to a reference (laboratory or field) spectra where an algorithm is applied to compute the degree of similarity between the two sets of spectra (Clark *et al.*, 1990). This technique requires *a priori* knowledge of specific minerals or objects in the scene, where spectral ranges which encompass known absorption features are defined (Gupta, 2003). The image and reference spectral data are continuum removed and a least-squares fit is calculated between the two, where the root mean square error (RMSE) of the fit gives the overall 'goodness-of-fit' and the band depth can indicate the abundance of a mineral (Gupta, 2003). The result is a 'spectral similarity map' which indicates both the distribution and relative abundance of mineral(s). However, this technique shares the limitations of absorption band characterisation, along with requiring a well developed reference library and knowledge of the imperfections in the data.

2.5.2.3 Spectral angle mapping Similar to spectral feature fitting, spectral angle mapping (SAM; Kruse *et al.*, 1993) is a technique which generates a spectral similarity map. The algorithm determines the spectral similarity of two spectra by calculating the angle between the spectra, treating them as vectors in a space with n dimensions (where n is the number of spectral bands). SAM is calculated using the image spectra and the reference spectra through the application of

$$\mathrm{SAM} = \cos^{-1}\left(\frac{\vec{t}\cdot\vec{r}}{||\vec{t}\,||\cdot||\vec{r}\,||}\right) \tag{9}$$

where t represents the spectrum of the target (endmember), r represents the spectrum of the reference spectrum and SAM is the spectral angle (in radians; 0 to 2π). This technique to determine similarity is insensitive to gain factors as the angle between two vectors is invariant with respect to the lengths of the vectors and allows for laboratory spectra to be directly compared to remotely sensed spectra (Kruse *et al.*, 1993). This technique is straightforward and can be quickly applied to an entire hyperspectral scene; often the entire wavelength range is utilised, though, in practice, it could be restricted to specific absorption features similar to the spectral feature fitting technique (Gupta, 2003). As well as sharing some of the same limitations as the spectral feature fitting technique, the technique also suppresses the lengths of vectors, which therefore removes or de-emphasises the effects of albedo (Gupta, 2003); this can be advantageous for identifying materials based solely on spectral shape (or spectral features) as illumination variations are removed.

2.5.3 Spectral unmixing

In almost all cases, the pixels in a hyperspectral scene are composed of mixed objects (Section 2.5.1; Gupta, 2003); each pixel in a scene is made up of a mixture of these spectrally diverse objects, or endmembers, and it is the collective response of the endmembers and their proportions that are measured at the sensor. It is therefore desirable to be able to 'unmix' these endmember spectra and their abundances (or proportions) to aid in their (geological) iden-

tification and subsequent mapping; this category of processing techniques are commonly known as spectral unmixing and offer advantages over the simple spectral matching techniques. We will review the state of the art techniques used for spectral unmixing of hyperspectral data in following sections.

2.5.3.1 Endmember: a brief definition Before continuing, it is necessary to outline exactly what is meant by the term *endmember*. As introduced in Section 2.5.1, a *spectral signature* is considered a unique representation of an individual material (Manolakis and Shaw, 2002). It is these *spectral signatures* which make up the well known 'spectral libraries' (e.g. Baldridge *et al.*, 2009), and these *spectral signatures* which are often used for techniques such as target detection (Clark *et al.*, 2003).

The notion of an endmember is not too dissimilar to that of a *spectral signature*. Here an endmember is defined as a unique spectrum derived from the hyperspectral scene itself. Endmembers are found directly from the image, regardless of the composition of materials (within individual pixels or within the scene itself) or imperfections in the dataset (e.g. sensor noise, atmospheric influence and so on) (Winter, 1999).

As a result of the mathematical complexity of finding endmembers (see Section 2.5.3.3), the imperfections found in real data and the high spatial and spectral resolution of hyperspectral imagery, it may be the case that not all endmembers are *recognisable spectra* (for example some may be related to sensor noise, or contain residual atmospheric effects). Additionally, it is almost certainly the case that not all endmembers can be identified *a priori* in real hyperspectral data (Chang and Du, 2004). However, it is through the careful interpretation of endmembers in reference to the local geological context, ancillary data (e.g. geochemical analysis) and knowledge of the imperfections within the data, that those endmembers which are *recognisable* are identified and used to produce *useful* abundance maps (Winter, 1999; Rogge *et al.*, 2009), which can be subsequently interpreted in a geological context.

2.5.3.2 Determining the number of endmembers Let us define the intrinsic dimensionality (ID) as the minimum number of parameters required to account for the observed properties of the data. In multivariate data, such as hyperspectral data, the ID cannot simply be determined by the number of components (the *component dimensionality*; e.g. the number of spectral bands). In very high dimensional data, such as hyperspectral data, the ID is expected to be much lower than the component dimensionality, as the data tend be distributed in a lower dimensional space (Chang and Du, 2004). For example, techniques such as Principal Component Analysis (PCA) and their eigenvalue distribution have been used to establish the ID (Richards, 2012), however, directly applying these techniques to hyerspectral imagery is difficult and may not be effective, even if applied (Chang and Du, 2004).

The ID of a hyperspectral image is considerably smaller than the component dimensionality, and accurately determining the ID is crucial for the success of endmember extraction and spectral mixture analysis (Chang and Du, 2004). The high spatial and spectral resolution of hyperspectral imagery means that the sensor is capable of uncovering many unknown endmembers (Section 2.5.3.1), which cannot be identified by visual inspection or known *a priori* (Chang and Du, 2004). In order to determine the number of endmembers (or signal sources, i.e. the intrinsic dimensionality) in a hyperspectral signal, a number of automated repeatable approaches based on mathematical and statistical analysis of the hyperspectral scene have been proposed; the two most popular methods are Virtual Dimensionality (VD) method (Chang and Du, 2004) and the Hyperspectral Signal Identification by Minimum Error (HySime) method (Bioucas-Dias and Nascimento, 2008).

The VD concept formulates the issue of whether a distinct signature is present or not in each of the spectral bands as a binary hypothesis testing problem, where a Neyman–Pearson detector is generated to serve as a decision-maker based on a prescribed false alarm probability (Chang and Du, 2004; Plaza *et al.*, 2011). The HySime uses a minimum mean squared error-based approach to determine the signal subspace in hyperspectral imagery (Bioucas-Dias and Nascimento, 2008). Studies have shown that both VD and HySime produce

the same estimated number of endmembers from a given hyperspectral scene (Plaza *et al.*, 2012). A brief explanation of each algorithm follows.

2.5.3.2.1 Virtual Dimensionality Virtual Dimensionality, or more specifically, Virtual Dimensionality using the Harsanyi–Farrand–Chang (VD-HFC) method, derived from the early works on hyperspectral data by Harsanyi *et al.* (1993), is briefly explained as follows (following Chang and Du, 2004). A correlation matrix and a covariance matrix are calculated from the hyperspectral data; the correlation and covariance eigenvalues provide an indication of the significance of each component, in terms of energy or variance. If there is no signal source contained in a particular component, the correspondent correlation eigenvalue and covariance eigenvalue are equal. Due to this, a binary composite hypothesis testing problem can be formulated using the difference between the correlation eigenvalue and its corresponding covariance eigenvalue. The null hypothesis represents the case of the zero difference, while the alternative hypothesis indicates the case that the difference is greater than zero. When the Neyman–Pearson test (Poor, 1994) is applied to each pair of correlation eigenvalue and its corresponding covariance eigenvalue, the number of times the test fails indicates how many signal sources are present in the image. In other words, a failure of the Neyman–Pearson test in a component indicates a truth of the alternative hypothesis, which implies that there is a signal source in this particular component.

2.5.3.2.2 HySime Following Bioucas-Dias and Nascimento (2008), the Hyperspectral Signal Identification by Minimum Error (HySime) technique starts by estimating the signal and the noise correlation matrices, using multiple regression. A subset of eigenvectors of the signal correlation matrix is then used to represent the signal subspace. This subspace is inferred by minimizing the sum of the projection error power with the noise power, which are, respectively, decreasing and increasing functions of the subspace dimension. Therefore, if the subspace dimension is overestimated, the noise power term is dominant, whereas if the subspace dimension is underesti-

mated, the projection error power term is the dominant. The overall scheme is computationally efficient, unsupervised, and fully automatic in the sense that it does not depend on any tuning parameters, whilst yielding comparable results to other techniques, such as VD-HFC (Bioucas-Dias and Nascimento, 2008).

2.5.3.3 Endmember extraction algorithms For successful SMA the extraction of spectral endmembers from an image is commonly preferred over the use of field or laboratory spectra for two main reasons; (1) library and field spectra may not represent all relevant endmember spectra of the surface components or are inadequate representations, and (2) image endmembers have the advantage of directly sampling surfaces in the scene (collected under the same conditions as the sensor) (Rogge *et al.*, 2009). The extraction of endmembers from hyperspectral imagery has undergone a large amount of research and numerous algorithms have been proposed in the literature (Du *et al.*, 2008). These can be broadly categorised into pure pixel and mixed pixel approaches (Figure 2.8), which are briefly outlined below. Reviews of endmember extraction techniques are given by some (Martínez *et al.*, 2006; Li *et al.*, 2007; Veganzones and Grana, 2008).

Due to the large number of endmember extraction algorithms in the published literature, the Remote Sensing end-user will often apply those algorithms which are widely available in commercial off-the-shelf software (e.g. the Environment for Visualising Images; ENVI, 2014) or open source algorithms (e.g. Endmember Induction Algorithms Toolbox; EIA, 2014), as many of the published techniques are difficult to implement due to their mathematical and computational complexity.

2.5.3.3.1 Pure pixel EEA Pure pixel approaches assume that the image contains pixels which are pure, or relatively pure spectra, meaning that little or no mixing with other endmembers has occurred within such a pixel. Pure pixel techniques have been widely used and a wealth of algorithms have been proposed in the literature (e.g. Boardman, 1993; Palmadesso *et al.*, 1995; Bate-

son and Curtiss, 1996; Winter, 1999; Ifarraguerri and Chang, 1999; Neville *et al.*, 1999; Ren and Chang, 2003; Gruninger *et al.*, 2004; Nascimento and Bioucas-Dias, 2005; Chang and Plaza, 2006; Chan *et al.*, 2011, 2012). These algorithms are based on the assumption that endmembers form a linear mixture model and can be extracted by exploiting the geometry, where endmembers are indentified by the vertices of a simplex, as illustrated in Figure 2.10. Perhaps the most widely used technique is the Pixel Purity Index (PPI; Boardman, 1993); this technique, whilst very widely used does suffer from a number of limitations (Chaudhry *et al.*, 2006). The PPI has two highly sensitive parameters, uses a randomised set of initial skewers, requires human intervention to manually select the final set of endmembers via an n-dimensional visualisation tool and is not an iterative process, therefore does not guarantee that the PPI-found endmembers are actually true endmembers (Chaudhry *et al.*, 2006). A number of automated and repeatable approaches have been implemented to overcome these limitations (e.g. Chaudhry *et al.*, 2006; Chang and Plaza, 2006), including techniques such as N-FINDR (Winter, 1999) and more recently, alternative techniques such as Vertex Component Analysis (VCA; Nascimento and Bioucas-Dias, 2005).

Additionally, a number of algorithms which consider the spatial distribution of endmembers (still under the pure pixel assumption) have been developed, in two main categories: (1) techniques which are applied prior to applying an endmember extraction technique such as Spatial–Spectral Preprocessing (SSPP; Zortea and Plaza, 2009) and superpixel segmentation (Thompson *et al.*, 2010), and (2) techniques which use spatial information and extract endmembers simultaneously, such as automated morphological endmember extraction (AMEE; Plaza *et al.*, 2002) and spatial–spectral endmember extraction (SSEE; Rogge *et al.*, 2007).

In the former category, the techniques have the advantage that any number of a wealth of existing EEAs can be applied but the endmembers will still have a spatial weighting. The SSPP technique requires an image to be classified prior to processing using the SSPP algorithm, where a k-means classification is often applied (Zortea and Plaza, 2009), though applying this classification step to

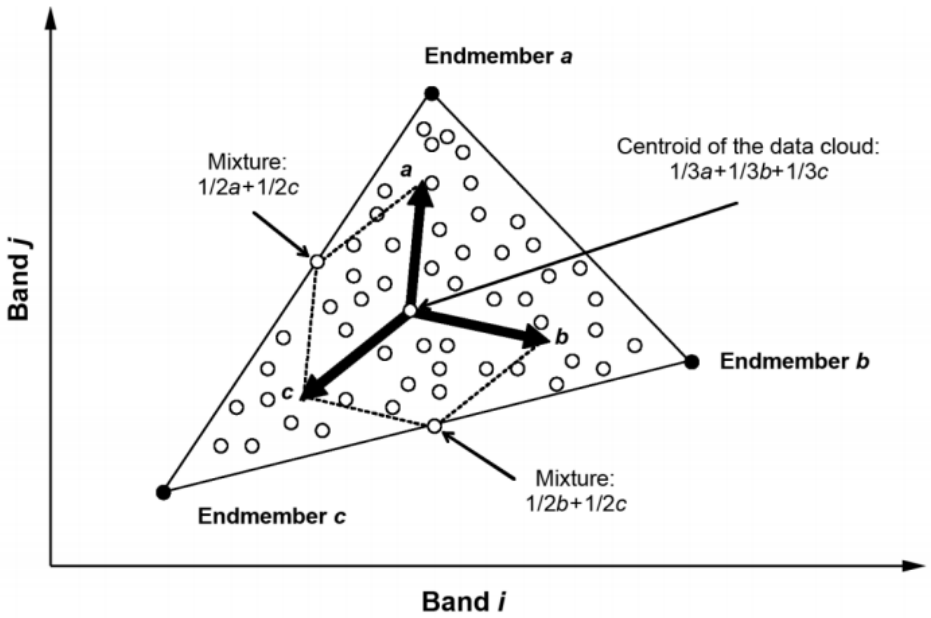

Figure 2.10: *An illustration of the linear mixture model and endmember identification from the simplex formed by Bands i and j. From Martínez* et al. *(2006).*

high-dimensional data can be prohibitively slow. The SSPP then weights pixels in the image based on their spectral importance in terms of its spatial context (Zortea and Plaza, 2009). The superpixel segmentation algorithm averages image spectra from homogeneous regions comprised of several pixels having similar values by intentional over-segmentation of the image which aggregates scene features into segments called superpixels (Thompson *et al.*, 2010; Gilmore *et al.*, 2011). The superpixel approach has been shown to be beneficial on low SNR datasets and can aid in deriving endmembers that more closely resemble manually derived endmembers (Thompson *et al.*, 2010). This is due to averaging several pixel spectra within a single superpixel and thus the technique reduces the noise variance proportionally to the superpixel area. However the technique can act to degrade spectral purity by aggregating multiple spectrally variable pixels and can suppress subtle spectral features (Thompson *et al.*, 2010).

Techniques in the latter category extract endmembers whilst considering the spatial component. For the AMEE approach, a computationally complex processing chain is applied where a morphological eccentricity index (MEI)

is defined by applying morphological image dilation and erosion techniques (Plaza *et al.*, 2002), though its performance on large datasets is very slow. The SSEE technique has number of tunable inputs and performs a singular value decomposition to determine spectral variance but imposes a spatial constraint when extracting endmembers (Rogge *et al.*, 2007).

In most cases spatial algorithms are much slower to process due to their increased computational complexity and non-vectorised implementation, along with the addition of a number of tunable parameters (e.g. window size). However, the superpixel endmember extraction technique includes a data reduction step by agglomerating neighbouring pixels into averaged spectral regions which is beneficial for low signal to noise ratio datasets and acts to speed up processing times (Thompson *et al.*, 2010).

2.5.3.3.2 Mixed pixel EEA The pure pixel approach has been quite successful when images contain pure pixels; however, given the presence of the mixing at different scales (even at microscopic levels), the pure pixel assumption is not always true, as some images may only contain pixels which are completely mixed (Plaza *et al.*, 2012).

The complexity of the problem is increased in a mixed pixel scenario, since the endmembers, or at least some of them, are not in the dataset (Bioucas-Dias, 2009). Techniques in this category follow from the seminal ideas of Craig (1994), based on the minimum volume transform (MVT). Other algorithms building from this work include the minimum volume constrained non-negative matrix factorization method (MVC-NMF; Miao and Qi, 2007), the minimum volume simplex analysis (MVSA) algorithm (Li and Staunton, 2008), the convex analysis-based minimum volume enclosing simplex algorithm (MVES; Chan *et al.*, 2009), the simplex identification via split augmented Lagrangian (SISAL) algorithm (Bioucas-Dias, 2009), and iterated constrained endmembers (ICE; Berman *et al.*, 2004).

Whilst these approaches can yield state of the art results, their major shortcoming is the time they take to process, as they are highly computationally complex to implement and run (Bioucas-Dias, 2009).

2.5.3.4 Spectral mixture analysis Spectral mixture analysis (SMA), also referred to as *spectral unmixing*, has been a goal from the pioneering days of hyperspectral imaging (Goetz *et al.*, 1985) and continues be of great importance in the study of hyperspectral image processing (Schaepman *et al.*, 2009). It is almost inevitable, regardless of the spatial resolution of the sensor, that a hyperspectral spectrum collected in the natural environment will be a mixture of the spectra of the various materials found within the spatial extent of the image (Adams *et al.*, 1986; Plaza *et al.*, 2011). The availability of hyperspectral sensors with a number of spectral bands that exceeds the number of spectral mixture components (Green *et al.*, 1998) has led to an over-determined system of equations where, given a set of endmembers (Section 2.5.3.1) unmixing through SMA to determine apparent pixel abundance fractions can be defined in terms of a numerical inversion process (Plaza *et al.*, 2011). There are two main approaches for SMA; linear and non-linear SMA.

Linear SMA assumes that the measured spectra at the sensor can be expressed as a linear combination of endmembers, weighted by their abundances (Keshava and Mustard, 2002). The linear SMA approach negates the potential effects of scattering or secondary reflections during the data acquisition, and hence, the measured spectrum can be expressed as a linear combination of the endmember spectral signatures to produce the relative abundances of the materials represented in the mixed pixel (Figure 2.11a).

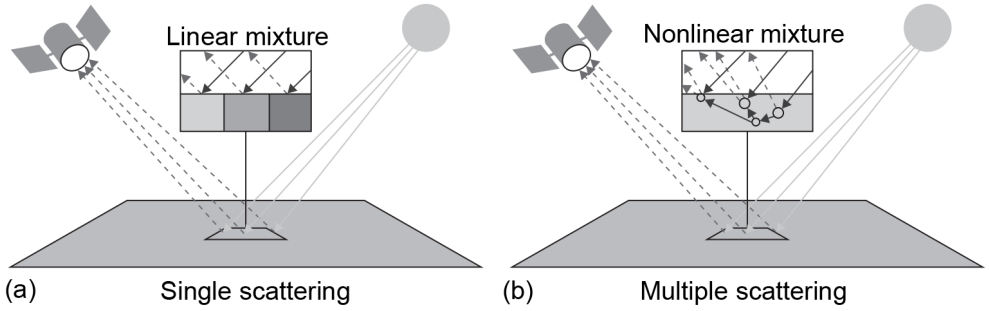

Figure 2.11: *Graphical interpretation of the linear SMA (a) versus the non-linear SMA (b). From Plaza* et al. *(2011).*

Although the linear model has practical advantages such as ease of implementation and flexibility in different applications (Chang, 2003), non-linear SMA may best characterize the resultant mixed spectra for certain endmember distributions, such as those in which the endmember components are randomly distributed throughout the field of view of the instrument (Guilfoyle *et al.*, 2001; Plaza *et al.*, 2009a). In those cases, the mixed spectra collected at the imaging instrument are better described by assuming that part of the source radiation has undergone multiple scattering prior to being measured at the sensor (Figure 2.11b).

In order to be able to correctly apply SMA to a hyperspectral dataset two requirements need to be fulfilled (Plaza *et al.*, 2011); (1) estimation of the number of endmembers present in the hyperspectral scene (see Section 2.5.3.2) and (2) correct extraction (or determination) of a set of endmembers (see Section 2.5.3.3), after which SMA can be applied to establish the correspondent abundance fractions of each endmember for each pixel. SMA techniques can be categorised into either linear or non–linear SMA, as explained in the following paragraphs.

2.5.3.4.1 Linear SMA Applying linear SMA to a given mixture requires that endmembers occur as spatially segregated patterns (Keshava and Mustard, 2002), which can be used to deconvolve a spectrum into abundances of its constituent endmember spectra using a least squares approach, given as (Rogge *et al.*, 2009)

$$R_b = \sum_{i=1}^{n} F_i S_{ib} + E_b \tag{10}$$

where R_b is the fractional abundance of the pixel at band b, F_i is the fractional abundance of endmember i, S_{ib} describes the reflectance of endmember i at band b, n is the number of endmembers and E_b is the error of the fit at band b. Equation 10 can produce fractional endmembers which are mathematically correct, but physically unreasonable (e.g. negative endmember contributions). Equation 10 is therefore solved subject to the constraints that fractional abudances sum-to-one (ASC; abundances sum-to-one constraint)

and fractional abundances are non-negative (ANC; abundance non-negative constraint) (Rogge *et al.*, 2009).

Fully constrained linear spectral unmixing (FCLSU), through the implementation of ASC and ANC is usually recommended to produce physically realistic fractional abundances (Heinz and Chang, 2001). However, abundances predicted using linear SMA are most accurate when only the endmembers that comprise a given pixel are used, with larger errors occurring when too few or too many endmembers are used (Heinz and Chang, 2001; Rogge *et al.*, 2009). A large number of studies have applied linear SMA (e.g. Small, 2001; Sabol *et al.*, 2002; Neville *et al.*, 2003; Lu *et al.*, 2004; Yang *et al.*, 2014; Magendran and Sanjeevi, 2014, amongst others).

2.5.3.4.2 Non–linear SMA In a non–linear model, the interaction between the endmembers and their fractional abundance is given by a non–linear function, which is not known *a priori*. Various techniques have been proposed in the field of machine learning, with neural networks some of the first non–linear SMA approaches proposed (Benediktsson *et al.*, 1990). Neural networks have demonstrated great potential to decompose mixed pixels due to their inherent capacity to approximate complex functions (Bishop, 2007). Although many neural network architectures exist for decomposition of mixed pixels in terms of non–linear relationships, mostly feed-forward networks of various layers, such as the multilayer perceptron (MLP), have been used (Plaza *et al.*, 2009b; Plaza and Plaza, 2010; Baraldi *et al.*, 2001). It has been shown in the literature that MLP-based neural models, when trained accordingly, generally outperform other non–linear models such as regression trees or fuzzy classifiers (Liu and Wu, 2005).

In addition to neural networks, other techniques such as Support Vector Machines (SVM) have also been used (Camps-Valls and Bruzzone, 2005; Plaza *et al.*, 2011) and have shown promise due to their higher classification accuracy with smaller training sets (Plaza *et al.*, 2011). SVMs can be used with a variety of kernels which can vastly increase their flexibility for non–linear SMA; the most commonly used kernels are the polynomial kernel, the Gaussian kernel

or the spectral angle mapper (SAM) kernel (Plaza *et al.*, 2009a, 2011). Other techniques including Bayesian statistical and bilinear models (Halimi *et al.*, 2011) and unmixing using a combined linear – non–linear fluctuation model have been proposed (Chen *et al.*, 2013). A comprehensive review of spectral unmixing was given in the seminal paper by Keshava and Mustard (2002); other reviews include Keshava (2003) and more recently, a paper by Dobigeon *et al.* (2014) summarising the cutting edge advances in this discipline.

The majority of non–linear SMA approaches evolved in the computer science and signal processing disciplines and often are not widely available to users in the Remote Sensing community. In addition, many of the techniques are often tested on small, synthetic datasets, hence their performance on large, real-world hyperspectral data is currently limited by the computational complexity of the techniques; however, recent advances have aimed to take advantage of parallel processing techniques to reduce computational time (Plaza *et al.*, 2008).

2.5.4 Thermal remote sensing case studies

The majority of geological mapping studies using thermal infrared remote sensing data have utilised multispectral infrared data. The ASTER and the TIMS sensors have demonstrated the utility of TIR data to discriminate a wide range of minerals, especially silicates, as well as proving useful for lithological mapping (Rowan and Mars, 2003; Chen *et al.*, 2007; Rogge *et al.*, 2009; Haselwimmer *et al.*, 2010, 2011; Salvatore *et al.*, 2014). Relevant examples using satellite data, including VNIR/SWIR and TIR data from the Polar regions are described in Section 2.6.

The development of airborne hyperspectral TIR sensors producing images with hundreds of contiguous spectral channels provides the potential for a step-change in the range and accuracy of compositional information retrievable remotely. Currently, there are a number of operational airborne hyperspectral TIR instruments, including the SEBASS, the AHS, TASI, and the OWL (van der Meer *et al.*, 2012). Previous studies using airborne hyperspectral TIR data have illustrated the exceptional potential of these types of sensors for mapping silicates, carbonates, sulphates, and clays (Hewson *et al.*, 2000; Cudahy *et al.*, 2001; Calvin *et al.*, 2001; Vaughan *et al.*, 2003b, 2005; Aslett *et al.*, 2008; Riley and Hecker, 2013; Kruse and McDowell, 2015). A number of key studies are briefly reviewed.

There are only a handful of studies which present geological mapping using airborne hyperspectral TIR data, the majority of which utilise the SEBASS sensor. SEBASS is a push broom scanner developed by Aerospace Corporation, consisting of an array of 128 $\times$ 128 Helium cooled SiAs detectors recording thermal data from 7.4 to 13.4 μm for a 128 pixel-wide swath at an instantaneous field of view (IFOV) of 1 milliradian.

In a technical report, Hewson *et al.* (2000) demonstrated the potential of SEBASS for mapping an epithermal-altered Tertiary volcanic complex containing areas of pervasive argillic, propylitic and silicic alteration in Oatman, Arizona. A detailed preprocessing chain was applied to the SEBASS data, including atmospheric correction, TES, noise removal using the minimum

noise fraction (MNF; Boardman and Kruse, 1994; Green *et al.*, 1998) and removal of bands at the extremes of the sensors wavelength range. Following this, spectral unmixing and feature fitting techniques were applied: the pure pixel model was assumed with endmembers extracted manually using the pixel purity index; mapping of endmembers was carried out using a matched filter (MF; Boardman *et al.*, 1995), a type of target detection algorithm, and spectral library measurements were used to identify and interpreted the extracted endmembers. The study showed that hyperspectral TIR imagery can successfully map areas of silicification, quartz-calcite veining, kaolinite-rich areas of alteration and/or weathering, and possibly alunite alteration, as well as discriminate different carbonates and identify grain size effects; however, mapping of phyllosillicates remained ambiguous (Hewson *et al.*, 2000).

The first peer-reviewed study utilising airborne hyperspectral TIR data was by Kirkland *et al.* (2002) who utilised SEBASS data for mapping carbonates at Mormon Mesa, Nevada, USA. Their study demonstrated that microscopic surface roughness, not readily apparent to the eye, introduced a cavity effect and volume scattering which reduced spectral contrast between geological units and placed a higher signal-to-noise (SNR) ratio requirement on airborne data; with a SNR of ~3000:1, SEBASS was able to detect and identify spectrally subtle materials through manual interpretations of airborne data with respect to high quality laboratory data and supporting geochemical and petrographic analyses (Kirkland *et al.*, 2002).

Vaughan *et al.* (2003b) utilised a series of SEBASS flightlines collected over Virginia City and Steamboat Springs, Nevada, USA at a spatial resolution of 2 m. The airborne data was atmospherically corrected using the in-scene atmospheric correction (ISAC) technique, followed by TES using the NEM method. Noise was removed from the SEBASS data using MNF prior to spectral unmixing; PPI was used to manually derive endmembers which were subsequently unmixed and classified using a mixture-tuned matched filter (Vaughan *et al.*, 2003b). The data were used to map silicate and sulphate minerals with agreement to laboratory and field spectroscopy, though the authors noted improvements in instrument calibration, atmospheric correction, and

information extraction techniques could yield improvements in mapping. The hyperspectral TIR data "nevertheless show[ed] significant advancement over multispectral thermal images" in their ability to map subtle spectral differences in mineralogy (Vaughan *et al.*, 2003b).

Vaughan *et al.* (2005) also performed a similar study at Steamboat Springs, Nevada, USA, to map minerals associated with an active geothermal and hot spring system using SEBASS imagery and field and laboratory spectroscopy, also employing the PPI to perform spectral unmixing. The utility of hyperspecral TIR for mapping rock forming minerals and alteration minerals at the well-known Cuprite mining site, Nevada, has also been demonstrated (Riley and Hecker, 2013). Using SEBASS data and a spectral feature fitting approach (due to the well exposed and vegetation free outcrops at Cuprite) Riley and Hecker (2013) were able to accurately map rock forming minerals associated with unaltered rocks as well as alteration minerals, validated using spectral library data and corroborated by comparison with VNIR/SWIR mapping.

2.6 Geological remote sensing in the Polar regions

2.6.1 Antarctic case studies

Prior to this research, no studies had been published on the use of airborne hyperspectral data for the purposes of lithological mapping in the Antarctic. There are a limited number of studies relating to the use of multispectral data for lithological mapping. Only one study has taken place on the Antarctic Peninsula; Haselwimmer *et al.* (2010) investigated the potential of multispectral Advanced Spacebourne Thermal Emission and Reflectance Radiometer (ASTER) for lithological mapping. For Antarctica as a whole there are very few published studies, with two studies undertaken in Northern Victoria Land, East Antarctica and one in the McMurdo Dry Valleys, West Antarctica.

In a study from the Tarn Flat region of Terra Nova Bay, Casacchia *et al.* (1999) analyzed Landsat Thematic Mapper (TM) and SPOT-XS data with reference to field multispectral reflectance measurements of rock samples acquired using an EXOTECH radiometer (with four broad bands in the VNIR region). Rock spectra of granite, glacial drift, detritus and mafic intrusive rocks displayed varying albedo in the VNIR region providing a basis for their discrimination at the wavelengths of the TM sensor. Satellite image processing included pan-sharpening the results of selective PCA (Crosta method) as applied to the Landsat TM data using the higher spatial resolution SPOT-XS image (using a RGB-IHS transformation). A mininum-distance supervised classification was applied to the output of this procedure using training areas defined for snow, ice and the different rock units. The classification effectively discriminated granite, detritus, and a mixed class of glacial drift/mafic intrusive rocks with results that were in close agreement with field observations.

Favretto and Geletti (2004) analysed ASTER VNIR/SWIR bands with the aim of discriminating granite and gabbro exposures over part of the Prince Albert mountain chain, Victoria Land. Image processing was undertaken with the Constrained Energy Minimization (CEM; Harsanyi, 1993) spectral mapping (target detection) algorithm using mineral library spectra as reference endmembers: biotite and serpentinite reference spectra were used

for the analysis as these reflect the composition of the granites and altered gabbros in the study area. The distribution of biotite and serpentinite in the ASTER processing results showed some agreement with field observations of the distribution of granite and gabbro (Favretto and Geletti, 2004). However, they made no attempt to mask snow, ice or shadowed rock from the ASTER data prior to their analysis, which caused significant misclassification in the mapping results (i.e. snow mapped as either biotite or serpentinite). The fact that the ASTER scene was acquired in early November suggests that shadowing and seasonal snow cover may have also been a particular problem for their analysis. Other criticisms of the study include the use of non-atmospherically corrected ASTER data and the somewhat arbitary choice of reference endmembers.

Haselwimmer *et al.* (2010) used ASTER VNIR/SWIR and TIR data from several sites from the Wright Peninsula region of Adelaide Island. To complement the satellite based ASTER data, reflectance spectra of approximately 50 weathered and fresh surface samples was collected under laboratory conditions. Prior to image analysis, the spectra of the samples was investigated to assess its potential for discrimination at ASTER wavelengths. Samples were convolved to ASTER bands and a limited set of lithological groups (rhyolitic volanic rocks and granitoids) displayed unique albedo and absorption features which showed potential for discrimination at ASTER wavelengths.

A combination of qualitative and quantitative image processing techniques were applied to the ASTER data to generate lithological information. Band ratios and PCA were used to produce RGB composite images which were effective at discriminating minerals that displayed AlOH and FeOH/MgOH absorption features in the VNIR/SWIR and features associated with quartzose, felsic and mafic lithologies in the TIR. The ASTER surface reflectance and thermal emission data was classified into distinct spectral classes broadly corresponding to different mineral assemblages and bulk rock compositions through a Matched Filter (MF) applied to image derived endmembers. Haselwimmer *et al.* (2010) concluded that ASTER data allowed for broad discrimination of the main rock types, with most success in discriminating granites to

those of intermediate composition (granodiorites) and difficulty in discriminating specific felsic intrusive lithologies (e.g. tonalite, quartz monzonite), due to their lack of distinctive features in the VNIR/SWIR and similarity at TIR wavelengths. They demonstrated that ASTER data are limited in their ability to discriminate uniquely different lithologies but do provide a range of lithologic information which can be used to assist field based mapping techniques, or used to refine or validate localised/inferred geological mapping.

Additionally, they noted that the influence of rock encrusting lichens caused "significant problems for lithological mapping using the VNIR/SWIR region" on the islands in the Ryder Bay region (Léonie, Anchorage and Lagoon Islands). Although sparsely developed, lichen cover does significantly impact the geological mapping approach; a finding supported by the ASTER results and the field observations, which suggested that the lichen cover has the greatest effect (Haselwimmer *et al.*, 2010).

More recently, Salvatore *et al.* (2014) used a combination of satellite remote sensing and laboratory spectroscopy to identify geochemical variations within the Ferrar Dolerite exposed in the McMurdo Dry Valleys. Dolerite units were analysed with the Advanced Land Imager (ALI) and ASTER thermal emission data. Using spectral unmixing techniques focusing on the VNIR and TIR regions, they were able to identify meso- and macro- scale alteration of dolerite sills, which had previously only been identified through laboratory and field analysis. Through linear unmixing of ASTER TIR data using laboratory data, they were able to identify spectrally pure outcrops of Dolerite; TIR data was used as deconvolving mixtures in the VNIR was more complex due to the significant contribution of volume scattered rays which refract into and out of individual mineral grains (Salvatore *et al.*, 2014). Laboratory data revealed a link between alteration and VNIR absorption features and TIR signatures of altered dolerites were identified, though only in fine grained dolerites exposed in the Beacon Valley. They note that addition of hyperspectral datasets could provide critical information on the presence, nature and distribution of alteration minerals in the McMurdo Dry Valleys; they particularly note

the absence of SWIR data which could have aided in the identification of phyllosilicates, sulphates and carbonates (Salvatore *et al.*, 2014, p. 18).

2.6.2 Arctic case studies

In comparison to the Antarctic there is significantly more published research on the use of remote sensing for lithological mapping in Arctic regions. These studies provide relevant analogues for this research given the paucity of case studies from the Antarctic. However, it is recognized that the physiography of the Antarctic Peninsula is different to the study areas discussed in this review. In particular, the peninsula is more extensively glaciated and rocks are less well exposed when compared to the Arctic study areas.

Most published studies from the Arctic have been from Greenland (Birnie *et al.*, 1989; Rivard and Arvidson, 1992; Thomassen *et al.*, 2002; Tukiainen and Thorning, 2005; Bedini, 2009) and northern Canada (An *et al.*, 1996; Wickert and Budkewitsch, 2004; Harris *et al.*, 2005; Rogge *et al.*, 2009) with some published work from the Svalbard archipelago (Lyberis *et al.*, 1990) and Russian Arctic islands (Lorenz, 2004). The older studies broadly encompass lithological mapping using multispectral satellite data, with more recent studies focusing on the analysis of airborne hyperspectral data for mineral mapping (Rogge *et al.*, 2009). A selection of these papers are discussed as part of this review.

Birnie *et al.* (1989) analyzed Landsat TM data in conjunction with broadband rock spectra with the aim of mapping the tertiary gabbroic rocks of East Greenland that included the Skaergaard intrusion. Remote sensing was considered suited to this task as the region was thought to be poorly vegetated and is almost impossible to access directly. Image processing of the TM data included the use of PCA and a supervised classification using training areas for the different lithological units (gneiss country rock and lithological units within the Skaergaard intrusion). The results enabled the delineation of the gabbroic intrusions from Precambrian gneissic country rocks but were not able to discriminate lithological units within the intrusions themselves, owing

to the subtle differences in reflectance of these rocks. They found a number of specific problems in the Greenland context of this work that reduced the ability to discriminate subtle differences in rock reflectance: (1) the TM data included seasonal snow cover with many mixed rock/snow pixels as well as perennial snow fields where no lithological information could be extracted; (2) lichens and mosses were actually better developed than previously thought and had a strong effect on rock reflectance; (3) melt water on southeast facing dip slopes and glacier-polished surfaces caused significant specular reflection from rocks; and (4) the region is heavily glaciated with significant recent glacial deposits (moraine and glacial flour) that directly obscure underlying bed rock or contribute to the reflectance of rock outcrops at the sub-pixel scale.

Rivard and Arvidson (1992) used Landsat TM data and field reflectance spectra to assess the potential of imaging spectroscopy to undertake lithological mapping of the Archean terranes of south west Greenland. The work analysed TM data for a portion of the island of Storo, southwestern Greenland and field reflectance spectra acquired from rocks and vegetation samples. The Arctic terrain in this part of Greenland includes abundant tundra vegetation and lichens that cause problems for the use of multispectral remote sensing. They aimed to establish if imaging spectroscopy could provide additional information for lithological discrimination. Their results of analysing the TM data confirmed that tundra completely obscures rock exposures and ubiquitous lichen cover does cause significant problems for lithological discrimination of the amphibolite, anorthosite, gneiss and granite outcrops on the island. The field reflectance spectra demonstrated that at the outcrop scale mineral absorption features are still retained from areas of mixed rock and lichens that could be used to discriminate different rocks. These results imply that hyperspectral imagery could be used for lithological mapping of lichen covered rock exposures, but would require unmixing techniques using rock and lichen endmembers (Rivard and Arvidson, 1992).

Various studies from northern Canada have been undertaken to assess the potential for using remote sensing to assist geological mapping. Wickert and

Budkewitsch (2004) investigated the effectiveness of lithological mapping using ASTER data of a folded sequence of shallow to deep marine sediments, and basalts exposed on Belcher Islands in Canada's Hudson Bay. The study area was selected as it had good bedrock exposure, little vegetation, low relief and existing high quality geological mapping. They analysed the reflective bands of a snow-free ASTER scene that was atmospherically corrected and orthorectified using a Shuttle Radar Topography Mission (SRTM) Digital Elevation Model (DEM). Spectral analysis of the calibrated ASTER reflectance data was achieved using qualitative and spectral mapping methods (Matched Filter, Spectral Angle Mapper). The results of ASTER data analysis were compared against the existing reliable field mapping, that indicated broad discrimination of lithologies exposed on Belcher Island was possible; the results presented in the paper suggest that only some of the 16 distinct units that had been previously mapped directly were discriminated using ASTER.

Harris *et al.* (2005) used airborne PROBE hyperspectral data to undertake lithological mapping of an area of southern Baffin Island, Canada. They applied spectral analysis to an atmospherically corrected and snow/ice/water-masked dataset, using the MNF transform to define image reference endmembers, which were then mapped using supervised classification and matched filtering procedures. The rock image endmembers displayed quite similar spectra owing to the effects of lichens but displayed enough variability as a function of the different rock mineralogies to enable lithological mapping. As a result two major lithological groups (metatonalites and metagabbros, using vegetation as a proxy) and three compositional units (psammites, quartzites, and monzogranites) were mapped; these results showed good general agreement with the existing published geological map and demonstrate the benefits of high spectral/spatial resolution data for lithological mapping in areas with significant lichens developed.

Other regions of the Arctic have received comparatively little attention as regards the use of remote sensing for lithological mapping. Lorenz (2004) fused Landsat TM data with high-resolution panchromatic Corona imagery (3m pixel size) in order to undertake geological mapping of October Revolu-

tion Island in the Severnaya Zemla archipelago, Russian Arctic. Good rock exposure and the relatively flat lying topography enabled a full structural interpretation of the study area. They also undertook simple qualitative image processing to discriminate different lithologies; this was assisted by masking areas of soil. Lyberis *et al.* (1990) attempted to use SPOT multispectral data coupled with rock reflectance measurements to discriminate different lithologies for part of the island of Spitsbergen in the Svalbard archipelago.

Perhaps the best analogue for hyperspectral remote sensing for geological mapping is the recent work of Rogge *et al.* (2009). Following from the earlier works by Harris *et al.* (2005), Rogge *et al.* (2009) utilised a hyperspectral dataset from Baffin Island, Canada. They applied multiple endmember extraction techniques in conjunction with linear SMA to produce a predictive geological map of a diverse assemblage of lithologic units that are part of the northeastern segment of the Paleoproterozoic Trans-Hudson orogen (Rogge *et al.*, 2009). The number of endmembers was arbitrarily chosen and endmembers were extracted and interpreted in context of spectra collected in the field and complementary geochemical analysis. The endmembers were then used to interpret fractional abundance images to produce a predictive lithological map; though the authors noted the significant influence of lichen in the study area and their endmember set included both lichen and rock/lichen mixture endmembers (Rogge *et al.*, 2009).

2.6.2.1 Influence of lichen There have been a number of studies into the optical properties of lichens to aid in the analysis of multispectral and hyperspectral imagery. Bechtel *et al.* (2002) determined that light transmission through lichens in the VNIR and SWIR was less than 3%, meaning that lichens can completely obscure light reflected from the underlying rock substrate. They also determined the spectral similarity of multiple lichen species in the SWIR, supporting earlier observations (Rivard and Arvidson, 1992). Zhang *et al.* (2004) demonstrated that there is linear mixing of lichen-rock spectral signatures, with spectral unmixing results showing high correlation ($R^2 > 0.9$). Feng *et al.* (2013) recently expanded from the solar domain by considering

the spectral properties of rock encrusting lichens in the midwave infrared (MIR; 3 to 5 μm) and TIR domains. Feng *et al.* (2013) determined that lichens display low reflectance and spectral contrast in the TIR, but could be used to mask pixels in imagery that encompass the greatest abundance of rock encrusting lichens to facilitate geological mapping.

The polar regions could be seen as ideal test sites for geological remote sensing studies, as they have extensive bedrock exposure and limited development of surface vegetation (Feng *et al.*, 2013) compared to more temperate environments. However, in these regions, lichens are typically the first colonisers on rock surfaces (Kiang *et al.*, 2007) and their presence can inhibit geological mapping by obscuring spectral features useful for mineral identification at solar wavelengths (Rivard and Arvidson, 1992; Bechtel *et al.*, 2002; Haselwimmer *et al.*, 2010; Feng *et al.*, 2013).

2.7 Summary

Hyperspectral imagery was originally developed for mineral exploration purposes and has proven one of the most useful contributions in the field of geological remote sensing, due to its ability aid in the mapping of lithological units or mineral assemblages (Goetz *et al.*, 1985). The TIR domain has great potential for investigating rock forming minerals and the potential to offer significant improvements over VNIR/SWIR data alone (van der Meer *et al.*, 2012).

In polar regions, the application of remote sensing data is particularly advantageous; from a geological mapping perspective there are still significant gaps in coverage (in Antarctica) owing to the difficulties of undertaking traditional field mapping techniques in such a harsh environment, especially in areas where topography can often restrict access completely; hence, geological remote sensing could offer significant advantages.

We note two key gaps in the present literature, which this study aims to address:

1. There is a paucity of studies utilising hyperspectral TIR data. Of the available published studies, the analytical approaches have not currently utilised the state of the art, automated and repeatable processing techniques, but instead focused on simpler spectral matching techniques, or utilised manually derived endmembers in spectral unmixing techniques.
2. There are no published studies using hyperspectral TIR in either (a) Antarctica or (b) a continental margin arc setting. The range of igneous rocks emplaced in continental margin arcs informs us about the tectonic history of the margin and even relatively subtle difference between granitoid types (e.g. tonalite, diorite, granodiorite, granite) are significant as they record variations in melting depths and the stress regime in the lithosphere. The TIR domain has potential for investigating key granitoid rock forming minerals, therefore there is scope to reveal new insights in to the Antarctic continental margin arc, if discrimination of granitoid types is possible.

3 Study area and datasets

3.1 Introduction

An airborne hyperspectral survey was conducted in Antarctica in February 2011. The British Antarctic Survey collaborated with ITRES Research Ltd. (ITRES) and Defence Research and Development Canada (DRDC, Suffield). DRDC's three hyperspectral sensors, the CASI-1500, SASI-600, and TASI-600, acquired approximately 1000 km^2 of airborne hyperspectral data covering parts of the VNIR, SWIR, and TIR regions of the electromagnetic spectrum from seven areas (Figure 3.1; Table 3.1).

The original planning and motivation for the hyperspectral data acquisition was to establish a high-resolution baseline vegetation survey. The Antarctic Peninsula (AP) has seen an increase in mean annual air temperature of ~3°C in the last 50 years (Vaughan *et al.*, 2003a), making it one of the most rapidly changing areas on the planet. The changing climate - a result of rising temperatures - has led to higher summer-growing season temperatures (Convey and Smith, 2006) and local glacial retreat (Pritchard and Vaughan, 2007). This has exposed new rock outcrops and areas of scree and soil for colonisation by terrestrial biota (Walther *et al.*, 2002; Convey and Smith, 2006). Due to the exceptional rates of change, the AP has been highlighted as a globally important barometer for identifying the biological consequences of climate change (Convey, 2003). To monitor and assess changes of AP vegetation, a robust, quantitative assessment of vegetation is required (Fretwell *et al.*, 2011). Field based techniques in the Antarctic face significant logistical challenges as a result of the climate and topography in addition to the limited spatial coverage and invasive nature of the work. A non-invasive, remote sensing approach provides many advantages over field based techniques. Work on the hyperspectral data for vegetation mapping is on-going (e.g. Black *et al.*, 2014a; Casanovas *et al.*, 2015; Appendix A); however, as hyperspectral imagery was originally developed for geological applications (Goetz *et al.*, 1985), this study was carried out to investigate the dataset for geological purposes.

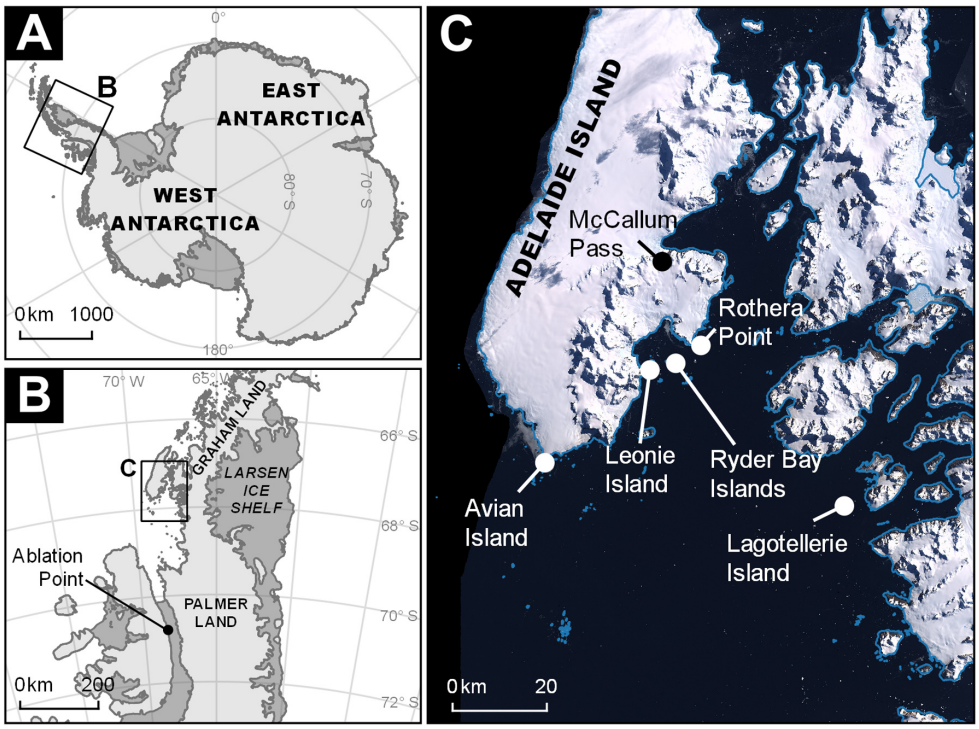

Figure 3.1: *Location map context of the Antarctic Peninsula within Antarctica (A), and the location of the seven sites of hyperspectral data acquisition on the Antarctica Peninsula (B and C).*

The seven survey areas were selected with a view to vegetation investigations, hence a number of sites were not suited to geological investigations. The decision not to pursue investigations in a number of areas was motivated by the following reasons: areas which were inaccessible in the field, areas which had strong influence of man-made features; and areas with near-homogenous lithologies (or in some cases, a combination of these) were not investigated further. This initially excluded the inaccessible areas of Ablation Point, Avian Island and Lagotellerie Island; the nature of the investigation into the hyperspectral data requires that ground truth samples and surveys be used to fully understand and interpret the hyperspectral data hence these areas were excluded.

This left the remaining areas close to the BAS main research station (Rothera) including the Ryder Bay islands (Anchorage Island, Lagoon and Kirsty Island), Rothera Point, Léonie Island and McCallum Pass. Rothera Point was excluded

due to the large presence and influence of man-made features, such as the airstrip, hangar and various buildings, as well as being composed entirely of granodiorite. Lagoon and Kirsty Island, Léonie Island and McCallum Pass were not investigated due to their near-homogeneous lithologies, which did not allow for investigating the potential of the data for discriminating different lithologies. Anchorage Island was selected as the study site; Anchorage Island has a range of lithologies, representative of a continental margin arc setting, the island has limited influence from man-made features, and its proximity to Rothera Point meant a field survey could be carried out.

The following sections review the Anchorage Island study area and its geological setting, the airborne hyperspectral data acquisition and the field spectral survey.

Instrument	Purpose	Specification
CASI-1500	Hyperspectral imaging in the VNIR	1500 across-track imaging pixels 72 spectral bands Spectral range of 367.6 - 1055.5 nm Spectral bandwidth of 9.6 nm 40° field of view 0.5 m ground resolution
SASI-600	Hyperspectral imaging in the SWIR	600 across-track imaging pixels 100 spectral bands Spectral range of 950 - 2450nm Spectral bandwidth of 15 nm 40° field of view 1.0 m ground resolution
TASI-600	Hyperspectral imaging in the TIR	600 across-track imaging pixels 32 spectral bands Spectral range of 8000 - 11000 nm Spectral bandwidth of 109.5 nm 40° field of view 1.0 m ground resolution
Applanix POS/AV 510	Inertial navigation system	3-axis SAGEM IMU Integrated dual frequency Trimble GPS reciever Real-time roll: 0.05 degrees Real-time pitch: 0.05 degrees Real-time heading: 0.1 degrees

Table 3.1: *Acquisition sensor information (ITRES, 2012).*

3.2 Study area and geological context

The Antarctic Peninsula is part of the proto-Pacific continental margin arc that was magmatically active at least from the Permain through to ~20 Ma. Continental margin arcs are the primary sites for the generation of new continental crust on Earth. Long lived continental margin arcs record multiple episodes of increased magmatism, cessation of magmatism, periods of extension and compression, and switching between dominantly volcanic or plutonic regimes (Burton-Johnson and Riley, 2015). The range of igneous rocks emplaced in continental margin arcs informs us about the tectonic history of the margin, and even relatively subtle difference between grani-

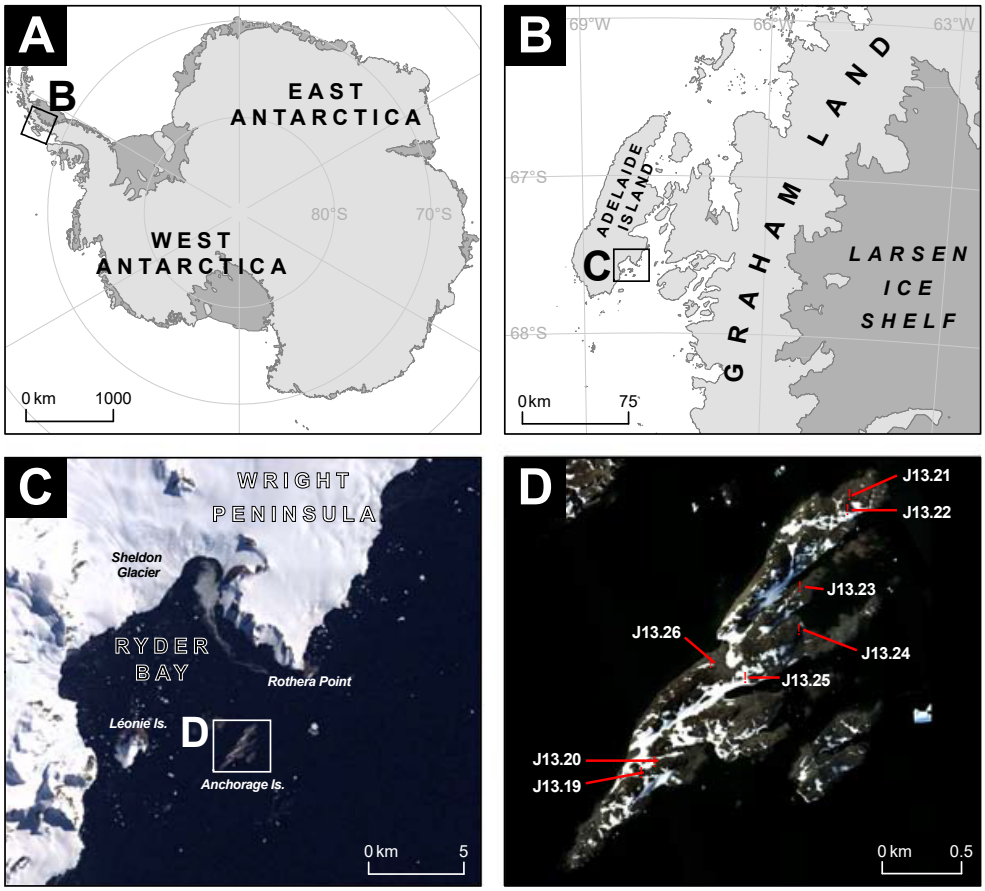

Figure 3.2: *Location maps showing the context within Antarctica (A), the location of Adelaide Island within the Antarctic Peninsula (B) and the location of Anchorage Island in the context of Ryder Bay (C; labelled). (D) shows a true colour composite of Anchorage Island with field localities (labelled red circles).*

toid types (e.g. tonalite, diorite, granodiorite, granite) are significant as they record variations in melting depths and the stress regime in the lithosphere (Burton-Johnson and Riley, 2015).

Anchorage Island is located in Ryder Bay to the south of the larger Adelaide Island, on the Antarctic Peninsula. The British Antarctic Survey (BAS) main research station is located close by on Rothera Point, Adelaide Island (Figure 3.2C). Anchorage Island was surveyed as part of a hyperspectral airborne campaign in February 2011 and visited for follow-up ground truth fieldwork in January/February 2014 (Figure 3.2D).

During the Middle-Late Jurassic, Adelaide Island was located on the western edge of the continental margin in a probable fore-arc position. Magmatism continued until at least 20 Ma with the emplacement of late-stage tonalite-granodiorite plutons and related silicic ignimbrites (Riley *et al.*, 2012).

A local-scale geological map of the study area, based on previous geological mapping updated with recent field observations, is shown in Figure 3.3. The main geologic unit on Anchorage Island is the Adelaide Island Intrusive Suite (AIIS). The AIIS is dominated by granodiorites, tonalites and gabbroic rocks; granodiorite and hybrid gabbro/granodiorite plutons are the most abundant. The granodiorite is leucocratic and is dominated by plagioclase (∼50–60 %), which often weathers orange/brown; quartz typically accounts for ∼10 % of the rock and K–feldspar ∼5 %. Mafic minerals are common (25 %), with green/brown amphibole abundant, along with minor amounts of biotite and epidote. The plutonic rocks are cut by dolerite and intermediate-felsic composition dykes, which are typically < 1 m thick, dip steeply ($> 75°$ to the southeast) and strike in the range 210–230°.

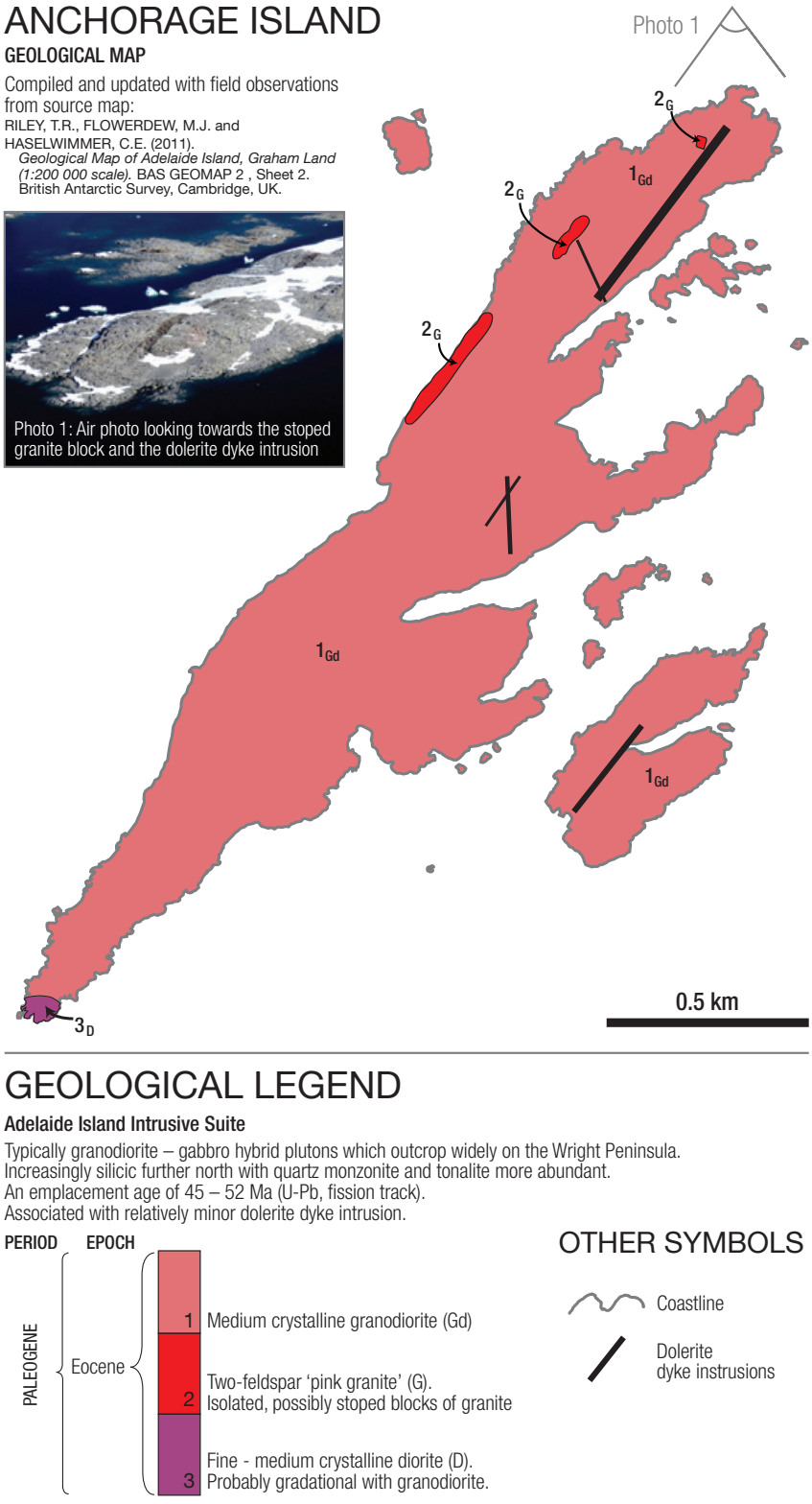

Figure 3.3: *Local scale geological map of Anchorage Island.*

3.3 Airborne hyperspectral data acquisition

The Anchorage Island airborne hyperspectral survey was conducted on 3rd February 2011. The three sensors, CASI, SASI, and TASI, acquired simultaneous hyperspectral data covering parts of the VNIR, SWIR, and TIR regions of the electromagnetic spectrum (Table 3.1). The acquisition system hardware and other equipment (inertial measurement unit and instrument control units) were installed on a single mounting plate in a BAS DeHavilland Twin Otter aircraft and flown unpressurised (Figure 3.4). Radiometric correction and geometric correction were carried out by ITRES Research. A total of 17 flight lines were orthorectified and a mosaicked image in calibrated at-sensor radiance units (Level 1B; Table 3.2) was delivered, at a ground spatial resolution of 0.5 m for CASI and 1 m for SASI and TASI.

Figure 3.4: *The sensor installation in the BAS Twin Otter aircraft (ITRES, 2012); Abbreviations are as follows: ICU, instrument control unit; IMU, inertial measurement unit.*

Data Level	Description
Level 0	Reconstructed, unprocessed instrument and payload data at full resolution, with any and all communications artifacts (e.g., synchronization frames, communications headers, duplicate data) removed.
Level 1A	Reconstructed, unprocessed instrument data at full resolution, time-referenced, and annotated with ancillary information, including radiometric and geometric calibration coefficients and georeferencing parameters (e.g., platform ephemeris) computed and appended but not applied to Level 0 data.
Level 1B	Level 1A data that have been processed to sensor units (not all instruments have Level 1B source data).
Level 2	Derived geophysical variables at the same resolution and location as Level 1 source data.
Level 3	Variables mapped on uniform space-time grid scales, usually with some completeness and consistency.
Level 4	Model output or results from analyses of lower-level data (e.g., variables derived from multiple measurements).

Table 3.2: *NASA's standard data processing levels.*
From: `http://science.nasa.gov/earth-science/earth-science-data/data-processing-levels-for-eosdis-data-products`.

3.4 Field reflectance and emission spectral survey

As part of this study, in February 2014, myself and colleagues at the British Antarctic Survey, ITRES Research and Defence Research and Development Canada (DRDC) collaborated to carry out a field campaign in the Ryder Bay area acquiring TIR emissivity spectra. A total of eight field localities were surveyed on Anchorage Island (Figure 3.2D) encompassing a northeast-southwest transect, though specific localities were selected due to their accessibility. At each locality, between 3 and 5 hand specimens were collected from representative lithological units, mafic enclaves and mineral viens (e.g. epidote, quartz) within close proximity (<10 m) of each field locality. Hand specimens were collected from weathered, nadir facing rock surfaces. Although varying levels of lichen cover were present, samples were measured from lichen-free (or minimal lichen covered) areas on each sample. Hand specimens were measured using an ABB (ABB, Affolternstrasse 44, CH-8050, Zurich, Switzerland) full spectrum reflectometer (FSR) to gather measurements of spectral reflectivity and emissivity. The FSR is a Fourier Transform Infrared (FTIR) spectrometer with a contact probe which uses a Michelson interferometer (MB-3000) with mercury cadmium telluride (MCT) and indium arsenide (InAs) detectors.

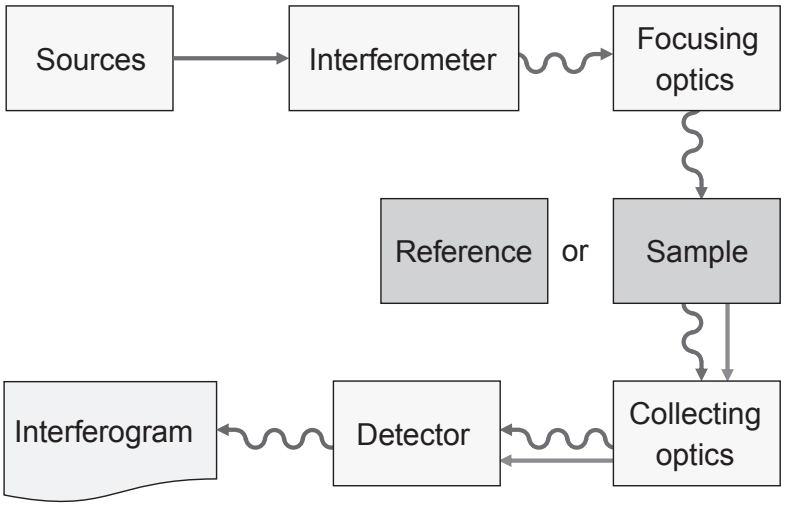

Figure 3.5: *Flowchart describing the operational process applied by the FSR instrument to derive interferograms which are subsequently Fourier transformed to produce spectral reflectance measurements.*

The FSR has a wavelength range from 0.7–14 μm, a spectral resolution of <1 nm and a spot size of ~4 mm. The FSR was developed by ABB for DRDC. The FSR represents a significant improvement over existing field FTIR spectrometers; the FSR is compact and portable, has a high signal to noise ratio due do its cooled MCT and InAs detectors, as well as covering a large spectral range from the visible all the way to the TIR. The FSR is also a contact probe instrument, similar to spectral radiometers conventionally use for VNIR/SWIR spectroscopy.

The spectral resolution of the FSR was set to 0.1 nm and the FSR was set up such that each spectrum produced by the instrument represented the average of 128 individual spectral measurements. A calibrated gold panel is built into the FSR allowing for the calculation of emissivity; the gold panel was used to recalibrate the FSR at the start of each batch of measurements at each field locality. Figures 3.5 and 3.6 show details and operational use of the FSR.

Figure 3.6: *Images showing practical use of the FSR in field and laboratory conditions.*

4 Methodology

4.1 Introduction

Geological remote sensing using optical data and spectral techniques have had a long history of research and development; the ability to derive 'laboratory-like' spectral data from airborne and spaceborne platforms allows for the direct identification of surface materials and lithologies (Goetz *et al.*, 1985). Spectral remote sensing has yielded unprecedented geological and lithological mapping capabilities, however other remote sensing technologies also offer utility for geological mapping (Gupta, 2003).

The microwave region of the electromagnetic spectrum, from 1 mm to 1 m, is a large atmospheric window suitable for remote sensing. From a geological perspective, techniques such as synthetic aperture radar (SAR) have been useful due to their ability to map geomorphological characteristics, terrain, relief, sub-surface structures and ground deformation, though lithological identification is not currently possible (Gupta, 2003). Additionally, active remote sensing technologies, such as LiDAR offer utility for geological mapping. High resolution DEMs, acquired by LiDAR, can be used to map geological structures through interpretation of terrain characteristics (e.g. Webster *et al.*, 2006) though again, lithological identification is not currently possible.

The afore mentioned techniques are complimentary to spectral techniques operating in the optical region of the electromagnetic spectrum, but are not considered in this study. Here, the optical domain is the focus, for several reasons: there has been no previous work utilising hyperspectral data in the Antarctic, there is a general paucity of studies and lack of defined methods for lithological mapping using hyperspectral TIR data, and a lack of hyperspectral TIR studies in a continental margin arc setting (Section 2). This thesis focuses on developing techniques relevant to hyperspectral (TIR) data in the polar context of the research, though it is anticipated that complimentary information could be provided through combination with other remote sensing technologies.

4.1.1 Preliminary analysis of visible and shortwave data

Whilst the VNIR/SWIR spectral range has been widely exploited for lithological mapping purposes, in the context of the Anchorage Island study area (Section 3.2), the use of VNIR/SWIR data is not advantageous. The igneous lithological units do not have distinguishing features at VNIR/SWIR wavelengths and any analysis will be complicated by the strong surficial coating of rock-encrusting lichens as demonstrated by previous studies (Haselwimmer *et al.*, 2010; Section 2.6.2).

The hyperspectral VNIR/SWIR data was subject to some preliminary analysis which revealed a number of issues that were compounded during the atmospheric correction process (Black *et al.*, 2014b; Appendix A) and subsequent derivation of surface reflectance data, outlined briefly as follows.

The spectral range of the CASI and SASI data (Table 3.1; page 59) has an approximate 100 nm overlap, between 950 nm and 1055.5 nm. Analysis revealed an offset in radiance values within this overlap range (Figure 4.1). In the overlap range CASI radiance values were found to be larger than the corresponding SASI radiance, with a trend of increasing radiance offset with increasing wavelength. This radiance offset is present in the radiometrically calibrated data and atmospherically corrected data. Several factors are likely to have produced the radiance offset.

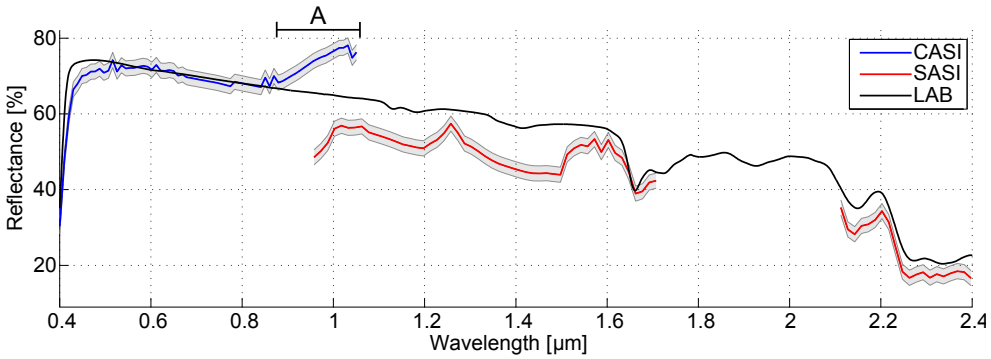

Figure 4.1: *Results from atmospheric correction of CASI (blue) and SASI data (red) compared to laboratory measurements (black) from a calibrated target within the scene. Label (A) highlights the overlapping spectral range of the two sensors as well as the systematic spike in CASI reflectance. From Black* et al. *(2014b).*

The first and most probable contributing factor is 2nd order light contributions. The CASI sensor's diffraction grating produces a 2nd order diffraction spectrum, whose blue end overlaps with the red-near infrared (NIR) end of the 1st order spectrum. Illumination conditions at the time of acquisition may have allowed this effect to lead to additive background signal at the red-NIR end. The second contributing factor could be the reduced calibration accuracy in the NIR end of the spectrum, as the CASI sensor is less sensitive at the longest wavelengths (S. Achal, *personal comm.*).

Thirdly, preliminary investigations also revealed a systematic underestimation of radiance values in the SWIR (from the SASI instrument). This is attributed to the conditions during acquisition. The instruments were operating in an unpressurised aircraft, with temperatures significantly outside the normal operational range; the SASI instrument was as much as 20° C (68° F) outside its normal operating range. These conditions meant there was a noticeable degradation in the response of the sensor, and hence the measured at-sensor radiance was lower in the SWIR data (Figure 4.2).

During the acquisition of hyperspectral data over Anchorage Island, the chang-

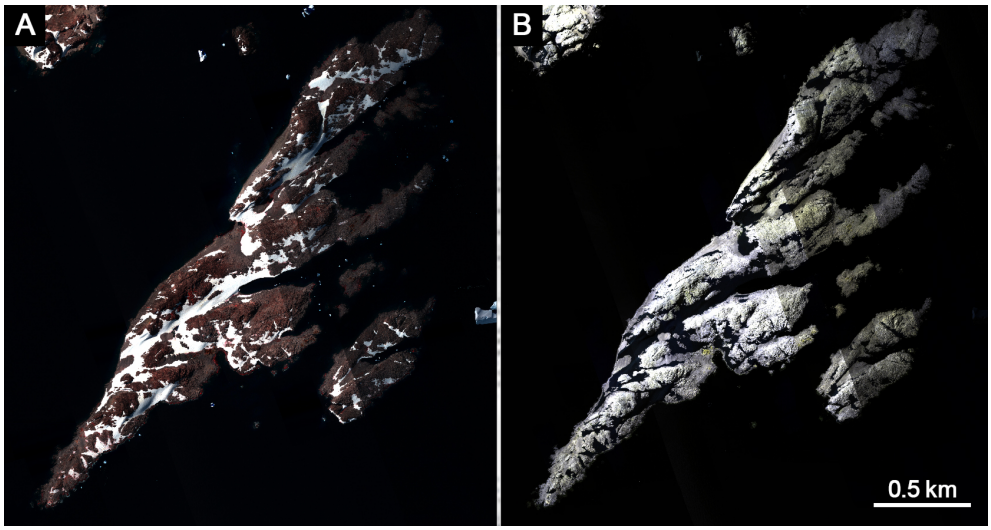

Figure 4.2: *(A) shows CASI true colour, atmospherically corrected image of Anchorage Island (R: 640.6 nm, G: 554.6 nm, B: 458.8 nm). (B) shows a SASI colour composite, atmospherically corrected image of Anchorage Island (R: 1557.5 nm, G: 1602.5 nm, B: 2202.5 nm).*

ing atmospheric conditions caused significant flight line illumination variations which could not be adequately compensated during the atmospheric correction process (Figure 4.2). A non-uniformly illuminated mosaic could cause significant problems in deriving appropriate geological endmembers; the imperfections in the data would lead to extracted endmembers which are not geologically interpretable, as a result of the sensor noise, residual atmospheric effects and illumination variations (Winter, 1999).

These reasons contributed to the decision not to pursue the analysis of the VNIR/SWIR data for geological purposes. However, the data provided useful insights into the ability to map and identify vegetation and lichen cover in a polar environment; further analysis was carried out using both satellite data and the hyperspectral VNIR/SWIR data to produce a new methodology for mapping of lichens on the Antarctic Peninsula (Black *et al.*, 2014a; Casanovas *et al.*, 2015; Appendix A).

4.1.2 Theoretical basis

To produce a lithological map using hyperspectral data the primary interest is the differentiation of distinct lithologies and mineralogical differences within individual pixels; therefore, the processing applied differs from techniques such as target detection, classification or spectral matching (Rogge *et al.*, 2009; Section 2.5). Here, state of the art spectral unmixing techniques were applied, in an automated manner, moving away from simpler spectral matching techniques or manual processes. The three steps required for the successful use of spectral unmixing techniques have been previously defined (Section 2.5.3): (1) identify the number of endmembers to extract from the hyperspectral image, (2) extract endmembers from the image using an endmember extraction algorithm (EEA) and (3) perform spectral mixture analysis (SMA) to determine the abundances of each endmember. During this process, the endmembers can be identified, either manually by an expert user with prior knowledge of the local geology, or through comparison to known reflectance/emittance of the likely mineral assemblages that make up individual rock units using

either spectral libraries or field spectral measurements (Harris *et al.*, 2005; Rogge *et al.*, 2009). A lithological map is then produced as the output of the automated processing chain.

Due to the high spatial resolution (1 m) of the hyperspectral data, a pure pixel scenario is assumed; this is consistent with other studies, where the pure pixel scenario has been successful with ground resolutions of up to tens of metres (Rogge *et al.*, 2009; Plaza *et al.*, 2011). The two major steps required for the success of the processing chain are (1) accurately determining the number of endmembers and (2) extraction of the endmembers from the image using an EEA (Section 2.5.3). In order to investigate the efficacy of these methods at a variety of signal to noise ratios, synthetically generated hyperspectral data was used. The use of synthetic data means that the endmembers are known in advance and the data mixed with differing noise levels allows a robust assessment of algorithms; both the inputs and outputs are known and can be measured (unlike with real hyperspectral data), therefore a straightforward accuracy assessment can be performed. The use of synthetic hyperspectral data for algorithm development and investigation has been widely demonstrated (e.g. Plaza *et al.*, 2002; Chang and Du, 2004; Nascimento and Bioucas-Dias, 2005; Rogge and Rivard, 2006; Bioucas-Dias and Nascimento, 2008; Bioucas-Dias, 2009).

A limitation of the use of synthetic hyperspectral data is that it does not allow for investigation of the spatial component. The inclusion of spatial weighting within the endmember extraction has been investigated by a number of studies that consider the spatial distribution of pixels when carrying out endmember extraction; techniques such as Spatial–Spectral Preprocessing (SSPP; Zortea and Plaza, 2009), Automated morphological endmember extraction (AMEE; Plaza *et al.*, 2002), spatial–spectral endmember extraction (SSEE; Rogge *et al.*, 2007) and superpixel endmember extraction (Thompson *et al.*, 2010). Here the synthetic data was randomly mixed and the 'pixels' randomly distributed, hence there was no spatial pattern to the synthetic 'image'; therefore, spatial techniques were not investigated when considering the on synthetic data (though they were applied when considering the real hyperspectral data).

The methodology is therefore split into two sections. Firstly, Section 4.2 focuses on the use of synthetic hyperspectral data generated from the measured field spectra. Using this synthetic data the two major steps required for the success of the processing chain are investigated: (1) determining the number of endmembers and (2) extracting the endmembers. Algorithms are compared for each of the two steps using synthetic data at various noise levels and the results validated. Following this, in Section 4.3, the challenge of processing real hyperspectral data is tackled. The ancillary geochemical and petrographic analyses of samples from Anchorage Island are presented, followed by the preprocessing, and finally the automated lithological mapping processing chain. The automated processing chain was developed with input from the synthetic data investigations as well as consideration of other algorithms which have proven performance on low SNR data and those which also consider the spatial component during processing.

4.2 Synthetic hyperspectral data

4.2.1 Spectral resampling

Field emissivity spectra collected by the FSR were convolved to the spectral response functions of the TASI sensor through

$$L_i = \frac{\int L_s(\lambda) r_i(\lambda) \delta\lambda}{\int r_i(\lambda) \delta\lambda} \tag{11}$$

where L_i is convolved emissivity, $L_s(\lambda)$ is the sample's reflectance at band i and wavelength λ, $r_i(\lambda)$ is the spectral response function of band i at wavelength λ_j, over the wavelength interval of the sample $\delta\lambda$.

4.2.2 Synthetic data generation

The synthetic hyperspectral data set comprises 10,000 random mixtures generated from 3 rock spectra measured in the field (granite, granodiorite and dolerite), along with a spectral library measurement of sea water. Each rock spectrum collected by the FSR was resampled to the spectral response function of the TASI sensor (Equation 11) resulting in a spectrum containing 32 bands spanning 8 to 11.5 μm with a spectral resolution of 109.5 nm (Figure 4.3).

The synthetic hyperspectral data was generated by mixing of the 4 spectra using a Dirichlet distribution (as defined in Lillesand *et al.*, 2004) to give the abundances of each mixture (e.g. Bioucas-Dias and Nascimento, 2008; Bioucas-Dias, 2009) where 5000 'pixels' were generated. During the generation of the synthetic data, zero-mean white additive Gaussian noise was included to simulate signal to noise ratios (SNR) ranging from 10:1 to 100:1 (e.g. Nascimento and Bioucas-Dias, 2005). The pure pixel assumption was implicit in the generation of the synthetic data, as no maximum purity level was specified during the synthetic mixing process; thus, one 'pixel' could contain 100% of a single spectrum (Nascimento and Bioucas-Dias, 2005).

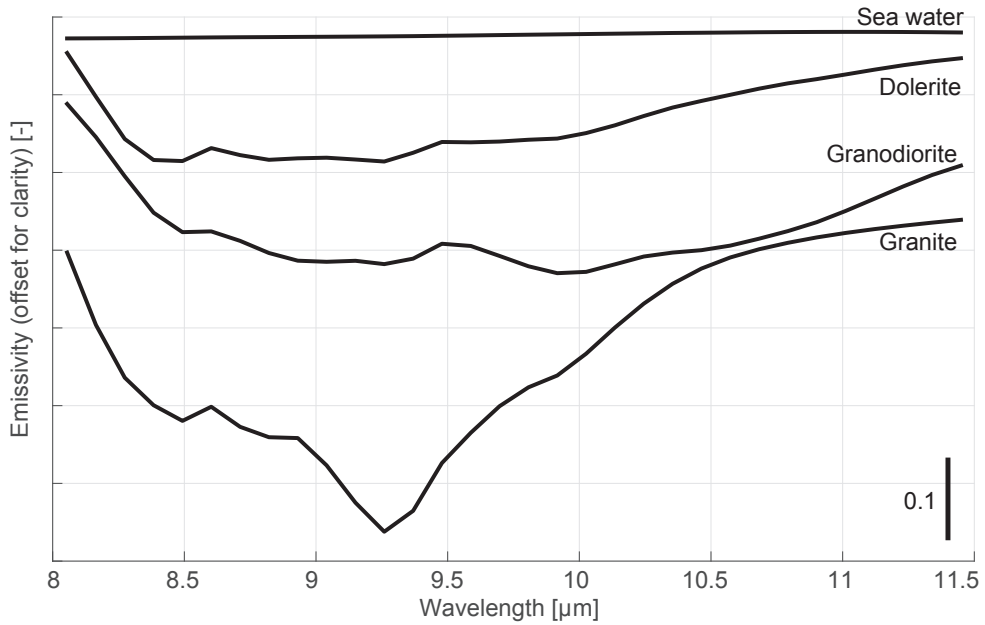

Figure 4.3: *Spectral profiles convolved to TASI wavelengths which were utilised in the generation of the synthetic hyperspectral data.*

4.2.3 Processing chain

4.2.3.1 Step 1: Determining the number of endmembers The first step is to determine the number of endmembers. For the investigation of this step, the two most popular techniques, VD-HFC[1] and HySime[2] were used, implemented in MATLAB (MathWorks, 2011). A detailed description of the implementation of the VD-HFC algorithm is described in Chang and Du (2004) and full details of the HySime algorithm are given by Bioucas-Dias and Nascimento (2008), as well as a summary presented in Section 2.5.3.2.

In order to assess the robustness of the algorithms in spite of noise, the signal to noise ratio (SNR) of the spectra in the synthetic data was varied from 10:1 to 100:1 in steps of 10. For each SNR value, the synthetic data was generated with 5000 'pixels' and the endmember extraction algorithms were applied to the synthetic data. To achieve a reliable result, this process was repeated 10,000 times for each SNR value. For each of the 10,000 runs the number of endmembers was calculated using the VD-HFC and HySime algorithms.

[1]VD-HFC: http://www.ehu.eus/ccwintco/uploads/f/f8/EIA_Toolbox_reduced_v04.zip
[2]HySime: http://www.lx.it.pt/~bioucas/code/demo_HySime.zip

4.2.3.2 Step 2: Endmember extraction In the second step, the endmembers are extracted. Here the pure pixel algorithms, N-FINDR[3] and VCA[4] were applied, again due to their implementation in the MATLAB environment, along with their relatively quick processing times and proven success at extracting endmembers (Winter, 1999; Nascimento and Bioucas-Dias, 2005; Chang and Plaza, 2006; Plaza *et al.*, 2012). These techniques are fully automated with their only inputs being the number of endmembers to extract and the image itself (in this case, fixed to 4). A detailed description of the implementation of the N-FINDR algorithm is described in Winter (1999) and full details of the VCA algorithm is given by Nascimento and Bioucas-Dias (2005).

For the endmember extraction, a similar approach to Step 1 was used. Again, the effectiveness of the algorithms under a range of signal to noise ratios was investigated. The same randomised initialisation process was used; 5000 'pixels' of synthetic data were generated at a range of SNR values from 10:1 to 100:1 in steps of 10, and each ran 10,000 times. For each run the endmembers were extracted and compared to input spectra, with the root mean square error (RMSE) calculated through

$$\mathrm{RMSE} = \frac{1}{n}\sum_{i=1}^{n}(\hat{Y}_i - Y_i)^2 \tag{12}$$

where $\hat{Y}_i$ represents the ith predicted reflectance value (of the extracted endmember) and Y_i represents the ith reflectance value of the library input spectra, and n represents the number of endmembers (4 in this case). The RMSE value was calculated with respect to each endmember and library spectra combination and the lowest value selected (i.e. the closest match). This yielded n RMSE values for each run which were then averaged to give an overall RMSE value.

[3]N-FINDR: http://sourceforge.net/projects/matlabhyperspec
[4]VCA: http://www.lx.it.pt/~bioucas/code/demo_vca.zip

4.3 Real hyperspectral data: Anchorage Island

4.3.1 Geochemical and petrographic analyses

Four samples representative of the main lithological units (granite, granodiorite and dolerite) were further investigated to understand their geochemistry; two granodiorite samples (J13.19.10 and J13.22.5), one granite (J13.21.10) and one dolerite sample (J13.22.10). Thin sections were examined using a petrological microscope, a FEI Quanta 650F QEMSCAN scanning electron microscope and a Cameca SX-100 electron microprobe. Backscattered electron (BSE) images were collected on the QEMSCAN using an accelerating voltage of 20 kV and a working distance of $\sim$ 13 mm. Point samples ($\sim$ 5 μm) were analysed using the electron microprobe (EPMA) to determine major element geochemistry and identify minerals and mineral phases from grains within thin sections. Point counting (Galehouse, 1971) was used to determine mineral composition; 500 points were counted in thin section on each of the four samples.

The samples were also analysed by X-ray fluorescence spectrometry (XRF) to determine whole-rock major and trace elements using a PANalytical Axios-Advanced XRF spectrometer at the University of Leicester. Powders from whole-rock samples were obtained through crushing in a steel jaw crusher and powdering in an agate ball mill. Major elements were determined from fused glass discs and trace elements from powder pellets. Loss on ignition (LOI) values were calculated by igniting $\sim$3 g of each sample in ceramic crucibles at 950 °C. Glass discs were prepared from 0.6 g of non-ignited powder and 3 g of lithium metaborate flux, melted in a Pt-Au crucible over a Spartan burner then cast into a Pt-Au mould. Powder pellets of 32 mm diameter were produced from mixing 7 g of fine ground sample powder with 12-15 drops of a 7% polyvinyl alcohol (PVA) solution (Moviol 8-88) and pressed at 10 tons per square inch.

4.3.2 Hyperspectral data preprocessing

Figure 4.4 shows a flowchart of the preprocessing steps. Radiometric correction and geometric correction were carried out by ITRES Research Ltd. using their propriety tools. In the first step, radiometric and spectral calibration coefficients were applied to convert the raw digital numbers into spectral radiance values. In the second step, the ITRES proprietary geometric correction software utilised the navigation solution, bundle adjustment parameters, and digital elevation models (DEMs) to produce georeferenced radiance image files for each flight line. In addition, flight lines were combined into an image mosaic of the area. The nearest neighbour algorithm was used to populate the image pixels so that radiometric integrity of the pixels could be preserved. At the image mosaicking stage, a minimised nadir angle approach was implemented such that the spectra of the pixel with the smallest off-nadir angle from overlapping adjacent flight lines was written to the final mosaic image.

Whilst the TIR domain is an atmospheric window, there is atmospheric influence which needs to be compensated for, especially for quantitative applications (Liang *et al.*, 2002). Here atmospheric correction was performed through the inversion of radiative transfer modelling, following a similar approach to our corrections of VNIR/SWIR Antarctic hyperspectral data (Black *et al.*, 2014b); simple in-scene based techniques (e.g. ISAC, AAC) were omitted due to their limitations as previously discussed (Section 2.3.1).

The basic radiative transfer equation in the TIR domain as given by Dash *et al.* (2002) is (where each term is a function of wavelength, λ, omitted for clarity)

$$L_s = L_p + \tau \cdot L_g + \tau \cdot [1 - \epsilon] \cdot \frac{F}{\pi} \tag{13}$$

where L_s is the total thermal radiance received at-sensor, L_p the thermal path radiance emitted by the atmosphere between the ground and the sensor, τ the ground-to-sensor transmittance, L_g the ground emitted radiance, ϵ the ground surface emissivity and F the downwelling thermal sky flux at the

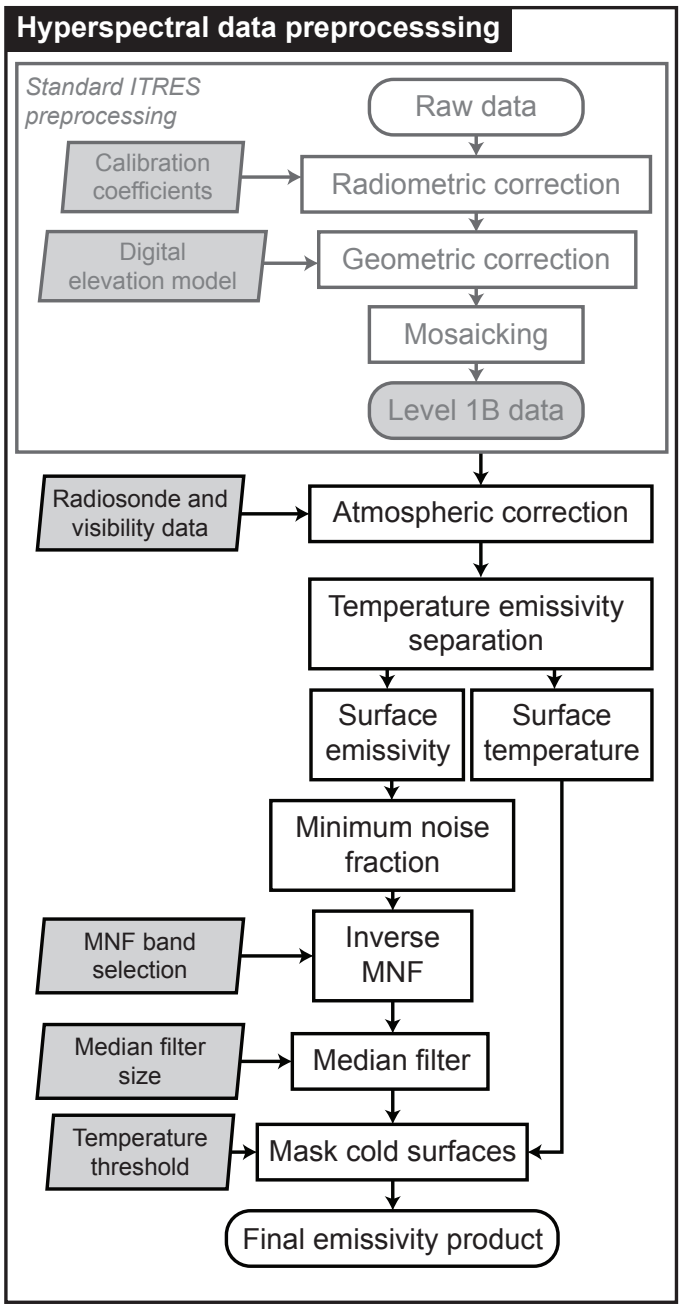

Figure 4.4: *Flow chart summarising the preprocessing of the hyperspectral imagery. Inputs and parameters are shown in the left column (light grey boxes). Abbreviated processing steps are as follows: MNF, minimum noise fraction.*

ground (Richter and Coll, 2002). The ATCOR-4 (Richter and Schläpfer, 2002, 2014) package was used, which applies Equation 13. The two inputs required by ATCOR-4 to approximate the atmospheric conditions are the visibility and column water vapour amount. Visibility data is continually measured at the nearby Rothera research station using an automated BIRAL HSS VPF-730 Combined Visibility & Present Weather Sensor. The water vapour value was derived using an assumed value of 2.0 $g\,cm^{-3}$ by comparison to radiosonde data. The mosaicked images were processed one flight line at a time to convert the at-sensor radiance into ground-leaving radiance. Following this, TES was performed using the maximum-minimum difference of emissivity technique (Gillespie *et al.*, 1998), selected due to its improvements over other TES techniques and its development for TIR data with many bands (Section 2.3.2).

Investigation of the emissivity imagery following atmospheric correction and TES showed lower than expected emissivity values at the lowest wavelengths (< 8.5 μm) and higher than expected emissivity values for remaining wavelengths (> 8.5 μm), along with residual atmospheric absorptions causing emissivity features (which could be misinterpreted in a geological context). This was likely due to the challenging acquisition conditions and poor calibration of the instrument, along with inadequate representation of the atmosphere due to approximations in the atmospheric correction process (Black *et al.*, 2014b). An empirical correction, through the EELM was applied. The EELM generates scalar multiplicative values for each band of the image through regression of the target image pixel spectra to the assumed "reference" spectra - this approach is comparable to the use of pseudo invariant features (PIFs; Freemantle *et al.*, 1992; Philpot and Ansty, 2011) and the empirical line method (ELM; Smith and Milton, 1999) which is commonly applied to VNIR/SWIR data (*e.g.* Tuominen and Lipping, 2011). Here EELM was applied utilising target pixels selected from granite, dolerite, snow and sea water (to cover a range of emissivity values); reference spectra were selected from spectral library measurements (snow and sea water from Baldridge *et al.*, 2009) and convolved field spectra (granite and dolerite).

High levels of salt and pepper noise along with within-in track striping and flight line illumination differences were still apparent in emissivity imagery so a final processing step was applied to perform noise reduction. To improve the signal to noise ratio (SNR), the minimum noise fraction (MNF; Boardman and Kruse, 1994; Green *et al.*, 1998) was applied, where its inverse transform using the channels with the least amount of noise were used create the final noise-reduced dataset. The first four channels of the MNF image (bands 1 to 4) were then used in the inverse MNF to produce the noise-reduced emissivity image. A median filter with a radius of 2 was applied to reduce noise in the spectral domain (e.g. Gilmore *et al.*, 2011).

The signal to noise ratio (SNR) of the imagery before and after preprocessing was investigated by utilising an area of sea water in the image and calculating the SNR through

$$\mathrm{SNR} = \frac{\mu_{ij}}{\sigma_{ij}} \tag{14}$$

where i and j are the rows and columns of the image, μ_{ij} is the mean of the pixels and σ_{ij} is the standard deviation of the pixels. The signal to noise ratio is often reported using the logarithmic decibel (dB) scale; the SNR in dB is defined through

$$\mathrm{SNR}_{dB} = 10\log_{10}(\mathrm{SNR}^2) = 20\log_{10}(\mathrm{SNR}) \tag{15}$$

Finally, prior to processing, the image was masked to remove snow/ice and sea water; a mask was generated from the temperature image where pixels $<$ 5 °C were removed.

4.3.3 Image processing and lithological mapping

In order to produce a lithological map, a six step processing chain was applied, shown in Figure 4.5. The processing chain is fully automated, with only a small number of inputs/parameters; algorithms were selected from the existing literature based on their ability to cope with the low SNR datasets. The six steps are: (1) superpixel segmentation; (2) identify the number of

endmembers to extract from the suerpixels; (3) extract endmembers from the image using an endmember extraction algorithm (EEA); (4) perform spectral mixture analysis (SMA; also known as spectral unmixing) to determine the fractional abundances each endmember; (5) produce a predictive classification map from endmember fractional abundances; (6) identify endmembers and label the predictive map classes to produce a lithological map.

These steps are fully automated in a MATLAB environment (MathWorks, 2011) and do not require any user interaction. Steps 1 to 5 require the hyperspectral scene and very few inputs. In this study, step 6 is also performed automatically with the additional input of the field spectral data (convolved to TASI spectral response functions; Equation 11) which are used to label the predictive map classes. In the absence of field spectral data, step 6 could be performed by an expert user with manual interpretation of endmembers (or comparison to spectral libraries) to label the predictive map classes. The following sections describe each step of the processing chain.

4.3.3.1 Step 1: Superpixel segmentation Firstly, superpixel segmentation which adds a spatial component to endmember extraction, was applied. This technique was selected due to its proven success on low SNR datasets, its highly optimised implementation (fast processing times) along with its noise reduction and data reduction ability (Section 2.5.3.3). Superpixels are homogeneous image regions comprised of several pixels having similar values and are generated by intentional over-segmentation of the emissivity image which aggregates scene features into smaller segments (Thompson *et al.*, 2010; Gilmore *et al.*, 2011).

Briefly, the superpixel segmentation uses graph based image segmentation (Felzenszwalb and Huttenlocher, 2004), where the pixel grid is shattered into an 8-connected graph with nodes connected by arcs representing the Euclidean spectral distance and the nodes are then iteratively joined using an agglomerative clustering algorithm (Felzenszwalb and Huttenlocher, 2004; Thompson *et al.*, 2010, 2013). A stable bias parameter, k controls the size of the superpixels, along with enforcing a minimum superpixel size and in a final

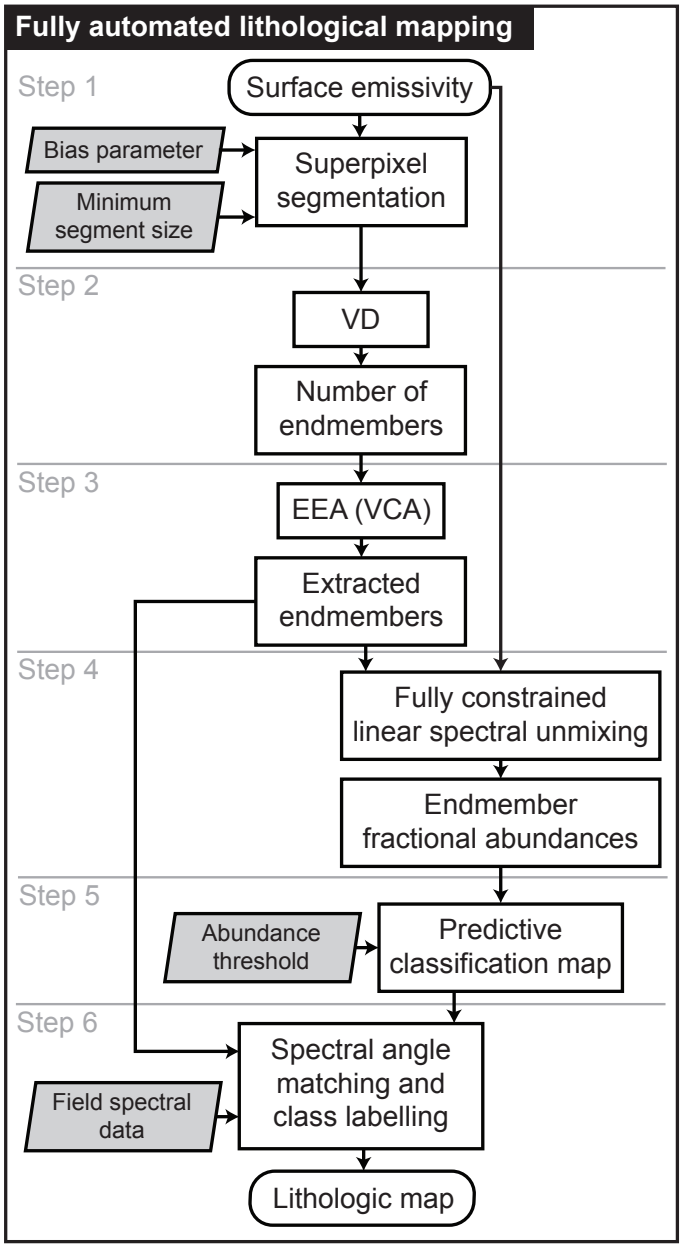

Figure 4.5: *Flow chart summarising the methods of the fully automated lithological mapping process. Inputs and parameters are shown in light grey boxes. Abbreviated processing steps are as follows: VD, virtual dimensionality; EEA, endmember extraction algorithm; VCA, vertex component analysis.*

step smaller regions are merged to their nearest adjacent clusters (Felzenszwalb and Huttenlocher, 2004; Thompson *et al.*, 2010). The superpixel approach has been shown to be beneficial on low SNR datasets and can aid in deriving endmembers which more closely resemble manually derived endmembers (Thompson *et al.*, 2010).

For the superpixel segmentation, the bias parameter k, which controls the size of the superpixels, was set to 0.1 and the minimum superpixel region size was set to 30 pixels using the Euclidean spectral distance as the divergence measure. These parameters were determined quantitatively to by investigating the sensitivity of the segmentation to small features, such as the stoped granite block in the North East of Anchorage Island (Figure 3.3). This step also serves as an image reduction step, thereby speeding up processing times; the raw image contains over 7.6 million pixels (3062×2489) and the superpixel segmentation reduces this to 9810 superpixels.

4.3.3.2 Step 2: Estimating the number of endmembers Following the generation of superpixels, Virtual Dimensionality (VD; Chang and Du, 2004) was used to determine the number of endmembers (n); the VD concept formulates the issue of whether a distinct signature is present or not in each of the spectral bands as a binary hypothesis testing problem, where a Newman-Pearson detector is generated to serve as a decision-maker based on a prescribed false alarm probability P_{fa} (Chang and Du, 2004; Plaza *et al.*, 2011). In preliminary investigations, the P_{fa} was varied from 10^{-3} to 10^{-6} however the estimated number of endmembers did not change; therefore the P_{fa} was fixed at 10^{-4} in line with previous studies (Chang and Du, 2004; Plaza *et al.*, 2011).

4.3.3.3 Step 3: Endmember extraction Vertex Component Analysis (VCA; Nascimento and Bioucas-Dias, 2005) was applied to extract n endmembers from the superpixels. VCA exploits the fact that endmembers occupy the vertices of a simplex and assumes the presence of pure pixels in the data. The algorithm iteratively projects data onto a direction orthogonal to the subspace spanned by the endmembers already determined and the new endmember

signature corresponds to the extreme of the projection. The algorithm iterates until the number of endmembers is exhausted. VCA has been shown to be comparable to state of the art endmember extraction algorithms, such as N-FINDR (Winter, 1999) and outperforms manual techniques such as the Pixel Purity Index (PPI; Boardman, 1993). VCA is an order of magnitude less computationally complex than other state of the art endmember extraction algorithms which results in significantly decreased processing times for large datasets (Nascimento and Bioucas-Dias, 2005).

4.3.3.4 Step 4: Spectral mixture analysis The endmembers derived from the VCA algorithm were used as input to step (4) where linear SMA is used to produce fractional abundances of the n endmembers using the original image. Due to its ease of implementation, fully constrained linear spectral unmixing (FCLSU; Heinz and Chang, 2001) was applied to derive fractional abundances of each endmember, given as

$$R_b = \sum_{i=1}^{n} F_i S_{ib} \tag{16}$$

where R_b is the fractional abundance of the pixel at band b, F_i is the fractional abundance of endmember i, S_{ib} describes the emissivity of endmember i at band b, and n is the number of endmembers. Equation 16 was solved subject to the constraints that fractional abundances sum-to-one (ASC; abundances sum-to-one constraint) and fractional abundances are non-negative (ANC; abundance non-negative constraint) (Rogge *et al.*, 2009). These algorithms were selected due to their availability and implementation in the MATLAB environment (MathWorks, 2011), along with their relatively quick processing times and proven success at extracting endmembers under moderate to high noise conditions (Nascimento and Bioucas-Dias, 2005; Chang and Plaza, 2006; Plaza *et al.*, 2012).

4.3.3.5 Step 5: Predictive map classification Utilising the abundance images a predictive classification map was generated following a similar approach to Rogge *et al.* (2009). The map was generated by determining the endmember with the maximum fractional abundance for each pixel and assigning that pixel to the given endmember class. For a pixel to be assigned to a particular class, the endmember abundance must be above a minimum fractional abundance threshold (or confidence level), otherwise a null class was assigned. The minimum fractional abundance was set to the intermediate value of 0.5 for practical purposes, however this value could be increased to identify spectrally purer regions (Rogge *et al.*, 2009).

4.3.3.6 Step 6: Class labelling The interpretation step was carried out to produce geological labels which were automatically applied to the classification map generated from step 5. The image derived endmember spectra were compared to field emissivity spectra (*e.g.* Harris *et al.*, 2005; Rogge *et al.*, 2009) through calculation of spectral angle (SA), also known as Spectral Angle Mapper (SAM; Kruse *et al.*, 1993). SA was calculating in reference to the image derived endmember spectra and the spectra collected in the field through the application of

$$\mathrm{SA} = \cos^{-1}\left(\frac{\vec{t}\cdot\vec{r}}{||\vec{t}\,||\cdot||\vec{r}\,||}\right) \tag{17}$$

where t represents the spectrum of the target (endmember), r represents the spectrum of the reference (field spectra) and SA is the spectral angle (in radians; 0 to 2π). This technique to determine similarity is insensitive to gain factors as the angle between two vectors is invariant with respect to the lengths of the vectors, and allows for laboratory spectra to be directly compared to remotely sensed spectra (Kruse *et al.*, 1993). Predictive map classes were automatically labelled by their closest match from the field spectral data (*e.g.* Rivard *et al.*, 2009) to produce a lithological map.

4.3.4 Image processing validation

In order to validate the findings, the root mean square error metric (RMSE) was used for assessment (e.g. Plaza *et al.*, 2012). The reconstructed hyperspectral image is defined as $\hat{y}_{ij}$, following

$$\hat{y}_{ij} = \sum_{n=1}^{n} (M_n \times S_n) \tag{18}$$

where i and j are the rows and columns of the image, n is the number of endmembers, M_n denotes the endmember spectrum of n and S_n denotes the fractional abundance of endmember n. Following this reconstruction the RMSE between the original hyperspectral image, y and the reconstructed hyperspectral image, $\hat{y}$ is calculated using

$$\mathrm{RMSE}(y, \hat{y}) = \left(\frac{1}{B} \sum_{j=1}^{B} [y_{ij} - \hat{y}_{ij}]^2 \right)^{\frac{1}{2}} \tag{19}$$

where B is the number of spectral bands and $\hat{y}_{ij}$ and y_{ij} are pixels of the original hyperspectral image and the pixels of the reconstructed hyperspectral image respectively. Summary statistics were calculated from RMSE pixels of each endmember class as well as the whole RMSE image. The RMSE metric is based on the assumption that a set of high quality endmembers may allow reconstruction of the original image with higher precision than a set of low quality endmembers, regardless of the presence of such endmembers in the original scene (Plaza *et al.*, 2012).

Additionally, spectra were extracted and compared from the original image and the reconstructed image (calculated from the endmembers and their fractional abundances) for granite and granodiorite from pixels of high purity (0.9 fractional abundance), medium purity (0.75 fractional abundance) and low purity (0.5 fractional abundance), including the RMSE metric, to validate the findings in a spectral context.

5 Results

5.1 Introduction

This chapter presents the results, split into two main sections. Firstly, in Section 5.2 the results from the synthetic data investigation are presented. Synthetic data was generated using field spectral data of the main representative lithological units from the study with a range of SNRs. Algorithms were compared for two processing steps: (1) determining the number of endmembers and (2) extracting endmembers. The synthetic data investigations allowed for an investigation of algorithm performance at different SNR values and informed the algorithm choice for the image processing chain which was applied in real hyperspectral data. Secondly, in Section 5.3 the results of the real hyperspectral data from Anchorage Island are presented, including the field data, image processing, lithological mapping and interpretation, and the validation of the results.

5.2 Synthetic data

5.2.1 Step 1: Determining the number of endmembers

Figure 5.1 shows a histogram comparing the results of the two methods for determining the number of endmembers, at different SNR and using different numbers of endmembers. Table 5.1 shows summary statistics.

The VD-HFC method performs consistently at all SNRs above 30:1. It outperforms the HySime technique for SNRs $\leqslant$ 40:1, where HySime incorrectly estimates the number of endmembers. At the SNR of 20:1, VD-HFC shows some variety in the number of endmembers, though for 9525 out of 10000 runs (95%), it correctly estimates 4 endmembers. Only at the lowest SNR (10:1) does VD-HFC fail where it incorrectly determines there are 3 endmembers. HySime yields consistently accurate results at SNRs of $\geqslant$ 50:1, correctly predicting 4 endmembers. At SNRs of 40:1 to 20:1, HySime incorrectly deter-

mines 3 endmembers, and at the lowest SNR of 10:1, incorrectly determines 2 endmembers. HySime does display consistency at all noise levels with a standard deviation of 0.

Overall, these results suggest that VD-HFC marginally outperforms HySime, but its performance could be compromised if the SNR is extremely low (10:1). However, even with low SNR values (20:1) this shortcoming is largely overcome and near 100% accuracy can be achieved. At all SNRs above 30:1, VD-HFC achieves 100% accuracy, whereas HySime only achieves this above 50:1.

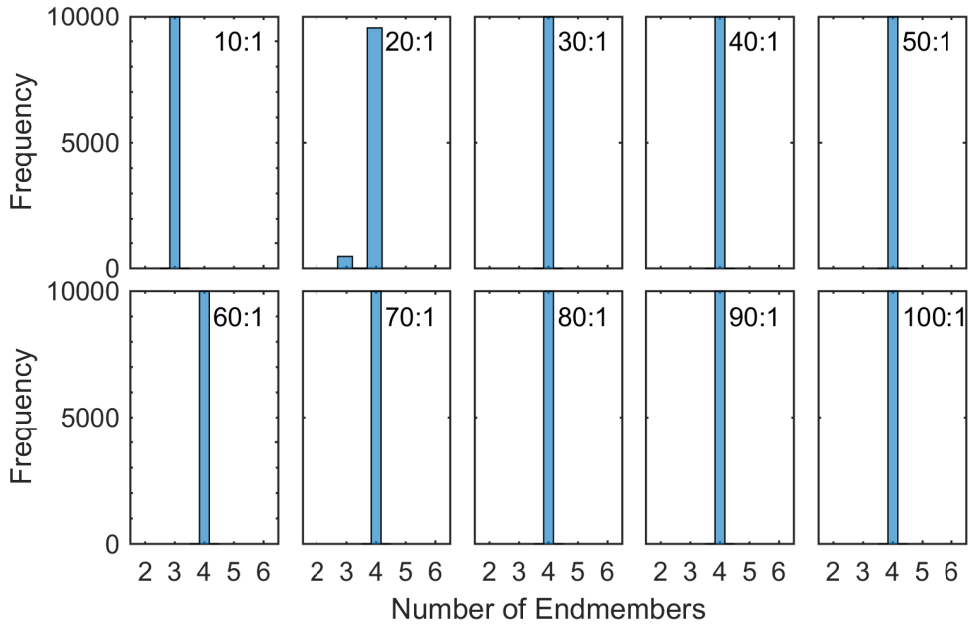

(a) *VD-HFC results*

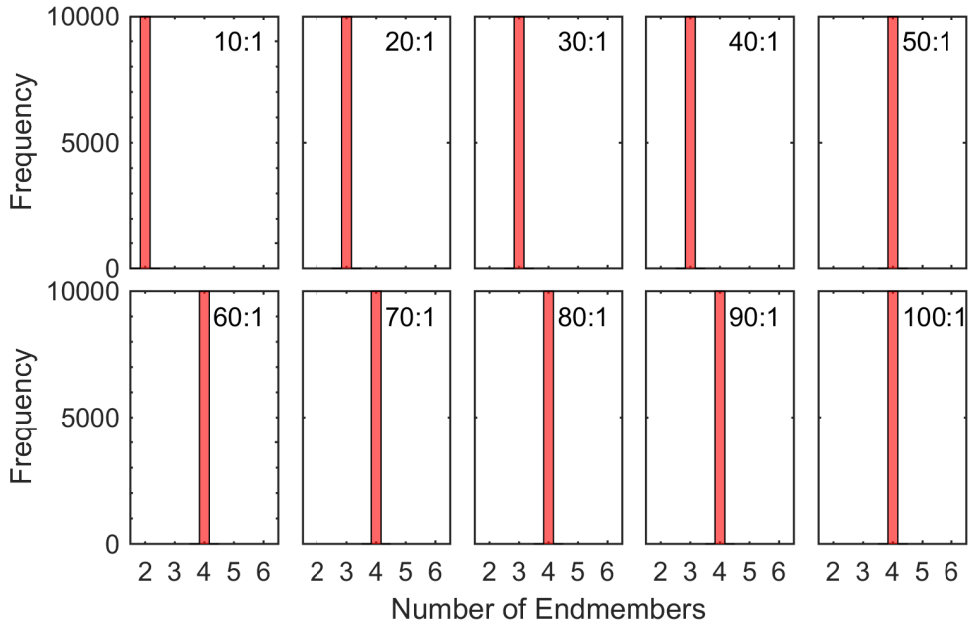

(b) *HySime results*

Figure 5.1: *Histograms for (a) VD-HFC and (b) HySime results for determining the number of endmembers ($n = 4$) at varying signal to noise ratio (annotated in the top right of each histogram).*

	VD-HFC		HySime	
SNR	Mean	StDev	Mean	StDev
10	3	0	2	0
20	3.95	0.21	3	0
30	4	0	3	0
40	4	0	3	0
50	4	0	4	0
60	4	0	4	0
70	4	0	4	0
80	4	0	4	0
90	4	0	4	0
100	4	0	4	0

Table 5.1: *Summary statistics of VD-HFC and HySime for determining the number of end-members at a different signal to noise ratio (SNR). StDev, standard deviation.*

5.2.2 Step 2: Endmember extraction

Figure 5.2 shows RMSE values for the two methods for extracting endmembers at different SNR. Table 5.2 shows summary statistics.

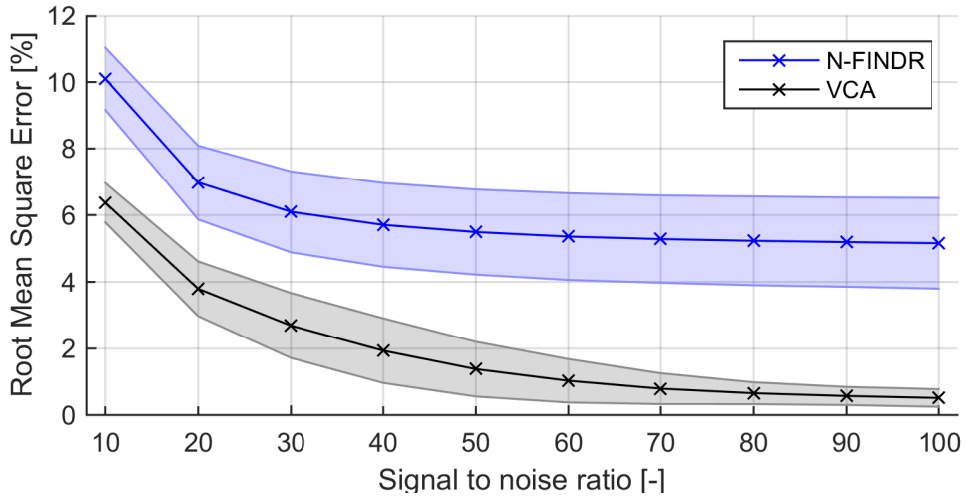

Figure 5.2: *Root Mean Square Error [%] values for the two different endmember extraction techniques at increasing signal to noise ratio (SNR).*

	N-FINDR		VCA	
SNR	Mean	StDev	Mean	StDev
10	10.10	0.94	6.38	0.59
20	6.98	1.11	3.78	0.82
30	6.09	1.20	2.70	0.97
40	5.70	1.25	1.95	0.97
50	5.48	1.30	1.39	0.83
60	5.35	1.31	1.03	0.65
70	5.25	1.30	0.80	0.47
80	5.22	1.33	0.66	0.34
90	5.20	1.36	0.57	0.27
100	5.15	1.34	0.51	0.24

Table 5.2: *Summary statistics of VCA and N-FINDR for extracting endmembers at a different signal to noise ratio (SNR). Values quoted are Root Mean Square Error (RMSE, %); StDev, standard deviation.*

For both N-FINDR and VCA, RMSE is reduced with increasing SNR. On the whole, N-FINDR does not perform as well as VCA, at all SNRs. Above SNRs of 50:1, N-FINDR plateaus with RMSE values at $\sim$ 5%. VCA consistently yields lower RMSE values than N-FINDR by a factor of almost 2. At higher SNRs, VCA's RMSE continues to decrease, though it begins to plateau at around 0.5% for SNRs above 80:1.

5.2.3 Summary

The synthetic data investigations revealed two algorithms which perform consistently well at low SNRs. To determine the number of endmembers, VD-HFC was selected due to its ability to accurately determine the number of endmembers at low SNRs and better performance than the HySime algorithm. For extracting endmembers, VCA outperformed N-FINDR by a factor of almost 2 and yielded low RMSE values even at low SNRs. These algorithms were therefore incorporated in the processing chain for real hyperspectral data, as described in the following sections.

5.3 Anchorage Island lithological mapping

5.3.1 Field spectral data

Table 5.3 shows whole-rock major and trace element data from XRF spectroscopy. Table 5.4 shows the modal abundances of minerals as determined from point counting. Spectral data collected from in situ samples are displayed in Figure 5.3. EPMA was used to identify minerals (Appendix B). The majority of Anchorage Island is composed of weathered granodiorite, however some areas contain amphibole rich granodiorites (J13.24, J13.25 and J13.26) and areas in the southwest of the island (J13.19 and J13.20) display strongly weathered and altered granodiorites.

The spectral variability of the granidiorites is shown in Figure 5.3A. Numerous dolorite dykes cut the granodiorite unit; a spectral measurement from a dolerite dyke in the northwest of Anchorage Island is shown in Figure 5.3B. The field spectra for dolerite and granodiorite show similar spectral

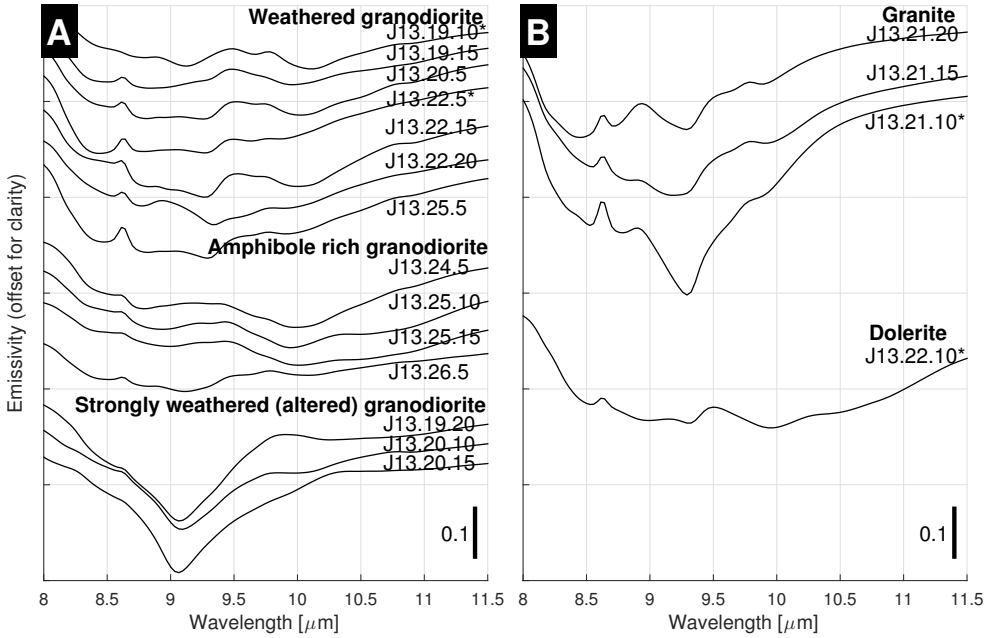

Figure 5.3: *Spectral emissivity measured in the field using a Fourier Transform Infrared Spectrometer (FTIR) of relevant lithological units from Anchorage Island. (A) shows granodiorite spectra (B) shows granite and dolerite spectra.*

Sample	J13.22.10	J13.19.10	J13.22.5	J13.21.10
Unit	Dolerite	Granodiorite		Granite
Major elements (%)				
SiO_2	54.40	55.19	59.59	78.29
TiO_2	1.02	0.94	0.87	0.20
Al_2O_3	16.62	18.18	16.35	11.64
Fe_2O_3†	8.66	8.55	6.67	0.86
MnO	0.12	0.11	0.15	0.01
MgO	3.96	3.29	3.52	0.16
CaO	8.57	7.49	6.16	0.53
Na_2O	3.14	4.04	3.51	2.74
K_2O	0.96	1.07	2.12	5.61
P_2O_5	0.24	0.18	0.19	0.02
SO_3	0.17	0.01	< 0.003	< 0.003
LOI	2.05	0.88	0.97	0.31
Total	99.92	99.93	100.09	100.38
Trace elements (ppm)				
As	6.7	8.4	5.1	4.4
Ba	365	432	698	476
Ce	44.2	27.9	48.4	11.4
Co	25.7	18.3	21.6	< 1.1
Cr	112	6	37	< 1
Cu	111	20	32	4
Ga	18.2	21.2	17.8	9.9
La	20.0	13.7	21.3	7.9
Mo	3.9	2.3	3.3	0.9
Nb	4.8	4.4	6.8	4.7
Nd	23.6	16.7	25.2	7.7
Ni	13	< 1	19	< 1
Pb	8.2	9.7	7.5	9.7
Rb	15.6	36.7	55.6	140.3
Sc	30.6	34.1	23.1	3.3
Sr	458	481	416	111
Th	6.9	3.5	10.2	17.3
U	2.6	1.3	1.4	2.5
V	229.0	267.8	159.2	10.9
Y	31	27	30	21
Zn	49	71	72	15
Zr	179	43	231	98

Table 5.3: *Geochemical analyses of Anchorage Island samples from XRF spectroscopy. † total iron (FeO and Fe_2O_3).*

Sample Unit	J13.22.5 Granodiorite	J13.22.10 Dolerite	J13.21.10 Granite
Point Count (%)			
Biotite			1.2
Chlorite	8.8		
Clinopyroxene		33	
Hornblende	12.6		
K-Feldspar			27.8
Muscovite		1.4	
Opaques	1	4.6	1
Plagioclase	44.8	61	35
Quartz	32.8		35

Table 5.4: *Results from point counting, where mineral counts are given as percentages. A total of 500 points were counted on each sample (n=500). Opaques likely indicate Magnetite.*

features; a small relative increase in emissivity at 8.6 μm and 9.5 μm, and two broad flat absorption features centred around 9 μm and 10 μm. The whole-rock XRF data shown in Table 5.3 supports the spectral similarity of the dolerite and granodiorite samples - there is very little difference in the chemical composition of these samples, hence the similar spectra of the samples. The amphibole rich granodiorite spectra display an additional weak feature at 10 μm with reduced magnitude of the emissivity maximum at 8.6 μm. The strongly weathered (and altered) granodiorite spectra are significantly different to weathered/amphibole rich granodiorite spectra, displaying a broad deep absorption at 9 μm and a smooth spectrum above 9.8 μm. We attribute the broad deep absorption centred around 9 μm to feldspar alteration (into clay minerals, e.g. sericite).

The spectrum of granite is dominated by a quartz signal which leads to an emissivity maximum at 8.7 μm and a deep feature with an emissivity minima at 9.4 μm (Figure 5.3B). Although similar spectral features to granodirote are present in the granites, the overall magnitude of the absorption features is much larger in the granite than in any of the granodiorite or dolerite spectra.

5.3.2 Data preprocessing

Figure 5.4 shows the first 10 bands of the MNF transform. As higher MNF components are considered, the levels of noise dramatically increase (Figure 5.4G-J). The MNF images also clearly highlight the differences between flight lines which cause 'striping' in the images (e.g. Figure 5.4E and F). The first four of these MNF components (Figure 5.4A-D) were retained (i.e. those with minimal striping effects) and processed through an inverse MNF transform prior to input in the superpixel and endmember extraction algorithms.

Figure 5.5 shows the SNR for the image after atmospheric correction and TES compared to the SNR for the final image after all preprocessing (atmospheric correction, TES, EELM and MNF noise reduction). Overall the SNR is increased from a mean value of 60:1 (35.6 dB) to 92:1 (39.3 dB) after preprocessing. With the exception of one band at ~ 9 μm, the SNR increased for all wavelengths, with significant increases seen at the higher wavelengths (> 10.5 μm). Whilst increases in SNR are seen after preprocessing, on the whole SNR values are relatively low and far lower than that which are regularly reported by others using airborne hyperspectral TIR sensors such as SEBASS; for example Vaughan *et al.* (2003b) report SNR values of 2000:1 (66 dB) using SEBASS data in Nevada. The low SNR values reported here are

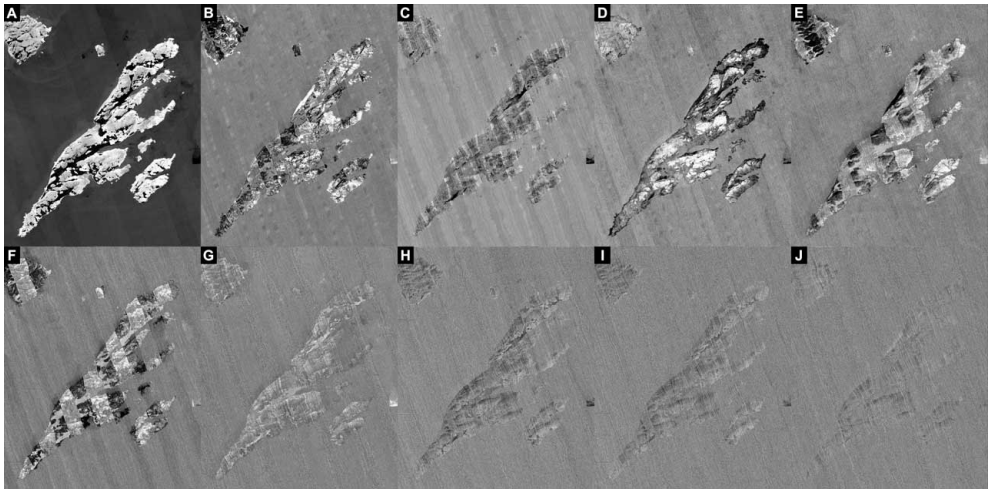

Figure 5.4: *Images for the first 10 components of the Minimum Noise Fraction (MNF) transform (A-J). Components 1 to 4 (A to D) were utilised in the inverse MNF procedure.*

likely a direct result of the challenging operating conditions in the Antarctic; the instruments were flown in an unpressurised aircraft, operating at temperatures which were up to 20 °C outside of the instrument's normal operating range, as well as being subject to repeated heating/cooling during storage and operation (Black *et al.*, 2014b).

Figure 5.6 shows a comparison of emissivity spectra following each step of preprocessing for spectra of snow and sea water. There is a clear improvement in the TASI emissivity spectra after all preprocessing, as residual atmospheric features (e.g. centred at 9.5 μm) has been removed and the TASI spectra very closely resemble the spectral library measures of snow and sea water.

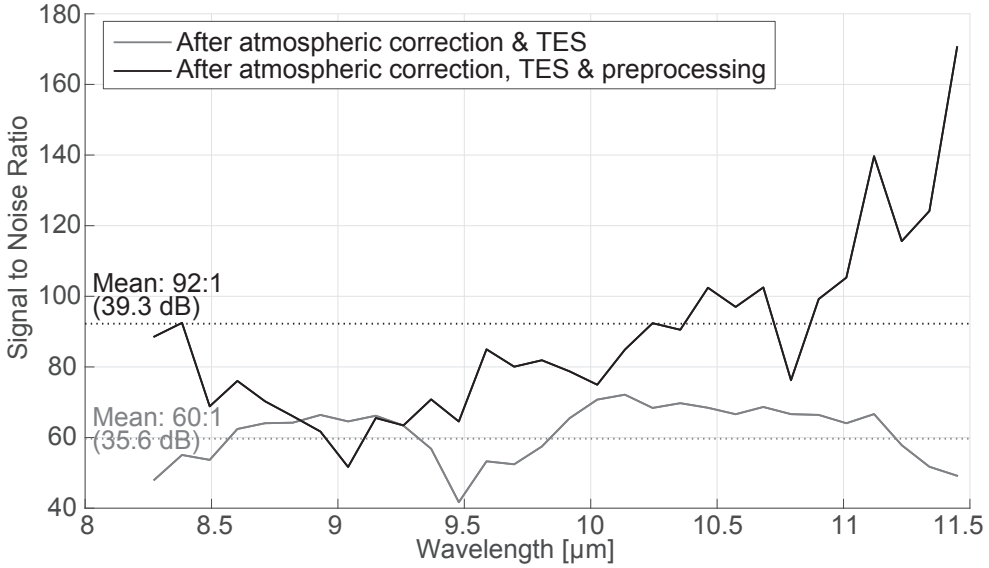

Figure 5.5: *Signal to noise ratio (SNR) calculated from the image after atmospheric correction and temperature emissivity separation (TES; grey line) compared to the SNR for the final image after all preprocessing (atmospheric correction, TES, emissive empirical line correction and minimum noise fraction for noise reduction) (black line). Mean values are shown in the annotations.*

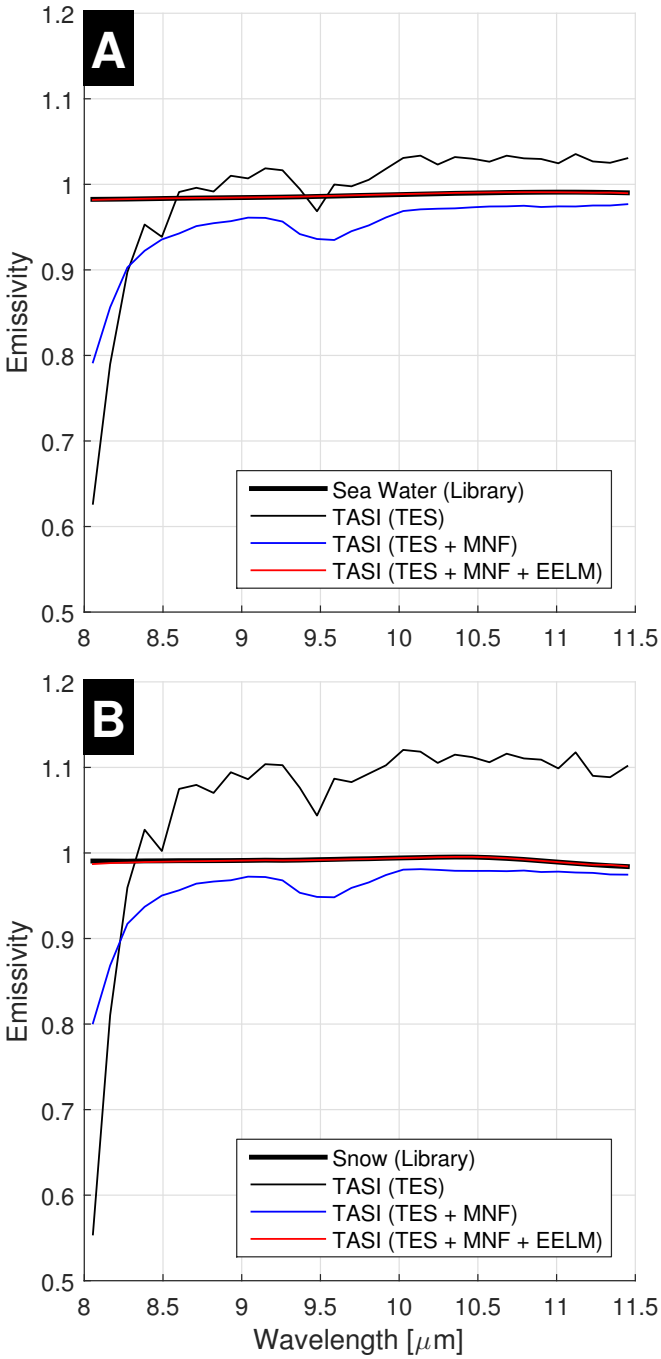

Figure 5.6: *Comparison of emissivity spectra of (A) sea water and (B) snow for the reference spectra (thick black line) and the TASI after each phase of preprocessing. TES, temperature emissivity separation; MNF, minimum noise fraction; EELM, emissive empirical line method.*

5.3.3 Lithological mapping and interpretations

A total of 9810 superpixels (Figure 5.7) were input into the VD algorithm which determined there were 5 endmembers. The endmembers were extracted using the VCA algorithm and are shown in Figure 5.8. Endmember abundances were determined using FCLSU; the abundances images were utilised to generate a classified map, where classes were assigned to the predominant endmember if the abundance was greater than 0.5.

The classes were subsequently labelled by automatic matching to the field spectral data; the closest match (in terms of spectral angle; Equation 17) was applied to label the endmembers (Figure 5.8) and their respective class in the predictive classification map (Figure 5.9). The results were validated through visual inspection of the classification map with respect to the local geological map (Figure 3.3), comparison of the endmember spectra and the ancillary data (Sections 3.4 and 4.3.1), as well as using the RMSE metric (Section 4.3.4

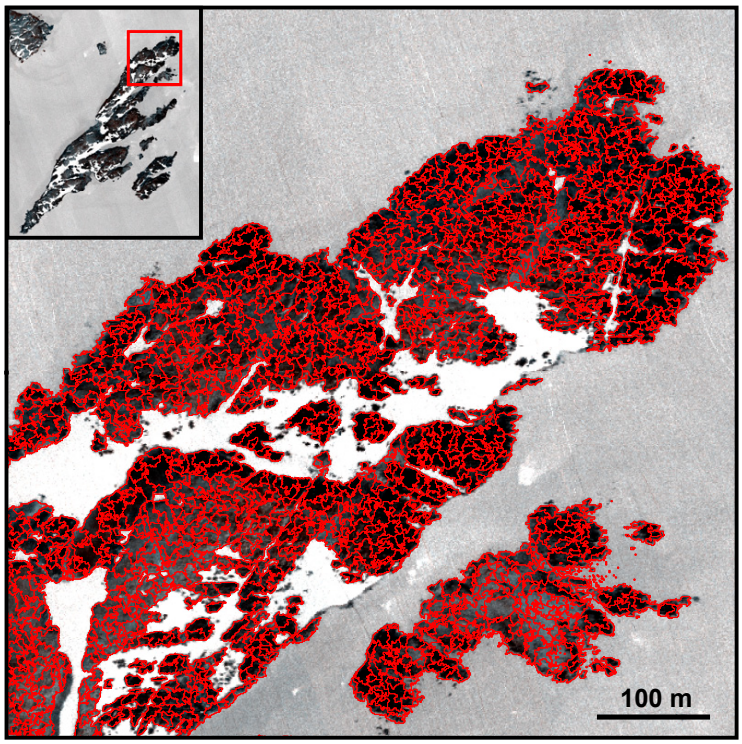

Figure 5.7: *Superpixel segmentation as applied to Anchorage Island. Inset, top left, shows the extent of the frame. Superpixel segments are outlined in red.*

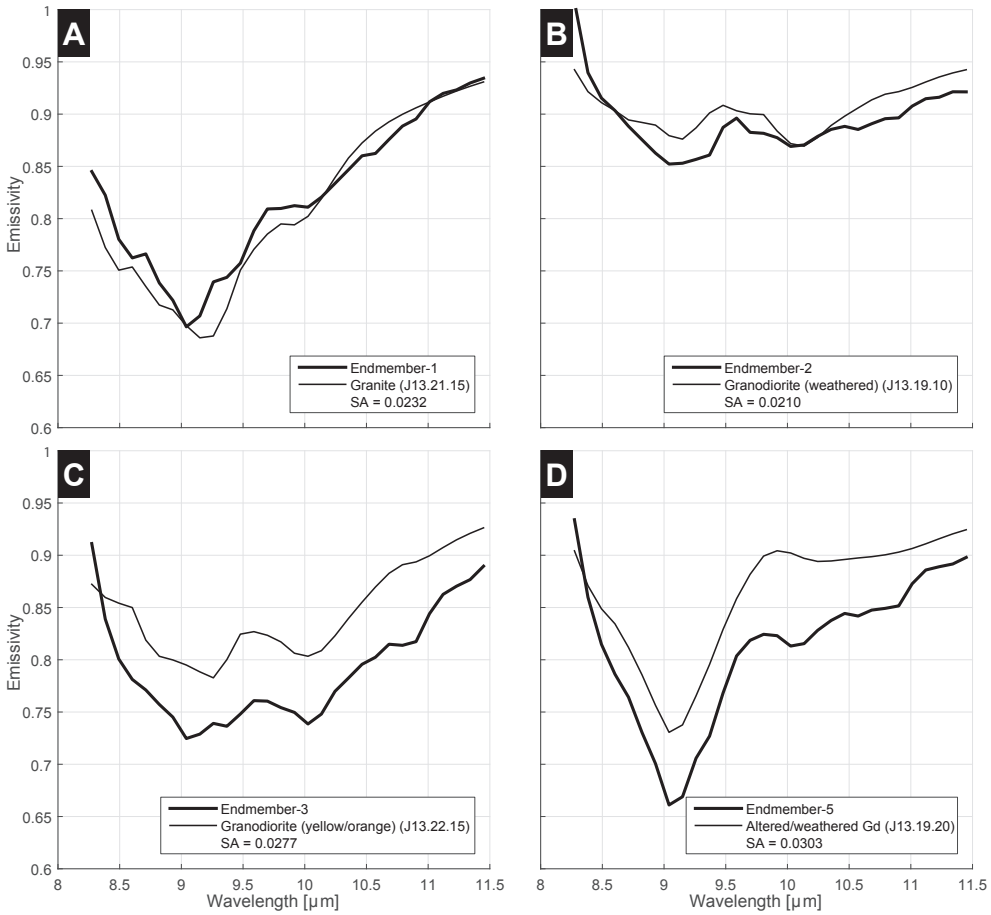

Figure 5.8: *Four extracted endmembers (thick line) and their closest match from the field spectral data (thin line). The spectral angle (SA), in radians, is shown in each figure legend.*

and Section 5.3.4). Endmember-4 was excluded as it represented sea water from pixels which were not captured at the masking step and is not discussed further. The final lithological map is shown in Figure 5.9.

For the four identified endmembers, a match was determined from the field spectra where the SA was $\leqslant 0.03$ radians; confident matches for granite, two types of weathered granodiorite and lichen coated granodiorite were found. The endmember spectra display absorption features consistent with the field measured spectra (Figure 5.3) and their mapped distributions (Figure 5.9) are largely in agreement with the generalised geological map (Figure 3.3).

The granite endmember (Endmember-1; Figure 5.8A) displays good agreement with the field spectral data and its distribution on the predictive map

(Figure 5.9A and B). We accurately delineate the stoped granite block in the northeast of Anchorage Island, along with the larger outcrops south of the granite block and along the northeast coast. The predictive map indicates the likelihood of additional outcrops of granite occurring predominantly in the northeast of Anchorage Island (Figure 5.9B).

Two of the endmembers (Endmember-2 and Endmember-3; Figure 5.8B and C) show good matches to granodiorite spectra measured in the field; both are measured from weathered granodiorite, however Endmember-3 is from yellow/orange weathered granodiorite. The spatial distribution of this endmember is largely limited to low lying coastal regions, perhaps indicating recent weathering due to coastal processes, which distinguishes it from the remaining granodiorite (Endmember-2). Endmember-3 also shows a higher abundance in the extreme southwest of Anchorage Island, corresponding to the diorite outcrop (c.f. Figure 3.3), though does not allow for distinguishing the diorite as a separate unit; this is likely as the diorite and granodiorite units would have a similar chemical composition and thus would be difficult to differentiate spectrally.

None of the endmembers correspond to the dolerite, most likely due to the chemical and spectral similarity to the granodiorite unit (Table 5.3; Figure 5.3). The granodiorite and dolerite were distinguished in the field due to the differences in their grain size; however, the spectral features present in the imagery do not allow for a distinction to be made. Even in the field spectra, there is little difference between the granodiorite and dolerite (Figure 5.3), hence there are no endmembers extracted that match dolerite. In this instance, other complimentary remote sensing techniques such as LiDAR (and derived products such as surface texture) could aid in the identification of the dolerite (Section 4.1).

At the wavelengths considered by the TASI sensor (8 to 11.5 μm), the processing chain has been able to differentiate granite and granodiorite, though struggled to find a clear distinction between the relatively similar chemical composition of the country rock (granodiorite) and the dolerite dykes on Anchorage Island. The ability to more accurately discriminate potassium

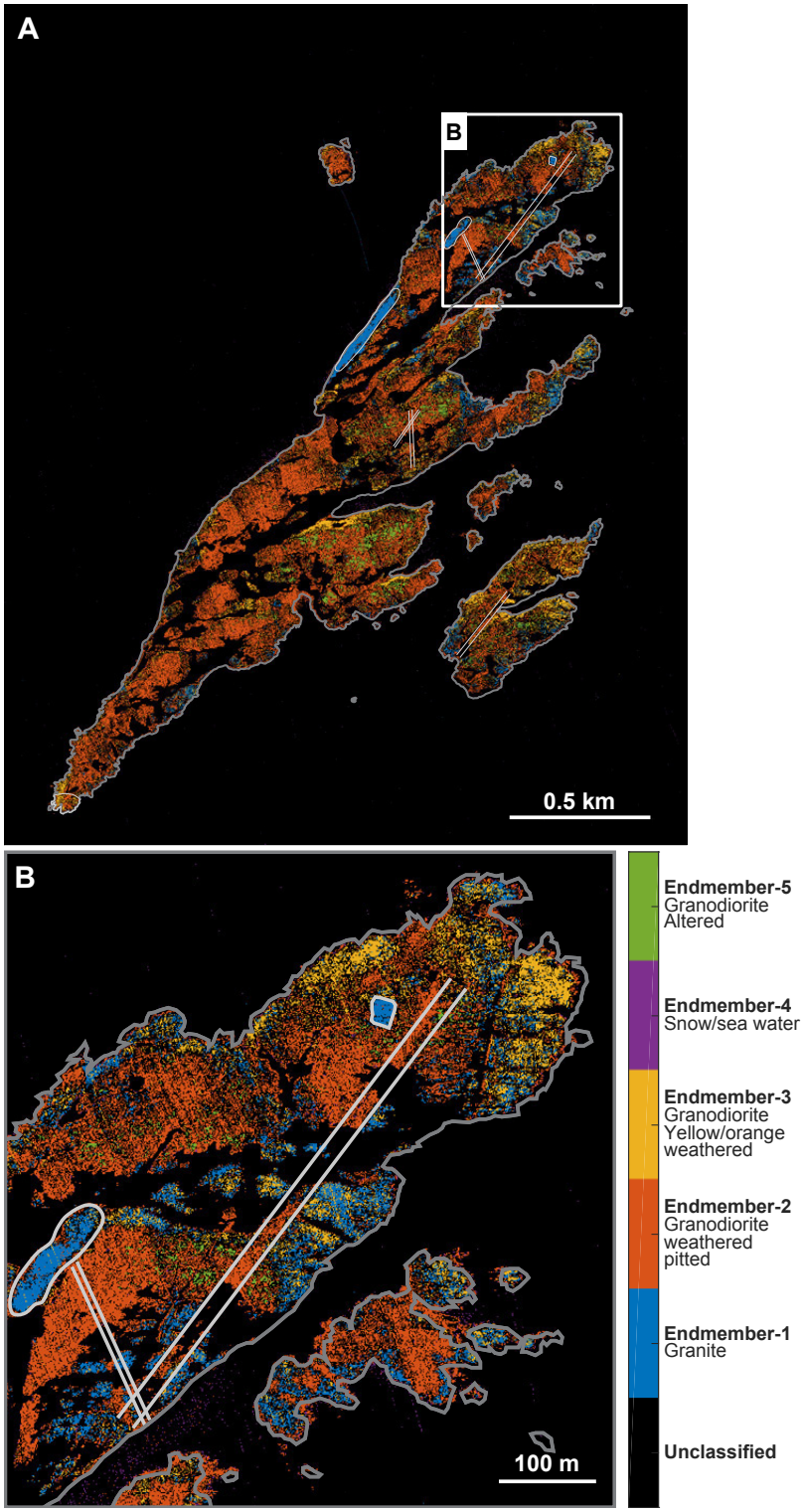

Figure 5.9: *Lithological map generated from the automated processing chain. (A) shows the whole of Anchorage Island and inset (B) shows an area of interest around a stoped granite block in the North East of Anchorage Isalnd. Compare Figure 5.10 for geological boundaries.*

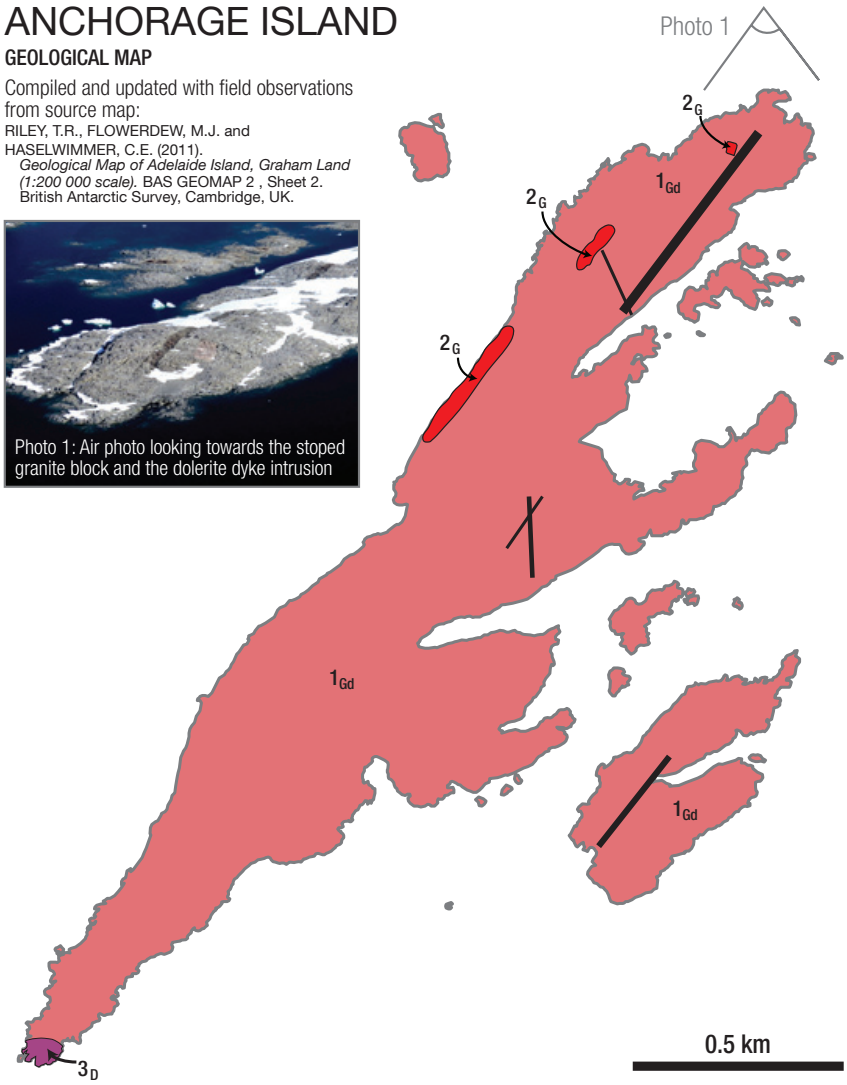

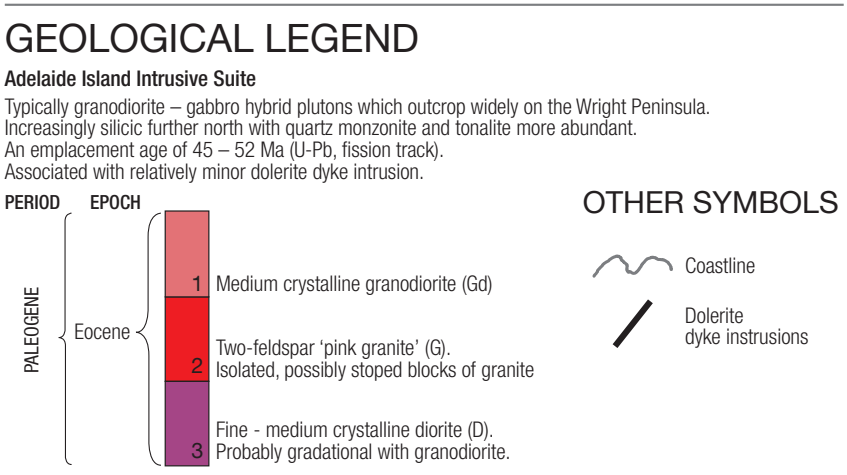

Figure 5.10: *Local scale geological map of Anchorage Island.*

and plagioclase feldspar(s) could be aided if data were available at wavelengths where additional features could aid in feldspar identification (e.g. 12-14 μm; Hecker *et al.*, 2012).

Specifically on Anchorage Island, the lithological mapping results presented in Figure 5.9, have yielded a new high resolution insight into small scale lithological variations present on the island. Prior to this study, the presence of stoped granite blocks on the island was not known, nor had the presence of granite been explicitly mapped. Only with the use of high resolution TIR hyperspectral data have such units been directly mapped (and subsequently validated during the field campaign).

The occurrence of granite *senso stricto* in continental margin arcs is rare, typically accounting for 1-2% of the total volume of granitoid rocks exposed at the surface (Waight *et al.*, 1998). Granites exposed at the surface on the western margin of the Antarctic Peninsula are rare and not previously identified at all from Adelaide Island (or the Ryder Bay islands, including Anchorage Island, prior to mapping carried out in this study). The identification of stoped blocks of granite within a granodiorite pluton indicates the presence of granite at relatively shallow depths (Waight *et al.*, 1998).

The lithological map presented here represents the first known lithological map derived in a completely automated manner, from the first ever airborne hyperspectral TIR dataset collected in the Antarctic. The geological insights gained from Anchorage Island are not ground breaking in the larger context of the Antarctic Peninsula, however the strong agreement with previous field geological mapping highlights the potential of these data for mapping igneous lithologies in a continental margin arc setting.

5.3.4 Validation of image processing

Figure 5.11 shows the RMSE histogram and image calculated through Equation 19. Summary statistics calculated for each of the predicated class pixels (Figure 5.9) within the RMSE image are shown in Table 5.5.

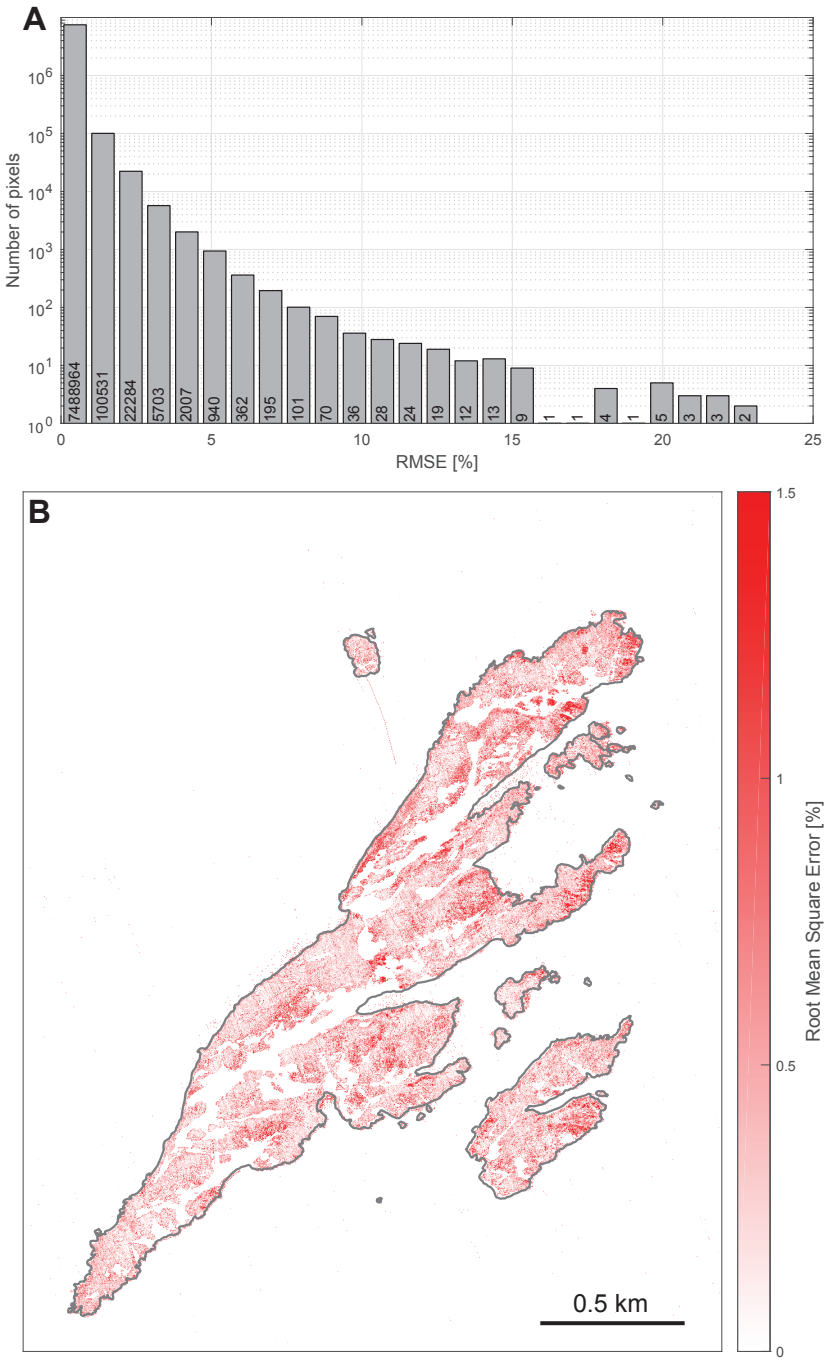

Figure 5.11: *(A) histogram of Root Mean Square Error (RMSE; %) values; note the log scale. (B) shows the RMSE image of Anchorage Island. Note: the colorbar is capped at 1.5% as the predominant distribution of RMSE values is below this threshold.*

Endmembers 1, 2 and 5 produce RMSE values of <0.5%, with standard deviations of ∼ 0.45% and a maximum RMSE of 7.83% (Endmember-1). These values indicate that the unmixing procedure with just 5 endmember spectra yielded a high quality reconstruction of the original image spectra for these classes. Endmember-3 has a mean RMSE significantly higher at 0.94% with an increased standard deviation of 1.25% and a maximum error of 23%; this indicates pixels which are classed as Endmember-3 have higher overall and specific reconstruction errors, likely a result of incorrect or inadequate endmember spectra for these pixels and hence higher errors. The spatial distribution of Endmember-3 is coincident with the previously mapped diorite unit on Anchorage Island, hence the higher RMSE values could indicate misclassification as there was no diorite spectral measurement present in the field spectral data.

On the whole, the average RMSE for the image is 0.58%; this figure is significantly higher than the RMSE values that are routinely achieved using VCA (e.g. RMSE of 0.1% in Plaza *et al.*, 2012), however this is likely a direct result of the low SNR of the imagery (Figure 5.5). As the SNR is reduced (below 1000:1, 60 dB) the performance of endmember extraction algorithms begins to degrade significantly and RMSE values increase (Plaza *et al.*, 2012). Conversely, with larger SNRs, the RMSE error will decrease and the performance of endmember extraction algorithms will improve (Nascimento and Bioucas-Dias, 2005; Plaza *et al.*, 2012). Other factors may also affect the RMSE values, including the pure pixel assumption and spectral mixture analysis techniques, as discussed in Section 6.4.2. However, these errors did

RMSE (%)	Mean	Max	StDev
Endmember-1	0.498	7.830	0.464
Endmember-2	0.473	3.447	0.439
Endmember-3	0.939	23.223	1.246
Endmember-5	0.425	5.952	0.451
All Endmembers	0.584	23.223	0.650

Table 5.5: *Root Mean Square Error statistics for each endmember class. StDev, standard deviation. All values shown are %.*

not inhibit the success of the processing chain.

Figure 5.12 shows the spectra of pixels from high, medium and low purity pixels, comparing the original image spectra with the reconstructed image spectra (from endmembers and their fractional abundances), for granite, granodiorite and altered granodiorite. In all cases the RMSE is $\leqslant 2$ %, indicating a good fit between the original and reconstructed spectra. The high purity pixels (Figure 5.12A) more closely resemble the original endmembers and their equivalent field spectra (c.f. Figure 5.8), indicating a good degree of reconstruction of the original spectra and that endmember lithologies are accurately represented. When considering the medium and low purity spectra (Figure 5.12B and C), the RMSE values are still low, indicating a high degree of fit between the original and reconstructed spectra; however, as the mixing of endmembers is increased, the pixel spectra begin to converge and become increasingly similar (especially at low purities, Figure 5.12C). This indicates that as pixels become increasingly mixed (lower fractional abundances) the pixel spectra are increasingly similar yielding lower confidence in assigning a distinct lithology for low purity pixels. In this study the abundance threshold was set to 0.5, however with careful examination of reconstructed and original image spectra, this threshold value could be increased to yield greater confidence in lithological units as pixel spectra would more closely resemble endmember spectra.

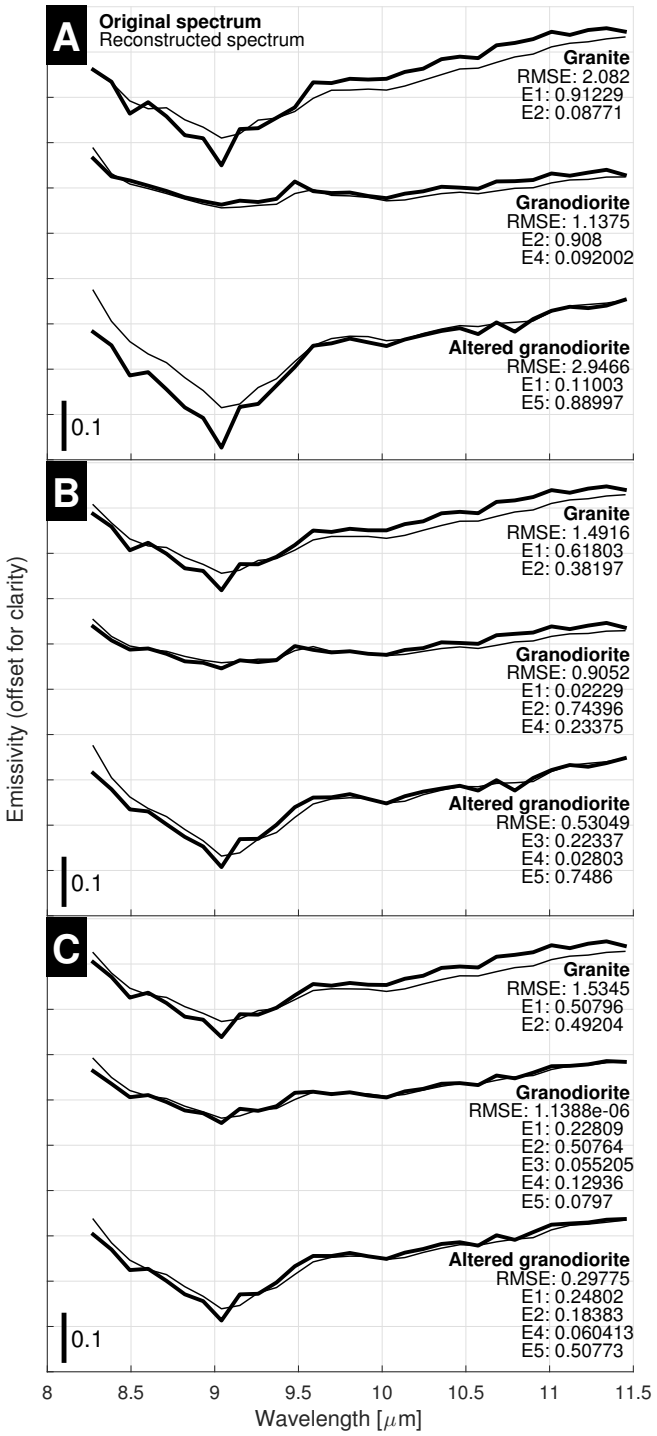

Figure 5.12: *Original image spectra (bold line) and their reconstructed spectra (thin line; calculated using the endmember spectra and the fractional abundances). Figure annotations are as follows: RMSE; root mean square error, %; E1 to E5; fractional abundances of endmember-1 to endmember-5. (A) high purity (0.9 fractional abundance) spectra, (B) medium purity (0.75 fractional abundance) spectra and (C) low purity (0.5 fractional abundance) spectra.*

6 Discussion

6.1 Automated lithological mapping

An automated lithological processing chain has been developed and applied to hyperspectral data from the Antarctic. The automated processing chain was effective despite the very low SNR of the Antarctic data; the low SNR was a result of the challenging conditions during data acquisition and inadequate calibration of the TASI sensor. A number of preprocessing techniques were applied to improve the SNR; these no-doubt played a role in the efficacy of the automated processing chain and lithological map production, though almost all studies apply similar techniques for noise removal so this is not a surprising finding (Section 6.3.3). Additionally, during the processing chain algorithms were applied which have been shown to be effective even with low SNR data. Superpixel segmentation yielded endmembers which were all identifiable through comparison to field spectral measurements (e.g. Harris *et al.*, 2005). The findings of Thompson *et al.* (2010) and Gilmore *et al.* (2011) are confirmed here; superpixel segmentation aids in the determination of *recognisable* endmembers which are interpretable in a geological context, despite low SNR values.

The processing chain uses spectral unmixing techniques which are automated with few number of inputs and does not rely on manual endmember identification or random initialisation, hence the results are completely repeatable, unlike studies which rely on subject manual endmember techniques, such as the PPI (Chaudhry *et al.*, 2006). This is the first such development of an automated processing chain for hyperspectral TIR data analysis and offers alternatives compared to previous studies, which used manually involved techniques or simpler spectral matching techniques (e.g. Vaughan *et al.*, 2003b, 2005).

The incorporation of a whole suite of remote sensing tools in combination with field mapping could yield the greatest geological information; an automatic processing chain for lithological mapping would be a valuable part

of the whole suite of remote sensing technologies. A combination of airborne geophysics (radar, gravity and magnetics) to provide regional scale crustal information with local scale remote sensing techniques such as SAR and LiDAR used to understand geomorphological characteristics, terrain, relief, sub-surface structures, ground deformation and geological structures, along with the direct lithological identification made possible using spectral remote sensing (VNIR/SWIR and TIR) would provide this full suite of geological remote sensing tools. With targeted field campaigns, remote sensing data could be validated by field observations, geochemical and spectral data, and thus offer unprecedented information at much higher resolution than could be obtained by traditional field mapping alone. Such combinations of remote sensing technologies are often practically difficult due to the multi disciplinary nature of the work and the complex and manually involved processing required by different remote sensing technologies (van der Meer *et al.*, 2012); though the development of automated techniques, such as that presented here, can aid in bridging the gap between the remote sensing and geology and directly addresses the current paucity of automated and repeatable approaches to produce lithological maps using hyperspectral data (van der Meer *et al.*, 2012).

The ability to automatically produce lithological maps from remote sensing data offers a number of key benefits, especially in the Polar regions (see Section 6.2). However, whilst automated processing chains offer great utility, they are nevertheless dependant on calibration and/or validation using ground measurements or observations. As such, the processing chain presented here is a complementary tool for the geologist and it is unlikely that such processing chains would ever supplant the role of the geologist, or negate the need for field observations.

In the following sections, the main outcomes of the research are discussed (Section 6.2), followed by the data, acquisition and quality (Section 6.3). In Section 6.4 the limitations of the technique, consideration of the algorithms applied, and a discussion on the future applicability of the processing chain are presented. Finally, some recommendations are presented in Section 6.5.

6.2 Outcomes of the research

6.2.1 Utility in the Antarctic

Field geological mapping on the Antarctic Peninsula has been regularly undertaken for more than 50 years; however, the harsh environment, severe terrain, and large size of the peninsula (around 522,000 km^2, about twice the size of the UK) still provide major constraints on geological mapping and coverage. Traditional field geological mapping on the Antarctic Peninsula involves campaigns lasting several months during the austral summer, with travel over glaciated terrain to accessible rock exposures such as nunataks, using snowmobiles and on foot/ski. Snowmobiles allow efficient travel over the ice and significant distances to be covered (∼100 km/day) but are limited in their ability to travel over steep or crevassed terrain where access to rock outcrop must be undertaken on foot or ski; this can involve significant time and effort given the conditions, distances involved and need for safe travel procedures in crevassed areas. As a result, traditional field mapping techniques are severely limited in the amount of coverage in any one field season. Although rock exposure varies across the peninsula, it is generally limited (∼10% of the land surface), which provides a significant barrier to compiling regional geological maps. In particular, the sparse distribution and limited extent of rock restricts the correlation of lithostratigraphic units and geological lineaments making it difficult to compile detailed local scale geological maps (Haselwimmer, 2010).

A variety of remote sensing methods have been used to support geological mapping and overcome some of the limitations of traditional field mapping, namely: aerial photography and satellite imagery are used to assist fieldwork by providing base-maps for planning fieldwork and safe travel routes. Airborne geophysics (radar, gravity and magnetics) have been used to provide regional scale crustal information that provides a framework for understanding the results of more local-scale geological mapping. Multispectral remote sensing (e.g. Haselwimmer *et al.*, 2010, 2011) and, now, hyperspectral remote sensing have been utilised for regional and local scale lithological mapping on

the Antarctic Peninsula. The results presented here show that hyperspectral TIR data has proven useful for granitoid discrimination at a local scale which could have implications for mapping continental margin arcs (Section 6.2.2). The results also show that the hyperspectral TIR data are a significant improvement compared with Antarctic lithological mapping using multispectral TIR data, which was not able to discriminate subtle differences in granitoids (Haselwimmer *et al.*, 2010, 2011).

The development of an automated processing chain is also advantageous; in the future, hyperspectral datasets simply serve as an input to the automated processing chain and lithological maps are produced which can complement or aid in targeting traditional field geological mapping. However, aside from the practical considerations of collecting hyperspectral data from an area as large as the Antarctic, a number of other challenging issues remain: there is a need for calibration/validation data and field observations to corroborate remote sensing results, there is limited rock exposure in the Antarctic from which hyperspectral imagery could be collected, the image preprocessing requires good knowledge and/or in situ data on the atmospheric conditions, and the cold polar environment makes it challenging to achieve high SNRs. These issues must be considered when acquiring data and applying the processing chain in the future, especially in the Antarctic (see also Section 6.4.3).

6.2.2 Utility in a continental margin arc setting

The petrogenetic relationships between different granitoid rock types in continental margin settings remain poorly understood (Waight *et al.*, 1998). Subtle differences in mineralogy between granitoid rock types, e.g. granodiorite, quartz diorite, tonalite and so on, can reflect a fundamental difference in petrogenesis, in turn reflecting differing sources, crustal contributions, depth of melting, direct melting of the subducted slab or remelting of a mixed source (Waight *et al.*, 1998). This information can then be used to infer the tectonic setting and likely position of the arc front and slab angle.

Accurately mapping the subtle differences in mineralogy over a large area, on

the scale of a continental margin, is close to impossible using traditional field techniques, however spectral remote sensing could prove useful for such a task. This study has demonstrated that spectral unmixing techniques have been able to accurately discriminate granitoid types with an automated processing chain able to differentiate granodiorite and granite. However, it is noted that the technique did act to suppress the subtle spectral differences between granodiorite and dolerite, probably due to their geochemical similarity and the superpixel segmentation technique which can inhibit the identification of subtle endmember sets. In the future, data acquired from a larger range of granitoids would be useful to determine the ability of the automated processing chain to distinguish a whole suite of granitoid rock types and thus its ability to provide new insights in the petrogenetic relationships of continental margin arcs.

6.3 Data, acquisition, and preprocessing

6.3.1 Sensor and data acquisition

The TASI sensor is one of very few commercially available pushbroom hyperspectral thermal sensor systems designed specifically for airborne use. The acquisition of TASI data in the Antarctic was a collaborative effort between BAS, ITRES Research Ltd. and DRDC. The TASI sensor had not previously been flown in the polar regions, or in a cold unpressurised aircraft. The noise equivalent delta temperature (NEΔT; i.e. the temperature difference which would produce a signal equal to the sensor's temporal noise) for TASI is quoted as 0.2° at 300 K however the operational conditions in the Antarctic meant this figure was not representative for quantifying the actual SNR achieved during the campaign. The calibration conditions of the sensor under laboratory conditions were significantly different, hence there was a high degree of noise in the images (salt-and-pepper and shot noise), as well as line-to-line illumination differences. Aside from the signal to noise ratio, the TASI sensor's optics performed well, despite the repeated heating and cooling cycles between storage and use in the aircraft. The images are

crisp in focus where the diffraction limited optics mean that there is little to no pixel smearing. Additionally the geometric preprocessing carried out by ITRES produced high spatial accuracy and good orthorectified mosaic images. The high quality DEMs, derived from photogrammetry using very high resolution imagery, aided in the orthorectification.

Other commercially available sensors such as the Specim AisaOWL may provide an advantage over the TASI sensor. The OWL includes dual calibrated blackbodies on-board the sensor which allows for in-situ calibration and perhaps could yield greater SNR in the cold Antarctic environment. Additionally, the OWL has a greater number of bands (96) covering a larger spectral range (7.7 - 12.3 μm) which could aid in spectral identification.

Whilst the original motivation of the hyperspectral study was to investigate vegetation, a number of areas close to the survey region would have been interesting geological targets (c.f Figure 6.1). For example, Reptile Ridge, which is proximal to the runway at Rothera point contains the Reptile Ridge Formation composed of ryholitic ignimbrites and tuffs which could have been investigated using the (VNIR/SWIR and) TIR data (e.g. Brandmeier *et al.*, 2013). Additionally areas towards the southern end of Adelaide Island and Jenny Island, where outcrops of the Adelaide Island Intrusive Suite, Milestone Bluff Formation and the Mount Liotard Formation occur, would have allowed for a more detailed investigation of the ability to discriminate lithological units of varying ages and compositions.

In terms of the data acquisition itself, flight lines were flown parallel with an approximately 50-60% overlap; this was to minimise the topographical effects and pixel-smear at the highly off-nadir angles at swath edges and allow for the creation of a mosaic with those effects reduced. However, the SNR of the data remained an issue and a number of flight line-to-line illumination differences and artefacts were present in the final mosaics which required additional preprocessing (e.g. Section 4.1.1; Section 4.3.2 and Figure 5.4). Under the challenging conditions and with time pressures during the data acquisition campaign in the Antarctic, some data was collected under marginal conditions, or using non-optimal flight plans (e.g. solar geometry), hence the

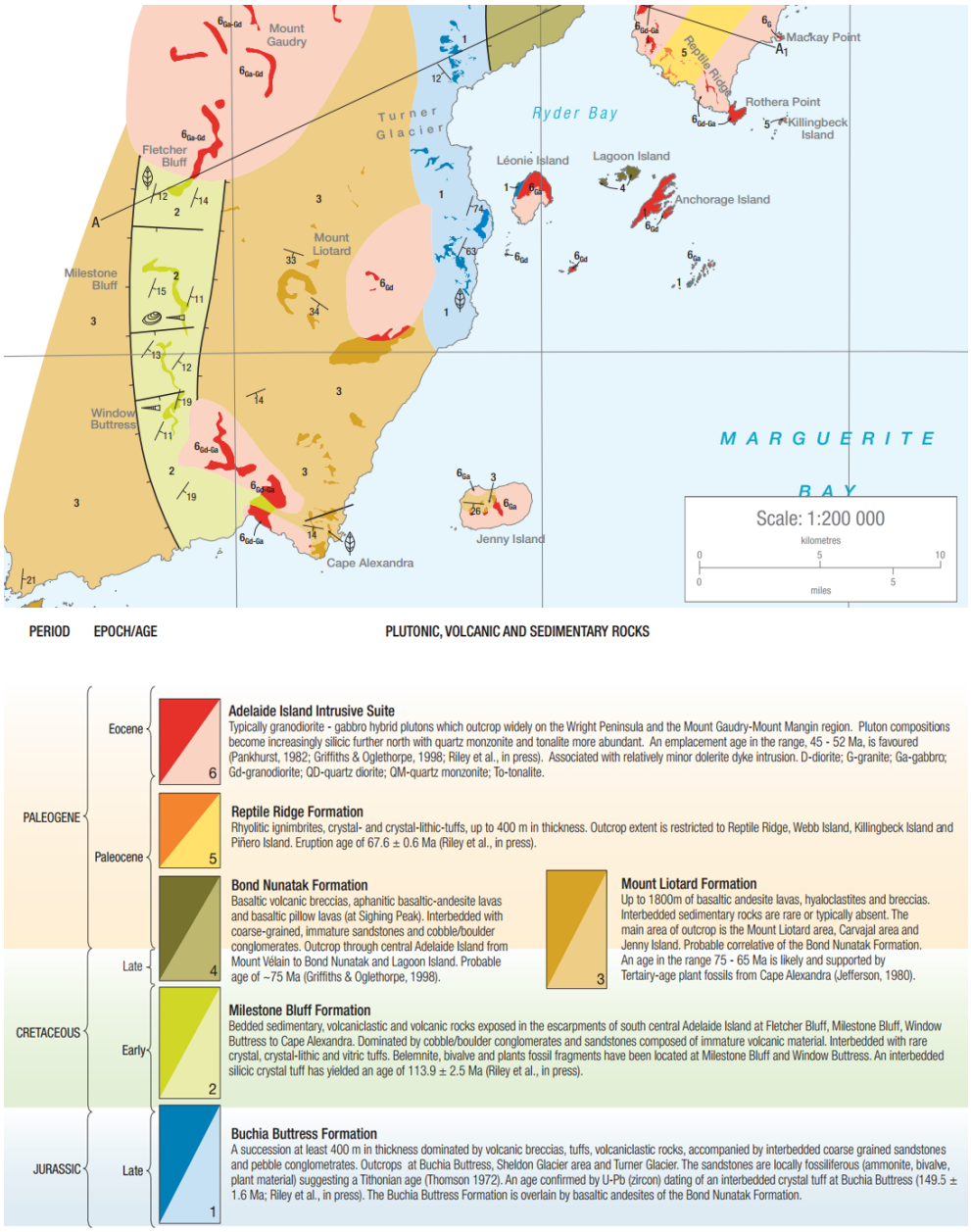

Figure 6.1: *Extract from the Adelaide Island Geological map showing the Marguerite Bay area.*

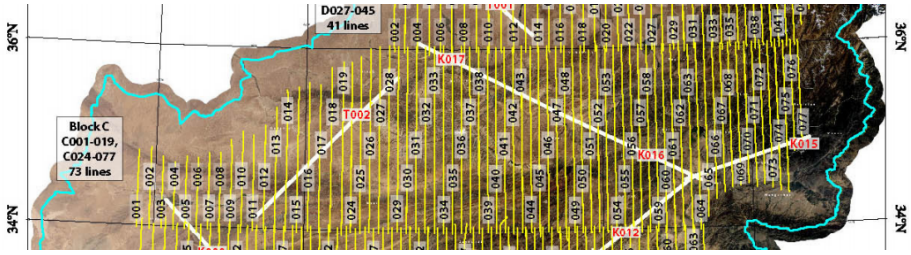

Figure 6.2: *Extract from the USGS Afghanistan hyperspectral survey showing cross-cutting calibration lines (white) over parallel flight lines (yellow) From Kokaly* et al. *(2008).*

low SNR values and lack of uniformity between neighbouring flight lines. These issues could be negated in future campaigns with appropriate planning and mitigation strategies. Additionally, limited ground targets prevented a robust calibration/validation of the atmospherically corrected and TES imagery (see Section 6.3.2). In other studies with limited calibration and ground targets, cross-cutting calibration lines have been flown perpendicular to the primary orientation of flight lines (e.g. Kokaly *et al.*, 2008; Figure 6.2). These cross-cutting calibration lines were later used to normalise illumination variation between flight lines to aid in generating seamless and normalised image mosaics, as well as to include data from limited ground calibration sites (Kokaly *et al.*, 2008). In the Antarctic, cross-cutting calibration lines would have been advantageous to aid in the normalisation of neighbouring flight lines and generation of mosaics as well as allowing for calibration if ground targets were deployed on cross-calibration flight lines.

6.3.2 Atmospheric correction and temperature emissivity separation

The atmospheric correction processing chain and results presented here represent the first known acquisition and subsequent processing of hyperspectral data in Antarctica. The presence of ground targets along with concurrent ground and atmospheric measurements in this study is typical of most hyperspectral campaigns; often there are not sufficient measurements to fully develop atmospheric profiles and aerosol models (to use as inputs to radiative transfer models), hence estimates are made and often standard atmospheric profiles and aerosol profiles are selected based on qualitative assessment of

environmental conditions. Additionally, there is not always a large enough number of ground based targets with the relevant concurrent spectral data to be used for both calibration and validation. The MODTRAN-5 LUTs used by ATCOR-4 were intended to be flexible enough to cover a wide variety of environments, sensor configurations, water vapour contents and flight parameters but have not been previously tested for airborne hyperspectral data in the Antarctic region.

Following the application of the atmospheric correction, results showed that workable emissivity data is obtainable. This is obtainable in spite of limited concurrent atmospheric and aerosol measurements, which is an often typical scenario. As there are no aerosol measurements collected near Anchorage Island, the maritime aerosol model (Shettle and Fenn, 1979) was selected based on the qualitative assessment of the atmospheric conditions and the assumption of a dominance of sea-salt aerosols in the coastal Antarctic environment (e.g. Rankin and Wolff, 2003). A detailed analysis of the performance of the atmospheric correction for VNIR/SWIR wavelengths is presented in Black *et al.* (2014b) (Appendix A). For the atmospheric correction of the hyperspectral TIR data, there were no calibrated ground targets present to perform a robust calibration/validation and accuracy assessment; hence, the quality of the atmospheric correction (and subsequent TES) was assessed through investigation of the SNR ratio and by comparison of image emissivity spectra to spectral library measurements (Section 5.3.2).

After atmospheric correction and TES, residual noise manifested emissivity features were present, most likely due to the unavailability of an Antarctic-specific atmospheric profile and aerosol model and the lack of adequate in-situ measurements to adequately recreate such inputs. This led to additional empirical corrections being performed (EELM) as the remnant atmospheric features could have been misinterpreted in a geological context, even though they may not have represented geological features. This approach has been recommended when considering VNIR/SWIR atmospheric corrections; in situations where there is a limited number of spectral ground truth measurements, a hybrid approach (radiative transfer and empirical corrections) can

improve atmospheric correction accuracy over the whole acquisition area (Tuominen and Lipping, 2011). The EELM was performed using pixels from snow, sea water, granite and dolerite; these targets were selected to cover a range of emissivity values (e.g. as in VNIR/SWIR approaches where dark and light targets are used; Smith and Milton, 1999) and were selected as they were easily identifiable in the imagery to generate target/reference spectra. However, the use of calibrated targets, such as controlled temperature pools and blackbody-like targets of constant emissivity (e.g. aluminium targets) would be preferred in future studies to provide a more robust set of ground targets specifically suitable for EELM (e.g. Distasio Jr. and Resmini, 2010).

These results suggest that commercially available atmospheric correction and TES algorithms are flexible enough to produce working emissivity data in Antarctica. However, residual atmospheric features remain and required additional empirical corrections to remove. It is recommended that, given the availability of a greater number of ground targets (>3), a similar hybrid approach of radiative transfer modelling and TES followed by empirical corrections, as applied here, would yield better results than radiative transfer modelling alone (a finding echoed by VNIR/SWIR studies, e.g. Smith and Milton, 1999; Tuominen and Lipping, 2011). Therefore, this study supports the conclusions of Tuominen and Lipping (2011) that, even in complex atmospheres where model based correction methods may struggle, more accurate results can be produced using combined correction methods compared to model based methods alone. It must also be noted that sensor calibration still remains challenging in this environment and these issues are manifested in the subsequent atmospheric correction and TES process.

Future studies should consider the influence of standard atmospheric profiles (McClatchey *et al.*, 1972) and aerosol models (Shettle and Fenn, 1979) with a view to measuring *in situ* atmospheric data while simultaneously acquiring hyperspectral data; this would aid in the generation of atmospheric profiles and aerosol models which serve as inputs during the atmospheric correction process and could reduce the level of uncertainty compared to using standard profiles. Such atmospheric data could also lead to the development of a

generic 'Antarctic' atmospheric profile and aerosol model, which may prove useful for future data acquisition (if *in situ* atmospheric data is not available).

6.3.3 Noise reduction

A number of steps were preformed to reduce the noise of the imagery and suppress the flight line illumination differences (Section 4.3.2), including the MNF transform and a median filter to remove residual shot noise as well as further EELM corrections to reduce atmospheric features in the emissivity spectrum. These preprocessing techniques and very common in almost all studies utilising hyperspectral data, where preprocessing techniques such as MNF are used to perform either dimensionality reduction or noise removal (e.g. Rowan and Mars, 2003; Vaughan *et al.*, 2003b, 2005; Harris *et al.*, 2005, 2006, 2010; Aslett *et al.*, 2008; Brandmeier, 2010; Thompson *et al.*, 2010, 2013; Gilmore *et al.*, 2011; Brandmeier *et al.*, 2013). The MNF is a proven technique as demonstrated by its wide use in a number of studies and this study further confirms its effectiveness.

Whilst these preprocessing techniques increased the SNR of the imagery, the significant flight line-to-line illumination differences significantly affected the VNIR/SWIR data (Section 4.1.1) and were also present in the TIR data (though not as prohibitive as VNIR/SWIR striping). As well as flying cross-calibration lines, a number of algorithms have been proposed in the literature for the reduction of line-to-line differences and cross-track correction to produce seamless mosaics which could be useful for future studies, if applied to the raw flightlines prior to producing image mosaics (e.g. Taylor, 2001; Palubinskas *et al.*, 2003; Zhao *et al.*, 2005; Asmat *et al.*, 2011; Rogge *et al.*, 2012).

6.4 Processing chain considerations

6.4.1 Limitations of the processing chain

Whilst the processing chain allowed for the distinction of various weathered granodiorites and granite, it was noted that it could not identify endmembers which corresponded to either the diorite or dolerite lithologic units on Anchorage Island. The geochemical similarity of these units would likely lead to subtle spectral differences and indicate this as a likely reason for the inability to discriminate these units (Section 5.3.3). However, this is a limitation of the processing chain. In continental margin arc settings, the discrimination of granitoids is important for establishing petrogenetic relationships (Section 6.2.2), meaning that a processing chain which can discriminate subtle lithological units, such as granite, granodiorite, dolerite, tonalite, quartz diorite and so on would be advantageous. These lithologies would inevitably have subtle spectral variations due to their chemical compositions, so sensor technologies and processing chains would need to be able to detect these subtle differences. It is noted that greater spectral information and more robust calibration could lead to increased SNR which would be advantageous (Section 6.3), along with combination with other remote sensing technologies to aid in lithological discrimination (e.g. Section 6.1).

During the development of the automated processing chain, algorithms were selected with two requirements in mind: (1) algorithms with proven success on low SNR data, and (2) algorithms which included a spatial component. As the dolerite dykes form linear features, algorithms which considered the spatial component should have been more readily able to delineate features such as dykes. However, the superpixel segmentation algorithm, whilst providing the benefit of decreasing noise, aggregates neighbouring pixels and therefore reduces or removes subtle spectral variance. This ultimately means that subtle spectral features may not be present in the superpixels, and thus not present in the extracted endmembers after applying an EEA; however, it should be noted that the detection of subtle spectral features is inevitably linked to the SNR of the data. In the future, if the operational SNR of TIR

data is increased (in the Antarctic), other EEAs could be considered as the first requirement (algorithms with proven success on low SNR data) could be reduced and other spatial EEAs could be considered (e.g. Plaza *et al.*, 2002; Rogge *et al.*, 2007; Zortea and Plaza, 2009).

During validation, the reconstructed image spectra (determined from the endmembers and their fractional abundances) were compared to the original image spectra. The fractional abundance threshold level used to assign pixels to a lithological unit (set to 0.5) is a parameter that controls the 'purity' of each endmember within a particular pixel, and thus the confidence is assigning a pixel to a lithological unit. As noted in Section 5.3.4, it was determined that as fractional abundances reduce, pixels are increasingly mixed and the confidence in assigning a distinct lithology is reduced. In future studies, the abundance level be increased to a higher value (e.g. 0.7) to increase the confidence in assigning lithological units. However, as a result the number of classified pixels will be reduced, so other techniques to classify null pixels, such as the moving window approach of Rogge *et al.* (2009) could be applied to refine the coverage of higher purity lithologies.

6.4.2 Algorithm considerations

Here a pure pixel scenario was considered – the assumption that at least one 'pixel' contains a pure endmember – due to the long history of research into pure pixel techniques for each step of the processing chain along with the optimised implementation and proven success of published algorithms (Section 2.5.3). The pure pixel approach has been successful when images contain pure pixels (Plaza *et al.*, 2012); however, given the presence of the mixing at different scales (even at microscopic levels), the pure pixel assumption is not always true, as some images may only contain pixels which are completely mixed (Plaza *et al.*, 2012).

The complexity of the problem is increased in a mixed pixel scenario, since the endmembers, or at least some of them, are not in the dataset (Bioucas-Dias, 2009). We note a point for future research into techniques in the mixed

pixel category, which follow from the seminal ideas of Craig (1994) based on the minimum volume transform, with a number of recently published algorithms building from this work (Berman *et al.*, 2004; Miao and Qi, 2007; Li and Staunton, 2008; Chan *et al.*, 2009; Bioucas-Dias, 2009). Currently, the major shortcoming of mixed-pixel techniques is long processing times due to their computational complexity (Bioucas-Dias, 2009). However mixed pixel techniques are an active area of research and as the algorithms mature they should be integrated into future studies. Additionally, the long established pure pixel methods should not yet be discounted; technological advances such as miniaturisation of sensors will inevitably lead to very high spatial resolution and reduced mixing as sensors are deployed from platforms such as Unmanned Aerial Vehicles (UAVs).

For spectral mixture analysis (SMA), also known as spectral unmixing, the fully constrained linear model was considered, due to its ease of implementation and flexibility in different applications (Chang, 2003). We have not considered linear unmixing using iterative spectral mixture analysis (ISMA; Rogge and Rivard, 2006), which seeks to minimise the error by unmixing on a per pixel basis using optimised endmember sets. Alternatively, non-linear SMA may best characterize the resultant mixed spectra for certain endmember distributions, such as those in which the endmember components are randomly distributed throughout the field of view of the instrument (Guilfoyle *et al.*, 2001; Plaza *et al.*, 2009a). In those cases, the mixed spectra collected at the imaging instrument are better described by assuming that part of the source radiation has undergone multiple scattering prior to being measured at the sensor.

In a non-linear model, the interaction between the endmembers and their fractional abundance is given by a non-linear function, which is not known *a priori*. Various techniques have been proposed in the field of machine learning, with neural networks some of first non-linear SMA approaches proposed (Benediktsson *et al.*, 1990). The performance of non-linear SMA algorithms on large, real-world hyperspectral data is currently limited by the computational complexity of the techniques; however, recent advances

have aimed to take advantage of parallel processing techniques to reduce computational time (e.g. Plaza *et al.*, 2008) and such algorithms remain an area for future research as their implementations become publicly available.

6.4.3 Future applicability of the processing chain

The processing chain presented here is fully automated and repeatable; after preprocessing, the six step processing chain is fully unsupervised, using few inputs and parameters, followed by predictive map generation and automatic class labelling using the field spectral data. The generic version of the processing chain is presented in Figure 6.3. This is a direct attempt to address the current paucity of such automated approaches in the geological remote sensing community (van der Meer *et al.*, 2012), and represents the first such approach presented for hyperspectral TIR data. We anticipate the technique could be applied by geologists without the need for 'expert' remote sensing knowledge or complicated image processing techniques / software packages, and the processing chain is more automated and less manually involved than traditional techniques. The automated workflow could be packaged in a 'wizard' style interface, similar to workflows developed for VNIR/SWIR data and currently available in commercial off-the-shelf software packages (e.g. ENVI), which could increase the uptake by geologists with guidance through the otherwise potentially complex workflow processing steps are parameter decisions. Indeed, this processing chain is particularly advantageous in the polar regions where higher detail lithological mapping can be obtained using remote sensing than compared with traditional field mapping.

The main parameters which affect the lithological mapping processing chain are the superpixel bias parameter and minimum size segment size. The parameters are discussed and explained in detail by Thompson *et al.* (2010). The bias and minimum segment size parameters control the size of the superpixels and should be scaled appropriately depending on the features of interest in each particular scene. The parameters used in this study were quantitatively determined by inspecting the superpixel segmentation image and considering

the scale of the geological areas of interest (e.g. dykes), however these parameters would require local tuning for other study areas, and particularly for other scales and image resolution (such as coarser resolution satellite imagery). The abundance threshold can be tuned to extract purer regions. However, this study has demonstrated the results obtained using a moderate threshold of 0.5; increasing this threshold to higher values would yield spectrally purer regions (e.g. Rogge *et al.*, 2009).

We have achieved the results presented here in spite of what might be described as 'extremely high noise conditions' (SNR $\leqslant$ 40 dB; Plaza *et al.*, 2012), thereby serving as a validation of the processing chain and its ability to operate effectively at low SNR values. We confirm the findings of the Thompson *et al.* (2010) and Gilmore *et al.* (2011) that superpixel segmentation aids in the determination of *recognisable* endmembers which are interpretable in a geological context despite low SNR values. Such a finding is crucial for future studies in the Antarctic where the environmental conditions mean that achieving high SNR values is much more challenging compared with temperate parts of the world. Indeed, this finding is also advantageous for many studies, not just the Antarctic, where challenging conditions can yield lower than expected SNRs; hence, it is advantageous that the processing chain can yield successful results even at low SNRs.

It is an important point to note for future applications that prior knowledge of the local geology (and/or vegetation) is required for the successful application of the processing chain. The identification of the image derived endmembers (step 6) was successful here, in large part due to availability of high quality field spectral measurements to allow for comparison along with ancillary data (geochemical analysis). However, in lieu of field spectral measurements, a user could produce geological interpretations with knowledge of the local geological context, an understanding of the imperfections in the hyperspectral imagery (e.g. residual noise due to inadequate atmospheric compensation) and the identification of endmembers could be aided through comparison to spectral libraries (e.g. Clark *et al.*, 1993b; Christensen *et al.*, 2000; Baldridge *et al.*, 2009).

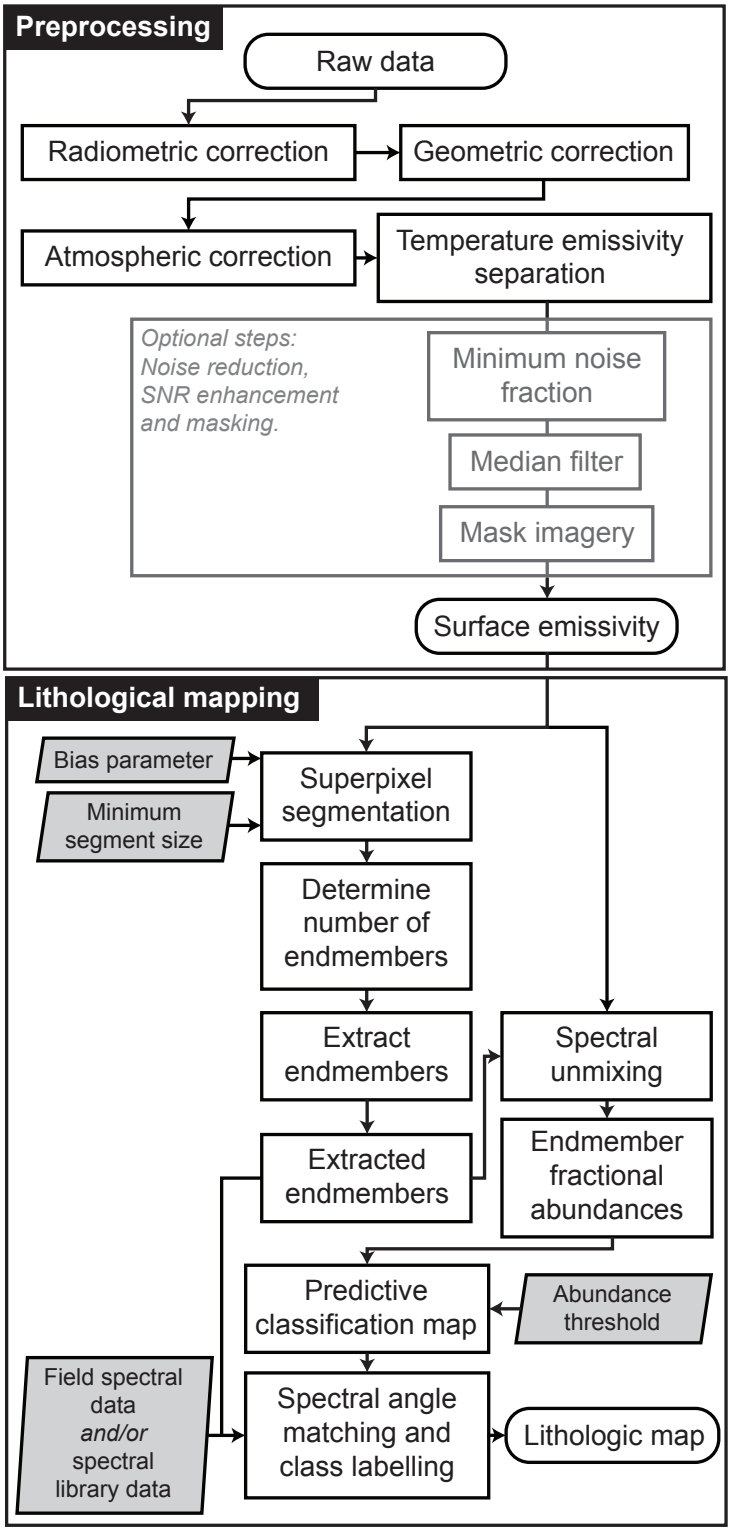

Figure 6.3: *A generic adaptation of the preprocessing steps and the subsequent lithological mapping processing chain; see also Figures 4.4 and 4.5.*

The techniques presented here could be easily transferred to other TIR data (or even VNIR/SWIR data), including currently available satellite data, such as ASTER, or even planned future satellite TIR data; for example, the HyspIRI satellite has a planned TIR instrument which includes 7 bands in the 7-13 μm spectral range (Hulley *et al.*, 2012). The coarser spatial and spectral resolution of this data would yield difficulties in the exact identification of minerals, though previous TIR data, such as ASTER, has been used to reliably discriminate a wide range of minerals, especially silicates, as well as proving useful for lithological mapping (e.g. Rowan and Mars, 2003; Chen *et al.*, 2007; Rogge *et al.*, 2009; Haselwimmer *et al.*, 2010, 2011; Salvatore *et al.*, 2014). Additionally, technological advances and increasing miniaturisation will eventually lead to the availability of UAV-deployable research grade hyperspectral sensors which could be used operationally by field geologists as a tool to compliment traditional field mapping techniques. The use of an automated processing chain in such a situation would be highly advantageous in delivering fast, automated and repeatable lithological mapping results which could aid and inform traditional mapping approaches operationally in the field.

6.4.4 Generic example: Lithological mapping at Cuprite

To demonstrate the generic applicability of the processing chain (both at another geographic location and using solar reflectance data) a brief example is presented for the well-known geological test site at Cuprite, USA. Cuprite is located in west-central Nevada where large areas of exposed Cambrian sediments and Tertiary volcanics were intensively altered in the mid- to late-Miocene (Abrams *et al.*, 1977). Imagery for this site has been extensively investigated and reported in the remote sensing literature because of minimal vegetation cover and the presence of large outcrops exposing a suite of spectrally distinct alteration minerals (e.g. Abrams *et al.*, 1977; Kruse *et al.*, 1990; Hook and Rast, 1990; Hook *et al.*, 1991; Clark *et al.*, 1993a; Kruse *et al.*, 1993; Abrams and Hook, 1995; Clark and Swayze, 1996; Resmini *et al.*, 1997; Rowan *et al.*, 2003). The data has also been used as a test example in many

papers developing algorithms for each of the processing steps (e.g. Winter, 1999; Plaza *et al.*, 2002; Nascimento and Bioucas-Dias, 2005; Chang and Plaza, 2006; Zhang *et al.*, 2008; Bioucas-Dias and Nascimento, 2008; Bioucas-Dias, 2009).

A hyperspectral data cube collected from Cuprite mining district in July 1995 using the Airborne Visible Infra-Red Imaging Spectrometer (AVIRIS) as part of an AVIRIS Group Shoot and is distributed as a tutorial dataset with the ENVI software (ENVI, 2014). The hyperspectral data is 400 × 350 pixels (8 × 7 km) with 50 bands of SWIR data (from 2 to 2.5 μm). The spatial and spectral resolutions are 20 m and 10 nm respectively. The data are supplied having been corrected to reflectance using the ATmospheric REMoval (ATREM; Gao *et al.*, 1993) and having residual noise minimized using the Empirical Flat Field Optimized Reflectance Transform (EFFORT; Boardman, 1998).

The generic processing chain, as outlined in Figure 6.3 (page 125) was applied. The preprocessing steps were not required as the data are available following atmospheric correction and EFFORT noise removal; the data has a high SNR (> 500:1) hence no further noise reduction techniques were applied. As with the Anchorage Island dataset the superpixel segmentation bias parameter k, was set to 0.1 and the minimum superpixel region size was set to 30 pixels using the Euclidean spectral distance as the divergence measure. The abundance threshold was fixed at 0.5 and in lieu of field spectral measurements, the United States Geological Survey (USGS) mineral spectral library (Clark *et al.*, 1993b) was used to automatically identify and label endmembers.

The processing chain identified and extracted 7 endmembers (other studies also identify 7 endmembers from the same dataset, e.g. Zhang *et al.*, 2008); the endmembers and lithological map are presented in Figure 6.4. For qualitative validation the results are presented alongside 'expert' mapping of the region also using AVIRIS data by Swayze *et al.* (2014) (Figure 6.5). Of the 7 extracted endmembers, only 6 could be reliably identified from the USGS spectral library. All of the endmembers have higher SA values than seen with the Anchorage Island data. This is likely result of having *in situ* field spectral data available for Anchorage Island and using library data for Cuprite; this high-

lights the differences between using library and field data as lower SA matches are seen with library data. The resulting lithological map (Figure 6.4B) agrees well with the results from Swayze *et al.* (2014) (Figure 6.5). The lithological map shows a similar pattern of alteration minerals and their distinct regions in the east (chert/chalcedony + alunite) and west (alunite + kaolinite) of the Cuprite image, however reduced spectral contrast in the endmember set (Figure 6.4A) does not allow for subtle spectral identification in areas such as the Alunite Hill or Buddingtonite Hill (compare Figure 6.5). This result echoes the findings of the Anchorage Island study area; the superpixel segmentation reduces the spectral contrast and can prevent the detection of subtle spectral features. This perhaps suggests that if appropriately high SNRs are achieved during data acquisition, the superpixel segmentation may act to inhibit the identification of spectrally subtle endmembers (Thompson *et al.*, 2010). However, this remains a point for future research and is inevitably a trade-off between SNR, data quality, and the ability to derive subtle lithological information from hyperspectral data.

Nevertheless, this brief example illustrates the future applicability of the processing chain at other study areas as well as using the solar reflective region.

This page has been intentionally left blank.

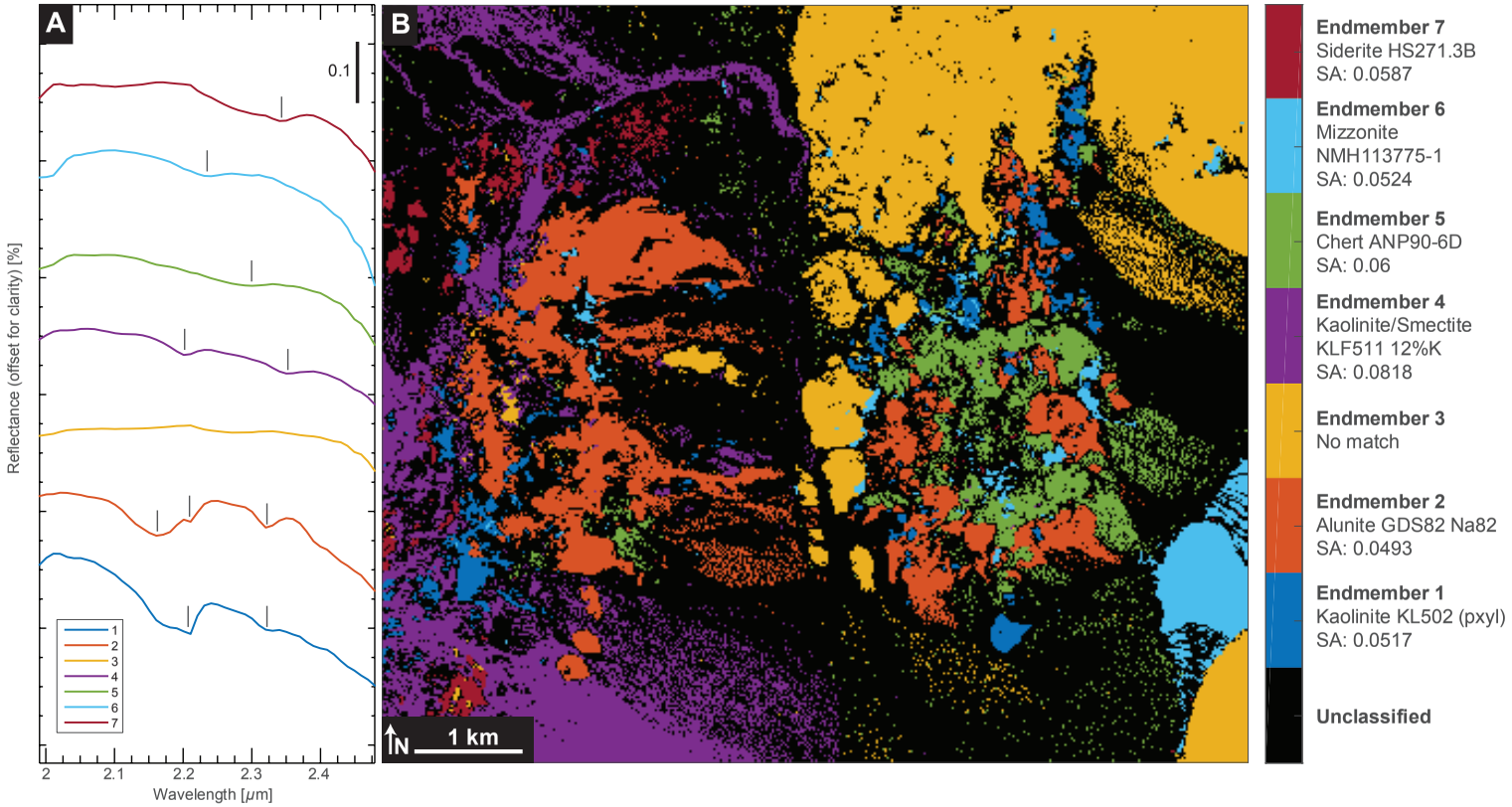

Figure 6.4: *Extracted endmembers (A) where vertical black lines indicate absorption features useful for mineral identification. (B) shows the resulting lithological map (B) for Cuprite, Nevada, USA using shortwave infrared (SWIR; 2 - 2.5 μm) data. Endmember labels are determined through spectral angle (SA) matching with the United States Geological Survey (USGS) mineral spectral library (Clark* et al., *1993b).*

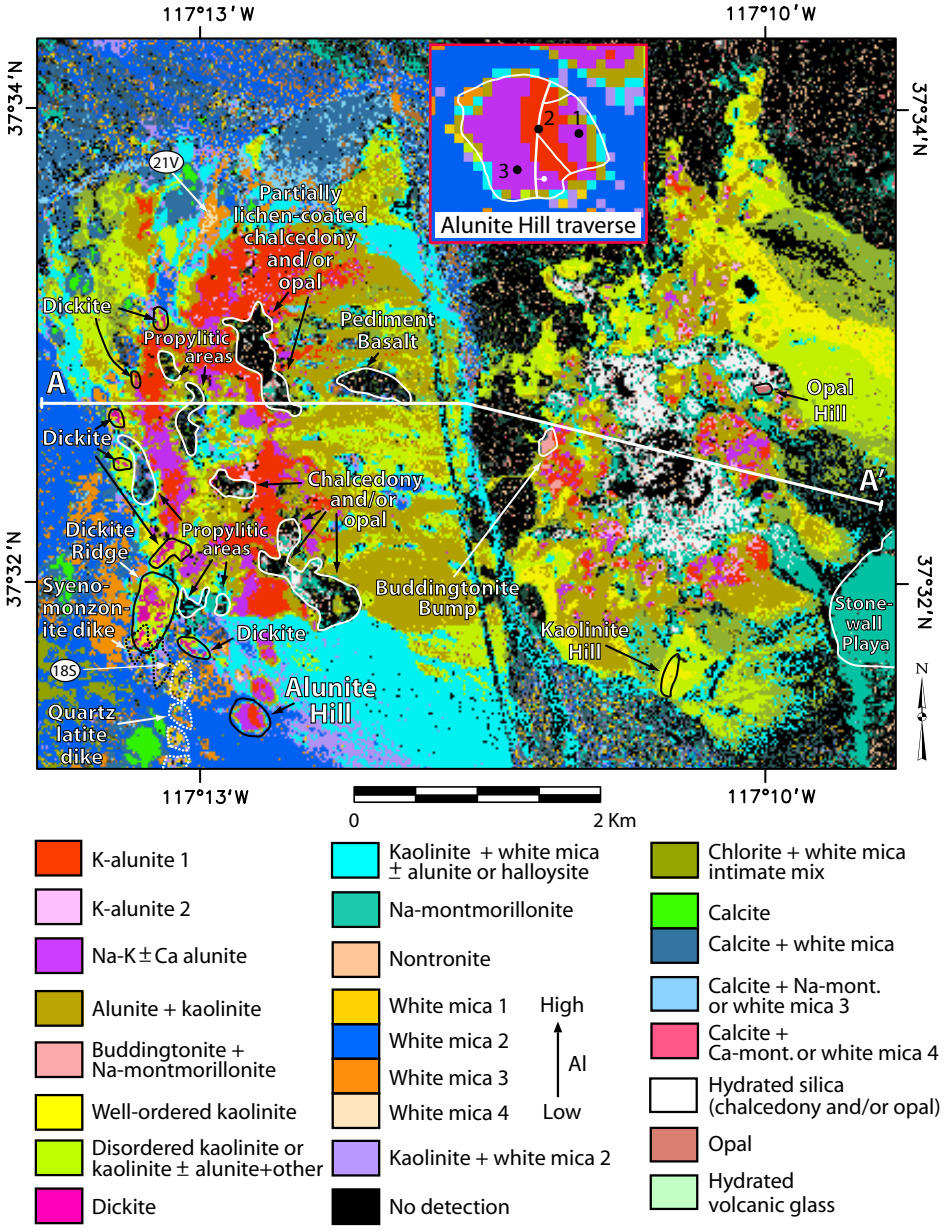

Figure 6.5: *Mineral mapping at Cuprite using AVIRIS SWIR data by Swayze* et al. *(2014). Derived from the 2 μm vibrational region mineral map centered on the hydrothermal alteration at Cuprite.*

6.5 Recommendations for future work

A number of key suggestions and recommendations are noted below; these include recommendations for (Antarctic) remote sensing in support of lithological mapping, and recommendations and lines of future research for the processing of hyperspectral data to produce lithological maps. To aid in calibration/validation and production of seamless image mosaics from hyperspectral imagery a number of points should be considered:

- A number of large, well distributed ground targets (those of known reflectance or emissivity, of a constant temperature or blackbody-like targets) to serve as calibration and validation targets for atmospheric correction and temperature emissivity separation
- Measurements of *in situ* atmospheric constituents (aerosols, ozone, water vapour) to constrain atmospheric parameters for radiative transfer modelling and possible generation of standard 'Antarctic' atmospheric profiles and aerosol models for future studies
- Overlapping flightlines as well as cross-cutting calibration lines to allow for flight-line levelling, cross-track correction and minimisation of illumination differences between neighbouring flight lines to produce seamless mosaics
- For thermal sensors on-board blackbodies may improve calibration; alternatively the calibration of instruments should occur under similar conditions to data acquisition which may improve the SNR

Whilst the processing chain was effective, there are still some possible lines for future research and algorithm development which could be considered, namely:

- Investigate the use of mixed pixel endmember extraction techniques as opposed to assuming the pure pixel scenario
- Non-linear spectral unmixing techniques, as these may best reflect the intimate mixing of materials within an individual pixel hence these techniques could yield more accurate fractional abundances

- A robust assessment of the large number of EEA algorithms, including a robust assessment of spatial EEAs using synthetic and real hyperspectral data; as code becomes publicly available and computational power increases (or with access to high performance computing or use of graphical processing units) a larger number of EEAs could be investigated using synthetic data to determine the optimal algorithm for identification of specific endmembers

Additionally, if future satellite launches with thermal sensors such as HyspIRI (Hulley *et al.*, 2012) are successful in may be possible to investigate techniques such as thermal inertia (TI) for lithological discrimination. Thermal inertia – that is, the ability of a material to withstand changes in temperature through a diurnal cycle – is a physically important property of a material which can help identify its characteristics (Gupta, 2003). TI, calculated from remote sensing data, has been used to aid geological mapping and lithological discrimination (Kahle *et al.*, 1976; Pratt and Ellyett, 1978; Gillespie, 1985; Cracknell and Xue, 1996; Majumdar, 2003; Nasipuri *et al.*, 2005, 2006; Ramakrishnan *et al.*, 2013). Additionally, since the launch of the Mars Global Surveyor (MGS), with it's Thermal Emission Spectrometer, several studies have utilised thermal inertia to aid in the mapping of features on the Martian surface (Sefton-Nash *et al.*, 2012; Ody *et al.*, 2013; Audouard *et al.*, 2014). Such techniques could be applied in the Antarctic, through satellite measurements either at the start or towards the end of the austral summer when a distinct day-night cycle is present in the Antarctic.

7 Conclusion

A fully automated processing chain to produce lithological maps using airborne hyperspectral thermal infrared data has been developed for data of a low signal to noise ratio; the first known development of such a processing chain. An airborne hyperspectral TIR dataset, collected for the first time from Antarctica, was used with the processing chain to accurately discriminate grantoids. The challenging conditions and cold temperatures in the Antarctic yielded data with a significantly lower SNR compared with data collected in more temperate environments. As a result, several preprocessing steps were employed to refine the imagery prior to analysis; atmospheric correction and temperature emissivity separation were applied, followed by further empirical corrections and noise removal through the minimum noise fraction technique. Areas of snow and sea water were subsequently masked using the temperature image.

The processing chain was established and applied to the preprocessed imagery. Firstly, superpixel segmentation was applied to aggregate homogeneous image regions comprised of several pixels having similar values into larger segments (superpixels). The superpixels were input into the VD algorithm to determine the number of endmembers, which were subsequently extracted using VCA and unmixed using FCLSU to generate abundances of each endmember. A predictive classification map was created where endmember fractions were thresholded (> 0.5). The endmembers extracted were automatically matched to their closest spectrum from the field spectral data, and the observations made in the field from these measurements were used to label the predictive map classes and generate a lithological map.

The fully automated processing chain was successful in identifying 4 geologically interpretable endmembers from the study area. Reconstruction of the hyperspectral image from the endmembers and their fractional abundances yielded a root mean square error (RMSE) of 0.58%. The RMSE value, almost twice as large as previous studies, is likely a result of the low SNR of the Antarctic data; nonetheless the processing chain was still able to accurately

discriminate the majority of lithological units with strong agreement to existing geological maps. The results were validated and interpreted in the context of the study area in conjunction with a full suite of ancillary data: detailed high quality ground reference spectral data collected using a field portable FTIR spectrometer, thin section and scanning electron microscope analysis, electron microprobe analysis, whole rock geochemical data and mineral modal analysis. The results are promising, with the thermal imagery allowing clear distinction between granitoid types. However, the distinction of fine grained, intermediate composition dykes is not possible, due to the close spectral similarity with the country rock (granodiorite). Nonetheless, the results show an improvement over previous lithological mapping using multispectral TIR data in the Antarctic and highlight the improved discrimination of subtle granitoids made possible through the use of hyperspectral TIR data.

The processing chain developed here is the first automated and repeatable processing chain developed for producing a lithological map from airborne hyperspectral thermal infrared data. It has the advantage of being effective at producing lithological maps from data of a low signal to noise ratio and offers improvements and repeatability compared to previously published techniques, which are based on simpler spectral matching techniques or involved manually derived endmembers. However, it is noted that the superpixel segmentation could inhibit the identification of spectrally subtle endmembers. The processing chain was also briefly demonstrated using SWIR data at Cuprite, Nevada; this highlights the transferability of the technique to other study areas, other spectral ranges and other sensors. Secondly, this study has tackled the challenges of processing of the first ever airborne hyperspectral data collected in the Antarctic and offers important recommendations for future hyperspectral campaigns in the region. This study could have implications in the future with the launch of spaceborne hyperspectral sensors which will yield repeated hyperspectral imagery of the polar regions, as well as with the development of UAV-borne hyperspectral remote sensing where an automated methodology for lithological mapping could be advantageous.

References

Abrams, M. and Hook, S. J. (1995). Simulated ASTER data for geologic studies. *Geoscience and Remote Sensing, IEEE Transactions on*, **33**(3):692–699.

Abrams, M. J., Ashley, R. P., Rowan, L. C., Goetz, A. F. H., and Kahle, A. B. (1977). Mapping of hydrothermal alteration in the Cuprite mining district, Nevada, using aircraft scanner images for the spectral region 0.46 to 2.36 μm. *Geology*, **5**(12):713–718.

Adams, J. B., Smith, M. O., and Johnson, P. E. (1986). Spectral mixture modeling: A new analysis of rock and soil types at the Viking Lander 1 site. *Journal of Geophysical Research: Solid Earth (1978–2012)*, **91**(B8):8098–8112.

Adler, H. H. and Kerr, P. F. (1963). Infrared absorption frequency trends for anhydrous normal carbonates. *American Mineralogist*, **48**(1-2):124.

An, P., Chung, C. F., and Rencz, A. N. (1996). Digital lithology mapping from airborne geophysical and remote sensing data in the Melville Peninsula, northern Canada, using a neural network approach. *International Journal of Rock Mechanics and Mining Sciences and Geomechanics Abstracts*, **33**:262A–262A.

Aslett, Z., Taranik, J. V., and Riley, D. N. (2008). Mapping Rock-Forming Minerals at Daylight Pass, Death Valley National Park, California, using SEBASS Thermal-Infrared Hyperspectral Image Data. In: *Geoscience and Remote Sensing Symposium, 2008. IGARSS 2008. IEEE International*, volume 3, pages III – 366–III – 369. doi:10.1109/IGARSS.2008.4779359.

Asmat, A., Milton, E., and Atkinson, P. (2011). Empirical correction of multiple flightline hyperspectral aerial image mosaics. *Remote Sensing of Environment*, **115**(10):2664–2673. ISSN 00344257. doi:10.1016/j.rse.2011.05.022.

Audouard, J., Poulet, F., Vincendon, M., Bibring, J. P., Forget, F., Langevin, Y., and Gondet, B. (2014). Mars surface thermal inertia and heterogeneities

from OMEGA/MEX. *Icarus*, **233**:194–213. ISSN 0019-1035. doi:10.1016/j.icarus.2014.01.045.

Baldridge, A. M., Hook, S. J., Grove, C. I., and Rivera, G. (2009). The ASTER spectral library version 2.0. *Remote Sensing of Environment*, **113**(4):711–715. ISSN 0034-4257. doi:10.1016/j.rse.2008.11.007.

Baraldi, A., Binaghi, E., Blonda, P., Brivio, P. A., and Rampini, A. (2001). Comparison of the multilayer perceptron with neuro-fuzzy techniques in the estimation of cover class mixture in remotely sensed data. *Geoscience and Remote Sensing, IEEE Transactions on*, **39**(5):994–1005.

Bateson, A. and Curtiss, B. (1996). A method for manual endmember selection and spectral unmixing. *Remote Sensing of Environment*, **55**(3):229–243.

Bechtel, R., Rivard, B., and Sánchez-Azofeifa, A. (2002). Spectral properties of foliose and crustose lichens based on laboratory experiments. *Remote Sensing of Environment*, **82**:389–396.

Becker, F. and Li, Z.-L. (1990). Temperature-Independant spectgral indices in thermal infrared bands. *Remote Sensing of Environment*, **32**:17–33.

Bedini, E. (2009). Mapping lithology of the Sarfartoq carbonatite complex, southern West Greenland, using HyMap imaging spectrometer data. *Remote Sensing of Environment*, **113**(6):1208–1219.

Ben-Dor, E., Malthus, T., Plaza, A., and Schläpfer, D. (2013). Hyperspectral Remote Sensing. In: M. Wendisch and J.-L. Brenguier (Editors), *Airborne Measurements for Environmental Research*, chapter 8, pages 419–465. Wiley-VCH, Berlin. ISBN 978-3-527-40996-9.

Benediktsson, J., Swain, P. H., and Ersoy, O. K. (1990). Neural network approaches versus statistical methods in classification of multisource remote sensing data. *IEEE Transactions on geoscience and remote sensing*, **28**(4):540–552.

Berman, M., Kiiveri, H., Lagerstrom, R., Ernst, A., Dunne, R., and Huntington, J. F. (2004). ICE: A statistical approach to identifying endmembers in hyperspectral images: Learning from Earth's Shapes and Colors. *IEEE transactions on Geoscience and Remote Sensing*, **42**(10):2085–2095.

Bioucas-Dias, J. M. (2009). A variable splitting augmented Lagrangian approach to linear spectral unmixing. In: *Hyperspectral Image and Signal Processing: Evolution in Remote Sensing, 2009. WHISPERS'09. First Workshop on*, pages 1–4. IEEE, Grenoble, France.

Bioucas-Dias, J. M. and Nascimento, J. M. P. (2008). Hyperspectral subspace identification. *Geoscience and Remote Sensing, IEEE Transactions on*, **46**(8):2435–2445.

Birnie, R. W., Parr, J. T., Naslund, H. R., Nichols, J. D., and Turner, P. A. (1989). Applications of landsat thematic mapper and ground-based spectrometer data to a study of the Skaergaard and other mafic intrusions of East Greenland. *Remote Sensing of Environment*, **28**:297–304.

Bishop, C. M. (2007). *Neural Networks for Pattern Recognition*. Oxford University Press.

Black, M., Casanovas, P., Convey, P., and Fretwell, P. (2014a). High resolution mapping of Antarctic vegetation communities using airborne hyperspectral data. In: *Proceedings of the Remote Sensing and Photogrammetry Society Annual Conference, Aberystwyth, Wales, UK*. doi:10.13140/2.1.5189.6648.

Black, M., Fleming, A., Riley, T., Ferrier, G., Fretwell, P., McFee, J., Achal, S., and Diaz, A. U. (2014b). On the Atmospheric Correction of Antarctic Airborne Hyperspectral Data. *Remote Sensing*, **6**(5):4498–4514. doi:10.3390/rs6054498.

Boardman, J. W. (1993). Automating spectral unmixing of AVIRIS data using convex geometry concepts. In: *Summaries 4th Annu. JPL Airborne Geoscience Workshop*, volume 1, pages 11–14. JPL Publication 93–26.

Boardman, J. W. (1998). *Post-ATREM polishing of AVIRIS apparent reflectance data using EFFORT: a lesson in accuracy versus precision*. Summaries of the Seventh JPL Airborne Earth Science Workshop, JPL Publication 99-17, vol. 1, p53.

Boardman, J. W. and Kruse, F. A. (1994). *Automated spectral analysis: A geologic example using AVIRIS data, North Grapevine Mountains, Nevada.* Proceedings of tenth thematic conference on geologic remote sensing (pp. I407–I418), Environmental Research Institute of Michigan.

Boardman, J. W., Kruse, F. A., and Green, R. O. (1995). Mapping Target Signatures Via Partial Unmixing of Aviris Data. *Summaries of the Fifth Annual JPL Airborne Earth Science Workshop. Volume 1 - AVIRIS Workshop*, pages 23–26.

Borel, C. (2008). Error analysis for a temperature and emissivity retrieval algorithm for hyperspectral imaging data. *International Journal of Remote Sensing*, **29**(17-18):5029–5045. ISSN 0143-1161. doi: 10.1080/01431160802036540.

Borel, C. C. (1998). Surface emissivity and temperature retrieval for a hyperspectral sensor. In: *Geoscience and Remote Sensing Symposium Proceedings, 1998. IGARSS'98. 1998 IEEE International*, volume 1, pages 546–549. IEEE.

Borengasser, M., Hungate, W. S., and Watkins, R. (2007). *Hyperspectral Remote Sensing: Principles and Applications*. Remote Sensing Applications Series. Taylor and Francis. ISBN 9781420012606.

Brandmeier, M. (2010). Remote sensing of Carhuarazo volcanic complex using ASTER imagery in Southern Peru to detect alteration zones and volcanic structures - a combined approach of image processing in ENVI and ArcGIS/ArcScene. *Geocarto International*, **25**(8):629–648. doi:10.1080/10106049.2010.519787.

Brandmeier, M., Erasmi, S., Hansen, C., Höweling, A., Nitzsche, K., Ohlendorf, T., Mamani, M., and Wörner, G. (2013). Mapping patterns of mineral

alteration in volcanic terrains using ASTER data and field spectrometry in Southern Peru. *Journal of South American Earth Sciences*, **48**:296–314. ISSN 08959811. doi:10.1016/j.jsames.2013.09.011.

Burton-Johnson, A. and Riley, T. R. (2015). Autochthonous v. accreted terrane development of continental margins: a revised in situ tectonic history of the Antarctic Peninsula. *Journal of the Geological Society*, **172**(6):822–835. doi:10.1144/jgs2014-110.

Calvin, W. M., Vaughan, R. G., Taranik, J. V., and Smailbegovic, A. (2001). Mapping natural and human influenced acid sulfate weathering near Reno, NV using the SEBASS hyperspectral instrument. In: *Geoscience and Remote Sensing Symposium, 2001. IGARSS '01. IEEE 2001 International*, volume 2, pages 727–729 vol.2. doi:10.1109/IGARSS.2001.976616.

Campbell, J. B. and Wynne, R. H. (2012). *Introduction to Remote Sensing, Fifth Edition*. Guilford Publications. ISBN 9781609181772.

Camps-Valls, G. and Bruzzone, L. (2005). Kernel-based methods for hyperspectral image classification. *Geoscience and Remote Sensing, IEEE Transactions on*, **43**(6):1351–1362.

Camps-Valls, G., Tuia, D., Bruzzone, L., and Atli Benediktsson, J. (2014). Advances in Hyperspectral Image Classification: Earth Monitoring with Statistical Learning Methods. *Signal Processing Magazine, IEEE*, **31**(1):45–54. ISSN 1053-5888. doi:10.1109/MSP.2013.2279179.

Casacchia, R., Mazzarini, F., Salvatori, R., and Salvini, F. (1999). Rock-type discrimination by field, TM and SPOT data, Tarn Flat, Antarctica. *International Journal of Remote Sensing*, **20**:403–420.

Casanovas, P., Black, M., Fretwell, P., and Convey, P. (2015). Mapping lichen distribution on the Antarctic Peninsula using remote sensing, lichen spectra and photographic documentation by citizen scientists. *Polar Research*, **34**(25633). doi:10.3402/polar.v34.25633.

Chan, T.-H., Chi, C.-Y., Huang, Y.-M., and Ma, W.-K. (2009). A Convex Analysis-Based Minimum-Volume Enclosing Simplex Algorithm for Hyperspectral Unmixing. *Signal Processing, IEEE Transactions on*, **57**(11):4418–4432. ISSN 1053-587X. doi:10.1109/TSP.2009.2025802.

Chan, T.-H., Liou, J.-Y., Ambikapathi, A., Ma, W.-K., and Chi, C.-Y. (2012). Fast algorithms for robust hyperspectral endmember extraction based on worst-case simplex volume maximization. In: *Acoustics, Speech and Signal Processing (ICASSP), 2012 IEEE International Conference on*, pages 1237–1240. Kyoto, Japan. ISSN 1520-6149. doi:10.1109/ICASSP.2012.6288112.

Chan, T.-H., Ma, W.-K., Ambikapathi, A., and Chi, C.-Y. (2011). A Simplex Volume Maximization Framework for Hyperspectral Endmember Extraction. *Geoscience and Remote Sensing, IEEE Transactions on*, **49**(11):4177–4193. ISSN 0196-2892. doi:10.1109/TGRS.2011.2141672.

Chang, C. I. (2003). *Hyperspectral Imaging: Techniques for Spectral Detection and Classification*. Hyperspectral Imaging: Techniques for Spectral Detection and Classification. Springer US. ISBN 9780306474835.

Chang, C.-I. and Du, Q. (2004). Estimation of number of spectrally distinct signal sources in hyperspectral imagery. *Geoscience and Remote Sensing, IEEE Transactions on*, **42**(3):608–619.

Chang, C.-I. and Plaza, A. (2006). A fast iterative algorithm for implementation of pixel purity index. *Geoscience and Remote Sensing Letters, IEEE*, **3**(1):63–67.

Chaudhry, F., Wu, C.-c., Liu, W., and Chang, C.-i. (2006). Pixel purity index-based algorithms for endmember extraction from hyperspectral imagery. In: C.-i. Chang (Editor), *Recent Advances in Hyperspectral Signal and Image Processing*, volume 661, chapter 2, pages 29–62. Transworld Research Network, Kerala, India, 1st edition. ISBN 8178952181.

Chen, J., Richard, C., and Honeine, P. (2013). Nonlinear unmixing of hyperspectral data based on a linear-mixture/nonlinear-fluctuation model. *Signal Processing, IEEE Transactions on*, **61**(2):480–492.

Chen, X., Warner, T. A., and Campagna, D. J. (2007). Integrating visible, near-infrared and short-wave infrared hyperspectral and multispectral thermal imagery for geological mapping at Cuprite, Nevada. *Remote Sensing of Environment*, **110**(3):344–356. ISSN 00344257. doi:10.1016/j.rse.2007.03.015.

Christensen, P. R., Bandfield, J. L., Hamilton, V. E., Howard, D. A., Lane, M. D., Piatek, J. L., Ruff, S. W., and Stefanov, W. L. (2000). A thermal emission spectral library of rock-forming minerals. *Journal of Geophysical Research*, **105**(E4):9735. ISSN 0148-0227. doi:10.1029/1998JE000624.

Clark, R. N. (1999). *Chapter 1: Spectroscopy of Rocks and Minerals, and Principles of Spectroscopy*. Manual of Remote Sensing, Volume 3, Remote Sensing for the Earth Sciences. John Wiley and Sons, New York.

Clark, R. N., King, T. V. V., Klejwa, M., Swayze, G. A., and Vergo, N. (1990). High spectral resolution reflectance spectroscopy of minerals. *Journal of Geophysical Research: Solid Earth*, **95**(B8):12653–12680. ISSN 2156-2202. doi:10.1029/JB095iB08p12653.

Clark, R. N. and Swayze, G. A. (1996). Evolution in imaging spectroscopy analysis and sensor signal-to-noise: An examination of how far we have come. In: *Summaries of the Sixth Annual JPL Airborne Earth Science Worksho, JPL Publication, March 4-8*, pages 4–8.

Clark, R. N., Swayze, G. A., and Gallagher, A. (1993a). Mapping minerals with imaging spectroscopy. *US Geological Survey, Office of Mineral Resources Bulletin*, **2039**:141–150.

Clark, R. N., Swayze, G. A., Gallagher, A., King, T. V., and Calvin, W. M. (1993b). *The U.S. Geological Survey digital spectral library: Version 1: 0.2 to 3.0 microns*. U.S. Geol. Survey Open File Report.

Clark, R. N., Swayze, G. A., Livo, K. E., Kokaly, R. F., Sutley, S. J., Dalton, J. B., McDougal, R. R., and Gent, C. A. (2003). Imaging spectroscopy: Earth and planetary remote sensing with the USGS Tetracorder and expert

systems. *Journal of Geophysical Research: Planets*, **108**(E12). ISSN 2156-2202. doi:10.1029/2002JE001847.

Convey, P. (2003). *Maritime Antarctic Climate Change: Signals from Terrestrial Biology*, volume 29 of *Antarctic Research Series*, pages 145–158. American Geophysical Union, Washington DC, USA. ISBN 9781118668450. doi: 10.1029/AR079p0145.

Convey, P. and Smith, R. I. L. (2006). Responses of terrestrial Antarctic ecosystems to climate change. In: J. Rozema, R. Aerts, and H. Cornelissen (Editors), *Plants and Climate Change*, volume 41 of *Tasks for vegetation science*, pages 1–12. Springer Netherlands. ISBN 978-1-4020-4442-7. doi: 10.1007/978-1-4020-4443-4.

Cracknell, A. P. and Xue, Y. (1996). Thermal inertia determination from space – a tutorial review. *International Journal of Remote Sensing*, **17**(3):431–461.

Craig, M. D. (1994). Minimum-volume transforms for remotely sensed data. *Geoscience and Remote Sensing, IEEE Transactions on*, **32**(3):542–552.

Cudahy, T. J., Wilson, J., Hewson, R., Linton, P., Harris, P., Sears, M., Okada, K., and Hackwell, J. A. (2001). Mapping porphyry-skarn alteration at Yerington, Nevada, using airborne hyperspectral VNIR-SWIR-TIR imaging data. In: *Geoscience and Remote Sensing Symposium, 2001. IGARSS '01. IEEE 2001 International*, volume 2, pages 631–633. doi:10.1109/IGARSS.2001.976573.

Dash, P., Göttsche, F.-M., Olesen, F.-S., and Fischer, H. (2002). Land surface temperature and emissivity estimation from passive sensor data: Theory and practice-current trends. *International Journal of Remote Sensing*, **23**(13):2563–2594. ISSN 0143-1161. doi:10.1080/01431160110115041.

Distasio Jr., R. and Resmini, R. (2010). Atmospheric compensation of thermal infrared hyperspectral imagery with the emissive empirical line method and the in-scene atmospheric compensation algorithms: a comparison. In: *Society of Photo-Optical Instrumentation Engineers (SPIE) Conference Series*,

volume 7695 of *Society of Photo-Optical Instrumentation Engineers (SPIE) Conference Series*. doi:10.1117/12.849898.

Dobigeon, N., Tourneret, J.-Y., Richard, C., Bermudez, J. C. M., McLaughlin, S., and Hero, A. O. (2014). Nonlinear unmixing of hyperspectral images: Models and algorithms. *Signal Processing, IEEE Transactions on*, (1):1–24.

Drury, S. A. (2001). *Image Interpretation in Geology*. Blackwell Science, Oxford, UK. ISBN 0748764992.

Du, Q., Raksuntorn, N., Younan, N. H., and King, R. L. (2008). End-member extraction for hyperspectral image analysis. *Applied Optics*, **47**(28):F77—-F84.

EIA (2014). *Endmember Induction Algorithms (EIAs) toolbox, version 0.2*. Grupo de Inteligencia Computacional, Universidad del País Vasco / Euskal Herriko Unibertsitatea (UPV/EHU), Spain.

ENVI (2014). *Environment for Visualising Images, version 5.1*. Exelis Vis, Boulder, Colorado, USA.

Favretto, A. and Geletti, R. (2004). Satellite imagery elaboration (ASTER sensor, TERRA satellite), in order to map rock distribution in extreme areas. The Prince Albert mountain chain (Victoria Land - Antarctica). In: *XXth ISPRS Congress*, page 1234. Istanbul.

Felzenszwalb, P. F. and Huttenlocher, D. P. (2004). Efficient graph-based image segmentation. *International Journal of Computer Vision*, **59**(2):167–181.

Feng, J., Rivard, B., Rogge, D., and Sánchez-Azofeifa, A. (2013). The longwave infrared (3-14μm) spectral properties of rock encrusting lichens based on laboratory spectra and airborne SEBASS imagery. *Remote Sensing of Environment*, **131**:173–181. ISSN 00344257. doi:10.1016/j.rse.2012.12.018.

Feng, J., Rivard, B., Rogge, D. M., and Grant, B. (2012). Spectral enhancement of sebass hyperspectral data and its application in mapping

of ultramafic rocks. In: *4th Workshop on Hyperspectral Image and Signal Processing: Evolution in Remote Sensing (WHISPERS)*, pages 1–4. doi: 10.1109/WHISPERS.2012.6874248.

Flynn, L. P., Harris, A. J., and Wright, R. (2001). Improved identification of volcanic features using landsat 7 etm+. *Remote Sensing of Environment*, **78**(1):180–193.

Freemantle, J. R., Pu, R., and Miller, J. R. (1992). Calibration of imaging spectrometer data to reflectance using pseudo-invariant features. In: *Proceedings of the 14th Canadian Symposium on Remote Sensing*, pages 1–4.

Fretwell, P. T., Convey, P., Fleming, A. H., Peat, H. J., and Hughes, K. A. (2011). Detecting and mapping vegetation distribution on the Antarctic Peninsula from remote sensing data. *Polar Biology*, **34**(2):273–281. ISSN 0722-4060. doi:10.1007/s00300-010-0880-2.

Galehouse, J. (1971). Point counting. In: R. E. Carver (Editor), *Procedures in Sedimentary Petrology*. John Wiley and Sons Canada, Limited.

Gao, B. C., Heidebrecht, K. B., and Goetz, A. F. H. (1993). Derivation of scaled surface reflectances from AVIRIS data. *Remote Sensing of Environment*, **44**(2):165–178.

Gillespie, A. R. (1985). Lithologic mapping of silicate rocks using TIMS. In: *Proceedings of the TIMS Data User's Workshop*, JPL Pub. 86-38 (Pasadena, CA, USA), pages 29–44.

Gillespie, A. R., Rokugawa, S., Matsunaga, T., Cothern, J. S., Hook, S. J., and Kahle, A. (1998). A temperature and emissivity separation algorithm for advanced spaceborne thermal emission and reflection radiometer (ASTER) images. *IEEE Transactions on Geoscience and Remote Sensing*, **36**:1113–1126.

Gilmore, M. S., Thompson, D. R., Anderson, L. J., Karamzadeh, N., Mandrake, L., and Castaño, R. (2011). Superpixel segmentation for analysis of hyperspectral data sets, with application to Compact Reconnaissance Imaging Spectrometer for Mars data, Moon Mineralogy Mapper data, and

Ariadnes Chaos, Mars. *Journal of Geophysical Research: Planets*, **116**(E7). ISSN 2156-2202. doi:10.1029/2010JE003763.

Goetz, A. F. H., Vane, G., Solomon, J. E., and Rock, B. N. (1985). Imaging Spectrometry for Earth Remote Sensing. *Science*, **228**(4704):1147–1153. doi:10.1126/science.228.4704.1147.

Green, R. O., Eastwood, M. L., Sarture, C. M., Chrien, T. G., Aronsson, M., Chippendale, B. J., Faust, J. A., Pavri, B. E., Chovit, C. J., Solis, M., and Others (1998). Imaging spectroscopy and the airborne visible/infrared imaging spectrometer (AVIRIS). *Remote Sensing of Environment*, **65**(3):227–248.

Gruninger, J. H., Ratkowski, A. J., and Hoke, M. L. (2004). The sequential maximum angle convex cone (SMACC) endmember model. In: *Defense and Security*, pages 1–14. International Society for Optics and Photonics.

Gu, D., Gillespie, A., Kahle, A., and Palluconi, F. (2000). Autonomous atmospheric compensation (AAC) of high resolution hyperspectral thermal infrared remote-sensing imagery. *IEEE Transactions on Geoscience and Remote Sensing*, **38**(6):2557–2570. ISSN 01962892. doi:10.1109/36.885203.

Guilfoyle, K. J., Althouse, M. L., and Chang, C.-I. (2001). A quantitative and comparative analysis of linear and nonlinear spectral mixture models using radial basis function neural networks. *Geoscience and Remote Sensing, IEEE Transactions on*, **39**(10):2314–2318.

Gupta, R. P. (2003). *Remote Sensing Geology*. Springer-Verlag, Berlin, Germany. ISBN 3-540-43185-3.

Halimi, A., Altmann, Y., Dobigeon, N., and Tourneret, J.-Y. (2011). Nonlinear Unmixing of Hyperspectral Images Using a Generalized Bilinear Model. *IEEE Transactions on Geoscience and Remote Sensing*, **49**(11):4153–4162. ISSN 0196-2892. doi:10.1109/TGRS.2010.2098414.

Harris, J., Rogge, D., Hitchcock, R., Ijewlie, O., and Wright, D. (2005). Mapping lithology in Canada's Arctic: application of hyperspectral data

using the minimum noise fraction transformation and matched filtering. *Canadian Journal of Remote Sensing*, **2193**(2005):2173–2193. doi:10.1139/E05-064.

Harris, J. R., McGregor, R., and Budkewitsch, P. (2010). Geological analysis of hyperspectral data over southwest Baffin Island: methods for producing spectral maps that relate to variations in surface lithologies. *Canadian Journal of Remote Sensing*, **36**(4):412–435. ISSN 0703-8992. doi:10.5589/m10-072.

Harris, J. R., Ponomarev, P., Shang, J., and Rogge, D. (2006). Noise reduction and best band selection techniques for improving classification results using hyperspectral data: application to lithological mapping in Canada's Arctic. *Canadian Journal of Remote Sensing*, **32**(5):341–354. ISSN 0703-8992. doi:10.5589/m06-029.

Harsanyi, J. C. (1993). *Detection and Classification of Subpixel Spectral Signatures in Hyperspectral Image Sequences*. Ph.D. thesis, University of Maryland.

Harsanyi, J. C., Farrand, W., and Chang, C.-I. (1993). Determining the number and identity of spectral endmembers: An integrated approach using Neyman-Pearson eigenthresholding and iterative constrained RMS error minimization. In: *Proceedings of the Ninth Thematic Conference on Geologic Remote Sensing: Exploration, Engineering, and Environment : 8-11 February 1993, Pasadena, California, USA*. Environmental Research Institute of Michigan.

Haselwimmer, C. E. (2010). *Lithological mapping on the Antarctic Peninsula using Advanced Spaceborne Thermal Emission and Reflection Radiometer (ASTER) data*. Phd thesis, Imperial College London.

Haselwimmer, C. E., Riley, T. R., and Liu, J. G. (2010). Assessing the potential of multispectral remote sensing for lithological mapping on the Antarctic Peninsula: case study from eastern Adelaide Island, Graham

Land. *Antarctic Science*, **22**(03):299–318. ISSN 0954-1020. doi:10.1017/S0954102010000015.

Haselwimmer, C. E., Riley, T. R., and Liu, J. G. (2011). Lithologic mapping in the Oscar II Coast area, Graham Land, Antarctic Peninsula using ASTER data. *International Journal of Remote Sensing*, **32**(7):2013–2035. ISSN 0143-1161. doi:10.1080/01431161003645824.

Hecker, C., Dilles, J. H., van der Meijde, M., and van der Meer, F. D. (2012). Thermal infrared spectroscopy and partial least squares regression to determine mineral modes of granitoid rocks. *Geochemistry, Geophysics, Geosystems*, **13**(3):Q03021. ISSN 1525-2027. doi:10.1029/2011GC004004.

Hecker, C., van der Meijde, M., and van der Meer, F. D. (2010). Thermal infrared spectroscopy on feldspars - Successes, limitations and their implications for remote sensing. *Earth-Science Reviews*, **103**(1-2):60–70. ISSN 00128252. doi:10.1016/j.earscirev.2010.07.005.

Heinz, D. C. and Chang, C.-I. (2001). Fully constrained least squares linear spectral mixture analysis method for material quantification in hyperspectral imagery. *Geoscience and Remote Sensing, IEEE Transactions on*, **39**(3):529–545.

Hewson, R., Hausknecht, P., Cudahy, T., Huntington, J., Mason, P., Hackwell, J., Nikitas, J., and Okada, K. (2000). *An Appraisal of the Hyperspectral Thermal-infrared SEBASS Data Recorded from Oatman, Arizona and a Comparison of Their Unmixed Results with AVIRIS*. Exploration and mining report 668F. CSIRO Exploration and Mining, Wembley, Western Australia.

Hook, S. J., Cudahy, T. J., Kahle, A. B., and Whitbourn, L. B. (1998). Synergy of active and passive airborne thermal infrared systems for surface compositional mapping. *Journal of Geophysical Research: Solid Earth (1978–2012)*, **103**(B8):18269–18276.

Hook, S. J., Dmochowski, J. E., Howard, K. A., Rowan, L. C., Karlstrom, K. E., and Stock, J. M. (2005). Mapping variations in weight percent silica

measured from multispectral thermal infrared imagery - Examples from the Hiller Mountains, Nevada, USA and Tres Virgenes-La Reforma, Baja California Sur, Mexico. *Remote Sensing of Environment*, **95**(3):273–289. ISSN 00344257. doi:10.1016/j.rse.2004.11.020.

Hook, S. J., Elvidge, C. D., Rast, M., and Watanabe, H. (1991). An evaluation of short-wave-infrared (SWIR) data from the AVIRIS and GEOSCAN instruments for mineralogical mapping at Cuprite, Nevada. *Geophysics*, **56**(9):1432–1440.

Hook, S. J., Gabell, A. R., Green, A. A., and Kealy, P. S. (1992). A comparison of techniques for extracting emissivity information from thermal infrared data for geologic studies. *Remote Sensing of Environment*, **42**(2):123–135. ISSN 0034-4257. doi:10.1016/0034-4257(92)90096-3.

Hook, S. J. and Rast, M. (1990). Mineralogic mapping using Airborne Visible Infrared Imaging Spectrometer (AVIRIS), Shortwave Infrared (SWIR) data acquired over Cuprite, Nevada. In: *Proceedings of the Second Airborne Visible Infrared Imaging Spectrometer (AVIRIS) Workshop, JPL Publication*, pages 54–90.

Hulley, G., Realmuto, V., Hook, S. J., and Ramsey, M. (2012). HyspIRI Thermal Infrared (TIR) Band Study Report. JPL Publication 12-6. Technical report, NASA Jet Propulsion Laboratory, California.

Hunt, G. and Salisbury, J. (1975). Mid-infrared spectral behavior of sedimentary rocks. Technical report.

Hunt, G. R. (1980). Electromagnetic radiation: the communication link in remote sensing. *Remote sensing in geology*, **2**:5–45.

Ifarraguerri, A. and Chang, C.-I. (1999). Multispectral and hyperspectral image analysis with convex cones. *Geoscience and Remote Sensing, IEEE Transactions on*, **37**(2):756–770.

ITRES (2012). Project Report: Airborne Hyperspectral Survey with British

Antarctic Survey: CASI-1500, SASI-600 and TASI-600. Technical Report May, ITRES, Calgary, Alberta, Canada.

Kahle, A., Gillespie, A., and Goetz, A. F. (1976). Thermal Inertia Imaging: A New Geologic Mapping Tool. *Geophysical Research Letters*, **3**(1):26–28.

Kahle, A. B., Madura, D. P., and Soha, J. M. (1980). Middle infrared multispectral aircraft scanner data: analysis for geological applications. **19**:2279–2290.

Kealy, P. S. and Gabell, A. R. (1990). Estimation of emissivity and temperature using alpha coefficients. In: *Proceedings of the second TIMS Workshop*, JPL Pub. 90-95 (Pasadena, CA, USA), pages 11–15.

Kealy, P. S. and Hook, S. J. (1993). Separating Temperature and Emissivity in Thermal Infrared Multispectral Scanner Data: Implications for Recovering Land Surface Temperatures. *IEEE Transactions on Geoscience and Remote Sensing*, **31**(6):1155–1164.

Keshava, N. (2003). A Survey of Spectral Unmixing Algorithms. *Lincoln Laboratory Journal*, **14**(1):55–78.

Keshava, N. and Mustard, J. F. (2002). Spectral unmixing. *Signal Processing Magazine, IEEE*, **19**(1):44–57.

Kiang, N. Y., Siefert, J., and Blankenship, R. E. (2007). Spectral signatures of photosynthesis. I. Review of Earth organisms. *Astrobiology*, **7**(1):222–251.

Kirkland, L., Herr, K., Keim, E., Adams, P., Salisbury, J., Hackwell, J., and Treiman, A. (2002). First use of an airborne thermal infrared hyperspectral scanner for compositional mapping. *Remote Sensing of Environment*, **80**(3):447–459. ISSN 00344257. doi:10.1016/S0034-4257(01)00323-6.

Kokaly, R. F., King, T., and Livo, K. E. (2008). Airborne Hyperspectral Survey of Afghanistan 2007: Flight Line Planning and HyMap Data Collection. Technical Report Open-File Report 2008-1235, USGS Afghanistan Project Product No. 186, United States Geological Survey, Virginia, USA.

Kramer, H. J. (2002). *Observation of the Earth and Its Environment: Survey of Missions and Sensors*. Engineering online library. Springer. ISBN 9783540423881.

Kruse, F. A., Calvin, W. M., and Seznec, O. (1988). Automated extraction of absorption features from airborne visible/infrared imaging spectrometer (AVIRIS) and geophysical and environmental research imaging spectrometer (GERIS) data. In: *Proc. Airborne Visible/Infrared Imaging Spectrometer (AVIRIS) Performance Evaluation Workshop, Jet Propulsion Laboratory, Pasadena, CA, JPL Pub*, pages 38–88.

Kruse, F. A., Kierein-Young, K. S., and Boardman, J. W. (1990). Mineral mapping at Cuprite, Nevada with a 63-channel imaging spectrometer. *Photogrammetric Engineering and Remote Sensing*, **56**:83–92.

Kruse, F. A., Lefkoff, A. B., and Dietz, J. B. (1993). Expert system-based mineral mapping in northern Death Valley, California/Nevada, using the airborne visible/infrared imaging spectrometer (AVIRIS). *Remote Sensing of Environment*, **44**(2):309–336.

Kruse, F. A. and McDowell, M. (2015). Analysis of multispectral and hyperspectral longwave infrared (LWIR) data for geologic mapping. In: M. Velez-Reyes and F. A. Kruse (Editors), *Proc. SPIE 9472, Algorithms and Technologies for Multispectral, Hyperspectral, and Ultraspectral Imagery XXI*, page 94721E. doi:10.1117/12.2176657.

Kuenzer, C. and Dech, S. (2013). Theoretical background of thermal infrared remote sensing. In: C. Kuenzer and S. Dech (Editors), *Thermal Infrared Remote Sensing*, volume 17 of *Remote Sensing and Digital Image Processing*, pages 1–26. Springer Netherlands. ISBN 978-94-007-6638-9. doi:10.1007/978-94-007-6639-6_1.

Landgrebe, D. A. (2005). *Signal Theory Methods in Multispectral Remote Sensing*. Wiley Series in Remote Sensing and Image Processing. Wiley. ISBN 9780471721253.

Lane, M. D. and Christensen, P. R. (1997). Thermal infrared emission spectroscopy of anhydrous carbonates. *Journal of Geophysical Research*, **102**(E11):25581. ISSN 0148-0227. doi:10.1029/97JE02046.

Li, M. and Staunton, R. (2008). Optimum Gabor filter design and local binary patterns for texture segmentation. *Pattern Recognition Letters*, **29**(5):664–672. ISSN 01678655. doi:10.1016/j.patrec.2007.12.001.

Li, S., Li, W.-z., Zhou, J.-j., and Zhuang, D.-f. (2007). A Review on Endmember Selection Methods in the Course of Mixed Pixel Decomposition of Remote Sensing Images. *Geography and Geo-Information Science*, **5**:9.

Li, Z.-L., Becker, F., Stoll, M. P., and Wan, Z. (1999). Evaluation of Six Methods for Extracting Relative Emissivity Spectra from Thermal Infrared Images. *Remote Sensing of Environment*, **69**(3):197–214. ISSN 0034-4257. doi:10.1016/S0034-4257(99)00049-8.

Liang, S., Fang, H., Chen, M., Shuey, C. J., Walthall, C., Daughtry, C., Morisette, J., Schaaf, C., and Strahler, A. (2002). Validating MODIS land surface reflectance and albedo products: methods and preliminary results. *Remote Sensing of Environment*, **83**(1-2):149–162. ISSN 0034-4257. doi:10.1016/S0034-4257(02)00092-5.

Lillesand, T. M., Kiefer, R. W., and Chipman, J. W. (2004). *Remote Sensing and Image Interpretation*. John Wiley & Sons Canada, Limited. ISBN 9780471451525.

Liu, W. and Wu, E. Y. (2005). Comparison of non-linear mixture models: sub-pixel classification. *Remote Sensing of Environment*, **94**(2):145–154.

Lorenz, H. (2004). Integration of Corona and Landsat Thematic Mapper data for bedrock geological studies in the high Arctic. *International Journal of Remote Sensing*, **25**(22):5143–5162.

Lu, D., Batistella, M., Moran, E., and Mausel, P. (2004). Application of spectral mixture analysis to Amazonian land-use and land-cover classification. *International Journal of Remote Sensing*, **25**(23):5345–5358.

Lubin, D. and Massom, R. (2006). *Polar Remote Sensing: Volume I: Atmosphere and Oceans*. Springer Praxis Books. Springer, USA. ISBN 9783540307853.

Lyberis, N., Parrot, J. F., Chorowicz, J., and Rudant, J. P. (1990). Geological features of the Spitsbergen region obtained from multispectral SPOT data and field radiometer measurements. *International Journal of Remote Sensing*, **11**(2):253–265.

Magendran, T. and Sanjeevi, S. (2014). Hyperion image analysis and linear spectral unmixing to evaluate the grades of iron ores in parts of Noamundi, Eastern India. *International Journal of Applied Earth Observation and Geoinformation*, **26**:413–426.

Majumdar, T. J. (2003). Regional thermal inertia mapping over the Indian subcontinent using INSAT-1D VHRR data and its possible geological applications. *International Journal of Remote Sensing*, **24**(11):2207–2220. doi:10.1080/01431160210161724.

Manolakis, D., Marden, D., and Shaw, G. A. (2003). Hyperspectral Image Processing for Automatic Target Detection Applications. *Lincoln Laboratory Journal*, **14**(1):79–116.

Manolakis, D. and Shaw, G. (2002). Detection algorithms for hyperspectral imaging applications. *Signal Processing Magazine, IEEE*, **19**(1):29–43. ISSN 1053-5888. doi:10.1109/79.974724.

Martin, S. (2014). *An Introduction to Ocean Remote Sensing*. Cambridge University Press, Cambridge, UK. ISBN 9781107019386.

Martínez, P. J., Pérez, R. M., Plaza, A., Aguilar, P. L., Cantero, M. C., and Plaza, J. (2006). Endmember extraction algorithms from hyperspectral images. *Annals of Geophysics*, **49**(1). doi:10.4401/ag-3156.

Maslanik, J. A. and Barry, R. G. (1990). Remote sensing in Antarctica and the Southern Ocean: applications and developments. *Antarctic Science*, **2**(2):105–121.

Massom, R. and Lubin, D. (2006). *Polar Remote Sensing: Volume II: Ice Sheets*. Springer Praxis Books. Springer, USA. ISBN 9783540305651.

MathWorks (2011). *MATLAB, version 7.12.0.635 (R2011a)*. The MathWorks Inc., Natick, Massachusetts.

McClatchey, R. A., Fenn, R. W., Selby, J. E. A., Volz, F. E., and Garing, J. S. (1972). Optical Properties of the Atmosphere. Technical report, Environmental Research Paper Air Force Geophysics Lab., Hanscom AFB, MA. Optical Physics Div.

Miao, L. and Qi, H. (2007). Endmember extraction from highly mixed data using minimum volume constrained nonnegative matrix factorization. *Geoscience and Remote Sensing, IEEE Transactions on*, **45**(3):765–777.

Nascimento, J. M. P. and Bioucas-Dias, J. M. (2005). Vertex component analysis: A fast algorithm to unmix hyperspectral data. *Geoscience and Remote Sensing, IEEE Transactions on*, **43**(4):898–910.

Nasipuri, P., Majumdar, T. J., and Mitra, D. S. (2006). Study of high-resolution thermal inertia over western India oil fields using ASTER data. *Acta Astronautica*, **58**(5):270–278. ISSN 00945765. doi:10.1016/j.actaastro.2005.11.002.

Nasipuri, P., Mitra, D., and Majumdar, T. (2005). Generation of thermal inertia image over a part of Gujarat: A new tool for geological mapping. *International Journal of Applied Earth Observation and Geoinformation*, **7**(2):129–139. ISSN 03032434. doi:10.1016/j.jag.2005.02.002.

Neville, R. A., Levesque, J., Staenz, K., Nadeau, C., Hauff, P., and Borstad, G. A. (2003). Spectral unmixing of hyperspectral imagery for mineral exploration: comparison of results from SFSI and AVIRIS. *Canadian Journal of Remote Sensing*, **29**(1):99–110.

Neville, R. A., Staenz, K., Szeredi, T., Lefebvre, J., and Hauff, P. (1999). Automatic endmember extraction from hyperspectral data for mineral

exploration. In: *21st Canadian Symposium on Remote Sensing. Ottawa, Ontario, Canada, 21-24 June 1999*, pages 1–8. Ottawa, Ontario, Canada.

Ody, A., Poulet, F., Bibring, J. P., Loizeau, D., Carter, J., Gondet, B., and Langevin, Y. (2013). Global investigation of olivine on Mars: Insights into crust and mantle compositions. *Journal of Geophysical Research – Planets*, **118**(2):234–262. ISSN 2169-9097. doi:10.1029/2012JE004149.

Palmadesso, P. J., Antoniades, J. A., Baumbeck, M., and Rickard, L. J. (1995). Use of filter vectors in hyperspectral data analysis. In: *Proc SPIE*, volume 2553, pages 148–157.

Palubinskas, G., Muller, R., and Reinartz, P. (2003). Mosaicking of optical remote sensing imagery. In: *Geoscience and Remote Sensing Symposium, 2003. IGARSS '03. Proceedings. 2003 IEEE International*, volume 6, pages 3955–3957 vol.6. doi:10.1109/IGARSS.2003.1295326.

Philpot, W. and Ansty, T. (2011). Analytical description of pseudo-invariant features (PIFs). In: *6th International Workshop on Analysis of Multi-temporal Remote Sensing Images (Multi-Temp)*, pages 53–56. doi:10.1109/Multi-Temp.2011.6005046.

Plaza, A., Benediktsson, J. A., Boardman, J. W., Brazile, J., Bruzzone, L., Camps-Valls, G., Chanussot, J., Fauvel, M., Gamba, P., Gualtieri, A., Marconcini, M., Tilton, J. C., and Trianni, G. (2009a). Recent advances in techniques for hyperspectral image processing. *Remote Sensing of Environment*, **113**:S110–S122. ISSN 00344257. doi:10.1016/j.rse.2007.07.028.

Plaza, A., Martinez, P., Pérez, R., and Plaza, J. (2002). Spatial/spectral endmember extraction by multidimensional morphological operations. *Geoscience and Remote Sensing, IEEE Transactions on*, **40**(9):2025–2041.

Plaza, A., Plaza, J., Martínez, G., and Sanchez, S. (2011). Hyperspectral Data Processing Algorithms. In: P. S. Thenkabail, J. G. Lyon, and A. Huete (Editors), *Hyperspectral Remote Sensing of Vegetation*, chapter 5, pages 121–138. CRC Press. ISBN 1439845379.

Plaza, J., Hendrix, E. M. T., García, I., Martín, G., and Plaza, A. (2012). On endmember identification in hyperspectral images without pure pixels: A comparison of algorithms. *Journal of Mathematical Imaging and Vision*, **42**(2-3):163–175.

Plaza, J. and Plaza, A. (2010). Spectral mixture analysis of hyperspectral scenes using intelligently selected training samples. *Geoscience and Remote Sensing Letters, IEEE*, **7**(2):371–375.

Plaza, J., Plaza, A., Perez, R., and Martinez, P. (2008). Parallel Classification of Hyperspectral Images Using Neural Networks. In: M. Grana and R. J. Duro (Editors), *Computational Intelligence for Remote Sensing*, chapter 8, pages 193–216. Springer. ISBN 3540793526.

Plaza, J., Plaza, A., Perez, R., and Martinez, P. (2009b). On the use of small training sets for neural network-based characterization of mixed pixels in remotely sensed hyperspectral images. *Pattern Recognition*, **42**(11):3032–3045.

Poor, H. V. (1994). *An Introduction to Signal Detection and Estimation*. Springer. ISBN 9780387941738.

Pratt, D. A. and Ellyett, C. D. (1978). Image registration for thermal inertia mapping, and its potential use for mapping of soil moisture and geology in Australia. In: *International Symposium on Remote Sensing of Environment, 12 th, Manila, Philippines*, pages 1207–1217.

Pritchard, H. D. and Vaughan, D. G. (2007). Widespread acceleration of tide-water glaciers on the Antarctic Peninsula. *Journal of Geophysical Research: Earth Surface (2003–2012)*, **112**(F3).

Quattrochi, D. A. and Luvall, J. C. (2004). *Thermal remote sensing in land surface processes*. CRC Press, Raton, FL, USA.

Ramakrishnan, D., Bharti, R., Singh, K. D., and Nithya, M. (2013). Thermal inertia mapping and its application in mineral exploration: results from

Mamandur polymetal prospect, India. *Geophysical Journal International*, **195**(1):357–368. ISSN 0956-540X. doi:10.1093/gji/ggt237.

Rankin, A. M. and Wolff, E. M. (2003). A year-long record of size-segregated aerosol composition at Halley, Antarctica. *Journal of Geophysical Research*, **108**(D24):4775. ISSN 0148-0227. doi:10.1029/2003JD003993.

Rees, W. G. (2005). *Remote Sensing of Snow and Ice*. Taylor & Francis, USA. ISBN 9781420023749.

Rees, W. G. (2012). *Physical Principles of Remote Sensing*. Topics in remote sensing. Cambridge University Press, Cambridge, UK. ISBN 9781139851374.

Ren, H. and Chang, C.-I. (2003). Automatic spectral target recognition in hyperspectral imagery. *Aerospace and Electronic Systems, IEEE Transactions on*, **39**(4):1232–1249. ISSN 0018-9251. doi:10.1109/TAES.2003.1261124.

Rencz, A. N. (1999). *Manual of Remote Sensing, Remote Sensing for the Earth Sciences*. Manual of Remote Sensing - Third Edition. Wiley, USA. ISBN 9780471294054.

Resmini, R. G., Kappus, M. E., Aldrich, W. S., Harsanyi, J. C., and Anderson, M. (1997). Mineral mapping with hyperspectral digital imagery collection experiment (HYDICE) sensor data at Cuprite, Nevada, USA. *International Journal of Remote Sensing*, **18**(7):1553–1570.

Richards, J. A. (2012). *Remote Sensing Digital Image Analysis: An Introduction*. Springer Science and Business Media; Berlin, Germany. ISBN 9783642300622.

Richter, R. and Coll, C. (2002). Bandpass-Resampling Effects for the Retrieval of Surface Emissivity. *Applied Optics*, **41**(18):3523–3529. doi:10.1364/AO.41.003523.

Richter, R. and Schläpfer, D. (2002). Geo-atmospheric processing of airborne imaging spectrometry data. Part 2: Atmospheric/topographic correction. *International Journal of Remote Sensing*, **23**(13):2631–2649. doi:10.1080/01431160110115834.

Richter, R. and Schläpfer, D. (2014). *Atmospheric / Topographic Correction for Airborne Imagery. ATCOR-4 User Guide, Version 6.2.1. DLR-IB 565-02/08*. Deutsches Zentrum für Luft- und Raumfahrt (DLR), Weßling, Germany.

Riley, D. N. and Hecker, C. A. (2013). Mineral mapping with airborne hyperspectral thermal infrared remote sensing at Cuprite, Nevada, USA. In: *Thermal Infrared Remote Sensing*, pages 495–514. Springer.

Riley, T. R., Flowerdew, M. J., and Whitehouse, M. J. (2012). U-Pb ion-microprobe zircon geochronology from the basement inliers of eastern Graham Land, Antarctic Peninsula. *Journal of the Geological Society*, **169**(4):381–393. ISSN 0016-7649. doi:10.1144/0016-76492011-142.

Rivard, B. and Arvidson, R. (1992). Utility of imaging spectrometry for lithologic mapping in Greenland. *Photogrammetric Engineering & Remote Sensing*, **58**(7):945–949.

Rivard, B., Zhang, J., Feng, J., and Sanchez-Azofeifa, G. A. (2009). Remote predictive lithologic mapping in the Abitibi Greenstone Belt, Canada, using airborne hyperspectral imagery. *Canadian Journal of Remote Sensing*, **35**(sup1):S95–S105. doi:10.5589/m10-002.

Rogge, D., Bachmann, M., Rivard, B., and Feng, J. (2012). Hyperspectral flight-line leveling and scattering correction for image mosaics. In: *Geoscience and Remote Sensing Symposium (IGARSS), 2012 IEEE International*, pages 4094–4097. ISSN 2153-6996. doi:10.1109/IGARSS.2012.6350984.

Rogge, D. and Rivard, B. (2006). Iterative spectral unmixing for optimizing per-pixel endmember sets. *Geoscience and Remote Sensing, IEEE*, **44**(12):3725–3736. ISSN 0196-2892. doi:10.1109/TGRS.2006.881123.

Rogge, D., Rivard, B., Harris, J., and Zhang, J. (2009). Application of hyperspectral data for remote predictive mapping, Baffin Island, Canada. *Reviews in Economic Geology*, **16**:209–222.

Rogge, D., Rivard, B., Zhang, J., Sanchez, A., Harris, J., and Feng, J. (2007). Integration of spatialâĂŞspectral information for the improved extraction

of endmembers. *Remote Sensing of Environment*, **110**(3):287–303. ISSN 00344257. doi:10.1016/j.rse.2007.02.019.

Rowan, L. C., Hook, S. J., Abrams, M. J., and Mars, J. C. (2003). Mapping hydrothermally altered rocks at Cuprite, Nevada, using the Advanced Spaceborne Thermal Emission and Reflection Radiometer (ASTER), a new satellite-imaging system. *Economic Geology*, **98**(5):1019–1027.

Rowan, L. C. and Mars, J. C. (2003). Lithologic mapping in the Mountain Pass, California area using Advanced Spaceborne Thermal Emission and Reflection Radiometer (ASTER) data. *Remote Sensing of Environment*, **84**(3):350–366. ISSN 00344257. doi:10.1016/S0034-4257(02)00127-X.

Sabins, F. F. (2007). *Remote Sensing: Principles and Interpretation*. Waveland Press, Long Grove, Illinois, USA. ISBN 9781577665076.

Sabol, D. E., Gillespie, A. R., Adams, J. B., Smith, M. O., and Tucker, C. J. (2002). Structural stage in Pacific Northwest forests estimated using simple mixing models of multispectral images. *Remote Sensing of Environment*, **80**(1):1–16. ISSN 00344257. doi:10.1016/S0034-4257(01)00245-0.

Salisbury, J. W. (1991). *Infrared (2.1-25 um) spectra of minerals*. Johns Hopkins studies in earth and space sciences. Johns Hopkins University Press. ISBN 9780801844232.

Salvaggio, C. and Miller, C. J. (2001). Methodologies and protocols for the collection of midwave and longwave infrared emissivity spectra using a portable field spectrometer. doi:10.1117/12.437046.

Salvatore, M. R., Mustard, J. F., Head, J. W. I. I. I., Marchant, D. R., and Wyatt, M. B. (2014). Characterization of spectral and geochemical variability within the Ferrar Dolerite of the McMurdo Dry Valleys, Antarctica: weathering, alteration, and magmatic processes. *Antarctic Science*, **26**(01):49–68. ISSN 1365-2079. doi:10.1017/S0954102013000254.

Schaepman, M. E., Ustin, S. L., Plaza, A. J., Painter, T. H., Verrelst, J., and

Liang, S. (2009). Earth system science related imaging spectroscopy - An assessment. *Remote Sensing of Environment*, **113**:S123—-S137.

Sefton-Nash, E., Catling, D. C., Wood, S. E., Grindrod, P. M., and Teanby, N. A. (2012). Topographic, spectral and thermal inertia analysis of interior layered deposits in Iani Chaos, Mars. *Icarus*, **221**(1):20–42. ISSN 0019-1035. doi:10.1016/j.icarus.2012.06.036.

Shaw, G. A. and Burke, H.-h. K. (2003). Spectral Imaging for Remote Sensing. *Lincoln Laboratory Journal*, **14**(1):3–28.

Shettle, E. and Fenn, R. W. (1979). Models for the aerosols of the lower atmosphere and the effects of humidity variations on their optical properties. Technical report, Environmental Research Paper Air Force Geophysics Lab., Hanscom AFB, MA. Optical Physics Div.

Shimoni, M., van der Meer, F., and Acheroy, M. (2007). Thermal imaging spectroscopy: Present technology and future dual use applications. In: *Proceedings 5th EARSeL Workshop on Imaging Spectroscopy. Bruges, Belgium*.

Small, C. (2001). Estimation of urban vegetation abundance by spectral mixture analysis. *International Journal of Remote Sensing*, **22**(7):1305–1334.

Smith, G. M. and Milton, E. J. (1999). The use of the empirical line method to calibrate remotely sensed data to reflectance. *International Journal of Remote Sensing*, **20**(13):2659–2662.

Sobrino, J. A., Li, Z.-L., and Stoll, M.-P. (1993). Impact of the atmospheric transmittance and total water vapor content in the algorithms for estimating satellite sea surface temperatures. *Geoscience and Remote Sensing, IEEE Transactions on*, **31**(5):946–952. ISSN 0196-2892. doi:10.1109/36.263765.

Swayze, G. A., Clark, R. N., Goetz, A. F. H., Livo, K. E., Breit, G. N., Kruse, F. A., Sutley, S. J., Snee, L. W., Lowers, H. A., Post, J. L., and Others (2014). Mapping advanced argillic alteration at Cuprite, Nevada, using imaging spectroscopy. *Economic Geology*, **109**(5):1179–1221.

Taylor, G. (2001). Strategies for overcoming problems when mosaicking airborne scanner images. *Earth Observation Magazine*, **10**(8):26–31.

Thomassen, B., Dawes, P. R., Steenfelt, A., and Krebs, J. D. (2002). Qaanaaq 2001: mineral exploration reconnaissance in North-West Greenland. *Geology of Greenland Survey Bulletin*, (191):133–143.

Thompson, D. R., Bornstein, B. J., Chien, S. A., Schaffer, S., Tran, D., Bue, B. D., Castano, R., Gleeson, D. F., and Noell, A. (2013). Autonomous Spectral Discovery and Mapping Onboard the EO-1 Spacecraft. *Geoscience and Remote Sensing, IEEE Transactions on*, **51**(6):3567–3579. ISSN 0196-2892. doi:10.1109/TGRS.2012.2226040.

Thompson, D. R., Mandrake, L., Gilmore, M. S., and Castano, R. (2010). Superpixel Endmember Detection. *Geoscience and Remote Sensing, IEEE Transactions on*, **48**(11):4023–4033. ISSN 0196-2892. doi:10.1109/TGRS.2010.2070802.

Tukiainen, T. and Thorning, L. (2005). Detection of kimberlitic rocks in West Greenland using airborne hyperspectral data: the HyperGreen 2002 project. *Geological Survey of Denmark and Greenland Bulletin, 7*.

Tuominen, J. and Lipping, T. (2011). Atmospheric correction of hyperspectral data using combined empirical and model based method. In: *EARSeL 7th SIG-Imaging Spectroscopy Workshop*.

van der Meer, F. (2004). Analysis of spectral absorption features in hyperspectral imagery. *International Journal of Applied Earth Observation and Geoinformation*, **5**(1):55–68. ISSN 03032434. doi:10.1016/j.jag.2003.09.001.

van der Meer, F. D. (1995). Spectral reflectance of carbonate mineral mixtures and bidirectional reflectance theory: Quantitative analysis techniques for application in remote sensing. *Remote Sensing Reviews*, **13**(1-2):67–94. doi:10.1080/02757259509532297.

van der Meer, F. D., van der Werff, H. M., van Ruitenbeek, F. J., Hecker, C. a., Bakker, W. H., Noomen, M. F., van der Meijde, M., Carranza, E.

J. M., Smeth, J. B. D., and Woldai, T. (2012). Multi- and hyperspectral geologic remote sensing: A review. *International Journal of Applied Earth Observation and Geoinformation*, **14**(1):112–128. ISSN 03032434. doi: 10.1016/j.jag.2011.08.002.

Vaughan, D. G., Marshall, G. J., Connolley, W. M., Parkinson, C., Mulvaney, R., Hodgson, D. A., King, J. C., Pudsey, C. J., and Turner, J. (2003a). Recent Rapid Regional Climate Warming on the Antarctic Peninsula. *Climatic Change*, **60**(3):243–274. ISSN 0165-0009. doi:10.1023/A:1026021217991.

Vaughan, R., Calvin, W. M., and Taranik, J. V. (2003b). SEBASS hyperspectral thermal infrared data: surface emissivity measurement and mineral mapping. *Remote Sensing of Environment*, **85**(1):48–63. ISSN 00344257. doi:10.1016/S0034-4257(02)00186-4.

Vaughan, R. G., Hook, S. J., Calvin, W. M., and Taranik, J. V. (2005). Surface mineral mapping at Steamboat Springs, Nevada, USA, with multi-wavelength thermal infrared images. *Remote Sensing of Environment*, **99**(1-2):140–158. ISSN 00344257. doi:10.1016/j.rse.2005.04.030.

Veganzones, M. A. and Grana, M. (2008). Endmember extraction methods: A short review. In: *12th International Conference on Knowledge-Based Intelligent Information and Engineering Systems, 3-5 September*, pages 400–407. Springer, Zagreb, Croatia.

Waight, T. E., Weaver, S. D., and Muir, R. J. (1998). Mid-Cretaceous granitic magmatism during the transition from subduction to extension in southern New Zealand: a chemical and tectonic synthesis. *Lithos*, **45**(1-4):469–482. ISSN 00244937. doi:10.1016/S0024-4937(98)00045-0.

Walther, G.-R., Post, E., Convey, P., Menzel, A., Parmesan, C., Beebee, T. J. C., Fromentin, J.-M., Hoegh-Guldberg, O., and Bairlein, F. (2002). Ecological responses to recent climate change. *Nature*, **416**(6879):389–395.

Wan, Z. and Li, Z.-L. (1997). A physics-based algorithm for retrieving land-surface emissivity and temperature from EOS/MODIS data. *Geoscience*

and Remote Sensing, IEEE Transactions on, **35**(4):980–996. ISSN 0196-2892. doi:10.1109/36.602541.

Watson, K. (1992). Spectral ratio method for measuring emissivity. *Remote Sensing of Environment*, **41**:113–116.

Webster, T. L., Murphy, J. B., Gosse, J. C., and Spooner, I. (2006). The application of lidar-derived digital elevation model analysis to geological mapping: an example from the Fundy Basin, Nova Scotia, Canada. *Canadian Journal of Remote Sensing*, **32**(2):173–193.

Weng, Q. and Quattrochi, D. A. (2006). *Urban Remote Sensing*. Taylor & Francis, USA. ISBN 9780849391996.

Wickert, L. M. and Budkewitsch, P. (2004). ASTER - a geological mapping tool for Canada's North. Case Study: The Belcher Islands, Hudson Bay, Nunavut, Canada. In: *Geoscience and Remote Sensing Symposium*, volume 2, pages 1300–1303. IEEE.

Winter, M. E. (1999). N-FINDR: an algorithm for fast autonomous spectral end-member determination in hyperspectral data. In: *SPIE's International Symposium on Optical Science, Engineering, and Instrumentation*, pages 266–275. International Society for Optics and Photonics.

Wulder, M. and Franklin, S. E. (2003). *Remote Sensing of Forest Environments: Concepts and Case Studies*. Springer, USA. ISBN 9781402074059.

Yang, J., He, Y., and Oguchi, T. (2014). An endmember optimization approach for linear spectral unmixing of fine-scale urban imagery. *International Journal of Applied Earth Observation and Geoinformation*, **27**:137–146.

Young, S. J., Johnson, B. R., and Hackwell, J. A. (2002). An in-scene method for atmospheric compensation of thermal hyperspectral data. *Journal of Geophysical Research*, **107**(D24):1–20. ISSN 0148-0227. doi:10.1029/2001JD001266.

Zhang, J., Rivard, B., and Rogge, D. (2008). The successive projection algorithm (SPA), an algorithm with a spatial constraint for the automatic search of endmembers in hyperspectral data. *Sensors*, pages 1321–1342.

Zhang, J., Rivard, B., and Sanchez-Azofeifa, A. (2004). Derivative spectral unmixing of hyperspectral data applied to mixtures of lichen and rock. *IEEE Transactions on Geoscience and Remote Sensing*, **42**(9):1934–1940. ISSN 0196-2892. doi:10.1109/TGRS.2004.832239.

Zhao, Y., Meng, Z., Wang, L., Miyazaki, S., Geng, X., Zhou, G., Liu, R., Kosaka, N., Takahashi, M., and Li, X. (2005). A new cross-track radiometric correction method (VRadCor) for airborne hyperspectral image of operational modular imaging spectrometer(OMIS). In: *Geoscience and Remote Sensing Symposium, 2005. IGARSS '05. Proceedings. 2005 IEEE International*, volume 5, pages 3553–3556. doi:10.1109/IGARSS.2005.1526614.

Zortea, M. and Plaza, A. (2009). Spatial preprocessing for endmember extraction. *Geoscience and Remote Sensing, IEEE Transactions on*, **47**(8):2679–2693.

Appendices

Appendix A: Papers

A number of papers were produced as part of this research. Their full references are listed below, followed by the papers themselves.

- **Black, M.**, Riley, T., Ferrier, G., Fleming, A., Fretwell, P. (2016). Automated lithological mapping using airborne hyperspectral thermal infrared data: A case study from Anchorage Island, Antarctica. *Remote Sensing of Environment*, **176**, 225-241. doi: 10.1016/j.rse.2016.01.022.
- **Black, M.**, Fleming, A., Riley, T., Ferrier, G., Fretwell, P., McFee, J., Achal, S., Diaz, A. U. (2014). On the Atmospheric Correction of Antarctic Airborne Hyperspectral Data. *Remote Sensing*, **6**(5), 4498-4514. doi: 10.3390/rs6054498
- **Black, M.**, Casanovas, P., Convey, P., Fretwell, P. (2015) High resolution mapping of Antarctic vegetation communities using airborne hyperspectral data. *Proceedings of Remote Sensing and Photogrammetry Society Annual Conference*, Aberystwyth, Wales, UK. September 3-5. doi: 10.13140/2.1.5189.6648
- Casanovas, P., **Black, M.**, Convey, P., Fretwell, P. (2015) Mapping lichen distribution on the Antarctic Peninsula using remote sensing, lichen spectra and photographic documentation by citizen scientists. *Polar Research*, **34**, 25633. doi: 10.3402/polar.v34.25633

Remote Sensing of Environment 176 (2016) 225–241

Contents lists available at ScienceDirect

Remote Sensing of Environment

journal homepage: www.elsevier.com/locate/rse

Automated lithological mapping using airborne hyperspectral thermal infrared data: A case study from Anchorage Island, Antarctica

Martin Black [a,b,*], Teal R. Riley [a], Graham Ferrier [b], Andrew H. Fleming [a], Peter T. Fretwell [a]

[a] British Antarctic Survey, High Cross, Madingley Road, Cambridge CB3 0ET, UK
[b] University of Hull, Department of Geography, Environment and Earth Sciences, Cottingham Road, Hull HU6 7RX, UK

ARTICLE INFO

Article history:
Received 4 September 2015
Received in revised form 20 January 2016
Accepted 28 January 2016
Available online xxxx

Keywords:
Hyperspectral
Thermal infrared
Geology
Automated
Mapping
Antarctica

ABSTRACT

The thermal infrared portion of the electromagnetic spectrum has considerable potential for mineral and lithological mapping of the most abundant rock-forming silicates that do not display diagnostic features at visible and shortwave infrared wavelengths. Lithological mapping using visible and shortwave infrared hyperspectral data is well developed and established processing chains are available, however there is a paucity of such methodologies for hyperspectral thermal infrared data. Here we present a new fully automated processing chain for deriving lithological maps from hyperspectral thermal infrared data and test its applicability using the first ever airborne hyperspectral thermal data collected in the Antarctic. A combined airborne hyperspectral survey, targeted geological field mapping campaign and detailed mineralogical and geochemical datasets are applied to small test site in West Antarctica where the geological relationships are representative of continental margin arcs. The challenging environmental conditions and cold temperatures in the Antarctic meant that the data have a significantly lower signal to noise ratio than is usually attained from airborne hyperspectral sensors. We applied preprocessing techniques to improve the signal to noise ratio and convert the radiance images to ground leaving emissivity. Following preprocessing we developed and applied a fully automated processing chain to the hyperspectral imagery, which consists of the following six steps: (1) superpixel segmentation, (2) determine the number of endmembers, (3) extract endmembers from superpixels, (4) apply fully constrained linear unmixing, (5) generate a predictive classification map, and (6) automatically label the predictive classes to generate a lithological map. The results show that the image processing chain was successful, despite the low signal to noise ratio of the imagery; reconstruction of the hyperspectral image from the endmembers and their fractional abundances yielded a root mean square error of 0.58%. The results are encouraging with the thermal imagery allowing clear distinction between granitoid types. However, the distinction of fine grained, intermediate composition dykes is not possible due to the close geochemical similarity with the country rock.

1. Introduction

Remote sensing in the solar reflective spectral range has been widely demonstrated to be an invaluable methodology to assist geological analysis (van der Meer et al., 2012). Hyperspectral data collected at visible and near infrared (VNIR; 0.4–1 μm) and shortwave infrared (SWIR; 1–2.5 μm) wavelengths have been widely reported in the literature for mapping mineral absorption features occurring within transition metals (i.e. Fe, Mn, Cu, Ni, Cr etc.) and alteration minerals that display absorption features associated with Mg-OH and Al-OH bonds (e.g. Abrams, Ashley, Rowan, Goetz, & Kahle, 1977; Abrams & Hook, 1995; Clark & Swayze, 1996; Clark, Swayze, & Gallagher, 1993; Hook, Elvidge, Rast, & Watanabe, 1991; Hook & Rast, 1990; Kruse, Kierein-Young, & Boardman, 1990; Kruse, Lefkoff, & Dietz, 1993b; Resmini, Kappus, Aldrich, Harsanyi, & Anderson, 1997; Rowan, Hook, Abrams, & Mars, 2003).

Although these reflectance-based datasets have been successful for mapping of minerals associated with alteration, from a geological perspective, mapping of rock-forming silicates is critical. When considering only VNIR/SWIR data there are significant limitations in the range and quality of the geological parameters that can be retrieved, as many important rock-forming minerals do not display diagnostic absorption features at VNIR/SWIR wavelengths (e.g. Drury, 2001; Gupta, 2003; van der Meer et al., 2012).

The longwave or thermal infrared (TIR; 8–14 μm) wavelength range has the capability of retrieving additional physical parameters and more accurately resolving the composition and physical condition of a material than solar reflected radiation (Hecker, Dilles, van der Meijde, & van der Meer, 2012; Hook, Cudahy, Kahle, & Whitbourn, 1998; Hook et al., 2005). Many common rock-forming minerals such as quartz, feldspars,

* Corresponding author at: 2Excel Aviation, The Tiger House, Sywell Aerodrome, Wellingborough Road, Sywell, Northampton, NN6 0BN, UK.
E-mail address: martinblack@2excelaviation.com (M. Black).

http://dx.doi.org/10.1016/j.rse.2016.01.022
0034-4257/

olivines, pyroxenes, micas and clay minerals have spectral features in the 8–14 μm wavelength region (van der Meer et al., 2012). For silicate minerals, a pronounced emittance minimum caused by fundamental Si-O stretching vibrations occurs near 10 μm (Hunt & Salisbury, 1975; Salisbury, 1991). The vibrational frequency, and thus the wavelength of the minimum, depends on the degree of coordination among the silicon-oxygen tetrahedra in the crystal lattice. Framework silicates, such as quartz and feldspar, have emittance minima at shorter wavelengths (9.3 and 10 μm, respectively) than do sheet silicates such as muscovite (10.3 μm) and chain silicates such as the amphibole minerals (10.7 μm) (Hunt, 1980). Emission Fourier transform infrared (FTIR) spectroscopy has been successfully used to predict modal mineralogy of rock-forming minerals such as feldspars, pyroxene, and quartz and their composition in igneous and metamorphic rocks (e.g. Feely & Christensen, 1999; Hamilton & Christensen, 2000; Hecker, van der Meijde, & van der Meer, 2010; Milam, McSween, Hamilton, Moersch, & Christensen, 2004). Carbonates have features associated with CO_3 internal vibrations both in the 6–8 μm region (Adler & Kerr, 1963; Hunt & Salisbury, 1975) and also at 11.4 and 14.3 μm due to C-O bending modes. Sulphate minerals have an intense feature near 8.7 μm caused by fundamental stretching motions (Lane & Christensen, 1997; van der Meer, 1995).

The majority of geological mapping studies using thermal infrared remote sensing data have utilised multispectral data; multispectral sensors measure a small number of (<20) broadly spaced, often non-contiguous bands (Kramer, 2002). The Advanced Spaceborne Thermal Emission and Reflection Radiometer (ASTER) and the Thermal Infrared Multispectral Scanner (TIMS) sensors have demonstrated the utility of TIR data to discriminate a wide range of minerals, especially silicates, as well as proving useful for lithological mapping (e.g. Chen, Warner, & Campagna, 2007; Haselwimmer, Riley, & Liu, 2010, 2011; Rogge, Rivard, Harris, & Zhang, 2009; Rowan & Mars, 2003; Salvatore, Mustard, Head, Marchant, & Wyatt, 2014); however, these satellite platforms are limited by their coarse spatial and spectral resolution.

The development of airborne hyperspectral TIR sensors producing images with tens to hundreds of contiguous spectral channels provided the potential for a step-change in the range of mineralogical information and accuracy of surface composition retrievable remotely. Currently, there are a number of operational airborne hyperspectral TIR instruments, including the Spatially Enhanced Broadband Array Spectrograph System (SEBASS), the Airborne Hyperspectral Scanner (AHS), the ITRES Thermal Airborne Spectrographic Imagery (TASI), and the Specim AisaOWL (van der Meer et al., 2012). Previous studies using airborne hyperspectral TIR data have illustrated the exceptional potential of these types of sensors for mapping silicates, carbonates, sulphates, and clays (e.g. Aslett, Taranik, & Riley, 2008; Calvin, Vaughan, Taranik, & Smailbegovic, 2001; Cudahy et al., 2001; Hewson et al., 2000; Kruse & McDowell, 2015; Riley & Hecker, 2013; Vaughan, Calvin, & Taranik, 2003; Vaughan, Hook, Calvin, & Taranik, 2005).

However, a number of issues relating to processing of the imagery remain, which significantly affects the accuracy of the temperature-emissivity separation and subsequently the quality of the interpretation of the generated mineralogical and lithological maps. These issues include the coarser spectral resolution and poorer spectral calibration of currently available instruments (compared to VNIR/SWIR instruments), inaccurate correction of the effects of the atmosphere, low signal-to-noise ratios and a lack of understanding of the influence of a wide range of compositional, morphological, topographical and environmental factors on the spectral emissivity signal received at-sensor (Feng, Rivard, Rogge, & Grant, 2012; Salvaggio & Miller, 2001; Shimoni, van der Meer, & Acheroy, 2007). The complexity of the processing chain (atmospheric correction and the underdetermined nature of temperature emissivity separation; Gillespie et al., 1998) and lack of defined methodologies for processing of hyperspectral airborne TIR datasets relative to the processing of VNIR and SWIR hyperspectral datasets is an additional factor in limiting the usefulness of the data and the quality of geological interpretation (van der Meer et al., 2012).

A key objective of this study was to develop a fully automated processing chain, robust to noise, in order to produce a lithological map from airborne hyperspectral TIR data. The processing chain, with minimal inputs and parameters, is designed to assist geologists in processing, analysing and interpreting hyperspectral TIR datasets; we use established techniques which are routinely applied to VNIR/SWIR datasets and integrate them into a fully automated processing chain applied to hyperspectral TIR data.

Additionally, this paper also presents the first known analysis of airborne hyperspectral TIR data from the Antarctic. We tackle the significant challenges presented by the extreme environment in the Antarctic, which produced a dataset with a very low signal to noise ratio. The results are validated and interpreted in the context of the study area in conjunction with a full suite of ancillary data: detailed high quality ground reference spectral data collected using a new, high resolution field portable FTIR spectrometer, thin section and scanning electron microscope analysis, electron microprobe analysis, whole rock geochemical data and mineral modal analysis.

2. Study area and datasets

2.1. Study area and geological context

The Antarctic Peninsula is part of the proto-Pacific continental margin arc that was magmatically active at least from the Permain through to ~20 Ma. The range of igneous rocks emplaced in continental margin arcs informs us about the tectonic history of the margin, and even relatively subtle difference between granitoid types (e.g. tonalite, diorite, granodiorite, granite) are significant as they record variations in melting depths and the stress regime in the lithosphere.

Anchorage Island is located in Ryder Bay to the south of the larger Adelaide Island, on the Antarctic Peninsula. The British Antarctic Survey (BAS) main research station is located close by on Rothera Point, Adelaide Island (Fig. 1C). Anchorage Island was surveyed as part of a hyperspectral airborne campaign in February 2011 and visited for follow-up ground truth fieldwork in January/February 2014 (Fig. 1D).

A local-scale geological map of the study area, based on previous geological mapping updated with recent field observations, is shown in Fig. 2. The main geologic unit on Anchorage Island is the Adelaide Island Intrusive Suite (AIIS). The AIIS is dominated by granodiorites, tonalites and gabbroic rocks; granodiorite and hybrid gabbro/granodiorite plutons are the most abundant. The granodiorite is leucocratic and is dominated by plagioclase (~ 50–60%), which often weathers orange/brown; quartz typically accounts for ~10% of the rock and K–feldspar ~5%. Mafic minerals are common (25%), with green/brown amphibole abundant, along with minor amounts of biotite and epidote. The plutonic rocks are cut by dolerite and intermediate-felsic composition dykes, which are typically <1 m thick, dip steeply (>75 ° to the southeast) and strike in the range 210–230°.

2.2. Airborne hyperspectral data

Airborne hyperspectral TIR imagery was acquired on the 3rd February 2011 by the ITRES TASI sensor with 32 spectral bands from 8 to 11.4 μm at a full-width half-maximum (FWHM) of 109.5 nm. The acquisition system hardware and other equipment (inertial measurement unit and instrument control units) were installed into a De Havilland Twin Otter aircraft and flown unpressurised. Radiometric correction and geometric correction were carried out by ITRES Research Ltd., where a total of 17 flight lines were orthorectified and a mosaicked image in calibrated at-sensor radiance units (Level 1B) at a ground spatial resolution of 1 m was delivered. The full preprocessing of the hyperspectral imagery is

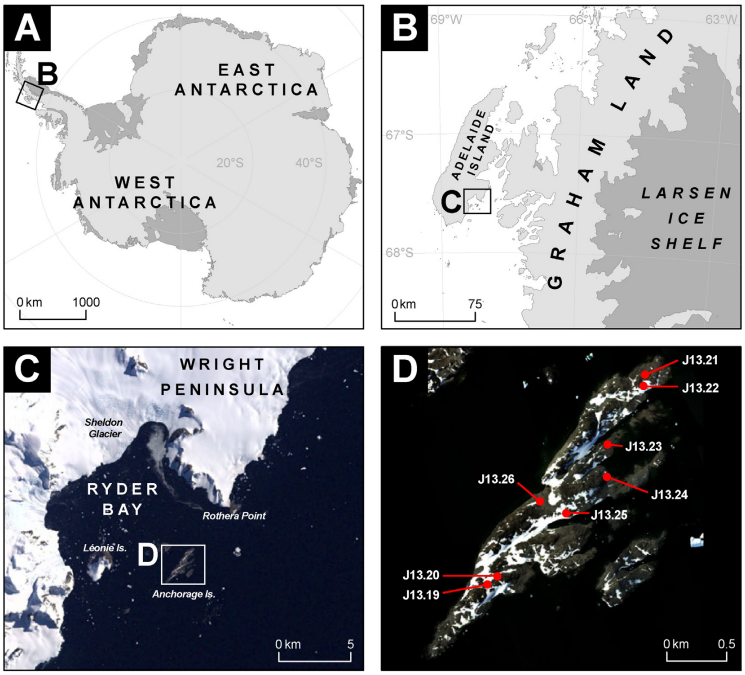

Fig. 1. Location maps showing the context of the study area within Antarctica (A), the location of Adelaide Island within the Antarctic Peninsula (B) and the location of Anchorage Island in the context of Ryder Bay (C; labelled). (D) shows a true colour composite of Anchorage Island with field localities labelled.

described in Section 3.3 and the automated lithological mapping in Section 3.4.

2.3. Field reflectance and emission spectral survey

Ground TIR emissivity spectra were acquired from the survey region during a field campaign in February 2014. A total of eight field localities were surveyed (Fig. 1D) encompassing a northeast-southwest transect across Anchorage Island, though specific localities were selected due to their accessibility. At each locality, between 3 and 5 hand specimens were collected from representative lithological units, mafic enclaves and mineral viens (e.g. quartz) within close proximity (<10 m) of each field locality. Hand specimens were collected from weathered, nadir facing rock surfaces. Although varying levels of lichen cover were present, samples were measured from lichen-free (or minimal lichen covered) areas on each sample. Hand specimens were measured using an ABB full spectrum reflectometer (FSR) to gather measurements of spectral reflectivity and emissivity.

The FSR is a FTIR spectrometer which uses a Michelson interferometer (MB-3000) with mercury cadmium telluride (MCT) and indium arsenide (InAs) detectors. It has a wavelength range from 0.7–14 μm, a spectral resolution of <1 nm and a spot size of ~4 mm. The FSR was developed by ABB for the Canadian Department for Research and Defence (DRDC). It represents a significant improvement over existing field FTIR spectrometers; it is compact and portable, has a high signal to noise ratio due do its cooled MCT and InAs detectors, as well as covering a large spectral range from the VNIR to TIR. The FSR is also a contact probe instrument, similar to spectral radiometers conventionally used for VNIR/SWIR spectroscopy. The spectral resolution was set to 0.1 nm and the instrument was set up such that each spectrum represented the average of 128 individual spectral measurements. A calibrated gold panel is built into the FSR allowing for the calculation of emissivity; the gold panel was used to recalibrate the instrument at the start of each batch of measurements at each field locality. Fig. 3 shows 18 spectra collected from exposed nadir facing samples (excluding samples from enclaves or vein material).

3. Methodology

The processing of the airborne hyperspectral TIR imagery was split into two main phases; (1) data preprocessing and (2) fully automated image processing and lithological mapping. To assist in the analysis of the results from the airborne remote sensing study a comprehensive field mapping survey was carried out supported by field reflectance and emission spectroscopy (Section 2.3). The field spectral data underwent spectral resampling (Section 3.1). Laboratory geochemical and petrographic analyses were carried out to determine mineralogical information and aid in interpretation of field spectral data (Section 3.2).

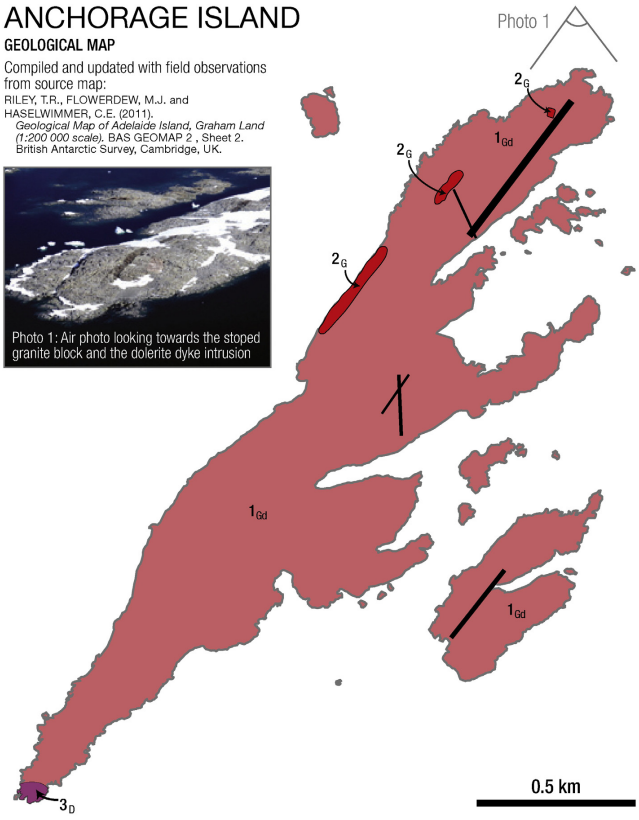

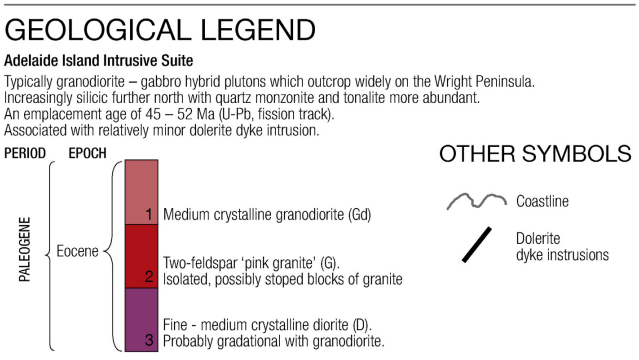

Fig. 2. Local scale geological map of Anchorage Island.

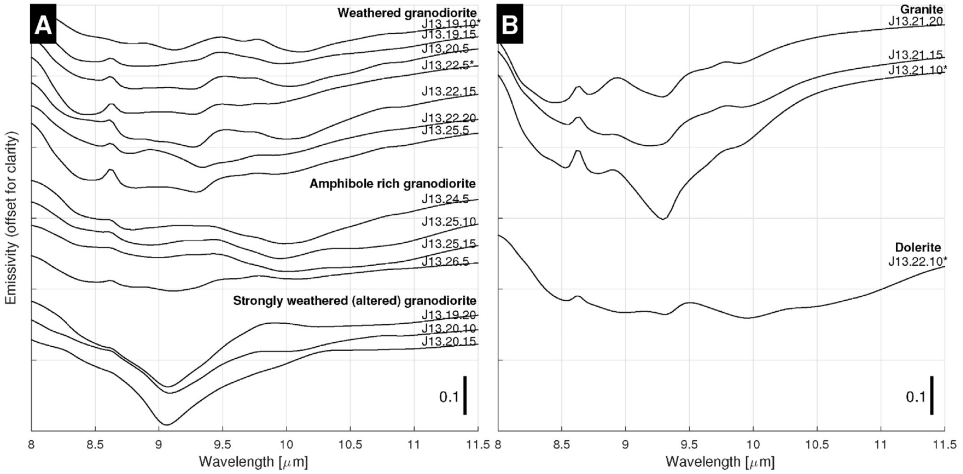

Fig. 3. Spectral emissivity measured in the field using a Fourier Transform Infrared Spectrometer (FTIR) of relevant lithological units from Anchorage Island. (A) shows granodiorite spectra (B) shows granite and dolerite spectra.

3.1. Spectral resampling

All of the emissivity spectra collected in the field (Fig. 3) using FSR were convolved to the spectral response functions of the TASI sensor through

$$\varepsilon i = \frac{\int \varepsilon_s(\lambda) r_i(\lambda) \delta\lambda}{\int r_i(\lambda) \delta\lambda} \quad (1)$$

where ε_i is convolved emissivity, $\varepsilon_s(\lambda)$ is the sample's emissivity at band i and wavelength λ, $r_i(\lambda)$ is the spectral response function of band i at wavelength λ_i, over the wavelength interval of the sample $\delta\lambda$.

3.2. Geochemical and petrographic analyses

Four samples representative of the main lithological units (granite, granodiorite and dolerite) were further investigated to understand their geochemistry; two granodiorite samples (J13.19.10 and J13.22.5), one granite (J13.21.10) and one dolerite sample (J13.22.10) were chosen. These samples were selected to ensure that each of the geological units on Anchorage Island were investigated; as weathered granodiorite represents the major lithological unit on Anchorage Island, two weathered granodiorite samples were chosen to determine their homogeneity. Thin sections were examined using a petrological microscope, a FEI Quanta 650F QEMSCAN scanning electron microscope and a Cameca SX-100 electron microprobe. Backscattered electron (BSE) images were collected on the QEMSCAN using an accelerating voltage of 20 kV and a working distance of ~13 mm. Major element geochemistry and the identification of minerals and mineral phases was carried out through electron microprobe analysis (EPMA) of points (~5) from grains within thin sections. Point counting (Galehouse, 1971) was used to determine mineral composition; 500 points were counted in thin section on each of the four samples.

The samples were also analysed by X-ray fluorescence spectrometry (XRF) to determine whole-rock major and trace elements using a PANalytical Axios-Advanced XRF spectrometer at the University of Leicester. Powders from whole-rock samples were obtained through crushing in a steel jaw crusher and powdering in an agate ball mill. Major elements were determined from fused glass discs and trace elements from powder pellets. Loss on ignition (LOI) values were calculated by igniting ~3 g of each sample in ceramic crucibles at 950 °C. Glass discs were prepared from 0.6 g of non-ignited powder and 3 g of lithium metaborate flux, melted in a Pt–Au crucible over a Spartan burner then cast into a Pt–Au mould. Powder pellets of 32 mm diameter were produced from mixing 7 g of fine ground sample powder with 12–15 drops of a 7% polyvinyl alcohol (PVA) solution (Moviol 8–88) and pressed at 10 tons per square inch.

3.3. Hyperspectral data preprocessing

Fig. 4 shows a flowchart of the preprocessing steps. Radiometric correction and geometric correction were carried out by ITRES Research Ltd. using their proprietary tools. In the first step, radiometric and spectral calibration coefficients were applied to convert the raw digital numbers into spectral radiance values. In the second step, the ITRES proprietary geometric correction software utilised the navigation solution, bundle adjustment parameters, and digital elevation models (DEMs) to produce georeferenced radiance image files for each flight line. In addition, flight lines were combined into an image mosaic of the area. The nearest neighbour algorithm was used to populate the image pixels so that radiometric integrity of the pixels could be preserved. Where the pixels of adjacent flight lines overlapped the pixel with the smallest off-nadir angle was written to the final mosaic image.

Whilst the TIR domain is an atmospheric window, there is atmospheric influence which needs to be compensated for, especially for quantitative applications (Liang et al., 2002). Here we performed atmospheric correction through the inversion of radiative transfer modelling, following a similar approach to our corrections of VNIR/SWIR Antarctic hyperspectral data (Black et al., 2014).

The basic radiative transfer equation in the TIR domain as given by (Dash, Göttsche, Olesen, & Fischer, 2002) is (where each term is a function of wavelength, λ, omitted for clarity)

$$L_s = L_p + \tau \cdot L_g + \tau \cdot [1-\varepsilon] \cdot \frac{F}{\pi} \quad (2)$$

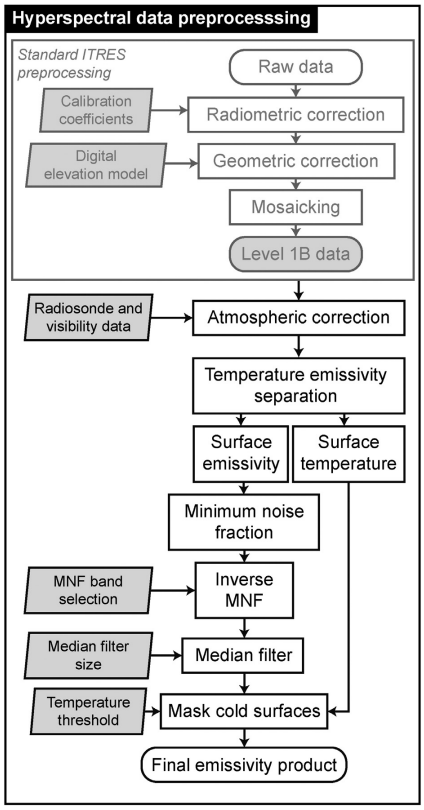

Fig. 4. Flow chart summarising the preprocessing of the hyperspectral imagery. Inputs and parameters are shown in light grey boxes. Abbreviated processing steps are as follows: MNF, minimum noise fraction.

where L_s is the total thermal radiance received at-sensor, L_p the thermal path radiance emitted by the atmosphere between the ground and the sensor, τ the ground-to-sensor transmittance, L_g the ground emitted radiance, ε the ground surface emissivity and F the downwelling thermal sky flux at the ground (Richter & Coll, 2002). We utilised ATCOR-4 (Richter & Schläpfer, 2002, 2014) to perform atmospheric correction; ATCOR-4 applies Eq. (2) by interpolating the required atmospheric parameters for each pixel based on their individual viewing geometry where the radiative transfer parameters are selected from a database of MODTRAN-5 (Berk et al., 2005) simulations. The two inputs required by ATCOR-4 to approximate the atmospheric conditions are the visibility and column water vapour amount. Visibility data is continually measured at the nearby Rothera research station using an automated BIRAL HSS VPF-730 Combined Visibility & Present Weather Sensor. The water vapour value was derived using an assumed value of 2.0 gcm^{-3} by comparison to radiosonde data. The mosaicked image was processed one flight line at a time to convert the at-sensor non-atmospherically corrected radiance into ground-leaving radiance. Temperature and emissivity separation (TES) was performed following atmospheric correction using the maximum-minimum difference of emissivity technique, which is commonly applied to ASTER TIR data (Gillespie et al., 1998).

Investigation of the emissivity imagery following atmospheric correction and TES showed lower than expected emissivity values, along with residual atmospheric absorptions. This was likely due to the challenging acquisition conditions and calibration conditions of the instrument, along with inadequate representation of the atmosphere due to the approximations in the atmospheric correction process (Black et al., 2014). An empirical correction, through the Emissive Empirical Line Method (EELM; Distasio & Resmini, 2010) was applied. The EELM generates scalar multiplicative values for each band of the image through regression of image pixel spectra to the assumed "target" spectra - this approach is comparable to the use of pseudo invariant features (PIFs; Freemantle, Pu, & Miller, 1992; Philpot & Ansty, 2011) and the empirical line method (ELM; Smith & Milton, 1999) which is commonly applied to VNIR/SWIR data (e.g. Tuominen & Lipping, 2011). Here we applied EELM utilising pixels selected from homogeneous regions of granite, dolerite, snow and sea water.

High levels of salt and pepper noise along with within-in track striping and flight line illumination differences were still apparent in emissivity imagery so an additional processing step was applied to improve the signal-to-noise ratio (SNR). The minimum noise fraction (MNF; Boardman & Kruse, 1994; Green et al., 1998) was applied. The MNF involves two cascaded principal component (PC) transformations; the first transformation, based on an estimated noise covariance matrix, decorrelates and rescales the noise in the data. The second step is a standard PC transformation of the noise-reduced data. The MNF is an effective technique for reducing a large hyperspectral dataset into fewer components which contain the majority of information (spectral variance) in a small number of components. Unlike a PC transform, the resulting axes (components) from MNF are not orthogonal (as in PC analysis) but are ordered by decreasing signal to noise ratio (Keshava & Mustard, 2002). After the MNF was applied, the first four MNF bands were then used in the inverse MNF to produce the noise-reduced emissivity image. Additionally a median filter with a radius of 2 was applied in the spectral domain to remove shot noise which was not addressed by the MNF noise reduction step (e.g. Gilmore et al., 2011).

We investigated the SNR of the image before and after preprocessing by utilising an area of sea water in the image and calculating the SNR through

$$SNR = \frac{\mu_{ij}}{\sigma_{ij}} \tag{3}$$

where i and j are the rows and columns of the image, μ_{ij} is the mean of the pixels and σ_{ij} is the standard deviation of the pixels. The signal to noise ratio is often reported using the logarithmic decibel (dB) scale; we can express the SNR in dB through

$$SNR_{dB} = 20 \log_{10}(SNR). \tag{4}$$

Finally, prior to processing, the image was masked to remove snow/ice and sea water. The mask was generated from the temperature image where pixels <5 °C were removed.

3.4. Image processing and lithological mapping

In order to produce a lithological map, we applied a six step processing chain, shown in Fig. 5. The processing chain is fully automated, with only a small number of inputs/parameters; algorithms were selected from the existing literature based on their ability to cope with low SNR datasets. The six steps are: (1) superpixel segmentation;

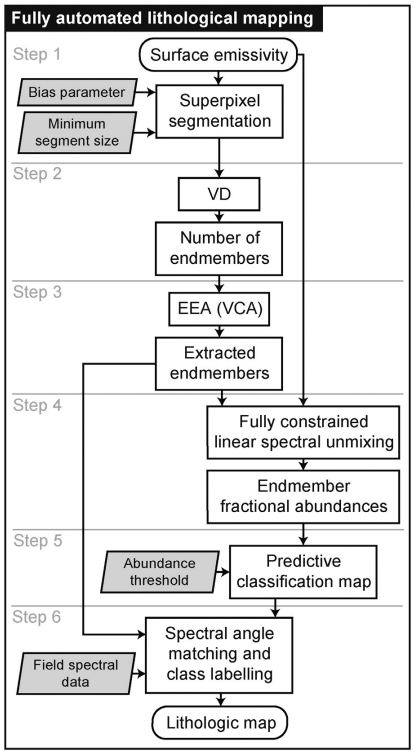

Fig. 5. Flow chart summarising the methods of the fully automated lithological mapping process. Input parameters are shown in light grey boxes. Abbreviated processing steps are as follows: VD, virtual dimensionality; EEA, endmember extraction algorithm; VCA, Vertex Component Analysis.

(2) identify the number of endmembers to extract from the superpixels; (3) extract endmembers from the image using an endmember extraction algorithm (EEA); (4) perform spectral mixture analysis (SMA; also known as spectral unmixing) to determine the fractional abundances each endmember; (5) produce a predictive classification map from endmember fractional abundances; (6) identify endmembers and label the predictive map classes to produce a lithological map.

Here we consider an endmember to be a unique spectrum derived from the hyperspectral scene itself. Endmembers are found directly from the image, regardless of the composition of materials (within individual pixels or within the scene itself) or any imperfections in the dataset (e.g. sensor noise, atmospheric influence and so on) (Winter, 1999). Through the careful interpretation of endmembers in reference to the local geological context, ancillary data (e.g. geochemical analysis) and knowledge of the imperfections within the data, endmembers which are *recognisable* are determined and interpreted in a geological context (Rogge et al., 2009; Winter, 1999).

These steps are fully automated in a MATLAB environment (MathWorks, 2011) and do not require any user interaction. Steps 1 to 5 require the hyperspectral scene and few parameters as input. In this study, we also perform step 6 automatically with the additional input of the field spectral data (convolved to TASI spectral response functions; Eq. (1)), which are used to automatically label the predictive map classes. In the absence of field spectral data, step 6 could be performed through manual interpretation of endmembers and subsequent labelling of the predictive map classes by an expert user. Due to the automated nature of the processing chain, the results are also completely repeatable unlike approaches which rely on manual endmember identification. The following sections describe each step of the processing chain.

3.4.1. Step 1: superpixel segmentation

Firstly, we apply superpixel segmentation, which adds a spatial component to endmember extraction. Superpixels are homogeneous image regions comprised of several pixels having similar values and are generated by intentional over-segmentation of the emissivity image which aggregates scene features into segments (Gilmore et al., 2011; Thompson, Mandrake, Gilmore, & Castano, 2010); the spectra of each of the original image pixels within a superpixel segment are averaged to produce the superpixel's spectrum.

Briefly, the superpixel segmentation uses graph-based image segmentation (Felzenszwalb & Huttenlocher, 2004), where the pixel grid is shattered into an 8-connected graph with nodes connected by arcs representing the Euclidean spectral distance and the nodes are then iteratively joined using an agglomerative clustering algorithm (Felzenszwalb & Huttenlocher, 2004; Thompson et al., 2010; Thompson et al., 2013). A stable bias parameter, k controls the size of the superpixels, a minimum superpixel size is enforced, and in a final step smaller regions are merged to their nearest adjacent clusters (Felzenszwalb & Huttenlocher, 2004; Thompson et al., 2010). The superpixel approach has been shown to be beneficial on low SNR datasets and can aid in deriving endmembers that more closely resemble manually derived endmembers (Thompson et al., 2010). This is due to averaging several pixel spectra within a single superpixel and thus the technique reduces the noise variance proportionally to the superpixel area. However the technique can act to degrade spectral purity by aggregating multiple pixels and can suppress subtle spectral features (Thompson et al., 2010).

For the superpixel segmentation we set the bias parameter k to 0.1 and the minimum superpixel region size to 30 pixels using the Euclidean spectral distance as the divergence measure. These parameters were determined quantitatively by investigating the sensitivity of the segmentation to small features, such as the stoped granite block in the northeast of Anchorage Island (Fig. 2). These parameters are determined based on the scale of features present in the scene and the spatial resolution of the imagery, thus may require local tuning on other imagery collected at different resolutions or where geological features occur at different scales. The superpixel segmentation step also serves as an image reduction step, thereby speeding up processing times; the raw image contains over 7.6 million pixels (3062×2489) and the superpixel segmentation reduces this to 9810 superpixels.

3.4.2. Step 2: estimating the number of endmembers

Following the generation of superpixels, Virtual Dimensionality (VD; Chang & Du, 2004) was used to determine the number of endmembers (n). The number of endmembers, or the intrinsic dimensionality (ID) of a hyperspectral image is considerably smaller than the component dimensionality (number of bands), and accurately determining the ID is crucial for the success of endmember extraction and spectral mixture analysis (Chang & Du, 2004). The high spatial and spectral resolution of hyperspectral imagery means that the sensor is capable of uncovering many unknown endmembers, which cannot be identified by visual inspection or known a priori (Chang & Du, 2004). In order to determine the number of endmembers (or signal sources, i.e. the intrinsic dimensionality) we applied the VD algorithm, prior to endmember extraction. The VD concept formulates the issue of whether a distinct signature is present or not in each of the spectral bands as a binary hypothesis

testing problem, where a Newman-Pearson detector is generated to serve as a decision-maker based on a prescribed false alarm probability P_{fa} (Chang & Du, 2004; Plaza, Plaza, Martnez, & Sanchez, 2011). In our preliminary investigations, we varied the P_{fa} from 10^{-3} to 10^{-6}, however, the estimated number of endmembers did not change; we therefore fixed the P_{fa} value to 10^{-4} in line with previous studies (Chang & Du, 2004; Plaza et al., 2011).

3.4.3. Step 3: endmember extraction

In step (3) we applied Vertex Component Analysis (VCA; Nascimento & Bioucas-Dias, 2005), to extract n endmembers from the superpixels. Vertex Component Analysis exploits the fact that endmembers occupy the vertices of a simplex and assumes the presence of pure pixels in the data. The algorithm iteratively projects data onto a direction orthogonal to the subspace spanned by the endmembers already determined and the new endmember signature corresponds to the extreme of the projection; iteration continues until the number of endmembers is exhausted. The algorithm has been shown to be comparable to state of the art endmember extraction algorithms, such as N-FINDR (Winter, 1999) and outperforms manual techniques such as the Pixel Purity Index (PPI; Boardman, 1993). It is an order of magnitude less computationally complex than other state of the art endmember extraction algorithms which yields significantly faster processing times for large datasets (Nascimento & Bioucas-Dias, 2005).

3.4.4. Step 4: spectral mixture analysis

The endmembers derived from the VCA algorithm were used as input to step (4) where linear SMA is used to produce fractional abundances of the n endmembers using the original image (without superpixel segmentation). Due to its ease of implementation, we applied fully constrained linear spectral unmixing (FCLSU; Heinz & Chang, 2001) to derive fractional abundances of each endmember, given as

$$R_b = \sum_{i=1}^{n} F_i S_{ib} \tag{5}$$

where R_b is the fractional abundance of the pixel at band b, F_i is the fractional abundance of endmember i, S_{ib} describes the emissivity of endmember i at band b, and n is the number of endmembers. Eq. (5) was solved subject to the constraints that fractional abundances sum-to-one (ASC; abundances sum-to-one constraint) and fractional abundances are non-negative (ANC; abundance non-negative constraint) (e.g. Rogge et al., 2009). This step results in fractional abundance images, where, for each pixel in the image, the abundance of each endmember is determined. The algorithms used at this and the preceding processing steps were selected due to their availability and implementation in the MATLAB environment (MathWorks, 2011), along with their relatively quick processing times and proven success at extracting endmembers under moderate to high noise conditions (Chang & Plaza, 2006; Nascimento & Bioucas-Dias, 2005; Plaza, Hendrix, Garca, Martn, & Plaza, 2012).

3.4.5. Step 5: predictive map classification

Utilising the abundance images a predictive classification map was generated following a similar approach to Rogge et al. (2009). The map was generated by determining the endmember with the maximum fractional abundance for each pixel and assigning that pixel to the given endmember class. For a pixel to be assigned to a particular class, the endmember abundance must be above a minimum fractional abundance threshold (or confidence level), otherwise a null class was assigned. The minimum fractional abundance was set to the intermediate value of 0.5 for practical purposes, however this value could be increased to identify spectrally purer regions (Rogge et al., 2009).

3.4.6. Step 6: class labelling

The interpretation (class labelling) step was carried out to produce geological labels which were automatically applied to the classification map generated from step (5). The image derived endmember spectra were compared to field emissivity spectra (e.g. Harris, Rogge, Hitchcock, Ijewlie, & Wright, 2005; Rogge et al., 2009) through calculation of spectral angle (SA), also known as Spectral Angle Mapper (SAM; Kruse et al., 1993a) through the application of

$$SA = cos^{-1}\left(\frac{\vec{t}\cdot\vec{r}}{\left\|\vec{t}\right\|\cdot\left\|\vec{t}\right\|}\right) \tag{6}$$

where t represents the spectrum of the target (endmember), r represents the spectrum of the reference (field spectra) and SA is the spectral angle (in radians; 0 to 2π). This technique to determine similarity is insensitive to gain factors as the angle between two vectors is invariant with respect to the lengths of the vectors, and allows for laboratory spectra to be directly compared to remotely sensed spectra (Kruse et al., 1993a). Predictive map classes were automatically labelled using their closest match from the field spectral data (e.g. Rivard, Zhang, Feng, & Sanchez-Azofeifa, 2009).

3.5. Image processing validation

In order to validate our findings, we use the root mean square error metric (RMSE) for assessment (e.g. Plaza et al., 2012). We define $\hat{y}_{ij}$ as the reconstructed hyperspectral image, following

$$\hat{y}_{ij} = \sum_{n=1}^{n} (M_n \times S_n) \tag{7}$$

where i and j are the rows and columns of the image, n is the number of endmembers, M_n denotes the endmember spectrum of n and S_n denotes the fractional abundance of endmember n. Following this reconstruction we calculate the RMSE between the original hyperspectral image, y and the reconstructed hyperspectral image, $\hat{y}$ as

$$RMSE(y,\hat{y}) = \left(\frac{1}{B}\sum_{j=1}^{B}\left[y_{ij}-\hat{y}_{ij}\right]^2\right)^{\frac{1}{2}} \tag{8}$$

where B is the number of spectral bands and $\hat{y}_{ij}$ and y_{ij} are pixels of the original hyperspectral image and the pixels of the reconstructed hyperspectral image respectively. Summary statistics were calculated from the RMSE of the pixels of each endmember class as well as the whole RMSE image.

Additionally, we also extract the original image spectra and the reconstructed image spectra (calculated from the endmembers and their fractional abundances). Using areas of granite and granodiorite we extract spectra from pixels of high purity (0.9 fractional abundance), medium purity (0.75 fractional abundance) and low purity (0.5 fractional abundance) and compare the spectra, their fractional abundances, and the RMSE values to validate the findings in a spectral context.

4. Results and discussion

4.1. Field data

Table 1 shows whole-rock major and trace element data from XRF spectroscopy. Table 2 shows the abundances of minerals as determined from point counting. Spectral data collected from in situ samples is

Table 1
Geochemical analyses of Anchorage Island samples from XRF spectroscopy.

Sample	J13.22.10	J13.19.10	J13.22.5	J13.21.10
Unit	Dolerite	Granodiorite		Granite
Major elements (%)				
SiO_2	54.40	55.19	59.59	78.29
TiO_2	1.02	0.94	0.87	0.20
Al_2O_3	16.62	18.18	16.35	11.64
Fe_2O_3†	8.66	8.55	6.67	0.86
MnO	0.124	0.112	0.147	0.013
MgO	3.96	3.29	3.52	0.16
CaO	8.57	7.49	6.16	0.53
Na_2O	3.14	4.04	3.51	2.74
K_2O	0.958	1.066	2.115	5.610
P_2O_5	0.241	0.176	0.185	0.018
SO_3	0.170	0.009	<0.003	<0.003
LOI	2.05	0.88	0.97	0.31
Total	99.92	99.93	100.09	100.38
Trace elements (ppm)				
As	6.7	8.4	5.1	4.4
Ba	365.0	432.2	698.4	475.5
Ce	44.2	27.9	48.4	11.4
Co	25.7	18.3	21.6	<1.1
Cr	112.0	6.4	37.0	<0.6
Cu	110.8	19.9	32.8	3.5
Ga	18.2	21.2	17.8	9.9
La	20.0	13.7	21.3	7.9
Mo	3.9	2.3	3.3	0.9
Nb	4.8	4.4	6.8	4.7
Nd	23.6	16.7	25.2	7.7
Ni	12.8	<0.7	18.7	<0.5
Pb	8.2	9.7	7.5	9.7
Rb	15.6	36.7	55.6	140.3
Sc	30.6	34.1	23.1	3.3
Sr	458.2	481.4	415.7	111.2
Th	6.9	3.5	10.2	17.3
U	2.6	1.3	1.4	2.5
V	229.0	267.8	159.2	10.9
Y	30.8	27.1	29.6	20.7
Zn	48.8	71.2	72.4	14.8
Zr	179.1	43.3	230.9	98.2

† Total iron (FeO and Fe_2O_3).

displayed in Fig. 3. The majority of Anchorage Island is composed of weathered granodiorite, however some areas contain amphibole rich granodiorites (J13.24, J13.25 and J13.26), and areas in the southwest of the island display strongly weathered and altered granodiorites (J13.19 and J13.20).

The spectral variability of the granidiorites is shown in Fig. 3A. Numerous dolorite dykes cut the granodiorite unit; a spectral measurement from a dolerite dyke in the northwest of Anchorage Island is shown in Fig. 3B. The field spectra for dolerite and granodiorite show similar spectral features; a small relative increase in emissivity at 8.6 and 9.5, and two broad flat absorption features centred around 9 and 10. The whole-rock XRF data shown in Table 1 support the spectral similarity of the dolerite and granodiorite samples — there is very little difference in the chemical composition of these samples, hence the similar spectra of the samples. The amphibole rich granodiorite spectra display an additional weak feature at 10 with reduced magnitude of the emissivity maximum at 8.6 μm. The strongly weathered (and altered) granodiorite spectra are significantly different to weathered/amphibole rich granodiorite spectra, displaying a broad deep feature at 9 μm and a smooth spectrum above 9.8 μm. We attribute the broad deep absorption centred around 9 μm to high temperature feldspar alteration into clay minerals (e.g. sericite).

Table 2
Results from point counting, where mineral counts are given as percentages. A total of 500 points were counted on each sample (n = 500).

Sample	J13.22.5	J13.22.10	J13.21.10
Unit	Granodiorite	Dolerite	Granite
Point count (%)			
Biotite			1.2
Chlorite	8.8		
Clinopyroxene		33	
Hornblende	12.6		
K-Feldspar			27.8
Muscovite		1.4	
Opaques	1	4.6	1
Plagioclase	44.8	61	35
Quartz	32.8		35

The spectrum of granite is dominated by a quartz signal which leads to an emissivity maximum at 8.7 μm and a deep feature with an emissivity minimum at 9.4 μm (Fig. 3B). Although similar spectral features to granodiorite are present in the granites, the overall magnitude of the absorption features in much larger in the granite than in any of the granodiorite or dolerite spectra.

4.2. TIR data preprocessing results

Fig. 6 shows the first 10 bands of the MNF transform. As higher MNF components are considered, the levels of noise dramatically increase (Fig. 6G–J). The MNF images also clearly highlight the differences between flight lines which cause 'striping'in the images (e.g. Fig. 6E and F). The first four of these MNF components (Fig. 6A–D) were retained and processed through an inverse MNF transform prior to input in the superpixel and endmember extraction algorithms.

Fig. 7 shows the SNR for the image after atmospheric correction and TES compared to the SNR for the final image after all preprocessing (atmospheric correction, TES, EELM and MNF noise reduction). Overall the SNR is increased from a mean value of 60:1 (35.6 dB) to 92:1 (39.3 dB) after preprocessing. With the exception of one band at ~9 μm, the SNR increased for all wavelengths, with significant increases seen at the higher wavelengths (>10.5 μm). Whilst increases in SNR are seen after preprocessing, on whole SNR values are relatively low and far lower than that which are regularly reported by others using airborne hyperspectral TIR sensors such as SEBASS; for example Vaughan et al. (2003) report SNR values of 2000:1 (66 dB) using SEBASS data in Nevada.

The low SNR values reported here are likely a direct result of the challenging operating conditions in the Antarctic; the instruments were flown in an unpressurised aircraft, operating at extreme temperatures which were up to 20 °C (68 °F) outside of the instrument's normal operating range, as well as being subject to repeated heating and cooling cycles during storage and operation (Black et al., 2014).

4.3. Predictive map generation and geological interpretations

A total of 9810 superpixels were input into the VD algorithm which determined there were 5 endmembers. The endmembers were extracted using the VCA algorithm and are shown in Fig. 8. Endmember abundances were determined using FCLSU; the abundances images were utilised to generate a classified map, where classes were assigned to the predominant endmember if the abundance was greater than 0.5.

The classes were subsequently labelled by automatic matching to the field spectral data; the closest match (in terms of spectral angle; (Eq. (6)) was applied to label the endmembers (Fig. 8) and their respective class in the predictive classification map (Fig. 9). The results were validated through visual inspection of the classification map with respect to the local geological map (Fig. 2), comparison of the endmember spectra and the ancillary data (Sections 2.3 and 3.2), as well as using the RMSE metric (Sections 3.5 and 4.4). Endmember-4 was excluded as it represented sea water from pixels which were not captured at the masking step and is not discussed further. The resulting lithological map is shown in Fig. 9.

For each endmember, a match was determined from the field spectra where the SA was ≤0.03 radians; we found confident matches for granite,

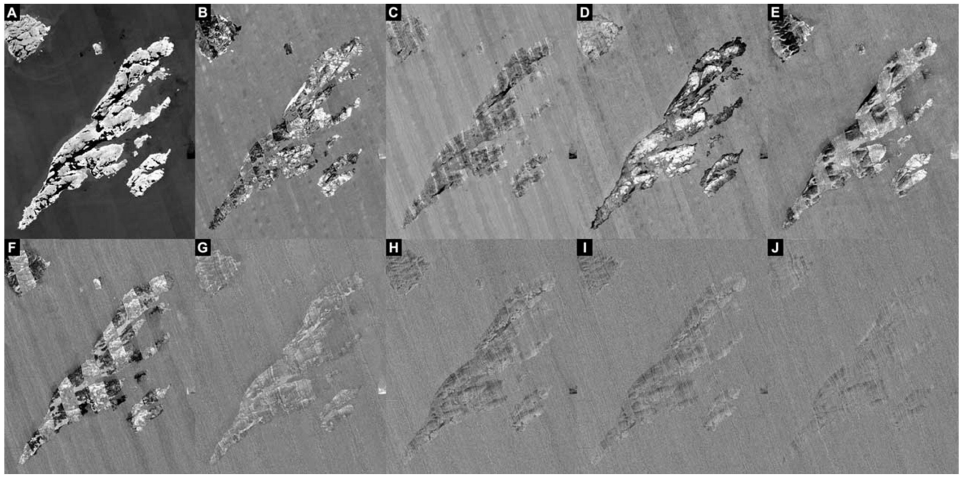

Fig. 6. Images for the first 10 components of the minimum noise fraction (MNF) transform (A-J). Components 1 to 4 (A to D) were utilised in the inverse MNF procedure.

two types of weathered granodiorite and altered granodiorite. The endmember spectra display absorption features consistent with the field measured spectra (Fig. 3) and their mapped distributions (Fig. 9) are largely in agreement with the generalised geological map (Fig. 2).

The granite endmember (Endmember-1; Fig. 8A) displays good agreement with the field spectral data and its distribution on the predictive map (Fig. 9A and B). We accurately delineate the stoped granite block in the northeast of Anchorage Island, along with the larger outcrops south of the granite block and along the northeast coast. The predictive map indicates the likelihood of additional outcrops of granite occurring predominantly in the northeast of Anchorage Island (Fig. 9B).

The occurrence of granite *senso stricto* in continental margin arcs is rare, typically accounting for 1–2% of the total volume of granitoid rocks exposed at the surface. Granites exposed at the surface on the western margin of the Antarctic Peninsula are rare and not previously identified at all from Adelaide Island (or the Ryder Bay islands, including Anchorage Island, prior to mapping carried out in this study). The identification of stoped blocks of granite within a granodiorite pluton indicates the presence of granite at relatively shallow depths.

Two of the endmembers (Endmember-2 and Endmember-3; Fig. 8B and C) show good matches to granodiorite spectra measured in the field; both are measured from weathered granodiorite, however Endmember-3 is from yellow/orange weathered granodiorite. The spatial distribution of this endmember is largely limited to low lying coastal regions, perhaps indicating recent weathering due to coastal processes, which distinguishes it from the remaining granodiorite (Endmember-2). Endmember-3 also shows a higher abundance in the extreme southwest of Anchorage Island, corresponding to the diorite outcrop (c.f. Fig. 2), though does not allow for distinguishing the diorite as a separate unit; this is likely as the diorite and granodiorite units would have a

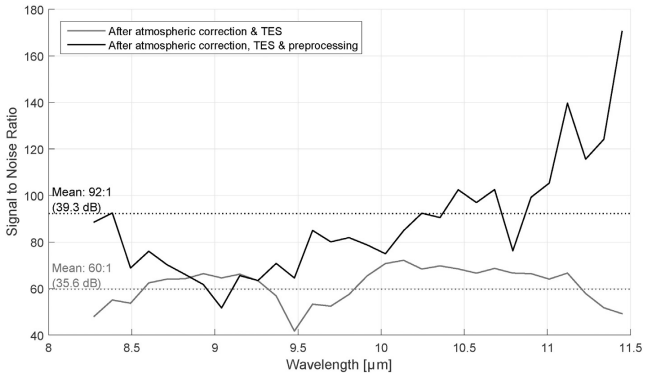

Fig. 7. Signal to noise ratio (SNR) calculated from the image after atmospheric correction and temperature emissivity separation (TES; grey line) compared to the SNR for the final image after all preprocessing (atmospheric correction, TES, emissive empirical line correction and minimum noise fraction for noise reduction) (black line). Mean values are shown in the annotations.

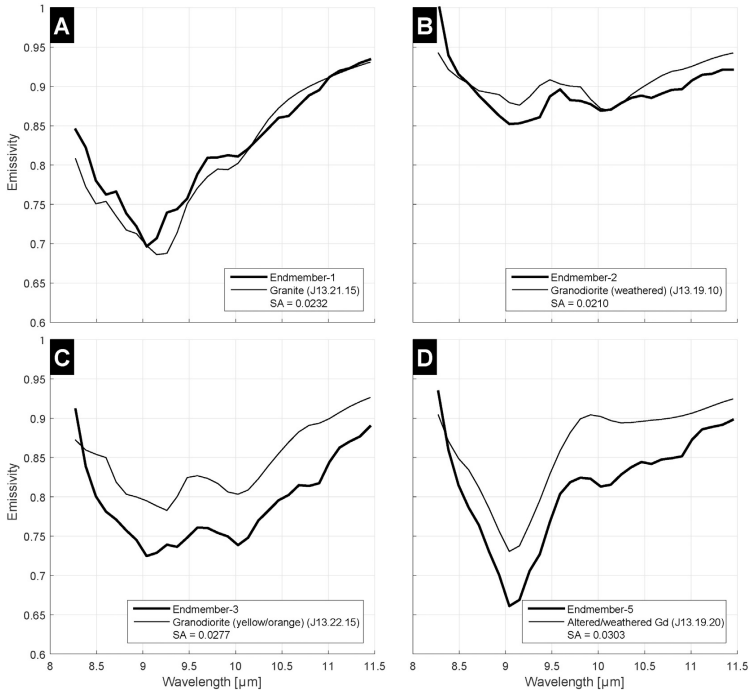

Fig. 8. Four extracted endmembers (thick line) and their closest match from the field spectral data (thin line). The spectral angle (SA), in radians, is shown in each figure legend.

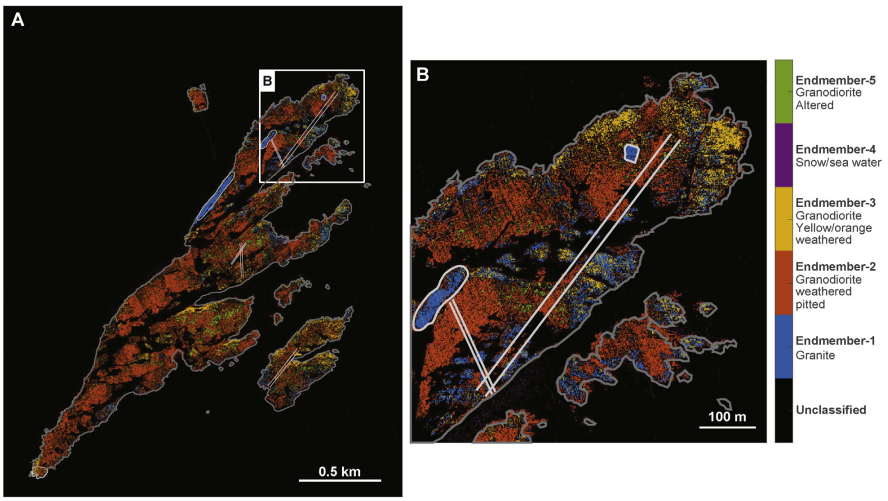

Fig. 9. Lithological map generated from the automated processing chain. (A) shows the whole of Anchorage Island and inset (B) shows an area of interest around a stoped granite block in the North East of Anchorage Isalnd. Compare Fig. 2 for geological boundaries.

similar chemical composition and thus would be difficult to differentiate spectrally. Endmember-5 shows a good agreement with a measured spectrum from the strongly altered granodiorite (Fig. 8D), with a deep emissivity feature centred at 9, however there are additional features located at 10 and 11 which are not seen in the field spectrum. Endmember-5 is largely distributed proximal to, or within the larger spatial lithological unit of the granodiorite (Endmember-2) and is distinct from the granite unit (Endmember-1). The yellow/orange weathered and altered grandiorites (Endmember-3 and Endmember-5 respectively) have their greatest abundance in the central southwest region of the Island (concurring with the field observations; Section 4.1).

None of the endmembers correspond to the dolerite, most likely due to the chemical and spectral similarity to the granodiorite unit (Table 1; Fig. 3). The granodiorite and dolerite were distinguished in the field due to the differences in their grain size; however, the spectral features present in the imagery do not allow for a distinction to be made. Even in the

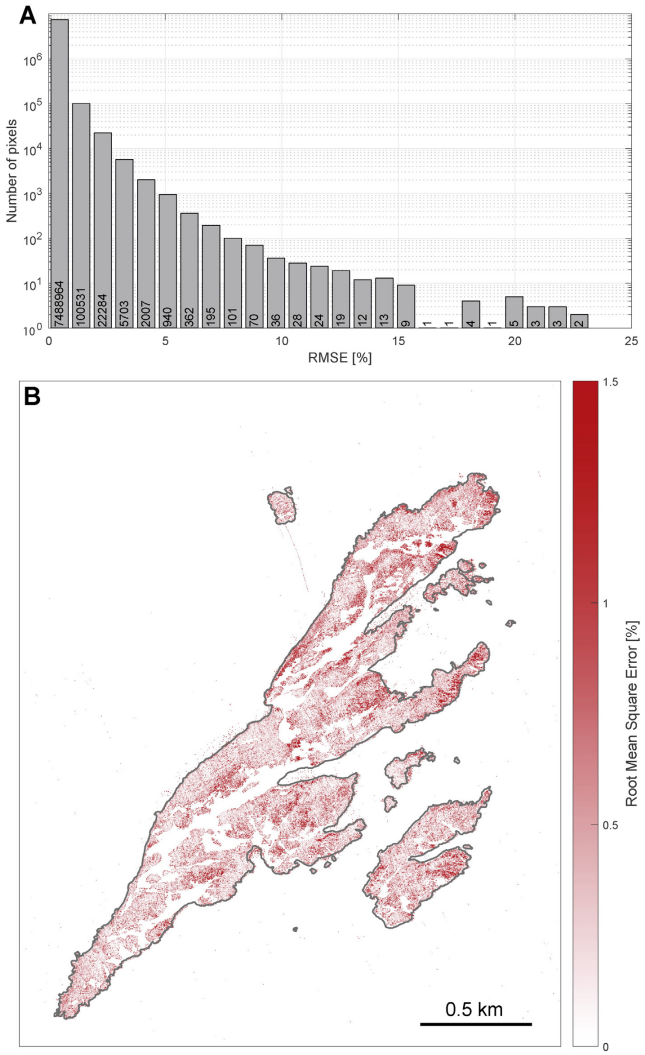

Fig. 10. (A) histogram of Root Mean Square Error (RMSE; %) values; note the log scale. (B) shows the RMSE image of Anchorage Island. Note: the color bar is capped at 1.5% as the predominant distribution of RMSE values is below this threshold.

field spectra, there is little difference between the granodiorite and dolerite (Fig. 3), hence there are no endmembers extracted that match dolerite.

At the wavelengths considered by the TASI sensor (8 to 11.5 μm), we have been able to differentiate granite and granodiorite, whilst struggled to find a clear distinction between the relatively similar chemical composition of the country rock (granodiorite) and the dolerite dykes on Anchorage Island. The ability to more accurately discriminate potassium and plagioclase feldspar(s) could be possible if data were available at wavelengths where additional features could aid in feldspar discrimination (e.g. 12–14 μm; Hecker et al., 2012).

4.4. Validation of image processing

Fig. 10 shows the RMSE histogram and image calculated through Eq. (8). Summary statistics calculated for each of the predicated class pixels (Fig. 9) within the RMSE image are shown in Table 3.

Endmembers 1, 2 and 5 produce RMSE values of <0.5%, with standard deviations of ~0.45% and a maximum RMSE of 7.83% (Endmember-1). These values indicate that the unmixing procedure with just 5 endmember spectra yielded a high quality reconstruction of the original image spectra for these classes. Endmember-3 has a mean RMSE which is significantly higher at 0.94% with an increased standard deviation of 1.25% and a maximum error of 23%; this indicates pixels which are classed as Endmember-3 have higher overall and specific reconstruction errors, likely a result of incorrect or inadequate endmember spectra for these pixels and hence higher errors.

On the whole, the average RMSE for the image is 0.58%; this figure is significantly higher than the RMSE values that are routinely achieved using VCA (e.g. RMSE of 0.1% in Plaza et al., 2012), however this is likely a direct result of the low SNR of the imagery (Fig. 7). As the SNR is reduced (below 1000:1, 60 dB) the performance of endmember extraction algorithms begins to degrade significantly and RMSE values increase (Plaza et al., 2012). Conversely, with larger SNRs, the RMSE error will decrease and the performance of endmember extraction algorithms will improve (Nascimento & Bioucas-Dias, 2005; Plaza et al., 2012). Other factors may also affect the RMSE values, including the pure pixel assumption and spectral mixture analysis techniques, as discussed in Section 4.5. However, these errors did not inhibit the success of the processing chain.

Fig. 11 shows the spectra of pixels from high, medium and low purity pixels, comparing the original image spectra with the reconstructed image spectra (from endmembers and their fractional abundances), for granite, granodiorite and altered granodiorite. In all cases the RMSE is ≤2%, indicating a good fit between the original and reconstructed spectra. The high purity pixels (Fig. 11A) more closely resemble the original endmembers and their equivalent field spectra (c.f. Fig. 8), indicating a good degree of reconstruction of the original spectra and that endmember lithologies are accurately represented. When considering the medium and low purity spectra (Fig. 11B and C), the RMSE values are still low, indicating a high degree of fit between the original and reconstructed spectra; however, as the mixing of endmembers is increased, the pixel spectra begin converge and become increasingly similar (especially at low purities, Fig. 11C). This indicates that as pixels become increasingly mixed (lower fractional abundances) the pixel spectra are similar yielding lower confidence in assigning a distinct lithology for low purity pixels. In this study we defined our abundance threshold at 0.5, however with careful examination of reconstructed and original image spectra, this threshold value could be increased to yield greater confidence in lithological units (as pixel spectra would more closely resemble endmember spectra).

Table 3
Root mean square error statistics.

RMSE (%)	Mean	Max	StDev
Endmember-1	0.498	7.830	0.464
Endmember-2	0.473	3.447	0.439
Endmember-3	0.939	23.223	1.246
Endmember-5	0.425	5.952	0.451
All Endmembers	0.584	23.223	0.650

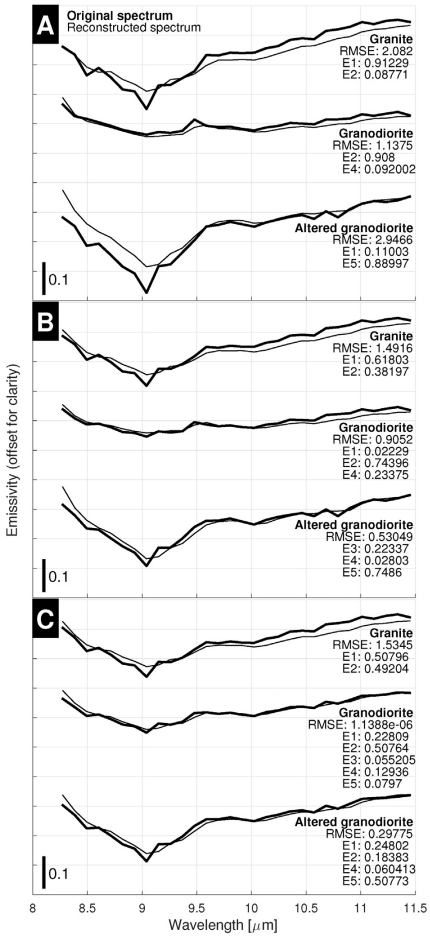

Fig. 11. Original image spectra (bold line) and their reconstructed spectra (thin line; calculated using the endmember spectra and the fractional abundances). Figure annotations are as follows: RMSE; root mean square error, %; E1 to E5; fractional abundances of endmember-1 to endmember-5. (A) high purity (0.9 fractional abundance) spectra, (B) medium purity (0.75 fractional abundance) spectra and (C) low purity (0.5 fractional abundance) spectra.

4.5. Processing chain and algorithm considerations

Here we considered a pure pixel scenario, the assumption that at least one 'pixel' contains a pure endmember spectrum. We note that a pure endmember spectrum represents an independent signal source

in the image and in some cases is not necessarily a geologically meaningful (or interpretable) spectrum; for example some endmember spectra could be related to image noise or atmospheric effects (Winter, 1999). However, processing hyperspectral imagery assuming a pure pixel scenario has been widely researched, with a variety of pure pixel techniques for each step of the processing chain along with the optimised implementation and proven success of published algorithms. The pure pixel approach has been successful when images contain pure pixels (Plaza et al., 2012); however, given the presence of the mixing at different scales (even at microscopic levels), the pure pixel assumption is not always true, as some images may only contain pixels which are completely mixed (Plaza et al., 2012).

The complexity of endmember extraction from hyperspectral imagery is increased in a mixed pixel scenario, since the endmembers, or at least some of them, are not in the image (Bioucas-Dias, 2009). We note a point for future research into mixed pixel endmember extraction techniques which follow from the seminal ideas of (Craig, 1994), based on the minimum volume transform, with a number of recently published algorithms building from this work (Berman et al., 2004; Bioucas-Dias, 2009; Chan, Chi, Huang, & Ma, 2009; Li & Bioucas-Dias, 2008; Miao & Qi, 2007). Currently, the major shortcoming of mixed-pixel techniques is long processing times due to their computational complexity (Bioucas-Dias, 2009). However mixed pixel techniques are an active area of research and as the algorithms mature they should be integrated into future studies. Additionally, the long established pure pixel methods should not yet be discounted; technological advances such as miniaturisation of sensors will inevitably lead to very high spatial resolution as sensors are deployed from platforms such as Unmanned Aerial Vehicles (UAVs).

For SMA, also known as spectral unmixing, we considered the fully constrained linear model due to its ease of implementation and flexibility in different applications (Chang, 2003). We have not considered linear unmixing using iterative spectral mixture analysis (ISMA; Rogge & Rivard, 2006), which seeks to minimise the error by unmixing on a per pixel basis using optimised endmember sets. Alternatively, non-linear SMA may best characterise the resultant mixed spectra for certain endmember distributions, such as those in which the endmember components are intimately mixed (Guilfoyle, Althouse, & Chang, 2001; Plaza et al., 2009). In those cases, the mixed spectra collected at the imaging instrument are better described by assuming that part of the source radiation has undergone multiple scattering prior to being measured at the sensor.

In a non-linear model, the interaction between the endmembers and their fractional abundance is given by a non-linear function, which is not known a priori. Various techniques have been proposed in the field of machine learning, with neural networks some of first non-linear SMA approaches proposed (Benediktsson, Swain, & Ersoy, 1990). The performance of non-linear SMA algorithms on large, real-world hyperspectral data is currently limited by the computational complexity of the techniques; however, recent advances have aimed to take advantage of parallel processing techniques to reduce computational time (e.g. Plaza, Plaza, Perez, & Martinez, 2008) and such algorithms remain an area for future research as their implementations become publicly available.

4.6. Future applicability of the processing chain

The processing chain presented here is fully automated and repeatable; after preprocessing, the six step processing chain is fully automated, using few inputs and parameters, followed by predictive map generation and automatic class labelling using the field spectral data. This is a direct attempt to address the current paucity of such automated approaches in the geological remote sensing community (van der Meer et al., 2012). We anticipate the technique could be applied by geologists without the need for 'expert' remote sensing knowledge or complicated image processing techniques/software packages, and the processing chain is more automated and less manually involved than traditional techniques. Indeed, this processing chain is particularly advantageous in the polar regions where higher detail lithological mapping can be obtained using remote sensing than compared with traditional field mapping.

The main parameters which affect the lithological mapping processing chain are the superpixel bias parameter and minimum size segment size. The parameters are discussed and explained in detail by (Thompson et al., 2010). The bias and minimum size segment size parameters control the size of the superpixels and should be scaled appropriately depending on the features of interest in each particular scene. The parameters used in this study were quantitatively determined by inspecting the superpixel segmentation image and considering the scale of the geological areas of interest (e.g. dykes), however these parameters would require local tuning for other study areas, and particularly for other scales and image resolution (such as coarser resolution satellite imagery). The abundance threshold can be tuned to extract purer regions, however we demonstrate the results here using a moderate threshold of 0.5; higher values would yield spectrally purer regions (e.g. Rogge et al., 2009).

We have achieved the results presented here in spite of what might be described as 'extremely high noise conditions' (SNR ≤ 40 dB; Plaza et al., 2012), thereby serving as a validation of the processing chain and its ability to operate effectively at low SNR values. We confirm the findings of the Thompson et al. (2010) and Gilmore et al. (2011), such that superpixel segmentation aids in the determination of *recognisable* endmembers which are interpretable in a geological context despite low SNR values. Such a finding is crucial for future studies in the Antarctic where the environmental conditions mean that achieving high SNR values is much more challenging compared with temperate parts of the world. Indeed, this finding is also advantageous for many studies, not just the Antarctic, where challenging conditions can yield lower than expected SNRs; hence, it is advantageous that the processing chain can yield successful results even at low SNRs.

It is an important point to note for future applications that prior knowledge of the local geology (and/or vegetation) is required for the successful application of the processing chain. The identification of the image derived endmembers (step 6) was successful here, in large part due to availability of high quality field spectral measurements to allow for comparison along with ancillary data (geochemical analysis). However, in lieu of field spectral measurements, a user could produce geological interpretations with knowledge of the local geological context, an understanding of the imperfections in the hyperspectral imagery (e.g. residual noise due to inadequate atmospheric compensation) and the identification of endmembers could be aided through comparison to spectral libraries (e.g. Christensen et al., 2000).

The techniques presented here could be easily transferred to other TIR data (or even VNIR/SWIR data), including currently available satellite data, such as ASTER, or even planned future satellite TIR data; for example, the HyspIRI satellite has a planned TIR instrument which includes 7 bands in the 7–13 μm spectral range (Hulley, Realmuto, Hook, & Ramsey, 2012). The coarser spatial and spectral resolution of this data would yield difficulties in the exact identification of minerals, though previous TIR data, such as ASTER, has been used to reliably discriminate a wide range of minerals, especially silicates, as well as proving useful for lithological mapping (e.g. Chen et al., 2007; Haselwimmer et al., 2010, 2011; Rogge et al., 2009; Rowan & Mars, 2003; Salvatore et al., 2014). Additionally, technological advances and increasing miniaturisation will eventually lead to the availability of UAV-deployable research grade hyperspectral sensors which could be used operationally by field geologists as a tool to compliment traditional field mapping techniques. The use of an automated processing chain in such a situation would be highly advantageous in delivering fast, automated and repeatable lithological mapping results which could aid and inform traditional mapping approaches operationally in the field.

5. Conclusion

We have presented a fully automated processing chain to produce lithological maps using airborne hyperspectral thermal infrared data in spite of low signal to noise ratios. We utilised an airborne hyperspectral TIR dataset, collected for the first time from Antarctica, to accurately discriminate grantoids. The challenging conditions and cold temperatures in the Antarctic yielded data with a significantly lower SNR compared with data collected in more temperate environments. As a result, several preprocessing steps were employed to refine the imagery prior to analysis; atmospheric correction and temperature emissivity separation were applied, followed by further empirical corrections and noise removal through the minimum noise fraction technique. Areas of snow and sea water were subsequently masked using the temperature image.

The processing chain was established and applied to the preprocessed imagery. Firstly, superpixel segmentation was applied to aggregate homogeneous image regions comprised of several pixels having similar values into larger segments (superpixels). The superpixels were input into the VD algorithm to determine the number of endmembers, which were subsequently extracted using VCA and unmixed using FCLSU to generate abundances of each endmember. A predictive classification map was created where endmember fractions were thresholded (>0.5). The endmembers extracted were automatically matched to their closest spectrum from the field spectral data, and the observations made in the field from these measurements were used to label the predictive map classes and generate a lithological map.

The fully automated processing chain was successful in identifying 4 geologically interpretable endmembers from the study area. Reconstruction of the hyperspectral image from the endmembers and their fractional abundances yielded a RMSE of 0.58%. The RMSE value, almost twice as large as previous studies, is likely a result of the low SNR of the Antarctica data; nonetheless the processing chain was still able to accurately discriminate the majority of lithological units with strong agreement to existing geological maps.

The results were validated and interpreted in the context of the study area in conjunction with a full suite of ancillary data: detailed high quality ground reference spectral data collected using a field portable Fourier transform infrared spectrometer, thin section and scanning electron microscope analysis, electron microprobe analysis, whole rock geochemical data and mineral modal analysis. The results are promising, with the thermal imagery allowing clear distinction between granitoid types. However, the distinction of fine grained, intermediate composition dykes is not possible due to the close spectral similarity with the country rock (granodiorite).

Acknowledgements

M Black is funded by a Natural Environment Research Council (NERC) PhD studentship in conjunction with the British Antarctic Survey (BAS) and the University of Hull (NERC Grant: NE/K50094X/1). The hyperspectral survey was funded by the UK Foreign and Commonwealth Office (FCO) and conducted by BAS, ITRES Research Ltd. and Defence Research & Development, Canada (DRDC). Fieldwork was supported by a Collaborative Gearing Scheme Grant (CGS-86). Field spectrometers were provided by the NERC Field Spectroscopy Facility (Loan No. 675.0613) and through Eldon Puckrin, DRDC. We gratefully acknowledge Eldon Puckrin, Stephen Achal and Alex Shipp for their support and assistance during fieldwork, and David Neave, Iris Buisman and Nick Marsh for their assistance with geochemical analysis. Anonymous reviewers are thanked for their comments on earlier versions of this manuscript.

References

Abrams, M., & Hook, S. J. (1995). Simulated ASTER data for geologic studies. *IEEE Transactions on Geoscience and Remote Sensing, 33*(3), 692–699.

Abrams, M. J., Ashley, R. P., Rowan, L. C., Goetz, A. F. H., & Kahle, A. B. (1977). Mapping of hydrothermal alteration in the Cuprite mining district, Nevada, using aircraft scanner images for the spectral region 0.46 to 2.36 μm. *Geology, 5*(12), 713–718.

Adler, H. H., & Kerr, P. F. (1963). Infrared absorption frequency trends for anhydrous normal carbonates. *American Mineralogist, 48*(1–2), 124.

Aslett, Z., Taranik, J. V., & Riley, D. N. (2008). Mapping rock-forming minerals at Daylight Pass, Death Valley National Park, California, using SEBASS thermal-infrared hyperspectral image data. *Geoscience and Remote Sensing Symposium, 2008. IGARSS 2008. Vol. 3*, IEEE International (pp. III-366-III-369).

Benediktsson, J., Swain, P. H., & Ersoy, O. K. (1990). Neural network approaches versus statistical methods in classification of multisource remote sensing data. *IEEE Transactions on Geoscience and Remote Sensing, 28*(4), 540–552.

Berk, A., Anderson, G. P., Acharya, P. K., Bernstein, L. S., Muratov, L., Lee, J., et al. (2005). MODTRAN5: A reformulated atmospheric band model with auxiliary species and practical multiple scattering options. *Proc. SPIE, 5655*, 88–95.

Berman, M., Kiiveri, H., Lagerstrom, R., Ernst, A., Dunne, R., & Huntington, J. F. (2004). ICE: A statistical approach to identifying endmembers in hyperspectral images: Learning from Earth's shapes and colors. *IEEE Transactions on Geoscience and Remote Sensing, 42*(10), 2085–2095.

Bioucas-Dias, J. M. (2009). A variable splitting augmented Lagrangian approach to linear spectral unmixing. *Hyperspectral Image and Signal Processing: Evolution in Remote Sensing, 2009. WHISPERS'09. First Workshop on. IEEE, Grenoble, France* (pp. 1–4).

Black, M., Fleming, A., Riley, T., Ferrier, G., Fretwell, P., McFee, J., et al. (2014). On the atmospheric correction of Antarctic airborne hyperspectral data. *Remote Sensing, 6*(5), 4498–4514.

Boardman, J. W. (1993). Automating spectral unmixing of AVIRIS data using convex geometry concepts. In: Summaries 4th annu. JPL airborne geoscience workshop. Vol. 1. *JPL Publication, 93–26*, 11–14.

Boardman, J. W., & Kruse, F. A. (1994). Automated spectral analysis: A geologic example using AVIRIS data, North Grapevine Mountains, Nevada. *Proceedings of tenth thematic conference on geologic remote sensing* (pp. I407–I418). Environmental Research Institute of Michigan.

Calvin, W. M., Vaughan, R. G., Taranik, J. V., & Smailbegovic, A. (2001). Mapping natural and human influenced acid sulfate weathering near Reno, NV using the SEBASS hyperspectral instrument. *Geoscience and Remote Sensing Symposium, 2001. IGARSS '01. Vol. 2.* (pp. 727–729). IEEE 2001 International (vol. 2).

Chan, T. -H., Chi, C. -Y., Huang, Y. -M., & Ma, W. -K. (2009). A convex analysis-based minimum-volume enclosing simplex algorithm for hyperspectral unmixing. *IEEE Transactions on Signal Processing, 57*(11), 4418–4432.

Chang, C. I. (2003). Hyperspectral imaging: Techniques for spectral detection and classification. *Hyperspectral imaging: techniques for spectral detection and classification*. US: Springer.

Chang, C. -I., & Du, Q. (2004). Estimation of number of spectrally distinct signal sources in hyperspectral imagery. *IEEE Transactions on Geoscience and Remote Sensing, 42*(3), 608–619.

Chang, C. -I., & Plaza, A. (2006). A fast iterative algorithm for implementation of pixel purity index. *IEEE Geoscience and Remote Sensing Letters, 3*(1), 63–67.

Chen, X., Warner, T. A., & Campagna, D. J. (2007). Integrating visible, near-infrared and short-wave infrared hyperspectral and multispectral thermal imagery for geological mapping at Cuprite, Nevada. *Remote Sensing of Environment, 110*(3), 344–356.

Christensen, P. R., Bandfield, J. L., Hamilton, V. E., Howard, D. A., Lane, M. D., Piatek, J. L., ... Stefanov, W. L. (2000). A thermal emission spectral library of rock-forming minerals. *Journal of Geophysical Research, 105*(E4), 9735.

Clark, R. N., & Swayze, G. A. (1996). Evolution in imaging spectroscopy analysis and sensor signal-to-noise: An examination of how far we have come. *Summaries of the Sixth Annual JPL Airborne Earth Science Worksho, JPL Publication, March 4–8* (pp. 4–8).

Clark, R. N., Swayze, G. A., & Gallagher, A. (1993). *Mapping minerals with imaging spectroscopy. 2039.* (pp. 141–150). US Geological Survey, Office of Mineral Resources Bulletin, 141–150.

Craig, M. D. (1994). Minimum-volume transforms for remotely sensed data. *IEEE Transactions on Geoscience and Remote Sensing, 32*(3), 542–552.

Cudahy, T. J., Wilson, J., Hewson, R., Linton, P., Harris, P., Sears, M., et al. (2001). Mapping porphyry–skarn alteration at Yerington, Nevada, using airborne hyperspectral VNIR-SWIR-TIR imaging data. *Geoscience and Remote Sensing Symposium, 2001. IGARSS '01. Vol. 2.* (pp. 631–633). IEEE 2001 International.

Dash, P., Göttsche, F. -M., Olesen, F. -S., & Fischer, H. (2002,). Land surface temperature and emissivity estimation from passive sensor data: Theory and practice-current trends. *International Journal of Remote Sensing, 23*(13), 2563–2594.

Distasio, R., Jr., & Resmini, R. (2010,). Atmospheric compensation of thermal infrared hyperspectral imagery with the emissive empirical line method and the in-scene atmospheric compensation algorithms: A comparison. *Society of Photo-Optical Instrumentation Engineers (SPIE) Conference Series. Vol. 7695 of Society of Photo-Optical Instrumentation Engineers (SPIE) Conference Series.*

Drury, S. A. (2001). *Image interpretation in geology*. Oxford, UK: Blackwell Science.

Feely, K. C., & Christensen, P. R. (1999). Quantitative compositional analysis using thermal emission spectroscopy: Application to igneous and metamorphic rocks. *Journal of Geophysical Research, Planets, 104*(E10), 24195–24210.

Felzenszwalb, P. F., & Huttenlocher, D. P. (2004). Efficient graph-based image segmentation. *International Journal of Computer Vision, 59*(2), 167–181.

Feng, J., Rivard, B., Rogge, D. M., & Grant, B. (2012,). Spectral enhancement of sebass hyperspectral data and its application in mapping of ultramafic rocks. *4th Workshop on Hyperspectral Image and Signal Processing: Evolution in Remote Sensing (WHISPERS)* (pp. 1–4).

Freemantle, J. R., Pu, R., & Miller, J. R. (1992). Calibration of imaging spectrometer data to reflectance using pseudo-invariant features. *Proceedings of the 14th Canadian Symposium on Remote Sensing* (pp. 1–4).

Galehouse, J. (1971). Point counting. In R. E. Carver (Ed.), *Procedures in sedimentary petrology*. John Wiley and Sons Canada, Limited.

Gillespie, A., Rokugawa, S., Matsunaga, T., Cothern, J., Hook, S., & Kahle, A. (1998). A temperature and emissivity separation algorithm for advanced spaceborne thermal emission and reflection radiometer (ASTER) images. *IEEE Transactions on Geoscience and Remote Sensing, 36*(4), 1113–1126.

Gilmore, M. S., Thompson, D. R., Anderson, L. J., Karamzadeh, N., Mandrake, L., & Castaño, R. (2011). Superpixel segmentation for analysis of hyperspectral data sets, with application to compact reconnaissance imaging spectrometer for Mars data, moon mineralogy mapper data, and ariadnes chaos, Mars. *Journal of Geophysical Research, Planets, 116*(E7).

Green, R. O., Eastwood, M. L., Sarture, C. M., Chrien, T. G., Aronsson, M., Chippendale, B. J., Faust, J. A., Pavri, B. E., Chovit, C. J., Solis, M., et al. (1998). Imaging spectroscopy and the airborne visible/infrared imaging spectrometer (AVIRIS). *Remote Sensing of Environment*, *65*(3), 227–248.

Guilfoyle, K. J., Althouse, M. L., & Chang, C. -I. (2001). A quantitative and comparative analysis of linear and nonlinear spectral mixture models using radial basis function neural networks. *IEEE Transactions on Geoscience and Remote Sensing, 39*(10), 2314–2318.

Gupta, R. P. (2003). *Remote sensing geology*. Berlin, Germany: Springer-Verlag.

Hamilton, V. E., & Christensen, P. R. (2000). Determining the modal mineralogy of mafic and ultramafic igneous rocks using thermal emission spectroscopy. *Journal of Geophysical Research, 105*(E4), 9717–9733.

Harris, J. R., Rogge, D., Hitchcock, R., Ijewlie, O., & Wright, D. (2005). Mapping lithology in Canada's Arctic: Application of hyperspectral data using the minimum noise fraction transformation and matched filtering. *Canadian Journal of Remote Sensing, 2193*(2005), 2173–2193.

Haselwimmer, C. E., Riley, T. R., & Liu, J. G. (2010). Assessing the potential of multispectral remote sensing for lithological mapping on the Antarctic Peninsula: Case study from Eastern Adelaide Island, Graham Land. *Antarctic Science*, *22*(03), 299–318.

Haselwimmer, C. E., Riley, T. R., & Liu, J. G. (2011). Lithologic mapping in the Oscar II Coast area, Graham Land, Antarctic Peninsula using ASTER data. *International Journal of Remote Sensing, 32*(7), 2013–2035.

Hecker, C., Dilles, J. H., van der Meijde, M., & van der Meer, F. D. (2012). Thermal infrared spectroscopy and partial least squares regression to determine mineral modes of granitoid rocks. *Geochemistry, Geophysics, Geosystems, 13*(3), Q03021.

Hecker, C., van der Meijde, M., & van der Meer, F. D. (2010). Thermal infrared spectroscopy on feldspars — Successes, limitations and their implications for remote sensing. *Earth-Science Reviews, 103*(1–2), 60–70.

Heinz, D. C., & Chang, C. -I. (2001). Fully constrained least squares linear spectral mixture analysis method for material quantification in hyperspectral imagery. *IEEE Transactions on Geoscience and Remote Sensing, 39*(3), 529–545.

Hewson, R., Hausknecht, P., Cudahy, T., Huntington, J., Mason, P., Hackwell, J., et al. (2000). An appraisal of the hyperspectral thermal-infrared SEBASS data recorded from Oatman, Arizona and a comparison of their unmixed results with AVIRIS. *Exploration and mining report 668F*. Wembley Western Australia: CSIRO Exploration and Mining.

Hook, S. J., & Rast, M. (1990). Mineralogic mapping using Airborne Visible Infrared Imaging Spectrometer (AVIRIS), shortwave Infrared (SWIR) data acquired over Cuprite, Nevada. *Proceedings of the Second Airborne Visible Infrared Imaging Spectrometer (AVIRIS) Workshop* (pp. 54–90). JPL Publication.

Hook, S. J., Cudahy, T. J., Kahle, A. B., & Whitbourn, L. B. (1998). Synergy of active and passive airborne thermal infrared systems for surface compositional mapping. *Journal of Geophysical Research - Solid Earth, 103*(B8), 18269–18276.

Hook, S. J., Dmochowski, J. E., Howard, K. A., Rowan, L. C., Karlstrom, K. E., & Stock, J. M. (2005). Mapping variations in weight percent silica measured from multispectral thermal infrared imagery – examples from the Hiller Mountains, Nevada, USA and Tres Virgenes-La Reforma, Baja California Sur, Mexico. *Remote Sensing of Environment*, *95*(3), 273–289.

Hook, S. J., Elvidge, C. D., Rast, M., & Watanabe, H. (1991). An evaluation of short-wave-infrared (SWIR) data from the AVIRIS and GEOSCAN instruments for mineralogical mapping at Cuprite, Nevada. *Geophysics*, *56*(9), 1432–1440.

Hulley, G., Realmuto, V., Hook, S., & Ramsey, M. (2012). HyspIRI thermal infrared (TIR) band study report. *Tech. rep.*. California: NASA Jet Propulsion Laboratory.

Hunt, G., & Salisbury, J. (1975). Mid-infrared spectral behavior of sedimentary rocks. *Tech. rep.*

Hunt, G. R. (1980). Electromagnetic radiation: the communication link in remote sensing. *Remote Sensing in Geology*, *2*, 5–45.

Keshava, N., & Mustard, J. F. (2002). Spectral unmixing. *IEEE Signal Processing Magazine, 19*(1), 44–57.

Kramer, H. J. (2002). Observation of the earth and its environment: survey of missions and sensors. *Engineering online library*. Springer.

Kruse, F. A., & McDowell, M. (2015, may). Analysis of multispectral and hyperspectral longwave infrared (LWIR) data for geologic mapping. In M. Velez-Reyes, & F. A. Kruse (Eds.), *Proc. SPIE 9472, Algorithms and Technologies for Multispectral, Hyperspectral, and Ultraspectral Imagery XXI* (pp. 94721E).

Kruse, F. A., Kierein-Young, K. S., & Boardman, J. W. (1990). Mineral mapping at Cuprite, Nevada with a 63-channel imaging spectrometer. *Photogrammetric Engineering and Remote Sensing, 56*, 83–92.

Kruse, F. A., Lefkoff, A. B., & Dietz, J. B. (1993b). Expert system-based mineral mapping in northern Death Valley, California/Nevada, using the airborne visible/infrared imaging spectrometer (AVIRIS). *Remote Sensing of Environment*, *44*(2), 309–336.

Kruse, F., Lefkoff, A., Boardman, J., Heidebrecht, K., Shapiro, A., Barloon, P., & Goetz, A. (1993a). The spectral image processing system (SIPS)—Interactive visualization and analysis of imaging spectrometer data. *Remote Sensing of Environment*, *44*(2–3), 145–163.

Lane, M. D., & Christensen, P. R. (1997). Thermal infrared emission spectroscopy of anhydrous carbonates. *Journal of Geophysical Research, 102*(E11), 25581.

Li, J., & Bioucas-Dias, J. M. (2008). Minimum volume simplex analysis: A fast algorithm to unmix hyperspectral data. *Geoscience and Remote Sensing Symposium. Vol. 3*. (pp. 250–253). Boston, Massachusetts, USA: IEEE International.

Liang, S., Fang, H., Chen, M., Shuey, C. J., Walthall, C., Daughtry, C., Morisette, J., Schaaf, C., Strahler, A., 2002. Validating MODIS land surface reflectance and albedo products: methods and preliminary results. Remote Sensing of Environment 83 (1-2) 149–162.

MathWorks (2011). *MATLAB, version 7.12.0.635 (R2011a)*. Natick, Massachusetts: The MathWorks Inc.

van der Meer, F. D. (1995). Spectral reflectance of carbonate mineral mixtures and bidirectional reflectance theory: Quantitative analysis techniques for application in remote sensing. *Remote Sensing Reviews, 13*(1–2), 67–94.

van der Meer, F. D., van der Werff, H. M. a., van Ruitenbeek, F. J. a., Hecker, C. a., Bakker, W.H., Noomen, M. F., et al. (2012). Multi- and hyperspectral geologic remote sensing: A review. *International Journal of Applied Earth Observation and Geoinformation, 14*(1), 112–128.

Miao, L., & Qi, H. (2007). Endmember extraction from highly mixed data using minimum volume constrained nonnegative matrix factorization. *IEEE Transactions on Geoscience and Remote Sensing, 45*(3), 765–777.

Milam, K. A., McSween, H. Y., Hamilton, V. E., Moersch, J. M., & Christensen, P. R. (2004). Accuracy of plagioclase compositions from laboratory and Mars spacecraft thermal emission spectra. *Journal of Geophysical Research, Planets, 109*(E4).

Nascimento, J. M. P., & Bioucas-Dias, J. M. (2005). Vertex component analysis: A fast algorithm to unmix hyperspectral data. *IEEE Transactions on Geoscience and Remote Sensing, 43*(4), 898–910.

Philpot, W., & Ansty, T. (2011). Analytical description of pseudo-invariant features (PIFs). *6th International Workshop on Analysis of Multi-temporal Remote Sensing Images (Multi-Temp)* (pp. 53–56).

Plaza, A., Benediktsson, J. A., Boardman, J. W., Brazile, J., Bruzzone, L., Camps-Valls, G., Chanussot, J., Fauvel, M., Gamba, P., Gualtieri, A., Marconcini, M., Tilton, J. C., & Trianni, G. (2009). Recent advances in techniques for hyperspectral image processing. *Remote Sensing of Environment*, *113*, S110–S122.

Plaza, A., Plaza, J., Martnez, G., & Sanchez, S. (2011). Hyperspectral data processing algorithms. In P. S. Thenkabail, J. G. Lyon, & A. Huete (Eds.), *Hyperspectral Remote Sensing of Vegetation. 5*. (pp. 121–138). Ch: CRC Press.

Plaza, J., Hendrix, E. M. T., Garca, I., Martn, G., & Plaza, A. (2012). On endmember identification in hyperspectral images without pure pixels: A comparison of algorithms. *Journal of Mathematical Imaging and Vision, 42*(2–3), 163–175.

Plaza, J., Plaza, A., Perez, R., & Martinez, P. (2008). Parallel classification of hyperspectral images using neural networks. In M. Grana, & R. J. Duro (Eds.), *Computational Intelligence for Remote Sensing, 8*. (pp. 193–216). Ch: springer.

Resmini, R. G., Kappus, M. E., Aldrich, W. S., Harsanyi, J. C., & Anderson, M. (1997). Mineral mapping with hyperspectral digital imagery collection experiment (HYDICE) sensor data at Cuprite, Nevada, USA. *International Journal of Remote Sensing*, *18*(7), 1553–1570.

Richter, R., & Coll, C. (2002). Bandpass-resampling effects for the retrieval of surface emissivity. *Applied Optics*, *41*(18), 3523–3529.

Richter, R., & Schläpfer, D. (2002). Geo-atmospheric processing of airborne imaging spectrometry data. Part 2: Atmospheric/topographic correction. *International Journal of Remote Sensing, 23*(13), 2631–2649.

Richter, R., & Schläpfer, D. (2014). *Atmospheric/Topographic Correction for Airborne Imagery. ATCOR-4 User Guide, Version 6.2.1. DLR-IB 565-02/08*. Weßling, Germany: Deutsches Zentrum für Luft- und Raumfahrt (DLR).

Riley, D. N., & Hecker, C. A. (2013). Mineral mapping with airborne hyperspectral thermal infrared remote sensing at Cuprite, Nevada, USA. *Thermal Infrared Remote Sensing* (pp. 495–514). Springer.

Rivard, B., Zhang, J., Feng, J., & Sanchez-Azofeifa, G. A. (2009). Remote predictive lithologic mapping in the Abitibi Greenstone Belt, Canada, using airborne hyperspectral imagery. *Canadian Journal of Remote Sensing, 35*(sup1), S95–S105.

Rogge, D., & Rivard, B. (2006). Iterative spectral unmixing for optimizing per-pixel endmember sets. *IEEE Geoscience and Remote Sensing*, *44*(12), 3725–3736.

Rogge, D., Rivard, B., Harris, J., & Zhang, J. (2009). Application of hyperspectral data for remote predictive mapping, Baffin Island, Canada. *Reviews in Economic Geology*, *16*, 209–222.

Rowan, L. C., & Mars, J. C. (2003). Lithologic mapping in the mountain pass, California area using advanced spaceborne thermal emission and reflection radiometer (ASTER) data. *Remote Sensing of Environment*, *84*(3), 350–366.

Rowan, L. C., Hook, S. J., Abrams, M. J., & Mars, J. C. (2003). Mapping hydrothermally altered rocks at Cuprite, Nevada, using the advanced spaceborne thermal emission and reflection radiometer (ASTER), a new satellite-imaging system. *Economic Geology*, *98*(5), 1019–1027.

Salisbury, J. W. (1991). Infrared (2.1–25 um) spectra of minerals. *Johns Hopkins Studies in Earth and Space Sciences*. Johns Hopkins University Press.

Salvaggio, C., & Miller, C. J. (2001). *Methodologies and protocols for the collection of midwave and longwave infrared emissivity spectra using a portable field spectrometer*.

Salvatore, M. R., Mustard, J. F., Head, J. W. I. I. I., Marchant, D. R., & Wyatt, M. B. (2014). Characterization of spectral and geochemical variability within the Ferrar Dolerite of the McMurdo Dry Valleys, Antarctica: Weathering, alteration, and magmatic processes. *Antarctic Science*, *26*(01), 49–68.

Shimoni, M., van der Meer, F., & Acheroy, M. (2007). Thermal imaging spectroscopy: Present technology and future dual use applications. *proceedings 5th EARSeL workshop on imaging spectroscopy* (Bruges, Belgium).

Smith, G. M., & Milton, E. J. (1999). The use of the empirical line method to calibrate remotely sensed data to reflectance. *International Journal of Remote Sensing*, *20*(13), 2659–2662.

Thompson, D. R., Bornstein, B. J., Chien, S. A., Schaffer, S., Tran, D., Bue, B. D., et al. (2013). Autonomous spectral discovery and mapping onboard the EO-1 spacecraft. *IEEE Transactions on Geoscience and Remote Sensing*, *51*(6), 3567–3579.

Thompson, D. R., Mandrake, L., Gilmore, M. S., & Castano, R. (2010). Superpixel endmember detection. *IEEE Transactions on Geoscience and Remote Sensing*, *48*(11), 4023–4033.

Tuominen, J., & Lipping, T. (2011). Atmospheric correction of hyperspectral data using combined empirical and model based method. *EARSeL 7th SIG-Imaging Spectroscopy Workshop*.

Vaughan, R. G., Hook, S. J., Calvin, W. M., & Taranik, J. V. (2005). Surface mineral mapping at Steamboat Springs, Nevada, USA, with multi-wavelength thermal infrared images. *Remote Sensing of Environment*, *99*(1–2), 140–158.

Vaughan, R., Calvin, W. M., & Taranik, J. V. (2003). SEBASS hyperspectral thermal infrared data: Surface emissivity measurement and mineral mapping. *Remote Sensing of Environment*, *85*(1), 48–63.

Winter, M. E. (1999). N-FINDR: An algorithm for fast autonomous spectral end-member determination in hyperspectral data. *SPIE's International Symposium on Optical Science, Engineering, and Instrumentation* (pp. 266–275). International Society for Optics and Photonics.

Remote Sens. **2014**, *6*, 4498-4514; doi:10.3390/rs6054498

OPEN ACCESS

remote sensing

ISSN 2072-4292

www.mdpi.com/journal/remotesensing

Article

On the Atmospheric Correction of Antarctic Airborne Hyperspectral Data

Martin Black [1,2,*], Andrew Fleming [1], Teal Riley [1], Graham Ferrier [2], Peter Fretwell [1], John McFee [3,†], Stephen Achal [4] and Alejandra Umana Diaz [4]

[1] British Antarctic Survey, High Cross, Madingley Road, Cambridge CB3 0ET, UK;
E-Mails: ahf@bas.ac.uk (A.F.); trr@bas.ac.uk (T.R.); ptf@bas.ac.uk (P.F.)

[2] Department of Geography, Environment and Earth Sciences, University of Hull, Hull HU6 7RX, UK;
E-Mail: g.ferrier@hull.ac.uk

[3] Defence Research and Development Canada-Suffield, Medicine Hat, AB T1A 8K6, Canada;
E-Mail: jemcfee@telus.net

[4] ITRES Research Ltd., 110, 3553-31st Street NW, Calgary, AB T2L 2K7, Canada;
E-Mails: sachal@itres.com (S.A.); alejandra@itres.com (A.U.D.)

[†] Current address: McFysics Consulting, Medicine Hat, AB T1B 2T4, Canada.

* Author to whom correspondence should be addressed; E-Mail: martin.black@bas.ac.uk;
Tel.: .+44-122-322-1400.

Received: 10 January 2014; in revised form: 9 May 2014 / Accepted: 9 May 2014 / Published: 16 May 2014

Abstract: The first airborne hyperspectral campaign in the Antarctic Peninsula region was carried out by the British Antarctic Survey and partners in February 2011. This paper presents an insight into the applicability of currently available radiative transfer modelling and atmospheric correction techniques for processing airborne hyperspectral data in this unique coastal Antarctic environment. Results from the Atmospheric and Topographic Correction version 4 (ATCOR-4) package reveal absolute reflectance values somewhat in line with laboratory measured spectra, with Root Mean Square Error (RMSE) values of 5% in the visible near infrared (0.4–1 μm) and 8% in the shortwave infrared (1–2.5 μm). Residual noise remains present due to the absorption by atmospheric gases and aerosols, but certain parts of the spectrum match laboratory measured features very well. This study demonstrates that commercially available packages for carrying out atmospheric correction are capable of correcting airborne hyperspectral data in the challenging environment present in Antarctica. However, it is anticipated that future results from atmospheric correction could be improved

by measuring *in situ* atmospheric data to generate atmospheric profiles and aerosol models, or with the use of multiple ground targets for calibration and validation.

Keywords: airborne hyperspectral data; atmospheric correction; Antarctica; radiative transfer modelling; MODTRAN; ATCOR

1. Introduction

Antarctica is a unique and geographically remote environment. Field campaigns in the region encounter numerous challenges including the harsh polar climate, steep topography, and high infrastructure costs. Additionally, field campaigns are often limited in terms of spatial and temporal resolution, and particularly, the topographical challenges presented in the Antarctic mean that many areas remain inaccessible. For example, despite more than 50 years of geological mapping on the Antarctic Peninsula, there are still large gaps in coverage, owing to the difficulties in undertaking geological mapping in such an environment [1]. Hyperspectral imaging may provide a solution to overcome the difficulties associated with field mapping in the Antarctic.

Hyperspectral sensors acquire data from a contiguous spectrum over a defined wavelength interval, which makes it possible to identify surface materials by their characteristic reflectance or emittance spectrum, and can yield information on features such as abundance and composition, including ion substitution in minerals [2,3]. It is possible to produce maps of mineral composition and abundance from hyperspectral imagery without rigorous ground truth measurements, due to the development of spectral reflectance libraries (e.g., [4]). A variety of software packages are capable of applying advanced image processing algorithms to hyperspectral imagery using such spectral reflectance libraries, and thus allowing the end-user to produce mineral maps with relative ease. A comprehensive review of geologic remote sensing, including the use of hyperspectral data, is given by van der Meer *et al.* [5].

The reflectance spectrum of a material can, in principle, be recovered from the observed radiance spectrum over regions in which the illumination is non-zero [6]. The reflectance spectrum is independent of the illumination and provides the best opportunity to identify materials by comparison with reference libraries [6]. In the case of solar illumination (*i.e.*, irradiance from the sun), many environmental and atmospheric effects complicate the process of deconvolving reflectance spectra from the measured radiance, and complex radiative transfer models are required [6]. These models usually simulate the incoming solar irradiance, subsequent atmospheric effects and the final at-sensor radiance; the effects of the intervening atmosphere on the solar irradiation can then be accounted for and reflectance spectra derived. The accurate removal of atmospheric absorption and scattering is required to produce measures of surface reflectance; a process known as atmospheric correction [7]. Atmospheric correction is a common preprocessing step and use of an appropriate, thorough correction is of great significance for interpretation of hyperspectral imagery and any subsequent processing such as classification [8]. A variety of tools exist to perform atmospheric correction with radiative transfer models now mature

enough to be used as a routine part of hyperspectral image processing; a comprehensive review of atmospheric correction techniques, including techniques based on radiative transfer, is presented in [7].

In the early 1990s, the Atmosphere Removal Algorithm (ATREM) [9] was developed to employ radiative transfer equations and produce atmospherically corrected spectral data. Since the development of ATREM, several packages have also been developed for atmospherically correcting multi- and hyperspectral data, including High-accuracy ATmospheric Correction for Hyperspectral Data (HATCH) [10], Fast Line-of-Sight Atmospheric Analysis of Spectral Hypercubes (FLAASH) [11,12] and a series of Atmospheric and Topographic Correction (ATCOR) codes [13,14].

The series of ATCOR codes have been continually updated and developed throughout the 1990s and 2000s, with the latest ATCOR-4 release using a large database containing results of radiative transfer calculations based on the MODTRAN-5 [15] radiative transfer model. Additional techniques for correcting adjacency effects, 3D code for correction of topographic effects and bi-direction reflectance distribution function (BDRF) in addition to haze and low cirrus cloud removal are included [14].

The unique atmospheric conditions present in Antarctica combined with the first known hyperspectral data acquisition afford the opportunity to assess the applicability of standard radiative transfer modelling and atmospheric correction techniques for deriving surface reflectance. Previous studies that have carried out atmospheric correction in Antarctica have used multispectral airborne [16] and multispectral satellite data [1] applying radiative transfer modelling techniques to produce reflectance data. However, atmospheric correction of airborne hyperspectral data has not been investigated (due to the previous unavailability of airborne hyperspectral data). This study presents initial results from an investigation into the applicability of the MODTRAN-5 [15] radiative transfer model and the ATCOR-4 atmospheric correction package [14] for producing atmospherically corrected airborne hyperspectral data in the unique Antarctic environment.

2. Study Area

Rothera Point (Figure 1) was surveyed in February 2011, using the ITRES (ITRES Research Ltd., 110, 3553-31st Street NW, Calgary, AB, T2L 2K7, Canada) CASI-1500 and SASI-600 instruments acquiring data in the visible near-infrared (VNIR; 0.4–1.0 μm) and shortwave infrared (SWIR; 1–2.5 μm) portions of the electromagnetic spectrum. Sensor information is presented in Table 1. The acquisition system hardware and other equipment were installed into a British Antarctic Survey (BAS) DeHavilland Twin Otter aircraft. The imagers were installed onto a single mounting plate for concurrent imaging. This arrangement allowed for uniform recording of all aspects of aircraft motion relative to the two imagers with respect to the Inertial Measurement Unit (IMU). The Instrument Control Units (ICUs) were installed at the fore section of the aircraft. Six flight lines were required to acquire hyperspectral data of the study area, and during the acquisition of the imagery, three large (6 m $\times$ 6 m) calibration targets were placed within the study area; white, grey and black targets, provided by the Natural Environment Research Council (NERC) Field Spectroscopy Facility [17].

Figure 1. Location maps showing the context within Antarctica (**A**); the location of Adelaide Island within the Antarctic Peninsula (**B**) and the location of Rothera Point in the context of Adelaide Island (**C**; black dot).

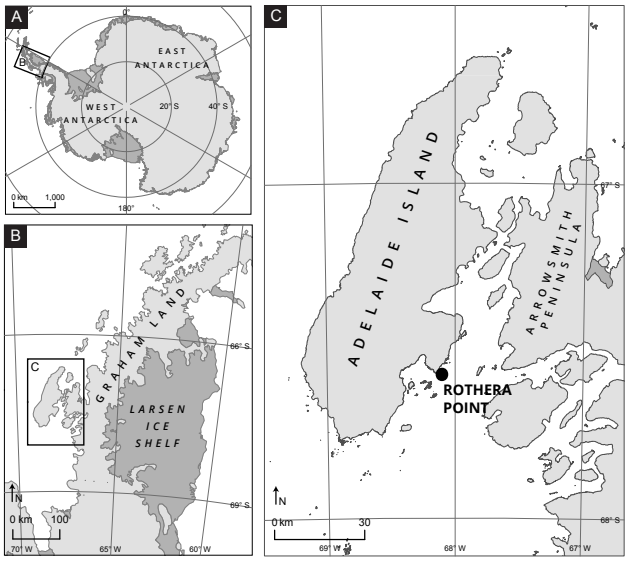

Table 1. Sensor acquisition information.

Instrument	Specification
CASI-1500	1500 across-track imaging pixels 72 spectral bands in 367.6–1055.5 nm Spectral bandwidth of 9.6 nm 40° field of view 0.5 m ground resolution
SASI-600	600 across-track imaging pixels 100 spectral bands in 950–2450 nm Spectral bandwidth of 15 nm 40° field of view 1 m ground resolution
Applanix POS/AV 510	3-axis SAGEM IMU Integrated dual frequency Trimble GPS receiver Real-time roll absolute accuracy (RMS): 0.008° Real-time pitch absolute accuracy (RMS): 0.008° Real-time heading absolute accuracy (RMS): 0.04°

Figure 2. CASI colour composite image mosaic of Rothera Point following radiometric and geometric correction, with inset showing the three calibration targets. Bands shown: Red: 650.2 nm, Green: 554.6 nm, Blue: 439.6 nm.

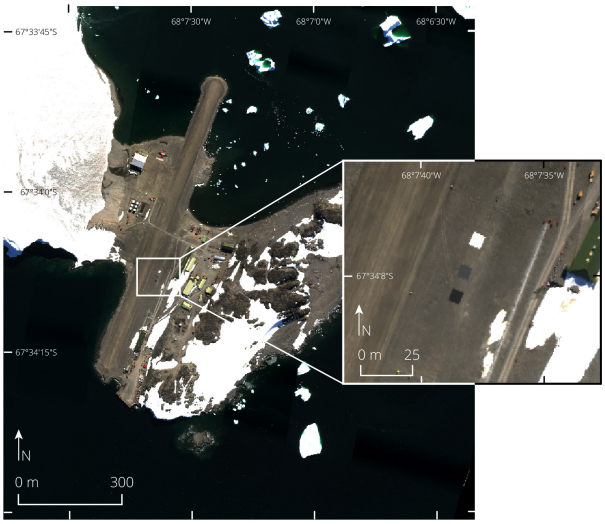

The spectral reflectance measurements of these calibration targets were acquired using an Analytical Spectral Devices (ASD) FieldSpec® Pro, which records continuous spectra across the 350–2500 nm wavelength region; the spectral resolution of the instrument was 3 nm at 700 nm, 10 nm at 1400 nm, and 12 nm at 2100 nm. Reflectance spectra were acquired in "White Reference" mode using a white Spectralon® panel as the reference target, measured at a nadir viewing angle with illumination provided by a tungsten halogen lamp at a 45° angle. Figure 2 shows a colour composite image of Rothera point showing the calibration targets.

3. Methods

3.1. Data Preprocessing

Standard preprocessing of hyperspectral data was carried out by ITRES to produce georeferenced and radiometrically corrected imagery. There are two major steps: Radiometric Correction and Geometric Correction, which were both carried out by ITRES' propriety tools. In the first step, radiometric and spectral calibration coefficients are applied to convert the raw digital numbers into spectral radiance values. Geometric correction utilizes measurements from the IMU and GPS to create a georeferenced mosaic image.

3.1.1. Radiometric Correction

The raw data are digitized at 14-bit resolution and are recorded as digital numbers (DN). The radiometric processing converted these digital numbers into spectral radiance values based upon calibration coefficient files, which were generated during laboratory calibration of the sensors. Due to the extreme operating conditions during acquisition (very cold temperatures), the image sensors were pushed to their limits and some anomalies were apparent in the image data, particularly in the SASI images. The SASI instrument's operating conditions were significantly different to the calibration conditions in the laboratory, hence scaling and spectral resampling adjustments, ranging from -5% to $+10\%$, were made to the calibration files to compensate for these environment effects and minimise the anomalies introduced as a result of the operating conditions.

3.1.2. Geometric Correction

After radiometric correction, the data was geometrically calibrated. The ITRES proprietary geometric correction software utilised the navigation solution, bundle adjustment parameters and Digital Elevation Models (DEMs) to produce georeferenced radiance image files for each flight line. In addition, flight lines were combined into an image mosaic of the area. The nearest neighbour algorithm was used to populate the image pixels so that radiometric integrity of the pixels could be preserved. At the image mosaicking stage, a minimised nadir angle approach was implemented such that the spectra of the pixel with the smallest off-nadir angle from overlapping adjacent flight lines was written to the final mosaic image.

3.1.3. Radiance Offset

The spectral range of the CASI and SASI data (Table 1) has an approximate 100 nm overlap, between 950 nm and 1055.5 nm. Preliminary investigations revealed an offset in radiance values within this overlap range. In the overlap range, CASI radiance values were found to be larger than the corresponding SASI radiance, with a trend of increasing radiance offset with increasing wavelength. This radiance offset is present in the radiometrically calibrated data. Several factors are likely to have produced the radiance offset.

The first and most probable contributing factor is second order light contributions. The CASI sensor's diffraction grating produces a second order diffraction spectrum, whose blue end overlaps with the red- near infrared (NIR) end of the first order spectrum. Illumination conditions at the time of acquisition may have allowed this effect to lead to additive background signal at the red-NIR end. The second contributing factor could be the reduced calibration accuracy in the NIR end of the spectrum, as the CASI sensor is less sensitive at the longest wavelengths.

Thirdly, preliminary investigations also revealed a systematic underestimation of radiance values in the SWIR (from the SASI instrument). This is attributed to the conditions during acquisition. The instruments were operating in an unpressurised aircraft, with temperatures significantly outside the normal operational range; the SASI instrument was as much as 20 °C (68 °F) outside its normal operating range. These conditions meant there was a noticeable degradation in the response of the sensor, and hence the measured at-sensor radiance was lower in the SWIR data.

3.2. Atmospheric Correction

The Antarctic has a distinct atmosphere, dominated by cold temperatures and unusual light conditions [18]. The atmosphere has stable stratification in the boundary layer, and is pristine, dry and isolated from the rest of the world's atmosphere by the polar vortex and the Southern Ocean [18]. To produce atmospherically corrected data, ATCOR-4 was used.

The at-sensor signal consists of three main components, as shown in Figure 3: scattered or path radiance L_1, reflectance radiance from the pixel under consideration L_2, and radiation reflected from the neighbourhood into the viewing direction (adjacency effect) L_3. Component L_2 is the only component that contains information on the surface properties of the pixel under consideration, therefore atmospheric correction aims to remove the L_1 and L_3 components. The atmospheric correction has to be performed iteratively to derive surface reflectance, ρ, for each pixel in the image data. The implementation is described in detail in Chapters 2 and 10 of [19] and in [14].

Figure 3. Schematic of the three solar radiation components in flat terrain and the pixel under consideration (ρ). Scattered or path radiance L_1, reflected radiance L_2, and radiation reflected from the local neighbourhood (adjacency effect) L_3.

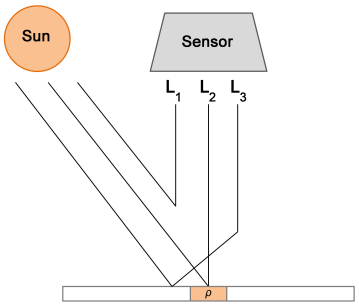

The MODTRAN-5 [15] radiative transfer model is used to generate Look-Up Tables (LUTs) that are used by ATCOR-4 to aid in the calculation of the L_n terms and the subsequent derivation of surface reflectance, ρ. The LUTs utilised by ATCOR-4 require significant computational effort to compute and are based on the "Mid-Latitude Summer" (MLS) profile [20]. LUTs are calculated using MODTRAN-5 with the scaled discrete ordinate radiance transfer (DISORT) option in regions where scattering is dominant and the more accurate correlated-k option in regions where absorption is dominant ([19], p. 154). ATCOR-4's LUTs were generated using the MLS profile and fixed water vapour contents of 0.4, 1, 2, 2.9, and 4 g/cm^2 (rather than the water vapour defined in the standard MLS model [20]). Water vapour is the main parameter that produces differences in radiance values and the other parameters are mostly stable [21]. This can be confirmed by simulating radiance values with each of the atmospheric profiles from [20] and fixed water vapour values in MODTRAN (*cf.* Figure 4). Full details of the algorithms applied by ATCOR-4 are detailed in [14,19]. The major processing phases of ATCOR-4 are outlined in Figure 5, "Preprocessing" and "Atmospheric Correction".

Figure 4. Radiance simulations using MODTRAN-5 with constant water vapour values and different atmospheric profiles.

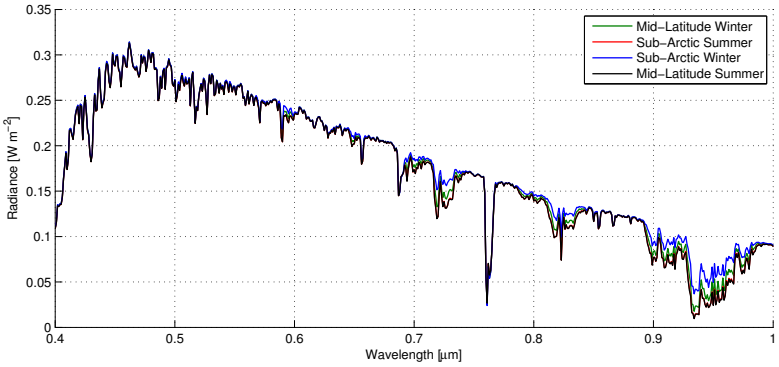

Figure 5. Overview of the major processing phases of ATCOR-4.

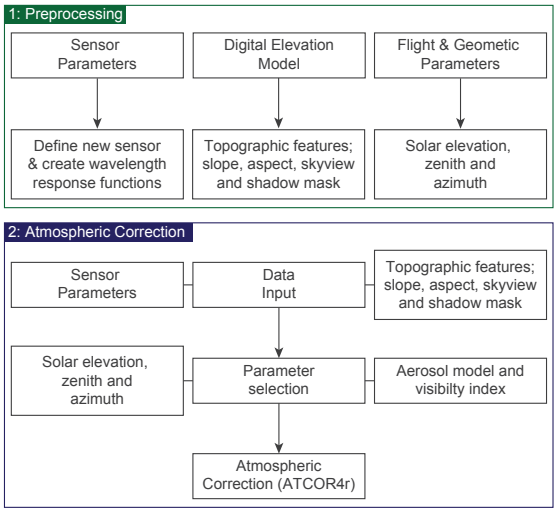

Standard input parameters (location, date and time) were used (Table 2). The other user-selectable parameters are the visibility, choice of aerosol model and choice of water vapour LUT. The visibility is measured hourly by the meteorologists at Rothera Point and the observation closest to data acquisition time was used. The maritime aerosol, interpolated to the flying height, was selected. Coincident meteorology data measured from a radiosonde launch at Rothera Point is shown in Figure 6 indicating the atmospheric conditions close to the time of image acquisition. Additionally, as implied by the measured

visibility (60 km), the operators' notes indicated that the "flight conditions were clear and calm, with blue skies and a few scattered clouds". With regards to water vapour, the LUT with a water vapour value of 2.0 g/cm^2 was selected. However, the choice of water vapour value is not significant because during processing water vapour is recalculated per-pixel; both the CASI-1500 and SASI-600 sensors have bands that lie within water vapour regions and thus the water vapour can be calculated from the image data (see Chapter 10.4.3 in [19] for further details on the water vapour retrieval algorithm).

Table 2. Geometry, flight and model parameters (AGL; Above Ground Level).

Parameter	Value
Date (DD/MM/YYYY)	07/02/2011
Time (HH:MM)	15:28 UTC
Solar Zenith (degrees)	53.8
Solar Azimuth (degrees)	23.6
Flight Heading (degrees)	76.1
Flight Altitude (m · AGL)	596.9
Visibility (km)	60
Atmospheric profile	MLS (2.0 g/cm^2)
Aerosol model	Maritime (597 m) [22]

Figure 6. Radiosonde data from 7 February 2011, launched at 11:38 UTC.

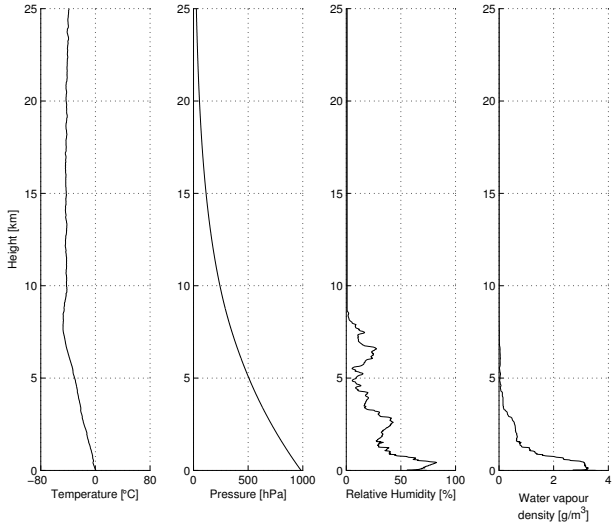

4. Results

The atmospheric correction results for each of the calibrated targets are presented in Figure 7. For the CASI data, there is a systematic overestimation in reflectance data for the grey and black targets. Between ∼0.86 µm and 1.1 µm there is a noticeable increase in reflectance (A) for the CASI data. This significant increase at the red–NIR end of the spectral range is likely a result of the second order light contribution from the blue end of the spectrum, resulting in additive background signal in the red–NIR end, therefore causing an increase in reflectance values. The SASI data shows a large systematic underestimation for the white target, but less so for the grey and black targets where results are close to or within the ±2% error margins.

Figure 7. Atmospheric correction results for the VNIR (CASI; blue) and SWIR (SASI; red) data (±2% error estimates are shaded grey) and laboratory spectra (LAB; black), for the three calibrated targets; white (**1**); grey (**2**); and black (**3**). Labels are discussed in the text. Root Mean Square Error (RMSE) values are shown for each target.

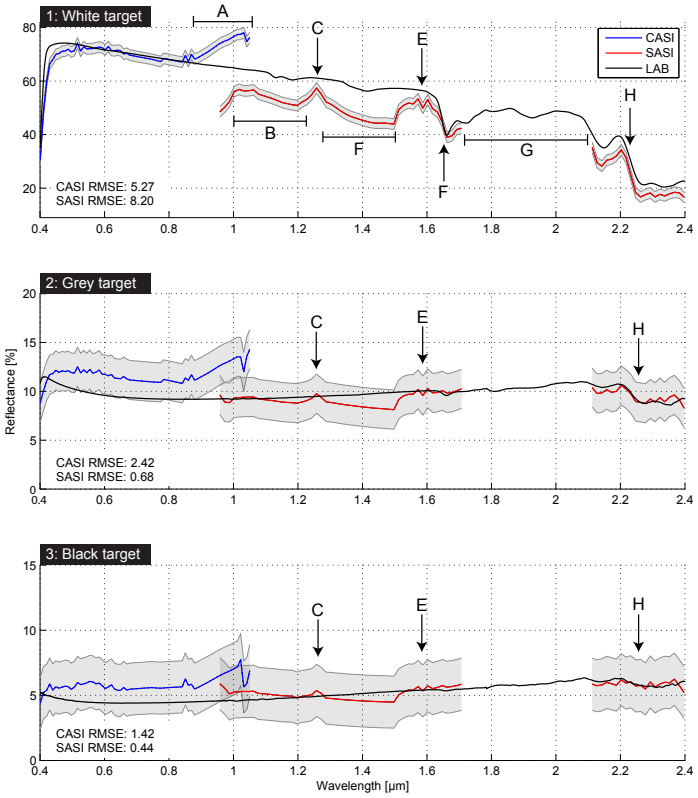

Numerous artefacts remain in the CASI and SASI data, most likely as a result of atmospheric gases and aerosols. The residual effects of water vapour (H_2O) are most noticeable; interpolation is carried out during the ATCOR-4 processing chain across areas of H_2O absorption from 1.0 µm to 1.2 µm (B), leaving a peak at 1.25 µm (C) and a secondary area of interpolation from ∼1.3 µm to 1.5 µm (D). A double peak is present at 1.6 µm due to CO_2 absorption (E). The absence of data between 1.7 µm and 2.1 µm (G) is due to the absorption by H_2O and CO_2, which reduces radiance transmission to almost zero in this portion of the spectrum. There are also some other minor artefacts, such as a double peak at 0.5 µm as a result of O_3 and a small peak at ∼0.85 µm likely a result of O_2.

In spite of these imperfections, two closely matched absorption features in the targets are found, the first at ∼1.65 µm (F) and the second at ∼2.2 µm (H).

5. Accuracies, Errors and Uncertainties

As discussed in Section 2, the instruments used for data acquisition were flown in an unpressurised BAS DeHavilland Twin Otter aircraft. This meant the instruments were subject to extreme changes in temperature between data acquisition and storage of the instruments in between flights, along with very cold operating conditions during data acquisition itself (up to 20 °C (68 °F) outside of the instrument's normal operating range). It was identified during the preprocessing of the data (Section 3.1) that the SASI instrument particularly suffered as a result of the heating and cooling cycles and the cold operating conditions it underwent during the data collection campaign in the Antarctic. As a result, during the radiometric correction of the SASI data (Section 3.1.1) larger adjustments were made to the calibration parameters to correct for the operating conditions in the Antarctic. This introduced some uncertainty in the data, which was observed in the raw data (Section 3.1.3) and is manifested in the atmospheric correction results (Section 4 and Figure 7) where the SASI data shows a systematic underestimation in reflectance values.

Following atmospheric correction, Root Mean Square Error (RMSE) values were calculated and are annotated on Figure 7. RMSE values were calculated from the ATCOR-4 results with respect to the laboratory measured spectra using Equation (1):

$$\text{RMSE} = \frac{1}{n}\sum_{i=1}^{n}(\hat{Y}_i - Y_i)^2 \tag{1}$$

where $\hat{Y}_i$ represents the ith predicted reflectance value (as calculated by ATCOR-4) and Y_i represents the ith laboratory measured reflectance value, where $n = 72$ for CASI and $n = 71$ for SASI. Whilst the SASI sensor measures 100 bands (Table 1), the actual number of usable bands is reduced to 71 (and hence $n = 71$), following the removal of the severely affected bands between between 1.7 µm and 2.1 µm (G), which are severely affected due to the absorption by H_2O and CO_2.

The atmospheric correction approach presented here is subject to uncertainties introduced through the application of the MODTRAN-5 standard atmospheric profiles and aerosol models [20,22]. Namely, these climatologically developed profiles are assumed to represent the true atmospheric conditions at the time of data acquisition. Radiosonde measurements were acquired from the same day (Figure 6), but there was a 4 hour difference between the radiosonde launch (11:38 UTC) and data acquisition (∼15:30 UTC). The variability and local scale differences in the atmosphere (e.g., [23]) mean that, even over this

relatively short time scale, applying the measured atmospheric parameters from the radiosonde launch would not necessarily be any more valid than applying the atmospheric profile from the MODTRAN-5 model; both methods are applying a profile with the assumption that it represents the true atmosphere at the time of data acquisition, thereby introducing uncertainty in the results.

These uncertainties could be removed by measuring the actual *in situ* atmospheric conditions using other instruments simultaneously whilst acquiring the image data. However, in this study, as is the case in most other studies applying similar techniques, simultaneous atmospheric measurements are unavailable. Despite making assumptions about atmospheric profiles and introducing uncertainties, the radiative transfer model and atmospheric correction approach has been applied successfully. As long as appropriate error metrics are calculated (e.g., RMSE) and the data is carefully applied in additional processing (e.g., spectral mapping) then these uncertainties can be managed and minimised throughout the entire processing chain.

6. Discussion

The atmospheric correction processing chain and results presented here represent the first known acquisition and subsequent processing of hyperspectral data in Antarctica. The presence of ground targets along with concurrent ground and atmospheric measurements in this study is typical of most hyperspectral campaigns; often there are not sufficient measurements to fully develop atmospheric profiles and aerosol models (to use as inputs to radiative transfer models), hence estimates are made and often standard atmospheric profiles and aerosol profiles are selected based on qualitative assessment of environmental conditions. Additionally, there are not always a large enough number of ground-based targets with the relevant concurrent spectral data to be used for both calibration and validation. The MODTRAN-5 LUTs used by ATCOR-4 were intended to be flexible enough to cover a wide variety of environments, sensor configurations, water vapour contents and flight parameters but have not been previously tested for airborne hyperspectral data in the Antarctic region.

Following the application of the atmospheric correction processing chain, the results showed that workable reflectance data is obtainable. This is obtainable in spite of limited concurrent atmospheric and aerosol measurements combined with assumptions about aerosol model parameters (for example, the maritime aerosol model was selected based on qualitative interpretations of the Antarctic environment), which is an often typical scenario. As there are no aerosol measurements collected at Rothera, the maritime aerosol model [22] was selected based on the qualitative assessment of the atmospheric conditions and the assumption of a dominance of sea salt aerosols in the coastal Antarctic environment (e.g., compare [24]). For the lower reflectance targets ($<$20%), the results from the both VNIR (CASI-1500) and SWIR (SASI-600) sensors fell within the expected $\pm$2% margins; however, this is likely an artefact of the low signal-to-noise ratio ($<$15:1) for low reflectance targets. The higher reflectance target (the white target) shows clear discrepancies, with absolute reflectance values differing by as much as 30%. The white target is perhaps more representative of the overall performance of the atmospheric correction due to its higher signal-to-noise ratio.

Despite the discrepancies between absolute reflectance values, absorption features for the white target (e.g., 1.65 µm and 2.25 µm) are clearly discerned; similar absorption features in the lower reflectance

(grey and black) targets also correlate well between the laboratory-measured and atmospherically corrected reflectance data. There is still residual noise manifested as small peaks and spikes in the reflectance data, which could complicate post-processing procedures, particularly those that rely on relative differences between peaks and troughs in spectra. The residual noise manifested in peaks and spikes are most likely due to the unavailability of an Antarctic-specific atmospheric profile and aerosol model, due the lack of adequate *in situ* measurements. Additionally, portions of the spectrum that are strongly affected by water vapour (e.g., the interpolation from 1.3 µm to 1.5 µm, and the lack of data between 1.7 µm and 2.1 µm) prove difficult to characterise; a finding that supports the conclusions of Zibordi and Maracci [16] who noted that uncertainties in calculating water vapour optical thickness could lead to "very significant error" ([16], p. 20).

These results suggest that commercially available atmospheric correction packages are flexible enough to produce working reflectance data in Antarctica. Performance is poorer with higher reflectance targets, though results fall within the expected error margins for lower reflectance targets. The ability to discriminate absorption features suggests that the atmospheric correction process would produce reflectance data capable of being applied in mapping techniques using absorption features (e.g., continuum removal). Particular care would have to be given when working with absolute reflectance values.

It is recommended that, given the availability of a greater number of ground targets (>3), a hybrid approach of radiative transfer modelling followed by the Empirical Line Method (ELM) [25] be applied for potentially improved results; for example Tuominen and Lipping [26] reported a reduction in Root Mean Square Error (RMSE) from 6.8% to 1.8% when combining the hybrid approach of radiative transfer modelling through ATCOR-4 and the ELM, compared with radiative transfer modelling alone. Therefore, following the conclusions of Tuominen and Lipping [26], it can be seen that even in complex atmospheres where model-based correction methods may struggle, more accurate results can be produced using combined correction methods compared with model- or empirical-based methods alone. It was also noted that even in situations when there is a limited number of spectral ground truth measurements, a hybrid approach can improve atmospheric correction accuracy over the whole acquisition area [26].

This approach was successfully applied to Advanced Spaceborne Thermal Emission and Reflection Radiometer (ASTER) VNIR/SWIR data by Haselwimmer *et al.* [1], who utilised the hybrid approach combining the FLAASH radiative transfer model [11,12] and an empirical correction. Haselwimmer *et al.* [1] utilised spectral measurements of the runway at Rothera Point assuming that the runway is a Pseudo-Invariant Feature (PIF) [27,28]. PIFs are large uniform targets whose spectral reflectance is assumed not to have changed over time [28]. In cases where appropriate PIFs have been identified and measured, they can provide a suitable ground truth feature for calibration or validation. PIFs can be used either as a substitute for or in conjunction with calibrated targets (such as those used in this study) to provide enough targets (>3) for the hybrid approach of radiative transfer modelling followed by empirical line correction. The identification of suitable PIFs in the Antarctic generally, and particularly in the regions where the airborne hyperspectral data was acquired, remains an area of on-going investigation. If a suitable number of targets are identified, the need for deploying calibrated

targets during image acquisition may be negated, as PIFs may allow for both calibration and validation of atmospheric correction methods.

It must also be noted that sensor calibration still remains challenging in this environment and these issues are manifested in the subsequent atmospheric correction process. Particularly notable effects of this can be observed in Figure 7, such as the offset between VNIR and SWIR (CASI and SASI) sensor values in the overlapping region (0.95 μm to 1.05 μm), as well as the significant underestimation of reflectance for the white target for the SWIR (SASI) data.

Future studies should consider the influence of radiative transfer models' standard atmospheric profiles [20] and aerosol model types [22] with a view to measuring *in situ* atmospheric data while simultaneously acquiring hyperspectral data; this would aid in the generation of atmospheric profiles and aerosol models that serve as inputs during the atmospheric correction process and reduce the level of uncertainty when assumed profiles are used. Such atmospheric data could also lead to the development of a generic "Antarctic" atmospheric profile and aerosol model, which may prove useful for future data acquisition (where measuring *in situ* atmospheric data is not possible).

7. Conclusions

This study has presented results from atmospheric correction of airborne hyperspectral data in Antarctica. The findings are significant as they represent (a) the first known acquisition and preprocessing of airborne hyperspectral data in Antarctica, and (b) the first assessment of atmospheric correction techniques applied to airborne hyperspectral data in Antarctica. The atmospheric correction technique utilised a radiative transfer model (MODTRAN-5) [15] in the Atmospheric and Topographic Correction version 4 package (ATCOR-4) [14].

Two sensors, imaging the visible near-infrared (VNIR; 0.4–1.0 μm) and shortwave infrared (SWIR; 1–2.5 μm), were deployed during the data acquisition. During the radiometric correction (preprocessing) of the data it was found that, as a result of the extreme temperature variations during the data collection, the SWIR sensor had decreased sensitivity, resulting in lower measured radiance values and systematic underestimation in reflectance values following atmospheric correction. The results from atmospheric correction revealed that obtaining surface reflectance of airborne hyperspectral data in the Antarctic is possible without *in situ* measurements of atmospheric parameters; reflectance data had maximal Root Mean Square Error (RMSE) values of 5% in the VNIR and 8% in the SWIR. However, residual noise remains present in the reflectance data as a result of using standard atmospheric profiles and aerosol models during the atmospheric correction process.

For future campaigns in Antarctica, it is recommended that instruments be sufficiently tested and calibrated to operate successfully in cold environments, with particular attention given to imagers operating in the SWIR. During acquisition it is recommended that (a) *in situ* atmospheric data be measured simultaneously whilst acquiring hyperspectral data to produce robust atmospheric and aerosol profiles that can be applied during the atmospheric correction process, and (b) ground truth data, such as calibrated targets or pseudo-invariant features, be present to allow for the validation of atmospheric correction results, as well as calibration of reflectance data using empirical correction techniques (if a sufficient number of ground targets allow, *i.e.*, >3).

Acknowledgements

The Hyperspectral Data used was collected during an airborne survey funded by the UK Foreign and Commonwealth Office (FCO) and conducted by the British Antarctic Survey, ITRES Research Ltd. and Defence Research & Development Suffield, Canada in February 2011. Loans for the calibrated targets and associated laboratory spectra were provided by the Natural Environment Research Council (NERC) Field Spectroscopy Facility. MB is funded by a Natural Environment Research Council (NERC) PhD studentship in conjunction with the British Antarctic Survey and the University of Hull (NERC Grant: NE/K50094X/1). Anonymous reviewers are thanked for their comments on earlier versions of the manuscript.

Author Contributions

Martin Black is the main author who performed the atmospheric correction and wrote the draft version of the manuscript. Andrew Fleming, Stephen Achal and John McFee were involved in the data acquisition. Stephen Achal and Alejendra Umana Diaz were responsible for the data preprocessing. Andrew Fleming, Peter Fretwell, Graham Ferrier and Teal Riley supervised and participated with the work throughout all phases. All authors provided assistance in writing, editing and organising the manuscript.

Conflicts of Interest

The authors declare no conflicts of interest.

References

1. Haselwimmer, C.E.; Riley, T.R.; Liu, J.G. Assessing the potential of multispectral remote sensing for lithological mapping on the Antarctic Peninsula: Case study from eastern Adelaide Island, Graham Land. *Antarct. Sci.* **2010**, *22*, 299–318.
2. Clark, R.N. Spectroscopy of Rocks and Minerals, and Principles of Spectroscopy; In *Manual of Remote Sensing*; Rencz, A.N., Ed.; John Wiley and Sons: New York, NY, USA, 1999; pp. 3–58.
3. Drury, S.A. *Image Interpretation in Geology*; Blackwell Science: Oxford, UK, 2001; p. 209.
4. Baldridge, A.; Hook, S.; Grove, C.; Rivera, G. The ASTER spectral library version 2.0. *Remote Sens. Environ.* **2009**, *113*, 711–715.
5. Van der Meer, F.D.; van der Werff, H.M.; van Ruitenbeek, F.J.; Hecker, C.A.; Bakker, W.H.; Noomen, M.F.; van der Meijde, M.; Carranza, E.J.M.; de Smeth, J.B.; Woldai, T. Multi- and hyperspectral geologic remote sensing: A review. *Int. J. Appl. Earth Obs. Geoinfor.* **2012**, *14*, 112–128.
6. Shaw, G.A.; Burke, H.H.K. Spectral imaging for remote sensing. *Linc. Lab. J.* **2003**, *14*, 3–28.
7. Gao, B.C.; Montes, M.J.; Davis, C.O.; Goetz, A.F. Atmospheric correction algorithms for hyperspectral remote sensing data of land and ocean. *Remote Sens. Environ.* **2009**, doi:10.1016/j.rse.2007.12.015.

8. Mahiny, A.S.; Turner, B.J. A comparison of four common atmospheric correction methods. *Photogramm. Eng. Remote Sens.* **2007**, *73*, 361–368.
9. Gao, B.C.; Heidebrecht, K.B.; Goetz, A.F. Derivation of scaled surface reflectances from AVIRIS data. *Remote Sens. Environ.* **1993**, *44*, 165–178.
10. Qu, Z.; Kindel, B.; Goetz, A.F.H. The High Accuracy Atmospheric Correction for Hyperspectral Data (HATCH) model. *IEEE Trans. Geosci. Remote Sens.* **2003**, *41*, 1223–1231.
11. Matthew, M.; Adler-Golden, S.; Berk, A.; Felde, G.; Anderson, G.; Gorodetzky, D.; Paswaters, S.; Shippert, M. Atmospheric Correction of Spectral Imagery: Evaluation of the FLAASH Algorithm with AVIRIS Data. In Proceedings of the 31st Applied Imagery Pattern Recognition Workshop, Washington, DC, USA, 16–18 October 2002; pp. 157–163.
12. Alder-Golden, S.; Berk, A.; Bernstein, L.S.; Richtsmeier, S.; Acharya, P.K.; Matthew, M.W.; Anderson, G.P.; Allred, C.L.; Jeong, L.S.; Chetwynd, J. H. FLAASH, a MODTRAN4 Atmospheric Correction Package for Hyperspectral Data Retrievals and Simulations. In Proceedings of the 7th JPL AVIRIS Airborne Earth Science Workshop, Pasadena, CA, USA, 11–12 January 1998; p. 6.
13. Schläpfer, D.; Richter, R. Geo-atmospheric processing of airborne imaging spectrometry data. Part 1: Parametric orthorectification. *Int. J. Remote Sens.* **2002**, *23*, 2609–2630.
14. Richter, R.; Schläpfer, D. Geo-atmospheric processing of airborne imaging spectrometry data. Part 2: Atmospheric/topographic correction. *Int. J. Remote Sens.* **2002**, *23*, 2631–2649.
15. Berk, A.; Anderson, G.P.; Acharya, P.K.; Bernstein, L.S.; Muratov, L.; Lee, J.; Fox, M.J.; Adler-Golden, S.M.; Chetwynd, J.H.; Hoke, M.L.; *et al*. MODTRAN5: A reformulated atmospheric band model with auxiliary species and practical multiple scattering options. *Proc. SPIE* **2005**, doi:10.1117/12.578758.
16. Zibordi, G.; Maracci, G. Reflectance of antarctic surfaces from multispectral radiometers: The correction of atmospheric effects. *Remote Sens. Environ.* **1993**, *43*, 11–21.
17. NERC Field Spectroscopy Facility. Available online: http://www.fsf.nerc.ac.uk (accessed on 7 January 2014).
18. Simpson, W.R.; von Glasow, R.; Riedel, K.; Anderson, P.; Ariya, P.; Bottenheim, J.; Burrows, J.; Carpenter, L.J.; Frieß, U.; Goodsite, M.E.; *et al*. Halogens and their role in polar boundary-layer ozone depletion. *Atmos. Chem. Phys.* **2007**, *7*, 4375–4418.
19. Richter, R.; Schläpfer, D. *Atmospheric/Topographic Correction for Airborne Imagery, ATCOR-4 User Guide, Version 6.2.1. DLR-IB 565-02/08*; Deutsches Zentrum für Luft- und Raumfahrt (DLR): Weßling, Germany, 2014; p. 225.
20. McClatchey, R.A.; Fenn, R.; Selby, J.A.; Volz, F.; Garing, J. *Optical Properties of the Atmosphere*; Technical Report AFCRL-72-0497; Environmental Research Paper Air Force Geophysics Lab, Optical Physics Division, Hanscom AFB: Boston, MA, USA, 1972.
21. Schläpfer, D. (ReSe Applications Schläpfer, Langeggweg 3, CH-9500, Wil, Switzerland). Personal communication, 2013.

22. Shettle, E.; Fenn, R. *Models for the Aerosols of the Lower Atmosphere and the Effects of Humidity Variations on Their Optical Properties*; Technical Report AFGL-TR-79-0214; Environmental Research Paper Air Force Geophysics Lab, Optical Physics Division, Hanscom AFB: Boston, MA, USA, 1979.
23. Harangozo, S.A.; Colwell, S.R.; King, J.C. An analysis of a 34-year air temperature record from Fossil Bluff (71S, 68W), Antarctica. *Antarct. Sci.* **1997**, *9*, 355–363.
24. Rankin, A.M.; Wolff, E.W. A year-long record of size-segregated aerosol composition at Halley, Antarctica. *J. Geophys. Res.: Atmos.* **2003**, *108*, 1–6.
25. Smith, G.M.; Milton, E.J. The use of the empirical line method to calibrate remotely sensed data to reflectance. *Int. J. Remote Sens.* **1999**, *20*, 2653–2662.
26. Tuominen, J.; Lipping, T. Atmospheric Correction of Hyperspectral Data Using Combined Empirical and Model Based Method. In Proceedings of the 7th European Association of Remote Sensing Laboratories SIG-Imaging Spectroscopy Workshop, Edinburgh, Scotland, UK, 11–13 April 2011.
27. Freemantle, J.; Pu, R.; Miller, J. Calibration of Imaging Spectrometer Data to Reflectance Using Pseudo-Invariant Features. In Proceedings of the 15th Canadian Symposium on Remote Sensing, Toronto, ON, Canada, 1–4 June 1992; pp. 1–4.
28. Philpot, W.; Ansty, T. Analytical Description of Pseudo-Invariant Features (PIFs). In Proceedings of the 6th International Workshop on the Analysis of Multi-temporal Remote Sensing Images (Multi-Temp), Trento, Italy, 12–14 July 2011; pp. 53–56.

High resolution mapping of Antarctic vegetation communities using airborne hyperspectral data

Martin Black[1,2*], Paula Casanovas[1], Peter Convey[1], and Peter Fretwell[1]

[1]*British Antarctic Survey, High Cross, Madingley Road, Cambridge, CB3 0ET, UK*
[2]*Department of Geography, Environment and Earth Sciences, University of Hull, Hull, HU6 7RX*

*Corresponding author. Email: martin.black@bas.ac.uk

Summary

The Antarctic Peninsula (AP) is one of the most rapidly changing environments on the planet; mean annual air temperatures have increased by ~3 ºC in the last 50 years. This climatic change has led to longer summers and higher summer-growing season temperatures and, coupled with local glacial retreat, new bare-ground is exposed for colonisation by pioneering vegetation communities. Due to the exceptional rates of environmental change the AP has been considered globally important in identifying the biological consequences of climate change. To monitor and assess changes of AP vegetation, a robust, quantitative assessment of vegetation is required. Previous studies have applied standard techniques, such as the Normalised Difference Vegetation Index (NDVI) to satellite data from the AP. Because the reflectance spectra of lichens, the dominant and most diverse component of the AP flora, differs from vascular plants in both the visible and near infra-red portion of the spectrum, any work using NDVI for the detection of vegetation might overlook the presence of lichens. This study presents a new spectral filtering technique which was applied to an airborne hyperspectral dataset to produce a high resolution map of vegetated areas from a test site on the AP.

1 Introduction

The Antarctic Peninsula (AP) has seen an increase in mean annual air temperature of ~3ºC in the last 50 years (Vaughan *et al*., 2003), making it one of the most rapidly changing areas on the planet. The changing climate as a result of rising temperatures, has led to higher summer-growing season temperatures (Convey and Smith, 2006) and as a result of local glacial retreat (Pritchard and Vaughan, 2007) new rock outcrops and areas of scree and soil are exposed for colonisation by terrestrial biota (Walther *et* al., 2002; Convey and Smith, 2006). Due to these exceptional rates of change the AP has been highlighted as a globally important barometer for identifying the biological consequences of climate change (Convey, 2003). To monitor and assess changes of AP vegetation, a robust, quantitative assessment of vegetation is required (Fretwell *et al.*, 2011). Field based techniques in the Antarctic incur significant logistical challenges as a result of the climate and topography in addition to the limited spatial coverage and invasive nature of the work. A non-invasive, remote sensing approach provides many advantages over field based techniques. Previous work using satellite remote sensing has shown that traditional approaches such as the Normalised Difference Vegetation Index (NDVI; Rouse *et al*., 1974) are difficult to apply in the Antarctic (Fretwell *et al*., 2011). It has already been recognized that any work using NDVI for the detection of vegetation might

overlook the presence of lichens even if their land cover is extensive (Petzold and Goward, 1988). The reflectance spectra of lichens and vascular plants are different in both, the visible near infrared (VNIR; 0.4 - 1 µm) and shortwave infrared (SWIR; 1 - 2.5µm) portion of the solar spectrum; in particular the depth of the visible – near-infrared step is characteristically smaller in lichens (Petzold and Goward, 1988; Haselwimmer and Fretwell, 2009). In the AP, where lichen contribution to vegetation diversity and extent increases in importance, NDVI would show decreasing spectral vegetation values, and areas completely covered with lichens could be erroneously classified as having sparse cover of vascular plants (Petzold and Goward, 1988).

High resolution airborne hyperspectral imagery has been widely used for a variety of applications, including vegetation monitoring, but has not yet been assessed in the Antarctic. The British Antarctic Survey and partners collected the first known airborne hyperspectral dataset over the Antarctic in February 2011. The simultaneous deployment of commercially available VNIR and SWIR spectrometers generated a dataset covering the 0.35 to 2.5 µm spectral range at a spectral resolution of 9.6-14 nm. This study presents results from high resolution mapping of Antarctic vegetation communities using this unique airborne hyperspectral dataset from a study area on the AP. Results from a new lichen matched filter technique are compared to the traditional NDVI approach.

2 Study Area

Lagoon and Kirsty Island (67^{o} 35' S, 68^{o} 16' W; Figure 1), in the Ryder Bay area of Antarctica, were surveyed in February 2011 acquiring hyperspectral imagery from multiple imaging spectrometers supplied by ITRES Research Ltd. (ITRES Research Ltd., 110, 3553-31st Street NW, Calgary, AB, T2L 2K7, Canada)

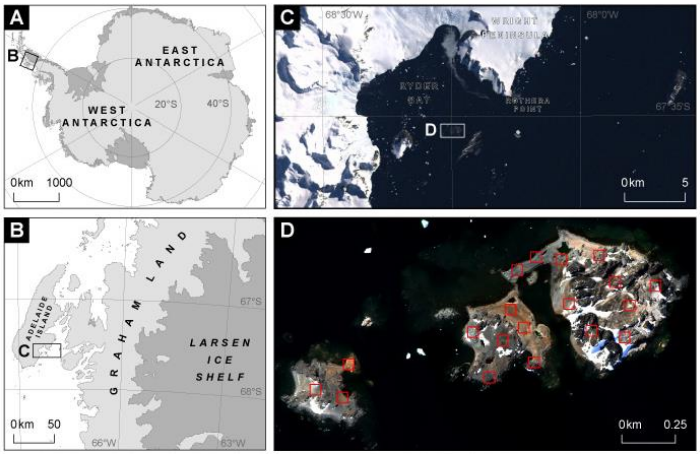

Figure 1. (A) the context of Adelaide Island within Antarctica; (B) The context of the Ryder Bay area within the Antarctic Peninsula; (C) the Ryder Bay area (with a Landsat colour image) showing extent of the hyperspectral area (Box labelled D); (D) hyperspectral colour composite image of Kirsty Island (Left) and Lagoon Island (Right) with areas visited during the field campaign shown in red squares.

3 Methodology

3.1 Data

Airborne hyperspectral data were collected from the ITRES Research Ltd. CASI-1500 and SASI-600 imaging spectrometers, with a total of 172 bands imaging from 0.4 to 2.5 µm. The imagery was geometrically and radiometrically corrected, followed by atmospheric correction using a radiative transfer modelling approach (see Black *et al*., 2014 for full details). The imagery was masked to removed surface and sea water along with snow/ice areas following the steps outlined by Harris and Rogge (2005).

The collection of lichen spectra from Lagoon and Kirsty Island was carried out using an Analytical Spectral Devices (ASD) FieldSpec Pro 3® spectrometer during a field campaign in January 2014. The ASD spectrometer records continuous spectra across the 0.3 to 2.5 µm spectral range. A total of 19 field stations were sampled (Figure 1), with spectral measurements derived from a 10 m^2 region. The presence of vegetation was confirmed at 17 of the 19 field stations.

3.2 Image Processing

Normalised Difference Vegetation Index (NDVI) was calculated using equation (1) (after Rouse *et al*., 1974)

$$NDVI = \frac{(NIR - VIS)}{(NIR + VIS)} \quad (1)$$

where *NIR* and *VIS* represent the spectral reflectance measurements acquired in the visible (~0.6 µm) and near-infrared (~0.8 µm) regions, respectively. The narrow spectral bands from the hyperspectral CASI imagery at 0.67 µm (*VIS*) and 0.8 µm (*NIR*) were used to calculate the NDVI (Haboudane *et al*., 2004).

We performed matched filtering (c.f. Harris and Rogge, 2005) using the lichen spectra of *Buellia* sp. collected in the field. It has been shown that a single lichen endmember can account for lichen contribution if normalisation is applied (Zhang *et al.*, 2005). As ground truthing, we used 17 of the 19 sites (10 x 10 m each) for which the presence of lichens was confirmed in the field (Figure 2). We compared the areas where the lichen filter showed presence of lichens and areas where NDVI values were greater than 0.2 (indicating that the presence of vegetation is almost certain; Fretwell *et al*., 2011).

4 Results

The matched filter successfully detected the presence of lichens at 95% of the field sites (16 of 17), whereas the NDVI only detected vegetation at 53% (9 of 17) of the sites.

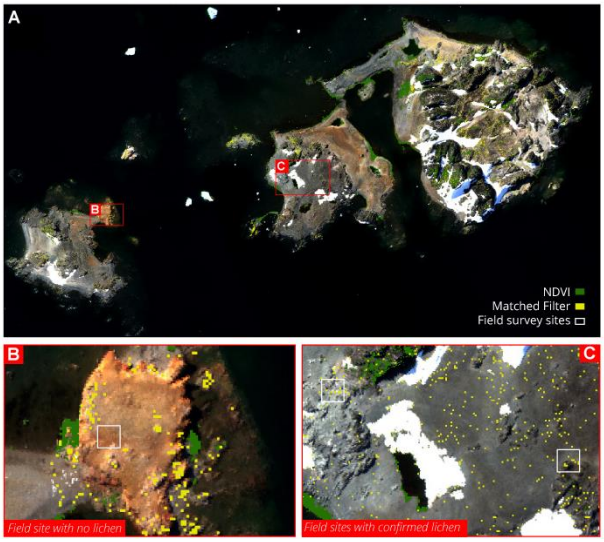

Figure 3. (A) Lagoon and Kirsty Island image with results from the matched filter (yellow) and NDVI (green) overlain; (B) inset showing a close up of Kirsty Island, where the white box indicates a field site without lichen presence; (C) inset showing a close up of western Lagoon island with field sites with confirmed lichen presence shown in white squares.

5 Discussion and Conclusions

Our data confirm that the use of a matched filtering technique allows for the detection of lichen flora in the Antarctic Peninsula, showing a considerable improvement over NDVI for the mapping of flora in this area. Our results highlight the importance of using techniques other than NDVI thresholds for the detection and mapping of vegetation in areas where lichens (and likely other non-vascular plants) are the main component of the communities; as is typical in high latitudes and high altitude environments. It has been proposed that NDVI thresholds are not the best technique for mapping distribution of lichens from remote sensing imagery (Petzold and Goward 1988, Haselwimmer and Fretwell 2009). However, this is the first study to compare NDVI threshold detection with an alternative technique for lichens in the Antarctic, and proposes a new methodology for mapping lichen distribution in the AP.

The results presented here suggest that studies based on the spectrum of only one species of lichen might be sufficient for the accurate mapping of lichen habitats in this environment, consistent with Petzold and Goward's (1988) study. The same technique proposed here could be applied in the future to intermediate spectral and spatial resolution imagery. Images of intermediate spectral and spatial resolution will be available in the future from planned satellite launches (e.g. WorldView-3, HyspIRI, Sentinel-2, EnMAP), and they will be of great importance in the study of vegetation in Polar Regions.

6 Acknowledgements

Hyperspectral Data used were collected during an airborne survey funded by the UK Foreign and Commonwealth Office and conducted by the British Antarctic Survey, ITRES Research Ltd. (http://www.itres.com) and Defence Research & Development Suffield, Canada (http://www.drdc-rddc.gc.ca) in February 2011. M Black is funded by a Natural Environment Research Council (NERC) PhD studentship in conjunction with the British Antarctic Survey and the University of Hull (NERC Grant: NE/K50094X/1). Fieldwork was supported by an Antarctic Funding Initiative CGS grant (CGS-086) and a spectrometer loan from the NERC Field Spectroscopy Facility (FSF Loan No.: 675.0613). P Casanovas was supported by the SCAR fellowship scheme 2013-14.

References

BLACK, M., FLEMING, A., RILEY, T., FERRIER, G., FRETWELL, P., MCFEE, J., ACHAL, S. & DIAZ, A.U. (2014). On the Atmospheric Correction of Antarctic Airborne Hyperspectral Data. *Remote Sensing*, **6**:4498–4514.

CONVEY, P. (2003). Maritime Antarctic Climate change: signals from terrestrial biology. In: Domack, E., Burnett, A., Leventer, A., Convey, P., Kirby, M., and Bindschadler, R. (eds), *Antarctic Peninsula climate variability: historical and palaeo-enivironmental perspectives. Antarctic Research Series, volume 79*. American Geophysical Union, Washington DC, USA.

CONVEY, P. and SMITH R. I. L. (1997) The terrestrial arthropod fauna and its habitats in northern Marguerite Bay and Alexander Island, maritime Antarctic. *Antarctic Science* **9:**12–26.

CONVEY, P. and SMITH, R.I.L. (2006). Responses of Antarctic ecosystems to climate change. *Planetary Ecology* **182**:1-10.

FRETWELL, P. T., CONVEY, P., FLEMING, A. H., PEAT, H. J., & HUGHES, K. A. (2011). Detecting and mapping vegetation distribution on the Antarctic Peninsula from remote sensing data. *Polar Biology*, **34**(2):273–281. doi:10.1007/s00300-010-0880-2

HABOUDANE, D., MILLER, J.R., PATTEY, E., ZARCO-TEJADA, P.J., STRACHAN, I.B. (2004). Hyperspectral vegetation indices and novel algorithms for predicting green LAI of crop canopies: Modeling and validation in the context of precision agriculture, *Remote Sensing of Environment*, **90**(3):337-352, doi:10.1016/j.rse.2003.12.013.

HARRIS, J., & ROGGE, D. (2005). Mapping lithology in Canada's Arctic: application of hyperspectral data using the minimum noise fraction transformation and matched filtering. *Canadian Journal of Remote Sensing*, **2193**(2005):2173–2193. doi:10.1139/E05-064

HASELWIMMER, C. and FRETWELL P. (2009) Field reflectance spectroscopy of sparse vegetation cover on the Antarctic Peninsula. Pages 1–4 First Workshop on Hyperspectral Image and Signal Processing: Evolution in Remote Sensing, 2009. WHISPERS '09.

PETZOLD, D. E. and GOWARD S. N. (1988). Reflectance spectra of subarctic lichens, *Remote Sensing of Environment* **24**:481–492.

PRITCHARD, H.D., and VAUGHAN, D.G. (2007). Widespread acceleration of tidewater glaciers on the Antarctic Peninsula. *Journal of Geophysical Research*, **112**, F3-F03S29.

ROUSE, J.W., HAAS, R.H., SCHELL, J.A., DEERING, D.W., HARLAN, J.C. (1974). *Monitoring the vernal advancements and retrogradation of natural vegetation*. NASA/GSFC, Final Report, Greenbelt, MD, USA (1974):1–137

VAUGHAN, D.G., MARSHALL, G.J., CONNELLY, W.M., PARKINSON, C., MULVANEY, R., HODGSON, D.A., KING, J.C., PUDSEY, C.J., and TURNER, J. (2003). Recent rapid regional climate warming on the Antarctic Peninsula. *Climate Change* **60**:243-274.

WALTHER, G.-R., POST, E., CONVEY, P., PARMESAN, C., MENZEL, M., BEEBEE, T.J.C., FROMENTIN, J.-M., HOEGH-GULDBERG, O. & BAIRLEIN, F. (2002). Ecological responses to recent climate change. *Nature* **416:**389-395.

ZHANG, J., B. RIVARD, and A. SANCHEZ-AZOFEIFA (2005) Spectral unmixing of normalized reflectance data for the deconvolution of lichen and rock mixtures, *Remote Sensing of Environment* **95:**57–66.

Polar Research

RESEARCH/REVIEW ARTICLE

Mapping lichen distribution on the Antarctic Peninsula using remote sensing, lichen spectra and photographic documentation by citizen scientists

Paula Casanovas, Martin Black, Peter Fretwell & Peter Convey

British Antarctic Survey, Natural Environment Research Council, High Cross, Madingley Road, Cambridge CB3 0ET, UK

Keywords
Antarctica; NDVI; matched filtering; Landsat; remote sensing.

Correspondence
Peter Convey, British Antarctic Survey, Natural Environment Research Council, High Cross, Madingley Road, Cambridge CB3 0ET, UK. E-mail: pcon@bas.ac.uk

Abstract

On the Antarctic Peninsula, lichens are the most diverse botanical component of the terrestrial ecosystem. However, detailed information on the distribution of lichens on the Antarctic Peninsula region is scarce, and the data available exhibit significant heterogeneity in sampling frequency and effort. Satellite remote sensing, in particular the use of the Normalized Difference Vegetation Index (NDVI), has facilitated determination of vegetation richness and cover distribution in some remote and otherwise inaccessible environments. However, it is known that using NDVI for the detection of vegetation can overlook the presence of lichens even if their land cover is extensive. We tested the use of known spectra of lichens in a matched filtering technique for the detection and mapping of lichen-covered land from remote sensing imagery on the Antarctic Peninsula, using data on lichen presence collected by citizen scientists and other non-specialists as ground truthing. Our results confirm that the use of this approach allows for the detection of lichen flora on the Antarctic Peninsula, showing an improvement over the use of NDVI alone for the mapping of flora in this area.

To access the supplementary material for this article, please see supplementary files under Article Tools online.

On the Antarctic Peninsula, lichens and bryophytes are the major botanical component of the terrestrial ecosystem (Smith 1984; Øvstedal & Smith 2001; Convey 2013). There are 404 described species of lichen documented in Antarctica, with 264 of these solely on the Antarctic Peninsula (Øvstedal & Smith 2001, 2009). Crustose, fruticose and foliose lichens are important or dominant elements in the extensive cryptogamic communities that form the typical vegetation of the Antarctic Peninsula region, especially along coasts (Øvstedal & Smith 2001; Convey 2013). However, even though the overall diversity of the Antarctic Peninsula flora is well known, most studies have focused on a limited number of locations. Detailed information on the distribution of lichens in the Antarctic Peninsula region is scarce, and the data available exhibit significant heterogeneity in sampling frequency and effort (Casanovas, Lynch & Fagan 2013), as is typical of existing biological data across the Antarctic terrestrial biome (Adams et al. 2006; Chown & Convey 2007; Terauds et al. 2012).

The relative paucity of botanists working in Antarctica, combined with logistic limitations, makes traditional methods for studying biodiversity at a large scale impractical (Chown & Convey 2007; Terauds et al. 2012; Casanovas, Lynch & Fagan 2013). With deglaciation exposing new habitat (Cook et al. 2005; Clarke et al. 2007; Convey 2011) and the increase in both tourism and national research operations in the area (Tin et al. 2009; Liggett et al. 2011), cost-effective and pragmatic but reliable wide-scale survey methods are needed to accelerate assessments of biodiversity (Wall et al. 2011).

Satellite remote sensing has facilitated determination of vegetation richness and cover distribution and can be used where field access is difficult (e.g., Stow et al. 2004; Waser

Citation: *Polar Research* 2015, *34*, 25633, http://dx.doi.org/10.3402/polar.v34.25633

et al. 2004; Johansen & Karlsen 2005; Laidler et al. 2008; Tommervik et al. 2012). Most studies which consider vegetation, including lichens, are based on the analysis of the Normalized Difference Vegetation Index (NDVI; Rouse et al. 1974). NDVI is based on the ratio of visible red light and near-infrared (Gates 2003) and has been used as a proxy to indicate the presence of chlorophyll in an imaged land area. On the Antarctic Peninsula region, Fretwell et al. (2011) presented the first small-scale map of vegetation generated using NDVI. However, with ground truthing for the classification of the imagery based on only two islands, they recognized the need for further work spanning a wider range of sites and habitats. Also, it has been recognized that work using NDVI to detect vegetation might overlook the presence of lichens even if their land cover is extensive (Petzold & Goward 1988). The reflectance spectra of lichens and vascular plants are different in both the visible and the infrared portions of the solar spectrum (0.4–1 μm); in particular, the depth of the visible to near-infrared step (0.6–0.7 μm) is characteristically smaller in lichens (Petzold & Goward 1988; Haselwimmer & Fretwell 2009). Therefore, at high latitudes, where lichen contribution to vegetation diversity and extent increases in importance, NDVI would show decreasing spectral vegetation values, and areas completely covered with lichens can be erroneously classified as having sparse cover of vascular plants (Petzold & Goward 1988). An alternative technique for detecting vegetation from satellite images is image classification (supervised or unsupervised). This classifies an entire pixel into a discrete land cover type, needing the land cover type not only to be of sufficient extent to completely dominate a pixel, but to dominate several pixels in the area of interest as samples for training and validation. As the vegetation communities on the Antarctic Peninsula are typically mixed as well as including neighbouring rocks, soil and/or snow at the scale of mid-resolution satellite images, these techniques are inappropriate.

Here, because of the good development of lichen-dominated communities in the Antarctic Peninsula region (Øvstedal & Smith 2001), we trial the potential of mapping their distribution directly by matching image pixel spectra with the reference spectra of lichens using a matched filtering algorithm (Harsanyi & Chang 1994) applied to mid-resolution (30 m) satellite imagery. This is a more appropriate technique, as partial unmixing can detect the presence of a given material (in our case lichens) at a sub-pixel scale. Such techniques have been widely used in lithological studies (e.g., Rowan & Mars 2003; Harris et al. 2005; Bedini 2011; Grebby et al. 2011) and have been recently applied for the mapping of lichens using very high-resolution imagery (Black et al. 2014; Rouse et al. 1974). The widely available mid-resolution satellite imagery, from satellite platforms such as Landsat, has been used for the study of vegetation in remote areas including work in the Arctic (e.g., Johansen & Karlsen 2005) and Antarctic (Fretwell et al. 2011). However, matched filtering techniques have not been applied using this mid-resolution satellite imagery. If successful, this approach will give much improved information on sub-pixel vegetation cover, community extent and composition.

Furthermore, citizen science approaches provide a practicable and useful tool for surveying areas where specialist expertise is unavailable (Krell 2004; Casanovas et al. 2014), providing a means of enhancing available biodiversity data. Data on lichen presence for visitor sites collected by means of photographic documentation by citizen scientists and other non-specialists are available for a number of visitor sites on the Antarctic Peninsula (Casanovas, Lynch, Fagan & Naveen 2013), and these data can be used for ground truthing in remote sensing studies.

Here, we test the use of known spectra of lichens for the detection and mapping of lichen-covered land from remote sensing imagery on the Antarctic Peninsula, using the data on lichen presence mentioned above as ground truthing. We also compare distribution maps generated using matched filtering of lichen spectra with those derived using NDVI. Our data demonstrate the potential for a more comprehensive and accurately differentiated description of the extent of the different major types of terrestrial vegetation on the Antarctic Peninsula region than is currently available. Such an output also has particular importance in enhancing the ability of the Antarctic Treaty Parties to assess remotely the evidence of cumulative impacts at locations under particularly intense pressure from human activity, such as popular visitor sites and areas that are the focus of research activity or other operations.

Methods

Lichen spectra

The lichen spectra used in this study correspond to *Buellia* sp., *Usnea* sp. and *Caloplaca* sp. These genera of lichen are very common and well represented in maritime Antarctic terrestrial ecosystems. Communities where *Buellia* and *Caloplaca* (two of several nitrophilous taxa present in the region) are abundant cover large expanses of coastal areas that are influenced by nutrients derived from seabird colonies and other vertebrate-derived nutrient sources (Øvstedal & Smith 2001). *Usnea* is one of the main components of another prominent coastal lichen community, with several species often covering from a

Citation: *Polar Research* 2015, *34*, 25633, http://dx.doi.org/10.3402/polar.v34.25633

few to several hundred square metres of coastal areas (Øvstedal & Smith 2001). The spectra of these three genera were collected on Lagoon Island (67°35′ S, 68°16′ W), Ryder Bay, off the west coast of the Antarctic Peninsula, where they are abundant.

Lichen spectra were collected using an Analytical Spectral Device (ASD; Boulder, CO, USA) FieldSpec Pro 3® spectrometer during a field campaign in January 2014. The ASD spectrometer records continuous spectra across the 350–2500 nm spectral range, with a spectral resolution of 3 nm at 700 nm, 10 nm at 1400 nm, and 12 nm at 2100 nm. The ASD spectrometer was configured to acquire spectral reflectance measurements in "white reference" mode, where a white Spectralon® panel (Labsphere, North Sutton, NH, USA) was used as the reference target; relative reflectance spectra of the materials under investigation are calculated by the instrument by dividing the measured white reference radiance by the measured target radiance. The ASD spectrometer was configured so that each spectrum collected represented the average of 50 individual spectral measurements. Re-calibration with the white reference panel was undertaken before collection of each spectrum to ensure the spectra were not affected by instrument drift. Spectral measurements were collected from exposed surfaces of the target, using a contact reflectance probe (which includes its own calibrated light source) with a target region of approximately 1 cm^2. The source spectra for the three species of lichen used in this study are shown in Fig. 1.

Landsat imagery analysis

This study was based on Landsat 8 and Landsat 7 Enhanced Thematic Mapper satellite imagery, which have a spatial resolution of 30 m in the multispectral bands (Supplementary Table S1). For each scene we converted the Landsat digital number values to surface reflectance values using published post-launch gains and offsets, correcting the scene for varying illumination (www.landsat.usgs.gov/Landsat8_Using_Product.php). Snow was masked on each scene using the Normalized Difference Snow Index (NDSI), selecting pixels with a NDSI greater than 0.4 (Dozier 1989; Klein et al. 1998). This method generates a normalized index using a green band and a short wavelength infrared band, as the higher reflectance of snow in the visible band and contrasting lower reflectance in the short wavelength infrared band permits separation of snow from other covers (Dozier 1989).

For each scene, we performed a matched filtering using the lichen spectra collected in the field to estimate the abundance of lichens using partial unmixing. This technique suppresses the response of a composite unknown background while maximizing the response of a known spectral signal of pure material or endmember (Harsanyi & Chang 1994). The scores for the matched filtering results are derived for each pixel by projecting the data onto a matched filter vector, which is the result of transforming the target spectrum onto the input data space. The resulting scores are normally distributed and have a mean of zero; values greater than zero show that a fraction of the target component (lichens in the case of this study) is present in a given pixel. The mathematical definition of the matched filter vector is given by Mundt et al. (2007), who also comprehensively describe the method.

It has been shown that the spectrum from a single species of lichen can be used to account for all lichen contributions in a given observed mixture, if normalization is

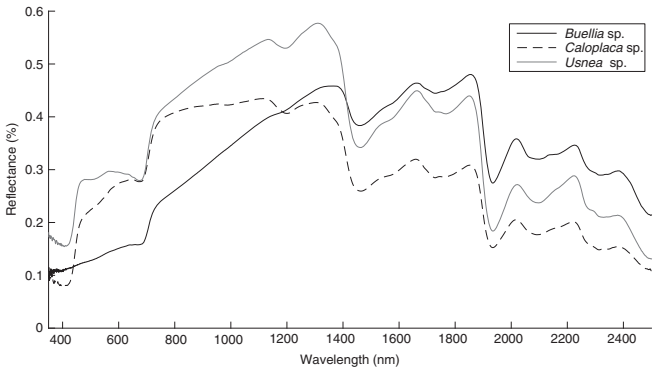

Fig. 1 Spectra of the three lichen genera used in this study.

applied to the lichen reflectance spectra from 2000 to 2400 nm (see Zhang et al. 2005). This is because the spectra of different species of lichens share a similar shape and brightness in the shortwave infrared region (Fig. 1; Zhang et al. 2005). We used three lichen endmembers for this analysis, as explained above, applying the normalization to the lichen reflectance spectra as suggested by Zhang et al. (2005), and tested whether their observation holds true for Antarctic lichens. We used a matched filtering threshold of 0.2 for all the scenes and all the lichen endmembers.

We also calculated NDVI values for each image. NDVI is based on the ratio of visible red light and near-infrared (Rouse et al. 1974; Gates 2003), and it is used to indicate the presence of chlorophyll in a land area represented by a pixel (values varying between -1.0 and $+1.0$, where values near $+1$ are pixels with very high chlorophyll content). We calculated NDVI for all the scenes using the Landsat 7 and 8 bands 3–4 and 4–5, respectively.

"Citizen science" ground-truthing data

As ground truthing, we used a database of lichen richness on the Antarctic Peninsula which combines a photographic "citizen science" approach for data collection with the use of parataxonomic units for the estimation of lichen presence (Casanovas, Lynch, Fagan & Naveen 2013; www.ipt.biodiversity.aq/resource.do?r=antarctic_peninsula_lichens). This database compiles lichen occurrence for sites that are frequently visited by tourists. Twenty-nine sites were photographically surveyed by researchers and tourists between 2009/10 and 2011/12 on the Antarctic Peninsula region. In general, the area allowed for free walking for visitors is smaller than 500 m around the centre of a given visiting site (when limited by cliffs or glaciers, or on very small islands, the area can be smaller). Even though the lichen cover is intermixed with rock, soil and snow, it is an important component of the overall surface cover in most sites studied. Supplementary Fig. S1 shows an example of the extent and form of the vegetated areas in the sites studied. Photographers were asked to take pictures of lichens within the target area. A test of identifications from the photographs using a reference data set of Antarctic lichen images from the US National Herbarium showed that all species used in the test can be detected and, for 74% of the images, the genus of the lichen was identified correctly by three independent classifiers. The observed richness by site varied, with a mean of 18 parataxonomic species and 11 parataxonomic genera (for further information, see Casanovas, Lynch, Fagan & Naveen 2013). In this study, we used 22 of the sites from this database (Supplementary Table S2; Fig. 2). *Buellia* sp. and *Caloplaca* sp. have been recorded in most sites, while *Usnea* sp. has been recorded in more than half the sites studied here (Supplementary Table S2).

Comparison analysis

We counted the number of pixels for which the matched filter showed lichen presence, and the number of pixels for which the different NDVI thresholds showed vegetation (0.05, 0.1 and 0.2) in a buffer of 500 m around the centre of the visiting area at each site. Fretwell et al. (2011) proposed three different thresholds for NDVI based on different probabilities of vegetation cover (higher than 0.05 is "probably" vegetated, higher than 0.1 is "very probable" and higher than 0.2 is "almost certain"). We recognize that there are several years' temporal difference between the vegetation surveys and the remotely sensed data. However, even though it has been demonstrated that lichens in parts of the Antarctic Peninsula region can grow as fast as elsewhere in the world, they only reach a maximum extension rate of 0.5–2.0 mm/year in the South Shetland Islands (Sancho & Pintado 2004). Therefore, we considered that this difference in time would introduce a very small source of error, if any.

We compared the number of sites where the lichen filter showed presence of lichens and those where NDVI values were greater than 0.2, 0.1 or 0.05, and both with the assessments of the ground-truthing sites, in order to

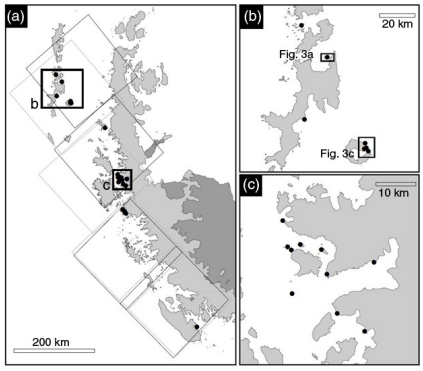

Fig. 2 (a) Location of the ground-truthing sites (open circles) along the Antarctic Peninsula, where the large black squares indicate the extent of the Landsat 7 tiles and the large grey squares indicate the extent of the Landsat 8 tiles. (b) The South Shetland Islands (Fig. 3) and (c) the Danco Coast area (close to Anvers Island). The projection of the maps is Lambert Azimuthal Equal Area.

Citation: *Polar Research* 2015, *34*, 25633, http://dx.doi.org/10.3402/polar.v34.25633

evaluate the accuracy of the detection capabilities of the lichen filter and NDVI. For the Landsat 8 imagery, we also compared the total area for which the lichen filter showed presence of lichens with the area for which the different NDVI thresholds showed presence of vegetation. These analyses used ENVI version 5.1 (Exelis Visual Information Solutions, Boulder, CO) and ArcGIS 10 (ESRI 2011, ArcGIS Desktop: Release 10, Redlands, CA: Environmental Systems Research Institute).

Results

We compared the sites where citizen science confirmed the presence of lichens to the remote sensing analysis (Supplementary Table S2, 22 and 15 sites for the Landsat 7 and 8 set of images, respectively). In the Landsat 7 imagery analysis, the matched filtering failed to detect the presence of lichens in only one (6.6%) of the sites studied (mean number of pixels from the three species of lichens studied), while at 46.6% of the sites the NDVI with a threshold of 0.2 did not detect the presence of any vegetation. In the Landsat 8 imagery analysis, at three (13.6%) of the sites the matched filtering failed to detect lichens, with positive detection at 86% of the sites, while at 59% of the sites the NDVI (0.2 threshold) did not detect any vegetation. However, an NDVI threshold of 0.05 detected vegetation as frequently as the matched filter in both set of images (Landsat 7 and 8). Figure 3 shows a comparison of the matched filter and NDVI results for two sites in the South Shetland Islands. Comparisons of the matched filtering and the three different thresholds for the NDVI data for both sets of images are given in Supplementary Table S3. Supplementary Figs. S2 and S3 show the results of the matched filtering results for the entire area studied for all Landsat 7 and 8 images.

Comparing analyses of the areas detected using the matched filtering by different species of lichens, the total area detected as being covered by lichens by the filter varied slightly when using the different species' spectra. When using the spectra from *Buellia* sp., the total area detected was greater than when using the other two species' spectra. However, the area detected using the latter fell almost completely within that detected using the other two species: 81.0% of the area detected by *Caloplaca* sp. and 97.9% of the area detected by *Usnea* sp. spectra was inside that detected using the *Buellia* sp. spectra; further, 83.2% of the area detected by the *Usnea* sp. spectra fell inside that detected using *Caloplaca* sp. spectra. The area identified as having NDVI values greater than 0.2, 0.1 or 0.05 overlapped by 46.2, 61.7 or 52.3%, respectively, with that detected by the lichen matched filter (Table 1). However, when comparing the detection of lichens at each site studied in each set of imagery (Landsat 7 and 8), the results varied depending on the species spectrum used (Supplementary Table S3), with the *Buellia* sp. spectrum giving the most detections on the Landsat 8 images and the *Usnea* sp. spectrum the most detections on the Landsat 7 images.

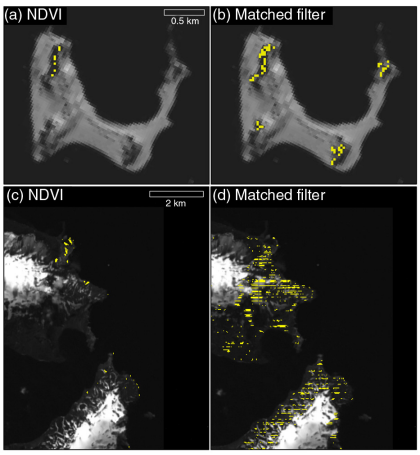

Fig. 3 (a) Normalized Difference Vegetation Index (NDVI; >0.2) analysis for north-west Deception Island and (c) Half Moon Island, South Shetland Islands (see Fig. 2), using Landsat 8 imagery. (b) Matched filtering analysis for north-west Deception Island and (d) Half Moon Island, using Landsat 7 imagery. (See Supplementary Table S1 for details on the Landsat scenes.) The projection of the maps is Lambert Azimuthal Equal Area.

Table 1 Areas covered by the pixels detected as lichen-covered by the matched filtering analysis and Normalized Difference Vegetation Index (NDVI), and the percentages of overlap between them

Type of endmember and NDVI	Area (pixels)	% Overlap
Buellia sp.	72 133	–
Caloplaca sp.	28 926	–
Usnea sp.	27 605	–
NDVI (0.05)	34 148	–
NDVI (0.1)	20 386	–
NDVI (0.2)	11 351	–
Buellia sp. over *Caloplaca* sp.	23 484	81.0
Buellia sp. over *Usnea* sp.	27 047	97.9
Usnea sp. over *Caloplaca* sp.	22 985	83.2
Buellia sp. over NDVI (0.06)	17 864	52.3
Buellia sp. over NDVI (0.1)	12 588	61.7
Buellia sp. over NDVI (0.2)	5251	46.2

Discussion

The use of a matched filtering technique for lichens allowed for the detection of lichen flora on the Antarctic Peninsula using mid-resolution satellite imagery, showing a significant improvement over NDVI for the mapping of flora in this area when using an NDVI threshold of 0.2 [conventionally taken to indicate the almost certain presence of vegetation (Fretwell et al. 2011)]. More research would be needed to establish if this technique overestimates the presence of lichens, as the citizen science database used for ground truthing does not have information on sites where lichens are known to be absent. Even though a lower NDVI threshold of 0.05 appeared to perform as well as the mean of the three species of lichen spectra in detecting the presence of lichens at a given site, the poor overlap between areas detected using the two approaches suggests that they are not identifying the same features. Our results highlight the importance of using techniques other than NDVI thresholds for supplementing detection and mapping of vegetation in areas where lichens are an important community component. While it has previously been noted that NDVI thresholds are not the best technique for mapping distribution of lichens (Petzold & Goward 1988; Haselwimmer & Fretwell 2009), the current study is the first to compare NDVI threshold detection with an alternative technique for lichens in the Antarctic. Here we present the first map of lichen cover for parts of the Antarctic Peninsula based on matched filtering detection of lichen spectra. This is a first step in developing more detailed studies of vegetation in this region using remote sensing, and more detailed ground-truthing field surveys including percentage cover of different types of vegetation, and areas with confirmed absence of specific vegetation types, are recommended for the future.

The results presented here suggest that studies based on the spectrum of only one species of lichen will be sufficient for mapping lichen habitats in this environment, consistent with the conclusion of Zhang et al. (2005). However, results obtained using *Buellia* sp. and *Usnea* sp. spectra identified lichen presence in a greater area than those using the *Caloplaca* sp. spectrum. More detailed field survey data are required to assess the accuracy of using different species spectra at different spatial scales, and future work should address the possibility of mapping different types of vegetation using their specific spectra. It has been shown that it is possible to differentiate lichen species using their spectra in the visible part of the spectrum (Bechtel et al. 2002) and it might, therefore, be possible to map lichen richness from high- and medium-resolution imagery.

The same technique as used here could be applied in the future to intermediate spectral and spatial resolution imagery. At present, we could not use other commercial imagery of medium resolution because of their lack of data in the short wavelength infrared region in which the lichen spectral signature is most characteristic (2000–2400 nm; Petzold & Goward 1988). Images of intermediate spectral and spatial resolution will become available from planned satellite launches (e.g., WorldView-3 and Sentinel2 satellites) and will be of great importance in the study of vegetation in the polar regions in the future.

As glaciers retreat on the Antarctic Peninsula region, lichens play an important role in the colonization and primary succession of newly exposed terrestrial habitat (Favero-Longo et al. 2012). Mapping lichen presence will greatly assist in documenting this process. Also, this technique could assist in the study of areas disturbed by the increasing regional fur seal population on the Antarctic Peninsula (Favero-Longo et al. 2011). Lichens can be used as indicators of long-term change trends in habitat distributions (irrespective of other human impacts, such as direct disturbance).

It has been shown that lichen cover, *Usnea* spp. formations in particular, can be used as a proxy for estimating areas with less snow during the cold season in the Antarctic (Vieira et al. 2014). This application is of importance on the Antarctic Peninsula, where snow mapping is difficult. On the other hand, lichen cover can also compromise geological mapping, as it can completely mask the spectra of underlying lithologies (Rowan & Mars 2003; Harris et al. 2005).

Shaw et al. (2014) recently argued that Antarctic biodiversity is poorly protected, with only 1.5% of the continent's ice-free area formally designated as Antarctic Specially Protected Areas, while Hughes et al. (2015) have calculated that across the entire Antarctic continent only 7 km^2 of "vegetated" land comes under this protection. Visitor Site Guidelines developed by the Antarctic Treaty Parties take into account the vegetation of some landing sites (e.g., Barrientos Island), because trampling and damage of vegetation is a potential human impact at popular tourist areas (Tejedo et al. 2009; Tejedo et al. 2012). However, the identification of appropriate areas for the conservation of vegetation, in particular lichens, is extremely difficult as field data on lichen cover are not available for most of Antarctica. The approach for mapping lichen cover on the Antarctic Peninsula proposed here is an important step forward in the understanding of lichen distribution and can assist in identifying areas for conservation.

Citation: *Polar Research* 2015, *34*, 25633, http://dx.doi.org/10.3402/polar.v34.25633

Acknowledgements

The study reported here was funded by a Natural Environment Research Council (NERC) Field Spectroscopy Facility Loan (no. 675.0613), the NERC Collaborative Gearing Scheme for fieldwork (CGS-086), a NERC PhD studentship (NE/K50094X/1) and the Scientific Committee on Antarctic Research Fellowship scheme 2013–14. PC and PF are core funded by NERC.

References

Adams B.J., Bardgett R.D., Ayres E., Wall D.H., Aislabie J., Bamforth S., Bargagli R., Cary C., Cavacini P., Connell L., Convey P., Fell J.W., Frati F., Hogg I.D., Newsham K.K., O'Donnell A., Russell N., Seppelt R.D. & Stevens M.I. 2006. Diversity and distribution of Victoria Land biota. *Soil Biology and Biochemistry 38*, 3003–3018.

Bechtel R., Rivard B. & Sanchez-Azofeifa A. 2002. Spectral properties of foliose and crustose lichens based on laboratory experiments. *Remote Sensing of Environment 82*, 389–396.

Bedini E. 2011. Mineral mapping in the Kap Simpson complex, central East Greenland, using HyMap and ASTER remote sensing data. *Advances in Space Research 47*, 60–73.

Black M., Casanovas P., Fretwell P. & Convey P. 2014. High resolution mapping of Antarctic vegetation communities using airborne hyperspectral data. Paper presented at the Remote Sensing and Photogrammetry Annual Conference. 2–5 September 2014, Aberystwyth, UK. doi: http://dx.doi.org/10.13140/2.1.5189.6648

Casanovas P., Lynch H.J. & Fagan W.F. 2013. Multi-scale patterns of moss and lichen richness on the Antarctic Peninsula. *Ecography 36*, 209–219.

Casanovas P., Lynch H.J. & Fagan W.F. 2014. Using citizen science to estimate lichen diversity. *Biological Conservation 171*, 1–8.

Casanovas P., Lynch H.J., Fagan W.F. & Naveen R. 2013. Understanding lichen diversity on the Antarctic Peninsula using parataxonomic units as a surrogate for species richness. *Ecology 94*, 2110–2110.

Chown S.L. & Convey P. 2007. Spatial and temporal variability across life's hierarchies in the terrestrial Antarctic. *Philosophical Transactions of the Royal Society B 362*, 2307–2331.

Clarke A., Murphy E.J., Meredith M.P., King J.C., Peck L.S., Barnes D.K.A. & Smith R.C. 2007. Climate change and the marine ecosystem of the western Antarctic Peninsula. *Philosophical Transactions of the Royal Society B 362*, 149–166.

Convey P. 2011. Antarctic terrestrial biodiversity in a changing world. *Polar Biology 34*, 1629–1641.

Convey P. 2013. Antarctic ecosystems. In S. Levin (ed.): *Encyclopedia of biodiversity*. 2nd edn. Pp. 179–188. San Diego, CA: Academic Press.

Cook A.J., Fox A.J., Vaughan D.G. & Ferrigno J.G. 2005. Retreating glacier fronts on the Antarctic Peninsula over the past half-century. *Science 308*, 541–544.

Dozier J. 1989. Spectral signature of alpine snow cover from the Landsat thematic mapper. *Remote Sensing of Environment 28*, 9–22.

Favero-Longo S.E., Cannone N., Roger Worland M., Convey P., Piervittori R. & Guglielmin M. 2011. Changes in lichen diversity and community structure with fur seal population increase on Signy Island, South Orkney Islands. *Antarctic Science 23*, 65–77.

Favero-Longo S.E., Worland M.R., Convey P., Smith R.I.L., Piervittori R., Guglielmin M. & Cannone N. 2012. Primary succession of lichen and bryophyte communities following glacial recession on Signy Island, South Orkney Islands, maritime Antarctic. *Antarctic Science 24*, 323–336.

Fretwell P.T., Convey P., Fleming A.H., Peat H.J. & Hughes K.A. 2011. Detecting and mapping vegetation distribution on the Antarctic Peninsula from remote sensing data. *Polar Biology 34*, 273–281.

Gates D.M. 2003. *Biophysical ecology*. New York: Courier Dover Publications.

Grebby S., Naden J., Cunningham D. & Tansey K. 2011. Integrating airborne multispectral imagery and airborne LiDAR data for enhanced lithological mapping in vegetated terrain. *Remote Sensing of Environment 115*, 214–226.

Harris J.R., Rogge D., Hitchcock R., Ijewliw O. & Wright D. 2005. Mapping lithology in Canada's Arctic: application of hyperspectral data using the minimum noise fraction transformation and matched filtering. *Canadian Journal of Earth Sciences 42*, 2173–2193.

Harsanyi J.C. & Chang C.-I. 1994. Hyperspectral image classification and dimensionality reduction: an orthogonal subspace projection approach. *Geoscience and Remote Sensing 32*, 779–785.

Haselwimmer C. & Fretwell P. 2009. Field reflectance spectroscopy of sparse vegetation cover on the Antarctic Peninsula. In: *First Workshop on Hyperspectral Image and Signal Processing: Evolution in Remote Sensing. Whispers '09*. Pp. 1–4. Piscataway, NJ: Institute of Electrical and Electronics Engineers.

Hughes K.A., Pertierra L.R., Molina-Montenegro M.A. & Convey P. 2015. Biological invasions in Antarctica: what is the current status and can we respond? *Biodiversity and Conservation 24*, 1031–1055.

Johansen B. & Karlsen S.R. 2005. Monitoring vegetation changes on Finnmarksvidda, northern Norway, using Landsat MSS and Landsat TM/ETM+ satellite images. *Phytocoenologia 35*, 969–984.

Klein A.G., Hall D.K. & Riggs G.A. 1998. Improving snow cover mapping in forests through the use of a canopy reflectance model. *Hydrological Processes 12*, 1723–1744.

Krell F.-T. 2004. Parataxonomy vs. taxonomy in biodiversity studies—pitfalls and applicability of "morphospecies" sorting. *Biodiversity and Conservation 13*, 795–812.

Laidler G.J., Treitz P.M. & Atkinson D.M. 2008. Remote sensing of Arctic vegetation: relations between the NDVI, spatial resolution and vegetation cover on Boothia Peninsula, Nunavut. *Arctic 61*, 1–13.

Liggett D., McIntosh A., Thompson A., Gilbert N. & Storey B. 2011. From frozen continent to tourism hotspot? Five

decades of Antarctic tourism development and management, and a glimpse into the future. *Tourism Management 32*, 357–366.

Mundt J., David T., Streutker R. & Glenn N.F. 2007. Partial unmixing of hyperspectral imagery: theory and methods. In: *Proceedings of the American Society of Photogrammetry and Remote Sensing 2007*. Bethesda, MD: American Society for Photogrammetry and Remote Sensing.

Øvstedal D.O. & Smith R.I.L. 2001. *Lichens of Antarctica and South Georgia: a guide to their identification and ecology*. Cambridge: Cambridge University Press.

Øvstedal D.O. & Smith R.I.L. 2009. Further additions to the lichen flora of Antarctica and South Georgia. *Nova Hedwigia 88*, 157–168.

Petzold D.E. & Goward S.N. 1988. Reflectance spectra of Subarctic lichens. *Remote Sensing of Environment 24*, 481–492.

Rouse J.W. Jr., Haas R.H., Schell J.A., Deering D.W. & Harlan J.C. 1974. *Monitoring the vernal advancements and retrogradation of natural vegetation. Final report*. Greenbelt, MD, National Aeronautics and Space Agency.

Rowan L.C. & Mars J.C. 2003. Lithologic mapping in the Mountain Pass, California area using Advanced Spaceborne Thermal Emission and Reflection Radiometer (ASTER) data. *Remote Sensing of Environment 84*, 350–366.

Sancho L.G. & Pintado A. 2004. Evidence of high annual growth rate for lichens in the maritime Antarctic. *Polar Biology 27*, 312–319.

Shaw J.D., Terauds A., Riddle M.J., Possingham H.P. & Chown S.L. 2014. Antarctica's protected areas are inadequate, unrepresentative, and at risk. *PLoS Biology 12*, e1001888, doi: http://dx.doi.org/10.1371/journal.pbio.1001888

Smith R.I.L. 1984. Terrestrial plant biology of the sub-Antarctic and Antarctic. In R.M. Laws (ed.): *Antarctic ecology*. Pp. 61–162. London: Academic Press.

Stow D.A., Hope A., McGuire D., Verbyla D., Gamon J., Huemmrich F., Houston S., Racine C., Sturm M., Tape K., Hinzman L., Yoshikawa K., Tweedie C., Noyle C.B., Silapaswan C., Douglas D., Griffith B., Jia G., Epstein H., Walker D., Daeschner S., Petersen A., Zhou L.M. & Myneni R. 2004. Remote sensing of vegetation and land-cover change in Arctic tundra ecosystems. *Remote Sensing of Environment 8*, 281–308.

Tejedo P., Justel A., Benayas J., Rico E., Convey P. & Quesada A. 2009. Soil trampling in an Antarctic specially protected area: tools to assess levels of human impact. *Antarctic Science 21*, 229–236.

Tejedo P., Pertierra L., Benayas J., Convey P., Justel A. & Quesada A. 2012. Trampling on maritime Antarctica. Can soil ecosystems be effectively protected through existing codes of conduct? *Polar Research 31*, article no. 10888, doi: http://dx.doi.org/10.3402/polar.v31i0.10888

Terauds A., Chown S.L., Morgan F., Peat H.J., Watts D.J., Keys H., Convey P. & Bergstrom D.M. 2012. Conservation biogeography of the Antarctic. *Diversity and Distributions 18*, 726–741.

Tin T., Fleming Z.L., Hughes K.A., Ainley D.G., Convey P., Moreno C.A., Pfeiffer S., Scott J. & Snape I. 2009. Impacts of local human activities on the Antarctic environment. *Antarctic Science 21*, 3–33.

Tommervik H., Bjerke J.W., Gaare E., Johansen B. & Thannheiser D. 2012. Rapid recovery of recently over-exploited winter grazing pastures for reindeer in northern Norway. *Fungal Ecology 5*, 3–15.

Vieira G., Mora C., Pina P. & Schaefer C.E. 2014. A proxy for snow cover and winter ground surface cooling: mapping Usnea sp. communities using high resolution remote sensing imagery (maritime Antarctica). *Geomorphology 225*, 69–75.

Wall D.H., Lyons W.B., Convey P., Howard-Williams C., Quesada A. & Vincent W.F. 2011. Long-term ecosystem networks to record change: an international imperative. *Antarctic Science 23*, 209.

Waser L.T., Stofer S., Schwartz M., Küchler M., Ivits E. & Scheidegger C. 2004. Prediction of biodiversity—regression of lichen species richness on remote sensing data. *Community Ecology 5*, 121–133.

Zhang J., Rivard B. & Sánchez-Azofeifa A. 2005. Spectral unmixing of normalized reflectance data for the deconvolution of lichen and rock mixtures. *Remote Sensing of Environment 95*, 57–66.

Relevant works carried out through collaborations with colleagues which included analytical techniques and methods developed during the PhD were produced as part of this research. Their full references are listed below, followed by the papers themselves.

- Neave, D.A., **Black, M.**, Riley, T.R., Gibson, S.A., Ferrier, G., Wall, F., Broom-Fendley, S. (2016). On the feasibility of imaging carbonatite-hosted rare earth element (REE) deposits using remote sensing. *Economic Geology*, **111**(3), 641-665. doi 10.2113/econgeo.111.3.641
- Burton-Johnson, A., **Black, M.**, Fretwell, P., Kaluza-Gilbert, J. (2015). A fully automated methodology for differentiating rock and ice in Antarctica from Landsat imagery: A new rock outcrop map and area estimation for the entire Antarctic continent. *The Cyrosphere Discuss.*, 2016, 1-16. doi: 10.5194/tc-2016-56.

Economic Geology, v. 111, pp. 641–665

On the Feasibility of Imaging Carbonatite-Hosted Rare Earth Element Deposits Using Remote Sensing*

David A. Neave,[1,†,**] Martin Black,[2,3] Teal R. Riley,[2] Sally A. Gibson,[1] Graham Ferrier,[3] Frances Wall,[4] and Sam Broom-Fendley[4]

[1] *Department of Earth Sciences, University of Cambridge, Downing Street, Cambridge CB2 3EQ, United Kingdom*

[2] *British Antarctic Survey, High Cross, Madingley Road, Cambridge CB3 0ET, United Kingdom*

[3] *Department of Geography, Environment and Earth Sciences, University of Hull, Hull HU6 7RX, United Kingdom*

[4] *Camborne School of Mines, College of Engineering, Mathematical and Physical Sciences, University of Exeter, Penryn Campus, Cornwall TR10 9FE, United Kingdom*

Abstract

Rare earth elements (REEs) generate characteristic absorption features in visible to shortwave infrared (VNIR-SWIR) reflectance spectra. Neodymium (Nd) has among the most prominent absorption features of the REEs and thus represents a key pathfinder element for the REEs as a whole. Given that the world's largest REE deposits are associated with carbonatites, we present spectral, petrographic, and geochemical data from a predominantly carbonatitic suite of rocks that we use to assess the feasibility of imaging REE deposits using remote sensing. Samples were selected to cover a wide range of extents and styles of REE mineralization, and encompass calcio-, ferro- and magnesio-carbonatites. REE ores from the Bayan Obo (China) and Mountain Pass (United States) mines, as well as REE-rich alkaline rocks from the Motzfeldt and Ilímaussaq intrusions in Greenland, were also included in the sample suite. The depth and area of Nd absorption features in spectra collected under laboratory conditions correlate positively with the Nd content of whole-rock samples. The wavelength of Nd absorption features is predominantly independent of sample lithology and mineralogy. Correlations are most reliable for the two absorption features centered at ~744 and ~802 nm that can be observed in samples containing as little as ~1,000 ppm Nd. By convolving laboratory spectra to the spectral response functions of a variety of remote sensing instruments we demonstrate that hyperspectral instruments with capabilities equivalent to the operational Airborne Visible-Infrared Imaging Spectrometer (AVIRIS) and planned Environmental Mapping and Analysis Program (EnMAP) systems have the spectral resolutions necessary to detect Nd absorption features, especially in high-grade samples with economically relevant REE accumulations (Nd > 30,000 ppm). Adding synthetic noise to convolved spectra indicates that correlations between Nd absorption area and whole-rock Nd content only remain robust when spectra have signal-to-noise ratios in excess of ~250:1. Although atmospheric interferences are modest across the wavelength intervals relevant for Nd detection, most REE-rich outcrops are too small to be detectable using satellite-based platforms with >30-m spatial resolutions. However, our results indicate that Nd absorption features should be identifiable in high-quality, airborne, hyperspectral datasets collected at meter-scale spatial resolutions. Future deployment of hyperspectral instruments on unmanned aerial vehicles could enable REE grade to be mapped at the centimeter scale across whole deposits.

Introduction

Rare earth element deposits and reflectance spectroscopy

Carbonatites, classified as rocks with >50% primary magmatic carbonate (Le Maître, 2002), and the alkaline igneous rocks with which they are often associated are the primary source of rare earth elements (REEs), and will remain so for the foreseeable future (Wall, 2014). With notable exceptions, such as the relatively extensive Bayan Obo and Mountain Pass deposits in China and the United States, respectively (Drew et al., 1990; Castor, 2008; Yang et al., 2011; Smith et al., 2015), carbonatite-hosted REE deposits are often small in areal extent but high in grade, i.e., have a total rare earth oxide content (ΣREO) >1 wt % (Chakhmouradian and Zaitsev, 2012; Wall, 2014). This enrichment is largely the result of late-stage, fluid-dominated, carbothermal processes that concentrate REEs in dikes and veins on the meter to tens-of-meter scale during the last stages of emplacement and cooling (Wall and Mariano, 1996; Wall and Zaitsev, 2004; Mitchell, 2005). Conversely, while major alkaline igneous rock-hosted REE deposits, such as Khibiny (also spelled Khibina in the geologic literature) and Lovozero in Russia, can be large in size, they are generally lower grade than their carbonatite counterparts (ΣREO <1 wt %; Wall, 2014). The high concentration of REEs in carbonatites makes them well suited for developing exploration and mapping strategies that exploit diagnostic features in the reflectance spectra of REE-rich materials (e.g., Rowan et al., 1986). In this contribution, we discuss the feasibility of imaging primarily carbonatite-hosted REE deposits by hyperspectral remote sensing at visible and near- to shortwave infrared

† Corresponding author: e-mail, d.neave@mineralogie.uni-hannover.de

* Supplementary Appendices to this paper are available at http://economicgeology.org/ and at http://econgeol.geoscienceworld.org/.

** Present address: Institut für Mineralogie, Leibniz Universität Hannover, Callinstr. 3, 30167 Hannover, Germany.

0361-0128/16/4392/641-25

Submitted: August 6, 2015
Accepted: December 11, 2015

(VNIR-SWIR) wavelengths (λ = 400–2,500 nm), using both airborne- and satellite-based platforms.

It is well established that a number of lanthanide elements exhibit strong, narrow absorption features in their reflectance spectra (Adams, 1965). Investigating the mechanisms by which spectral absorption features are generated is beyond the scope of this study and detailed discussions of REE spectroscopy are best found in the physical and chemical literature (e.g., Dieke, 1970; Görller-Walrand and Binnemans, 1998). In summary, absorptions characteristic of lanthanide elements are thought to arise from 4*f*-4*f* intraconfigurational electron transitions that result from the 4*f* shell (radius ~0.3 Å) being partially shielded by the 5*s* and 5*p* shells (radius ~2 and 1 Å, respectively) and thus largely nonparticipatory in bonding (Liu, 2005). REE absorption features are therefore elemental in nature rather than vibrational; they depend on the absolute concentration of REE atoms rather than on their bonding environments (Clark, 1995). While the identification of REEs in mineral and rock spectra is theoretically straightforward, with the notable exceptions of monazite-(Ce), bastnäsite-(Ce), parisite-(Ce,) and synchysite-(Ce), there are few published REE-rich reference spectra currently available to the remote sensing community (Fig. 1; Clark et al., 2007; Turner et al., 2014). The most complete presentation of REE-bearing rock spectra remains that of Rowan et al. (1986), who provided VNIR-SWIR spectra from four carbonatite-alkaline complexes in North America (Mountain Pass, Oka, Iron Hill, and Gem Hill), albeit in nondigital form.

As reviewed by Turner et al. (2014), a number of REE-rich carbonatite and alkaline centers have been successfully imaged using both space- and airborne reflectance spectroscopy. For example, lithologic maps of Mountain Pass in the United States and Khanneshin in Afghanistan have been produced using multispectral Advanced Spaceborne Thermal Emission and Reflection Radiometer (ASTER) instrument (Rowan and Mars, 2003; Mars and Rowan, 2011). However, the coarse spatial and spectral resolutions of satellite-based multispectral instruments severely limit their ability to detect REE absorption features: the only potential identification of REE-rich material from satellite data published to date was at Mountain Pass (Rowan and Mars, 2003). Mapping REE-rich rocks at finer spatial and spectral resolutions has also been carried out using airborne hyperspectral instruments. Examples include mapping the Iron Hill carbonatite-alkaline complex in the United States with the hyperspectral Airborne Visible-Infrared Imaging Spectrometer (AVIRIS) instrument (Rowan et al., 1995) and the Sarfartoq carbonatite complex in Greenland with the HyMap® system (Bedini, 2009). Despite the presence of characteristic REE absorption features in the reflectance spectra of field samples, no REE absorptions were reported from either of these AVIRIS and HyMap® datasets (Rowan et al., 1995; Bedini, 2009). Nevertheless, Nd and Sm absorptions have been reported in AVIRIS spectra collected over the Sulphide Queen area of Mountain Pass, thereby demonstrating the potential role of hyperspectral remote sensing in imaging REE deposits (Rowan and Mars, 2003). Furthermore, Boesche et al. (2015) successfully delimited high Nd occurrences in a monazite-mineralized outcrop of the Fen complex in Norway using a ground-based HySpex hyperspectral imaging system.

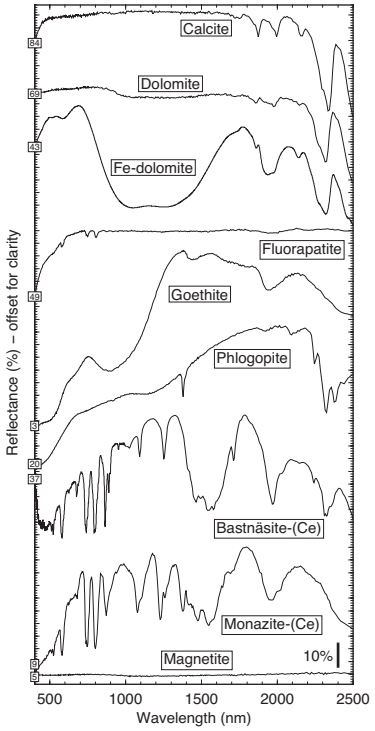

Fig. 1. Reference VNIR-SWIR spectra from common minerals found in REE-rich carbonatites. All spectra are sourced from the USGS spectral library (Clark et al., 2007), apart from the spectrum for bastnäsite that is from Turner et al. (2014). Note the complexity of bastnäsite-(Ce), monazite-(Ce), and fluorapatite spectra that result from REE-related absorptions. Deep Nd absorption features are observed within the 500- to 900-nm wavelength interval. Absolute reflectance values are shown at 400 nm.

As hyperspectral mapping capabilities and image processing techniques continue to improve, characterizing mineral deposits using reflectance spectroscopy will become an evermore robust method. For example, the next generation of remote sensing satellites such as the Environmental Mapping Program (EnMAP) will carry spaceborne Earth observation fully into the hyperspectral era (Stuffler et al., 2007; Guanter et al., 2015). However, many questions relating to the identification of REE deposits by remote sensing remain largely unanswered. First, what are the detection limits for identifying REEs in carbonatites and alkaline igneous rocks by reflectance spectroscopy under ideal conditions, i.e., how well do spectral properties correlate with REE grade? Second, do deposit lithology and mineralogy affect the ability to resolve REEs? Third, under what conditions might REE absorption features be resolvable by various classes of remote sensing instrument?

Approach and scope

Igneous rocks classified as carbonatites can be generated by a range of petrologic processes (Mitchell, 2005): by low-degree melting of a mantle source (Wallace and Green, 1988; Harmer and Gittins, 1998); by extensive fractional crystallization of carbonated alkaline magmas (Gittins, 1989); and by liquid immiscibility between carbonate and silicate melts (Freestone and Hamilton, 1980; Brooker and Kjarsgaard, 2011). The petrogenesis of alkaline rocks can be equally diverse (Fitton and Upton, 1987) and is often closely linked with the generation of carbonatites (Woolley and Kjarsgaard, 2008). Carbonatites and alkaline igneous rocks are often compositionally variable both within and between magmatic centers and are frequently associated with extensive fenites and contact aureoles. The crystallization of REE minerals generally occurs late in the emplacement history of carbonatites and is largely secondary in nature (Wall and Mariano, 1996). Notable exceptions include the growth of primary bastnäsite-(Ce) at Mountain Pass (Mariano, 1989) and burbankite at Khibina (Zaitsev et al., 2002).

We present reflectance spectra collected from a range of well-characterized carbonatites and carbonatite-related REE ores, as well as from two alkaline igneous centers in Greenland: Motzfeldt and Ilímaussaq. Our sample suite includes samples from currently active REE mines (Bayan Obo in China, Mountain Pass in the United States, and Mount Weld in Australia), as well as samples from exploration projects with significant future mining potential (Ilímaussaq in Greenland). The reflectance spectra presented here significantly expand the spectral library of REE-rich reference material available to the remote sensing community from mineral spectra to spectra on the whole-rock scale (cf. Rowan et al., 1986; Clark et al., 2007; Turner et al., 2014). Furthermore, we use petrographic, geochemical, and spectral information from the same hand specimens to investigate relationships between spectral features, REE grade, and mineral assemblage. Nevertheless, our new spectra are presented with two important caveats. First, although analytical strategies were designed to mitigate the effects of sample heterogeneity at the hand specimen scale, the extreme petrologic variability present within carbonatite and alkaline complexes means that the spectral properties we measure cannot simply be expanded from single samples to the outcrop scale; individual hand specimens are not perfectly representative of their host complexes. Second, the petrographic and geochemical data we present have been collected primarily to contextualize spectral data: placing our samples within a detailed petrogenetic framework for each magmatic system is beyond the scope of this study.

Sample Sources

Carbonatites and REE ores from the following locations were sourced from the Natural History Museum in London: Bayan Obo in China, Uyaynah in the United Arab Emirates, and Fort Portal in Uganda. Carbonatites from the following locations were sourced from collections at Camborne School of Mines, University of Exeter: Oka and St. Honoré in Canada, Kangankunde, Tundulu, and Songwe in Malawi, Fen in Norway, Jacupiranga in Brazil, Kaiserstuhl in Germany, Mount Weld in Australia, and Phalaborwa in South Africa. Carbonatites from Tororo and Sukulu in Uganda, Chilwa Island and Kangankunde in Malawi, Mountain Pass in the United States, Panda Hill in Tanzania, and Sokli in Finland were sourced from the Harker Collection at the University of Cambridge. Carbonatites and alkaline rocks from Qeqertaasaq, Tikiusaaq, and Ilímaussaq in Greenland were obtained from collections at the University of St Andrews. Alkaline igneous rocks from Motzfeldt in Greenland were supplied by SRK Consulting (UK) Ltd. The geographic distribution of these samples is summarized in Figure 2.

Analytical Methods

VNIR-SWIR reflectance spectra were collected from a total of 42 hand specimens during the course of this study. On the basis of sample availability and VNIR-SWIR REE absorption strengths, different combinations of analyses were carried out on different samples (Tables 1–5 document which analyses were performed on each sample). Thermal infrared (thermal IR; λ = 8–15 μm) reflectance spectra were also collected for a subset of 20 samples; absorptions at thermal IR wavelengths can be used to characterize and map the presence of different rock-forming mineral groups such as silicates, carbonates, and phosphates and can thus play a role in delimiting carbonatite complexes (Christensen et al., 2000; Ninomiya et al., 2005; Mars and Rowan, 2011). Whole-rock compositions of 13 samples were collated from published datasets (Woolley et al., 1991; Eby et al., 2009) collated from previously collected but unpublished datasets or supplied by industrial collaborators (SRK Consulting (UK) Ltd.). New whole-rock data were acquired for a additional 18 samples that span much of the petrologic variability present within our sample suite. Mineral assemblages were determined using optical and electron microscopy, except where supplied by collaborators or available in the literature.

Petrography and microscopy

Thin sections were investigated using a petrographic microscope and an FEI Quanta 650F QEMSCAN in the Department of Earth Sciences at the University of Cambridge. Backscattered electron (BSE) images were collected on the QEMSCAN, using an accelerating voltage of 20 kV and a working distance of 13 mm. Optical phase identification was assisted by using the Bruker XFlash electron dispersive X-ray (EDX) spectroscopy system integrated into the QEMSCAN, with counting times of 15 to 30 s on both spectrometers. Particular care was taken during sample preparation to ensure that chips taken for thin section production were representative of the surfaces analyzed spectroscopically.

X-ray fluorescence spectroscopy

A total of 18 whole-rock samples were analyzed by X-ray fluorescence spectrometry (XRF) for major and trace elements. Samples were cut into 10- to 15-cm^3 blocks, washed in distilled water, and dried prior to crushing in a steel jaw crusher and powdering in an agate ball mill in the Department of Earth Sciences at the University of Cambridge. Fused glass disks and pressed powder pellets were prepared for major and trace element analyses on a PANalytical Axios-Advanced XRF spectrometer in the Department of Geology at the University of Leicester.

Fused glass disks were prepared at the University of Leicester using sample powders that had been dried overnight in

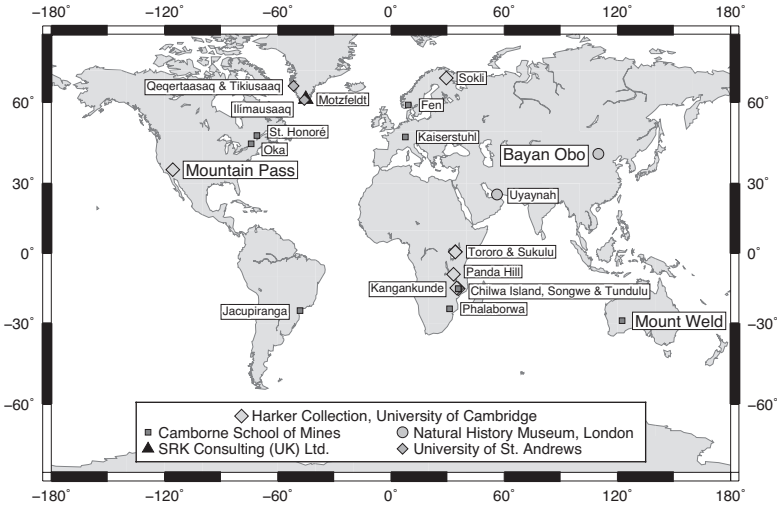

Fig. 2. Map showing the geographic distribution of samples used in this study, as well as the collections from which they were sourced. Bayan Obo, Mountain Pass, and Mount Weld represent currently active REE mine sites and are labeled in a larger font.

order to remove adsorbed water. Loss on ignition (LOI) values were calculated by igniting ~3 g of each sample in ceramic crucibles at 950°C, apart from the kakortokite sample from Ilímaussaq that was ignited in a disposable LECO crucible at 750°C because of its low solidus temperature. Fusion disks of carbonate-rich samples with high LOI values (LOI = 10–40 wt %) were then prepared from 0.6 g of nonignited powder and 3 g of lithium tetraborate flux that were melted in a Pt-Au crucible over a Spartan burner and cast into a Pt-Au mold. Carbonate-poor samples with low LOI values (LOI <10 wt %) were prepared from 0.6 g of ignited powder and 3 g of lithium metaborate flux.

Powder pellets were prepared at the University of Cambridge by mixing 10 g of each sample powder with approximately 20 drops of binding agent (2% polyvinyl alcohol solution) in a clean glass beaker. This mixture was then placed in a die and subjected to a pressure of 15 t/in^2 to form smooth, well-compacted pellets for analysis.

VNIR-SWIR reflectance spectroscopy

VNIR-SWIR (λ = 400–2,500 nm) reflectance spectra were collected using an Analytical Spectral Device (ASD)'s FieldSpec Pro FR spectroradiometer at the Natural Environment Research Council Field Spectroscopy Facility at the University of Edinburgh. The ASD spectroradiometer has a spectral range of 350 to 2,500 nm, although data from the shortest wavelengths (350–400 nm) were found to be noisy over the integration times used (25 cycles of 17 ms per measurement). Spectra were collected at sampling intervals of 1.4 nm at 350 to 1,000 nm and 2 nm at 1,000 to 2,500 nm with the following full width at half maximum (FWHM) spectral resolutions: 5.6 nm at ~435 nm, 3.5 nm at ~700 nm, and 4.9 nm at ~910 nm at VNIR wavelengths (determined by measurement of an Hr-Ar lamp at the Natural Environment Research Council Field Spectroscopy Facility) and ~11 nm at SWIR wavelengths (determined by the U.S. Geological Survey Spectroscopy Lab using the same class of ASD; http://speclab.cr.usgs.gov/spectral.lib06/ds231/index.html). Absolute reflectance values were calculated by calibrating each batch of ~20 repeat measurements against a Spectralon white reference panel that was also measured at the end of each batch to monitor for instrumental drift. Individual measurements sample an ellipse approximately 10 × 5 mm in size.

In order to maximize the quality of VIS-SWIR spectra, ~50- × 50-mm flat surfaces were cut into the samples and polished coarsely to ensure good optical coupling with the ASD contact probe. The effect of compositional heterogeneity on sample spectra was mitigated by averaging over up to 94 evenly spaced repeat measurements taken from across sample surfaces. The typical 1σ precision of individual spectra estimated from repeat measurements of an identical field of view is <0.5% relative.

Thermal IR thermal emission spectroscopy

Thermal IR (λ = 8–15 μm) reflectance spectra of 20 samples were calculated from thermal emission spectra measured using a Midac M4410-S Fourier transform infrared field spectrometer equipped with a ZnSe beam-splitter and Stirling pump-cooled MCT detector at the Natural Environment Research Council Field Spectroscopy Facility, using Kirchhoff's law (Nicodemus, 1965): $\varepsilon = 1 - r$, where r = reflectance and ε = emissivity. Although the full spectral range of the

spectrometer is 1.5 to 15.4 μm (7,800–650 cm^{-1}), reflectance was only calculated at thermal IR wavelengths where analytical noise was sufficiently low to resolve emissivity values (8–15 μm). Spectra were collected with a spectral resolution of 0.5 cm^{-1} and at a constant working distance of 75 mm. This working distance results in a field of view of ~40 × 40 mm, which is approximately equivalent to sample area integrated over multiple ASD measurements.

Sample radiance was determined using a two-temperature black body calibration method where black body temperatures of 45° and 80°C were selected to bracket sample temperatures of 50° to 70°C (e.g., Hook and Kahle, 1996; Korb et al., 1996). In order to overcome the substantial errors in thermal emission spectra introduced from uncertainties in measuring the temperature of samples, calculations were performed using temperatures determined from an algorithm that assumes a maximum emissivity of 0.98 within the 8- to 13-μm window (Kahle and Alley, 1992). Emissivity was subsequently calculated from radiance by subtracting downwelling radiance (DWR) measurements collected using an Infra-Gold® plate (ε <0.06). Thermal IR spectra presented in this contribution are thus subject to a number of assumptions and should only be considered as guideline values. The typical 1σ precision of thermal emission spectra within 8 to 15 μm estimated from repeat measurements is 2% relative.

Geologic Contexts and Mineral Assemblages

Bayan Obo (China), Mountain Pass (United States), and Mount Weld (Australia)

The Bayan Obo Fe-REE-Nb deposit in China, which currently dominates global REE supply (Wall, 2014), experienced a convoluted and potentially unique petrogenetic history that has been reviewed comprehensively by Smith et al. (2014). Major REE minerals include bastnäsite-(Ce), monazite-(Ce), parisite-(Ce), and huanghoite-(Ce) (Fig. 3A). Apatite is also present but contains significantly lower concentrations of REEs than the REE minerals (Campbell and Henderson, 1997). The samples used in our study were described in detail by Smith et al. (2000), and span four paragenetic groups: Disseminated Monazite stage, Banded Ore, Fluorite stage, and Barite stage (Table 1).

Prior to the onset of mining at Bayan Obo in China, the Sulphide Queen carbonatite at Mountain Pass in the United States was the world's largest light (L)REE source (Castor, 2008). Active mining restarted in 2010. Mountain Pass is particularly noteworthy for the great abundance of bastnäsite-(Ce) (Table 1; Fig. 3B; Olson et al., 1954), which is thought, almost uniquely, to have crystallized directly from a carbonatite melt (Mariano, 1989).

Mount Weld in Western Australia started processing ore in 2011 and is one of the main LREE mines outside of China. Lottermoser (1990) provided a detailed petrologic description of this highly weathered complex. The primary REE-bearing minerals present in the ankeritic carbonatite investigated in this study are apatite, monazite-(Ce) and synchysite-(Ce) (Table 1).

East and South Africa

Kangankunde, Tundulu, Songwe, and Chilwa Island are located within the Chilwa alkaline province of Malawi (Garson,

Table 1. Samples from Bayan Obo, Mountain Pass, and Mount Weld

Sample no.	Collection[1]	Collection sample no.	Brief description	Locality	Country	Mineralogy[4]	REE mineralogy[4]	ASD	FTIR	Whole-rock	Reference
CR-01	NHM	1996,P4(20)[2]	Disseminated Monazite stage	Bayan Obo	China	Dol, Cal, Mag, (Amph)	Mz	Y	Y	Y	Smith et al. (2000)
CR-02	NHM	1996,P4(11)[2]	Banded Ore	Bayan Obo	China	Aeg, Fl, Bt	Ap, Bast, Mz	Y	Y	Y	Smith et al. (2000)
CR-03	NHM	1996,P4(18)[2]	Fluorite stage	Bayan Obo	China	Fl, Mag,	Ap, Bast, B3S, Par	Y		Y	Smith et al. (2000)
CR-04	NHM	1995,P3(6)[2]	Barite stage	Bayan Obo	China	Aeg, Bt, Cal, Nb-Ti phases	Bast, B2S, Par, Huang	Y	Y	Y	Smith et al. (2000)
CR-25	CSM	MW16C	Ankerite carbonatite	Mount Weld	Australia	Ank, Cal	Ap, Mz, Syn	Y			
CR-36	Harker	115531[3]	Carbonatite	Mountain Pass	United States	Cal, Dol, Bt	Bast	Y	Y	Y	

[1] Collection abbreviations: NHM = Natural History Museum in London, CSM = Camborne School of Mines, Harker = Harker Collection at the University of Cambridge
[2] BM no.
[3] Harker Collection no.
[4] Mineralogical abbreviations: Ab = albite, Aeg = aegerine, Amph = alkali amphibole, Ank = ankerite, Ap = apatite, B2S-B3S = intermediate fluorocarbonates, Bast = bastnäsite, Bt = barite, Cal = calcite, Fl = fluorite, Huang = huanghoite, Mag = magnetite, Mz = monazite, Par = parasite, Phl = phlogopite, Pyr = pyrochlore, Qz = quartz, Sr = strontianite

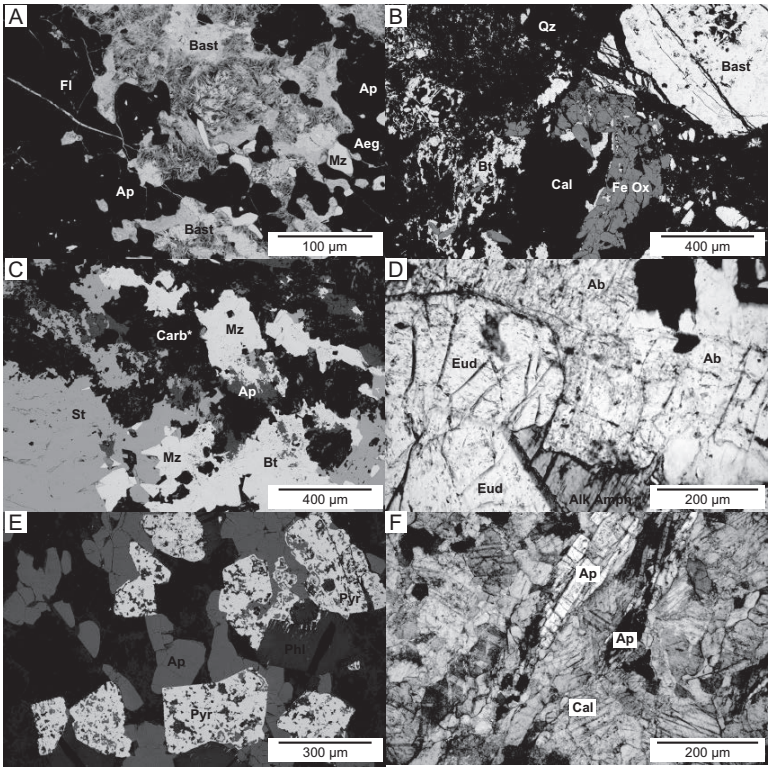

Fig. 3. Backscattered electron (BSE) and optical photomicrographs of key REE-rich samples. A. BSE image of the Banded Ore from Bayan Obo, China (CR-02). B. BSE image of a sample from Mountain Pass, United States (CR-36). C. BSE image of a sample from Kangankunde, Malawi (CR-16). D. Photomicrograph with plane polars of kakortokite from Ilímaussaq, Greenland (CR-46). E. BSE image of a sample from St. Honoré, Canada (CR-15). F. Photomicrograph with crossed polars of Fen, Norway (CR-17). Mineral labels are as follows: Ab = albite, Aeg = aegirine, Alk Amph = alkali amphibole, Ap = apatite, Bast = bastnäsite, Bt = barite, Carb = calcite-dolomite-ankerite mix, Carb* = calcite-dolomite-ankerite-Mn carbonate, Cal = calcite, Eud = eudialyte, Fe Ox = Fe oxides, Fl = fluorite, Mz = monazite, Phl = phlogopite, Pyr = pyrochlore, Qz = quartz, and St = strontianite.

1965). While igneous rocks from these complexes are highly variable, Fe-rich compositions dominated by ankerite and magnetite are the most common (Table 2). Wall and Mariano (1996) provided a detailed discussion of REE mineralization in Kangankunde, where REE mineralogy is dominated by monazite-(Ce) and bastnäsite-(Ce) (Fig. 3C). The REE fluorcarbonate synchysite-(Ce) is present in samples from Tundulu and Songwe, with florencite and apatite also hosting minor REE components (Broom-Fendley et al., 2016). Apatite and pyrochlore are the major REE-bearing phases at Chilwa Island, though bastnäsite and florencite can also be present (Simonetti and Bell, 1994).

Tororo and Sukulu in Uganda lie within the same dominantly calciocarbonatitic igneous complex (Williams, 1952; McCormick and Le Bas, 1996). Apatite is the major REE host in these centers (Table 2) and has been the subject of fluid inclusion studies interrogating the origins of carbonate-rich liquids (Rankin, 1977; Ting et al., 1994). The REE-poor Fort Portal extrusive carbonatite, also located in Uganda, is described in detail by Eby et al. (2009).

Although the Panda Hill complex of Tanzania is a largely calciocarbonatitic in nature, magnesiocarbonatite and ferrocarbonatite are also present (Basu and Mayila, 1986). REEs are primarily hosted in apatite and pyrochlore (Table 2), with the latter being sufficiently abundant to represent a potential Nb resource (Mitchell, 2015).

The Proterozoic Phalaborwa (Palabora) complex of South Africa is unusually Cu rich (Eriksson, 1989), with apatite

Table 2. Samples from East and South Africa

Sample no.	Collection[1]	Collection sample no.	Brief description	Locality	Country	Mineralogy[4]	REE mineralogy[4]	ASD	FTIR	Whole-rock	Reference
CR-10	NHM	1998-P2(24)[2]	Carbonatite	Fort Portal	Uganda	Cal, Spur, Mag, Phl	Ap	Y		Y (published)	Eby et al. (2009)
CR-16	CSM	KKDE18.10.12	Monazite carbonatite	Kangankunde	Malawi	Ank, Mag	Mz, Syn, Bast	Y	Y	Y	
CR-20	CSM	T0281	Banded carbonatite	Tundulu	Malawi	Ank/Cal, Str	Ap, Syn	Y		Y	
CR-21	CSM	T0282	Banded carbonatite	Tundulu	Malawi	Ank/Cal, Str	Ap, Syn	Y	Y	Y	
CR-22	CSM	T0167	REE-rich ankerite carbonatite	Songwe	Malawi	Ank, Mag, Cal,	Ap, Pyr, Syn, Bast	Y	Y	Y	
CR-23	CSM	T0208	Carbonatite	Songwe	Malawi	Cal, Mag	Ap	Y		Y	
CR-24	CSM	T0210	Calcite carbonatite	Songwe	Malawi	Cal, Mag	Ap	Y	Y	Y	
CR-26	CSM	PTC-1	Carbonatite (Transgressive)	Phalaborwa - Palabora	South Africa	Cal, Mag	Ap	Y			
CR-29	Harker	61759[3]	Carbonatite	Tororo	Uganda	Cal, Phl, Mag	Ap	Y	Y	Y	
CR-31	Harker	62506[3]	Carbonatite	Sukulu	Uganda	Cal, Bi, Mag	Ap,Pyr			Y	
CR-33	Harker	72628[3]	Apatite carbonatite	Chilwa Island	Malawi	Cal, Mag, Fl,	Ap	Y		Y	
CR-35	Harker	72632[3]	Monazite carbonatite	Kangankunde	Malawi	Cal, Mag	Mz		Y		
CR-37	Harker	116583[3]	Phlogopite pyrochlore carbonatite	Panda Hill	Tanzania	Cal, Bi, Mag	Pyr	Y		Y	
CR-38	Harker	116602[3]	Altered carbonatite with large pyrochlores	Panda Hill	Tanzania	Ank, Mag	Ap, Pyr	Y	Y	Y	

[1] Collection abbreviations: NHM = Natural History Museum in London, CSM = Camborne School of Mines, Harker = Harker Collection at the University of Cambridge

[2] BM nos.

[3] Harker Collection no.

[4] Mineralogical abbreviations: Ank = ankerite, Ap = apatite, Bast = bastnäsite, Bi = biotite, Cal = calcite, Fl = fluorite, Mag = magnetite, Mz = monazite, Phl = phlogopite, Pyr = pyrochlore, Spur = spurrite, St = strontianite, Syn = synchysite

crystals from the central transgressive carbonatite containing appreciable quantities of REEs (Ce ~3,000 ppm; Dawson and Hinton, 2003).

Greenland and Canada

The Jurassic Tikiusaaq and Qeqertaasaq carbonatites of west Greenland are likely to be associated with the incipient rifting of the Labrador sea (Tappe et al., 2007). While exploration of these complexes is ongoing, Tappe et al. (2009) discussed the petrology of Tikiusaaq in relationship to possible kimberlite-carbonatite associations. Ancylite-(Ce) is the dominant REE phase in these carbonatites alongside parisite-(Ce), though small quantities of the HREE mineral churchite-(Y) have been reported from Tikiusaaq (Table 3).

Both the Motzfeldt and Ilímaussaq alkaline igneous intrusions are located within the Proterozoic (1300–1140 Ma) Gardar province of southwest Greenland. Jones and Larsen (1985) provided a geochemical framework for the Motzfeldt intrusion as well as documenting the occurrence of REE-rich phases such as apatite and eudialyte. McCreath et al. (2013) discussed the chemistry of REE-bearing pyrochlore minerals from within the Peralkaline Microsyenite Suite of the Motzfeldt Sø formation that have been analyzed in this study (Table 3). Given the petrologic heterogeneity of the dominantly peralkaline Ilímaussaq intrusion (Ferguson, 1970; Bailey et al., 2001), we have only investigated the properties of a eudialyte-rich kakortokite (albite + eudialyte + amphibole; Fig. 3D) that may represent a future REE resource (Ferguson, 1970; Wall, 2014).

Oka and St. Honoré are located within the Ontario carbonatite province of Ontario and western Quebec (Erdosh, 1979). Apatite and pyrochlore represent the main REE-bearing phases in these complexes (Table 3; Fig. 3E). St. Honoré is the largest current source of Nb outside of Brazil (Mitchell, 2015).

Scandinavia and Germany

The Sokli complex of Finland lies at the western limit of the Kola alkaline province and has been described in detail by Vartiainen and Paarma (1979). Apatite is present at high modal proportions within carbonatite and phoscorite portions of the complex and is the major REE hosting mineral (Table 4). REEs are particularly abundant in weathered apatite-rich material at the surface.

Apatite is also the main host of REEs in samples from Fen in Norway and Kaiserstuhl in Germany (Andersen, 1988; Hornig-Kjarsgaard, 1998; Table 4; Fig. 3F), though accumulations of monazite within the Fen complex have been mapped recently by Boesche et al. (2015).

Other locations

The extrusive carbonatite samples from Uyaynah in the United Arab Emirates were collected from a tectonic window through the Semail Ophiolite Complex and are described in detail by Woolley et al. (1991). REEs are primarily hosted in allanite and apatite at Uyaynah (Table 5).

Huang et al. (1995) provided a geochemical overview of the Jacupiranga carbonatite of Brazil that is especially rich in apatite (Table 5), with further whole-rock analyses provided by Hornig-Kjarsgaard (1998).

Table 3. Samples from Greenland and Canada

Sample no.	Collection[1]	Collection sample no.	Brief description	Locality	Country	Mineralogy[2]	REE mineralogy[2]	ASD	FTIR	Whole-rock
CR-11	SRK	10517	Microsyenitte	Motzfeldt	Greenland	Ksp, Arfv, Aeg, Fl	Pyr	Y	Y	Y (supplied)
CR-12	SRK	10518	Microsyenitte	Motzfeldt	Greenland	Ksp, Arfv, Aeg, Fl	Pyr	Y		Y (supplied)
CR-13	SRK	10519	Microsyenitte	Motzfeldt	Greenland	Ksp, Arfv, Aeg, Fl	Pyr	Y	Y	Y (supplied)
CR-14	CSM	OKA-1	Biotite-rich calcite carbonatite	Oka	Canada	Cal, Mag, Mont	Ap, Pyr	Y	Y	Y
CR-15	CSM	StH-1	Biotite-rich carbonatite	St Honoré	Canada	Cal, Bi, Mag	Ap, Pyr	Y	Y	Y
CR-46	St. Andrews		Kakortokite (nepheline syenite)	Ilímaussaq	Greenland	Ab, Arfv	Eud	Y		Y
CR-47	St. Andrews		Carbonatite	Tikiusaaq	Greenland	Cal	Ancy, Chu	Y		
CR-48	St. Andrews		Carbonatite	Qeqertaasaq	Greenland	Cal	Ancy, Par	Y		
CR-49	St. Andrews		Carbonatite	Qeqertaasaq	Greenland	Cal	Ancy, Par	Y		

[1] Collection abbreviations: SRK = SRK Consulting (UK) Ltd, CSM = Camborne School of Mines

[2] Mineralogical abbreviations: Ab = albite, Aeg = aegerine, Ancy = ancylite, Ap = apatite, Arfv = arfvedsonite, Bi = biotite, Cal = calcite, Chu = churchite, Eud = eudialyte, Fl = fluorite, Mag = magnetite, Mont = monticellite, Par = parasite, Pyr = pyrochlore

Whole-Rock Geochemistry

Major element compositions

With the exception of lavas from Uyaynah and Fort Portal (CR-05–CR-10), all samples in this study are intrusive rocks. Most samples are carbonate rich and have compositions that can be summarized using the ternary classification diagram of Woolley and Kempe (1989; Fig. 4). Full major element compositions are provided in the supplementary material. While most carbonatites form a single array from calciocarbonatite to ferrocarbonatite compositions, three compositions lie toward the center of the diagram: CR-15 from St. Honoré lies on the tie line between magnesio- and ferrocarbonatites but is strongly affected by magnetite accumulation; CR-16 from Kangankunde lies within the ferrocarbonatite field; and CR-33 from Chilwa Island lies within the magnesiocarbonatite field. Despite its high REE content, CR-36 from Mountain Pass is one of the purest calciocarbonatites investigated.

Samples CR-01 to CR-04 from Bayan Obo cannot be readily classified based on their major element chemistry. Nevertheless, the high MgO content of CR-01 from the Disseminated Monazite is consistent with its original petrogenesis as a dolomitic marble (Smith et al., 2015). All samples from Bayan Obo also have appreciable Fe_2O_3 contents reflecting the high degree of Fe mineralization across the complex.

Although no major element data are available for samples CR-11 to CR-13 from the silicate Motzfeldt intrusion, Bradshaw (1988) reported peralkaline syenite compositions (atomic (Na + K)/Al) >1) from the same rock unit, the Peralkaline Microsyenite Formation. Sample CR-46, a kakortokite from the Ilímaussaq intrusion, is rich in alkalis and can be classified as a nepheline syenite (Le Bas et al., 1986). A low total of 90.1 wt % reflects the sample's high Zr, Nb, REE, F, and Cl contents. When Zr, Nb, and REEs are recalculated as oxides, a total of 103.0 wt % is obtained.

REE- and Nb-poor samples (such as CR-33 and CR-42 from Chilwa Island and Sokli, respectively) have major element

Fig. 4. Classification of carbonatites following the scheme of Woolley and Kempe (1989).

Table 4. Samples from Scandinavia and Germany

Sample no.	Collection[1]	Collection sample no.	Brief description	Locality	Country	Mineralogy[3]	REE mineralogy[3]	ASD	FTIR	Whole-rock
CR-17	CSM	Fen202/76	Calcite carbonatite	Fen	Norway	Cal, Bi	Ap	Y	Y	Y
CR-19	CSM	Intrusive	Calcite carbonatite	Kaiserstuhl	Germany	Cal, Mag, Ol	Ap	Y		Y
CR-42	Harker	117676[2]	Phyrochlore sovite	Sokli	Finland	Cal, Mag	Ap	Y	Y	Y
CR-43	Harker	117677[2]	Coarse sovite	Sokli	Finland	Cal, Mag	Ap	Y		Y

[1] Collection abbreviations: CSM = Camborne School of Mines, Harker = Harker Collection at the University of Cambridge
[2] Harker Collection no.
[3] Mineralogical abbreviations: Ap = apatite, Bi = biotite, Cal = calcite, Fl = fluorite, Mag = magnetite. Ol = olivine

(including LOI) totals that approach 100%. However, a number of samples initially appear to have unacceptably low totals (~50 wt % including LOI). Although analytical accuracy and precision are affected by the extreme and variable compositions of these samples, such low totals result primarily from the high concentration of elements that typically occur in trace quantities in most other igneous rocks. If Ce, La, Nb, Nd, Sr, Y, and Zr are recalculated as oxides, then most samples have totals that lie between 97 and 103 wt %. Remaining exceptions include F-rich samples, such as fluorite-bearing CR-03 from Bayan Obo, and Ba-rich samples, such as CR-02 from Bayan Obo and CR-36 from Mountain Pass. However, recalculating Ba as BaO results in the overestimation of totals (supplementary material), indicating that Ba was poorly quantified in these samples.

REE contents

Sample REE systematics are summarized in Figure 5 and Nd contents are provided in Table 6. Full trace element compositions are provided in the supplementary material. Trace element concentrations in many samples lie above the range of XRF calibration possible with the standards available (~2,000 ppm for most elements and ~2,800 ppm in the case of Nd), and the resulting analyses must be treated as semiquantitative. Trace element quantification by XRF is further hampered by complex X-ray interferences resulting from extreme and variable matrix effects. While achieving full quantification is beyond the resources of this exploratory study, relative errors in whole-rock trace element contents are unlikely to exceed 20% except in the case of Ba. Encouragingly, REE contents of samples CR-02 and CR-36 are of the same order as values reported from Bayan Obo and Mountain Pass ores by Smith et al. (2014) and Castor (2008), respectively.

Measured REE abundances vary by more than three orders of magnitude, with Nd contents varying from ~140 to ~43,300 ppm (Fig. 5). Most samples show enrichments in LREEs, with chondrite-normalized concentrations ordered as follows La > Ce > Nd > Y. The highest Nd concentrations are found in CR-02 from Bayan Obo (~38,600 ppm), CR-16 from Kangankunde (~43,300 ppm) and CR-36 from Mountain Pass (~30,800 ppm). Thin sections of these samples show evidence of extensive REE mineralization: CR-02 contains abundant fibrous bastnäsite-(Ce) as well as monazite-(Ce) (Fig. 3A); CR-16 contains abundant monazite-(Ce) (Fig. 3C); and CR-36 contains euhedral bastnäsite-(Ce) (Fig. 3B). Apatite- and pyrochlore-bearing samples have lower Nd contents (<1,000 ppm), with the following exceptions: CR-13 from Motzfeldt, CR-21 from Tundulu, and CR-22–24 from

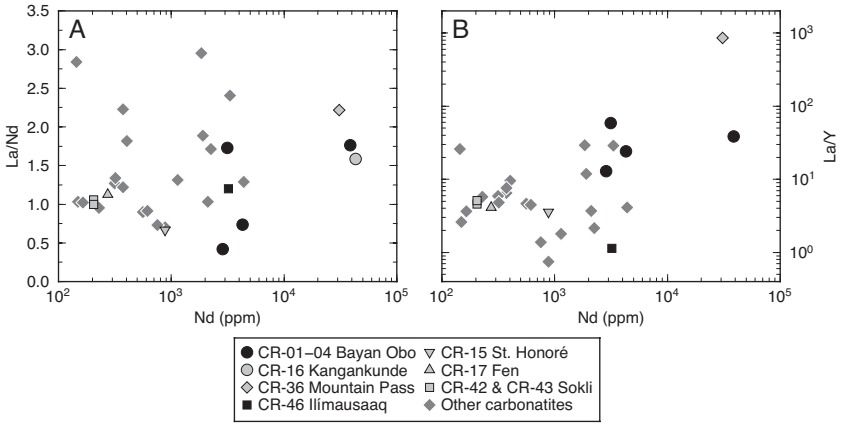

Fig. 5. Plots summarizing sample REE systematics. A. La/Nd vs. Nd. B. La/Y vs. Nd.

Table 5. Samples from Other Locations

Sample no.	Collection[1]	Collection sample no.	Brief description	Locality	Country	Mineralogy[3]	REE mineralogy[3]	ASD	FTIR	Whole-rock	Reference
CR-05	NHM	1991-P10(16)[2]	Carbonatite	Uyaynah	UAE	Cal, Mag	Ap	Y	Y	Y (published)	Woolley et al. (1991)
CR-06	NHM	1991-P10(11)[2]	Carbonatite	Uyaynah	UAE	Cal, Mag	Ap, All	Y		Y (published)	Woolley et al. (1991)
CR-07	NHM	1991-P10(15)[2]	Carbonatite	Uyaynah	UAE	Cal, Mag	Ap	Y		Y (published)	Woolley et al. (1991)
CR-08	NHM	1991-P10(1)[2]	Carbonatite	Uyaynah	UAE	Cal, Bi	Ap, All	Y	Y	Y (published)	Woolley et al. (1991)
CR-09	NHM	1991-P10(49)[2]	Carbonatite	Uyaynah	UAE	Cal, Amph, Bi	Ap	Y		Y (published)	Woolley et al. (1991)
CR-18	CSM	Jaq91/70	Apatite carbonatite	Jacupiranga	Brazil	Cal, Mag, Ol	Ap	Y			

[1] Collection abbreviations: NHM = Natural History Museum, London, CSM = Camborne School of Mines
[2] BM no.
[3] Mineralogical abbreviations: Ap = apatite, All = allanite, Amph = amphibole, Bi = biotite, Cal = calcite, Mag = magnetite, Ol = olivine

Songwe. Eudialyte-bearing CR-46 from Ilímaussaq contains ~3,200 ppm Nd (Fig. 3F).

Reflectance Spectra

VNIR-SWIR reflectance spectra

The diverse nature of reflectance spectra collected in this study reflects the substantial geochemical, mineralogical, and textural variability within our sample suite. Nevertheless, it is possible to divide the sample suite into six groups based on the minerals that dominate each spectrum. All measured spectra are provided in the supplementary material.

Magnetite-dominated spectra: Samples from the Bayan Obo Fluorite stage (CR-03), Uyaynah (CR-05–CR-09), and Fort Portal (CR-10) have low absolute reflectance (≤15%) at VNIR-SWIR wavelengths (Fig. 6) that reflect abundant magnetite in the case of the Bayan Obo sample and disseminated, fine-grained magnetite in the cases of the Uyaynah and Fort Portal samples (Smith et al., 1985; Clark, 1995). A number of samples show weak absorptions at ~2,300 nm that indicate the presence of CO_3 groups. Reflectance maxima at 500 to 700 nm in samples CR-08 and CR-10 from Uyaynah and Fort Portal are indicative of Fe-rich carbonate (Gaffey, 1985; Woolley et al., 1991). Weak absorption features at ~744 and ~802 nm in spectra from the Bayan Obo Fluorite stage (CR-03) are consistent with the presence of bastnäsite-(Ce) and parisite-(Ce)-hosted Nd, but are significantly damped by magnetite (Figs. 1, A1A). Although CR-15 from St. Honoré has a CO_3 absorption feature centered at ~2,300 nm corresponding to the presence of calcite (Gaffey, 1985), other spectral features are difficult to resolve because the low overall reflectance of this pyrochlore-rich sample (Fig. 3E).

Fe-poor carbonate-dominated spectra: Samples from Oka (CR-14), Jacupiranga (CR-18), Mountain Pass (CR-36), Sokli (CR-42, CR-43), and Qeqertaasaq (CR-48, CR-49) exhibit largely flat spectra of generally high absolute reflectance (up to ~55%) onto which narrow absorption features are

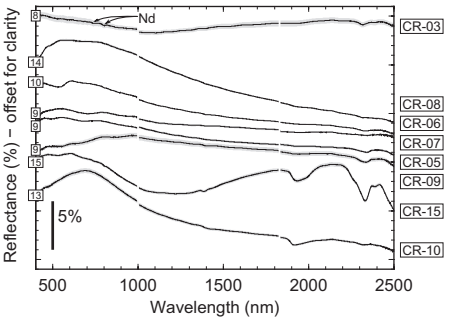

Fig. 6. Mean VNIR-SWIR spectra of samples dominated by magnetite collected using an ASD spectroradiometer under laboratory conditions (CR-03, n = 37; CR-05, n = 43; CR-06, n = 34; CR-07, n = 9; CR-08, n = 53; CR-09, n = 19; CR-10, n = 20; CR-15, n = 75). Gray envelopes show the standard errors of the mean spectra. Absolute reflectance values are shown at 400 nm. Sample locations and rock types for spectra can be found in Tables 1–5.

Table 6. Summary of Sample Nd Contents and Absorption Feature Properties (absorption center, absorption full width half maximum (FWHM), absorption depth, and absorption area)

Sample	Nd (ppm)	Absorption center (nm) (Gaussian fit)				Absorption FWHM (nm) (Gaussian fit)				Absorption depth (%) (Gaussian fit)				Normalized absorption area			
Absorption feature (nm)		~583	~744	~802	~871	~583	~744	~802	~871	~583	~744	~802	~871	~583	~744	~802	*~871*
CR-01	3135	582	745	801	870	15.6	21.8	22.6	16.7	0.58	1.21	1.12	0.24	0.54	1.56	1.65	0.33
CR-02	38571	582	745	802	870	15.8	22.3	23.7	16.1	1.12	2.06	2.01	0.70	1.35	3.50	3.84	0.92
CR-03	2869	583	741	800	879	25.2	26.9	18.6	31.7	0.08	0.10	0.14	0.06	0.27	0.38	0.36	0.29
CR-04	4297	583	745	802	869	15.7	22.2	22.2	14.8	0.99	1.51	1.66	0.49	0.93	2.12	2.44	0.52
CR-05	559													0.03	0.07	0.02	0.10
CR-06	1907				881				26.3				0.04	0.02	0.09	0.06	0.13
CR-07	614	589				23.2				0.06				0.15	0.07	0.08	0.07
CR-08	3305													0.01	0.04	0.01	0.04
CR-09	1850													0.03	0.05	0.03	0.04
CR-10	229													0.04	0.06	0.03	0.05
CR-11	374	575		801	883	22.4		21.3	26.9	0.06		0.06	0.04	0.15	0.00	0.12	0.09
CR-12	402	575		801	881	21.2		21.5	30.0	0.12		0.09	0.05	0.16	0.01	0.10	0.07
CR-13	2248	575		801		21.2		19.5		0.12		0.09		0.16	0.02	0.07	0.04
CR-14	316	586	744	803	877	19.5	22.9	15.2	23.4	0.11	0.15	0.16	0.05	0.06	0.12	0.08	0.04
CR-15	878		744	803	880		25.8	16.9	28.0		0.07	0.10	0.04	0.01	0.13	0.12	0.08
CR-16	43302	582	745	802	870	15.7	22.7	24.0	17.4	0.66	1.34	1.51	0.53	0.90	2.19	2.49	0.65
CR-17	274	583	744	802	870	14.4	19.9	18.1	14.6	0.80	0.90	0.97	0.21	0.31	0.49	0.52	0.10
CR-18		585	747	805	875	17.0	20.3	18.5	19.5	0.83	0.88	1.05	0.24	0.37	0.49	0.58	0.14
CR-19	144		741	804	879		17.1	17.6	25.7		0.07	0.14	0.04	0.02	0.04	0.09	0.04
CR-20	884	584	744	802	874	17.7	19.0	15.5	27.4	0.11	0.16	0.25	0.04	0.13	0.15	0.18	0.05
CR-21	4402	582	742	800	866	13.2	20.4	17.5	10.0	0.21	0.44	0.56	0.20	0.29	0.68	0.73	0.19
CR-22		585	743	802		18.4	24.9	17.0		0.07	0.07	0.13		0.16	0.21	0.22	0.05
CR-23	1139			800				19.0				0.12		0.02	0.04	0.18	0.05
CR-24	2115	582	741	799	866	14.2	18.2	16.4	11.5	0.12	0.32	0.41	0.11	0.13	0.34	0.38	0.11
CR-25		588	740			24.0	20.0			0.06	0.09			0.14	0.19	0.03	0.06
CR-26		583	744	801	872	17.0	20.1	17.9	13.7	2.47	3.26	3.18	0.76	0.81	1.32	1.25	0.25
CR-29	149	583	743	801	875	12.3	22.3	14.8	23.0	0.20	0.27	0.34	0.09	0.10	0.25	0.20	0.09
CR-31	164		744	803	874		19.7	18.7	20.6		0.36	0.47	0.09	0.03	0.25	0.33	0.07
CR-33	753		741	802			27.4	15.3			0.04	0.09		0.02	0.08	0.09	0.05
CR-35		582	745	802	870	15.7	22.3	23.8	16.4	1.10	2.86	3.09	0.91	1.51	4.25	4.84	1.07
CR-36	30848	582	743	800	868	13.8	21.7	19.8	12.0	0.49	1.17	1.34	0.67	0.37	1.04	1.07	0.35
CR-37	375	583	743	800	872	15.3	20.9	17.0	23.5	0.33	0.42	0.49	0.12	0.16	0.29	0.28	0.10
CR-38	320			801				20.7				0.05		0.08	0.03	0.05	0.05
CR-42	205	584	744	803	874	15.3	22.2	16.8	16.9	0.19	0.25	0.28	0.06	0.14	0.29	0.26	0.06
CR-43	205	585	745	803	876	14.3	22.7	14.9	21.7	0.08	0.18	0.20	0.05	0.06	0.22	0.16	0.07
CR-46	3221		744	804	879		20.3	20.7	25.2		0.23	0.22	0.05	0.15	0.22	0.25	0.07
CR-47		583	746	802	873	15.8	21.8	19.9	20.9	1.22	1.64	1.97	0.44	0.90	1.29	1.47	0.33
CR-48		583	746	802	872	17.1	22.8	22.3	20.1	2.00	3.63	3.85	0.88	0.87	1.88	2.06	0.44
CR-49		583	746	803	872	17.8	23.4	24.0	20.7	2.76	6.59	6.37	1.52	1.38	3.39	3.53	0.75

superimposed (Fig. 7). Deep absorption features at ~2,300 nm without a broad absorption feature centered on ~1,200 nm are characteristic of Fe-poor calcite and dolomite (Figs. 1, A1B, A2A; Gaffey, 1985). Broad absorption features at ~1,900 nm related to H_2O may represent either hydrated minerals (e.g., ancylite-(Ce)), fluid inclusions, or adsorbed water (Gaffey, 1985; Rowan et al., 1986). However, assigning H_2O (and OH^-) features to specific minerals is of limited use in a remote sensing context: this information is lost in air- and spaceborne datasets because of atmospheric H_2O (see later). Sharp drops in reflectance below 500 nm in most samples probably reflect the presence of Mn within calcite (Gaffey, 1985). The steep drop in reflectance below 600 nm in the Mountain Pass sample (CR-36) is consistent with the presence of barite (Figs. A1B, A2B; Clark et al., 2007; Castor, 2008).

Narrow absorption features at ~583, ~744, ~802, and ~871 nm in samples from Jacupiranga (CR-18), Mountain Pass (CR-36), and Qeqertaasaq (CR-48, CR-49) can be attributed to Nd hosted primarily within apatite, bastnäsite-(Ce) and ancylite-(Ce), respectively (Rowan et al., 1986). Minor absorption features at ~583, ~744, and ~802 nm in samples from Oka (CR-14) and Sokli (CR-42, CR-43) correspond to the presence of Nd at lower concentrations; the high overall reflectance of these samples makes these small spectral features resolvable. Absorption features associated with other REEs are difficult to assign unambiguously; while complex absorption features at ~1,550 and ~1,970 nm are likely to have Pr and Sm components, they also encompass OH^-, H_2O, and Nd features (Turner et al., 2014). Furthermore, contributions from HREEs are difficult to assess because currently published spectral libraries include only LREE-rich minerals (e.g., Clark et al., 2007; Turner et al., 2014).

Fe-rich carbonate-dominated spectra: Samples from the Bayan Obo Disseminated Monazite stage (CR-01), Fen (CR-17), Mount Weld (CR-25), Phalaborwa (CR-26), Tororo (CR-29), Sukulu (CR-31), and Panda Hill (CR-37) have distinctive "M"-shaped reflectance spectra (Fig. 8). Broad absorption features centered at ~1,200 nm are consistent with Fe-bearing calcite, dolomite, and ankerite (Figs. 1, A1C; Gaffey, 1985; Mars and Rowan, 2011). CO_3 absorption features centered at ~2,300 nm are prominent in all spectra. Additional CO_3 absorptions at ~1,880, ~2,000, and ~2,160 nm are visible in most samples, apart from those from Bayan Obo. H_2O absorption features are also present, and OH^- features at ~1,400 nm are clear in samples from Tororo (CR-29) and Panda Hill (CR-37).

The strongest Nd absorption features within this group occur in apatite-bearing samples from Fen (CR-17) and Phalaborwa (CR-26), and monazite-(Ce)-bearing samples from the Bayan Obo Disseminated Monazite stage (CR-01). Apatite- and pyrochlore-bearing samples from Tororo (CR-29), Sukulu (CR-31), and Panda Hill (CR-37) show only weak Nd absorptions despite having a higher overall reflectance than CR-01, which is consistent with the low REE content of minerals in these samples (Fig. A1C). Furthermore, no features

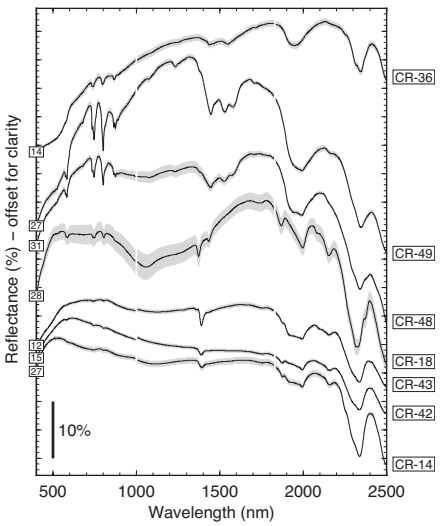

Fig. 7. Mean VNIR-SWIR spectra of samples dominated by Fe-poor carbonates collected using an ASD spectroradiometer under laboratory conditions (CR-14, n = 71; CR-18, n = 17; CR-36, n = 68; CR-42, n = 34; CR-43, n = 39; CR-48, n = 63; CR-49, n = 57). Gray envelopes show the standard errors of the mean spectra. Absolute reflectance values are shown at 400 nm. Sample locations and rock types for spectra can be found in Tables 1–5.

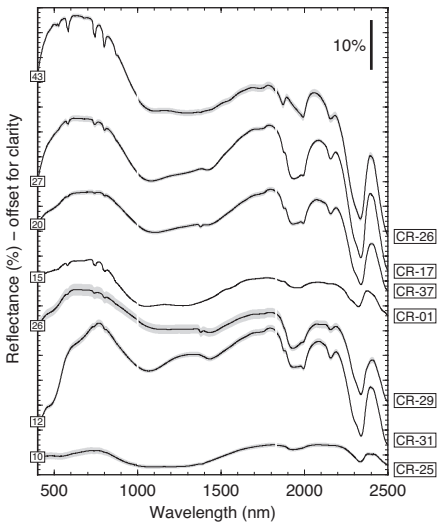

Fig. 8. Mean VNIR-SWIR spectra of samples dominated by Fe-rich carbonates collected using an ASD spectroradiometer under laboratory conditions (CR-01, n = 94; CR-17, n = 43; CR-25, n = 20; CR-26, n = 15; CR-29, n = 39; CR-31, n = 44; CR-37, n = 52). Gray envelopes show the standard errors of the mean spectra. Absolute reflectance values are shown at 400 nm. Sample locations and rock types for spectra can be found in Tables 1–5.

associated with Pr or Sm can be identified in these spectra. Sample CR-25 has a low overall reflectance, which impedes the identification REE absorptions.

Fe oxide-carbonate mixed spectra: Samples from Kangankunde (CR-16, CR-35), Kaiserstuhl (CR-19), Songwe (CR-22–CR-24), Chilwa Island (CR-33), Panda Hill (CR-38), and Tikiusaaq (CR-47) have sloping spectra with reflectance values that generally increase from 400 to 1,800 nm (Fig. 9). Absorptions at ~2,300 nm reflect the presence of CO_3 in all of these samples, though magnetite is also an important constituent of many of these samples (Figs. 1, A1D). Broad absorption features centered at 950 to 1,000 nm present to varying degrees within this group of spectra are characteristic of goethite that probably formed by the alteration of primary magnetite or by exsolution from Fe-rich carbonates (Fig. A2C; Clark et al., 2007).

Strong Nd, Pr, and Sm absorption features in samples from Kangankunde (CR-16, CR-35) can be attributed to the high modal abundance of moderately coarse monazite-(Ce) (~500 μm) in these samples (Figs. 1, 3C), though smaller quantities of bastnäsite-(Ce) and other REE-rich phases such strontianite may also contribute (Fig. A1D; Wall and Mariano, 1996). Prominent Nd absorption features in CR-47 from Tikiusaaq can be accounted for by the presence of significant quantities of ancylite-(Ce). Unfortunately, no published spectra of ancylite-(Ce) that would enable us to confirm this association are known to the authors.

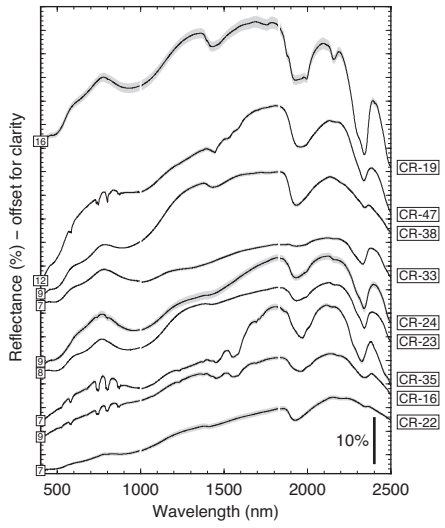

Fig. 9. Mean VNIR-SWIR spectra of samples dominated by mixtures of Fe oxides and carbonates collected using an ASD spectroradiometer under laboratory conditions (CR-16, n = 96; CR-19, n = 41; CR-22, n = 41; CR-23, n = 38; CR-24, n = 48; CR-35, n = 54; CR-38, n = 39; CR-47, n = 49). Gray envelopes show the standard errors of the mean spectra. Absolute reflectance values are shown at 400 nm. Sample locations and rock types for spectra can be found in Tables 1–5.

REE-dominated spectra: Samples from the Bayan Obo Banded Ore (CR-02) and Barite stage (CR-04) have largely flat reflectance spectra, onto which numerous complex absorption features are superimposed (Fig. 10). These samples contain abundant colorless aegirine with largely featureless reflectance spectra at 500 to 800 nm (Ribeiro Da Costa et al., 2013). Most prominent absorptions in these spectra from Bayan Obo can be attributed to Pr, Sm, and Nd (Fig. 1). In addition to bastnäsite-(Ce), monazite-(Ce) and parisite-(Ce) occur in the Banded Ore (Fig. A1E). Huanghoite-(Ce) is present also alongside other REE fluorcarbonates in the Barite stage (Smith et al., 2000). The depth of REE absorptions are possibly enhanced by the unusually coarse grain size of REE minerals in these samples (~1 mm; Smith et al., 2014).

Alkaline igneous rock spectra: Samples from Motzfeldt (CR-11–CR-13, CR-45) and Ilímaussaq (CR-46) are variably altered silicate rocks and contain no carbonate (Fig. 10). All four Motzfeldt samples have a similar spectra that are best attributed to the presence of hematite (Fig. A2D; Clark et al., 2007): reflectance increases steeply between 600 and 700 nm before decreasing across smooth absorption features centered at ~860 nm. Absorption features at ~1,400 and ~1,900 nm in samples from Motzfeldt probably correspond to the presence of OH^--bearing alteration materials rather than primary hydrous minerals.

Sample CR-46 from Ilímaussaq is significantly less altered than samples from Motzfeldt and is composed of albite, eudialyte, and interstitial alkali amphibole. Given that albite has a largely featureless reflectance spectrum at VNIR-SWIR wavelengths, and that reflectance generally increases as a function of wavelength in amphiboles (Clark et al., 2007), we attribute most spectral features in CR-46 to eudialyte (Fig.

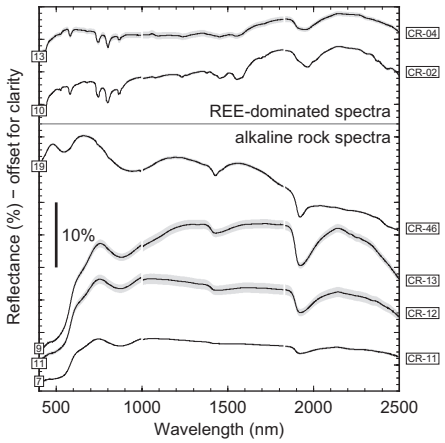

Fig. 10. Mean VNIR-SWIR spectra of samples dominated by REEs and of alkaline rock samples collected using an ASD spectroradiometer under laboratory conditions (CR-02, n = 94; CR-04, n = 83; CR-11, n = 21; CR-12, n = 37, CR-13, n = 38, CR-46, n = 73). Gray envelopes show the standard errors of the mean spectra. Absolute reflectance values are shown at 400 nm. Sample locations and rock types for spectra can be found in Tables 1–5.

A1F). Eudialyte thus appears to be characterized by paired reflectance maxima at ~480 and ~680 nm in line with previous measurements of eudialyte-bearing samples from the Red Wine Intrusive Suite (Kerr et al., 2011). Small absorption features centered at ~744 and ~802 nm reflect the presence of Nd within the eudialyte.

Thermal IR reflectance spectra

A selection of representative thermal IR reflectance spectra are presented in Figure 11. Although absorption features associated with REEs are primarily located at VNIR-SWIR wavelengths, thermal IR spectra contain information crucial for lithologic mapping (Hook et al., 1994; Ninomiya et al., 2005). Thermal IR datasets can thus play important roles in identifying and delimiting carbonatite and alkaline complexes (Oppenheimer, 1998; Mars and Rowan, 2011). Reference thermal IR spectra for common rock-forming minerals are provided by Christensen et al. (2000) and Clark et al. (2007).

Carbonatite thermal IR spectra are readily distinguished from other igneous rock spectra by a prominent CO_3 peak at ~11.3 μm (Christensen et al., 2000). Carbonate peaks are readily clearly visible in samples from Oka (CR-14), St. Honoré (CR-15), Tororo (CR-29), Kangankunde (CR-35), and Sokli (CR-42; Fig. 11). The only other significant features in these carbonate-dominated spectra are pairs of peaks centered at ~9.0 and ~9.5 μm separated by an absorption feature at ~9.2 μm that are best accounted for by the presence of phosphates, i.e., apatite (Christensen et al., 2000). A similarly positioned feature in sample CR-35 from Kangankunde REE-rich probably corresponds to the presence of the REE phosphate monazite-(Ce). Although a modest carbonate peak is observed in sample CR-36 from Mountain Pass, barite appears to have a stronger effect on the thermal IR spectrum: barite generates the small and large peaks centered at ~8.4 and ~9.1 μm, respectively (Clark et al., 2007).

Samples CR-02 and CR-11 from the Bayan Obo Banded Ore and Motzfeldt Peralkaline Microsyenite Suite contain little or no carbonate material and have thermal IR spectra dominated by silicate minerals (Christensen et al., 2000). Although relationships between silicate mineralogy and reflectance are complex, the broad series of peaks at 8.1 to 10.5 μm in CR-11 can be ascribed to alkali feldspar and it its breakdown products. The slightly narrower peak at 8.6 to 10.6 μm in CR-02 can be attributed to aegirine, though some fine features may relate to the presence of apatite (~9.2 μm) or even Sm (~10 μm; Clark et al., 2007).

Spectral Features as Proxies for REE Mineralogy and Grade

Although it is possible to resolve Pr and Sm absorption features in some REE-rich samples, features associated with Nd are both more prevalent and more prominent. Given that REEs have

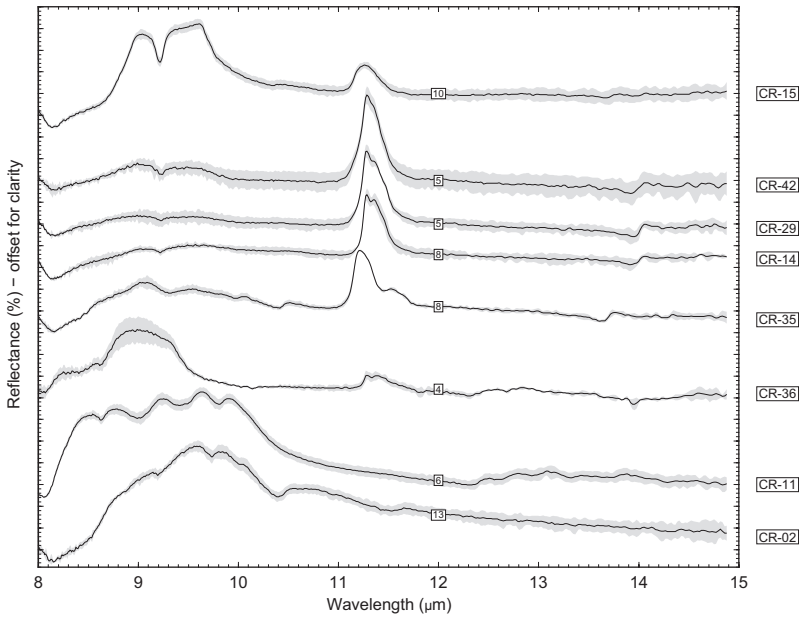

Fig. 11. Selected mean thermal IR reflectance spectra calculated from thermal emission spectra collected using a Fourier thermal IR spectrometer under laboratory conditions (n = 2–4) Gray envelopes show the standard errors of the mean spectra. Absolute reflectance values are shown at 12 μm. Sample locations and rock types for spectra can be found in Tables 1–5.

very similar physicochemical properties and partitioning behaviors, Nd represents an ideal pathfinder element for much of the REE spectrum. While identifying heavy (H)REE absorption, features associated with Ho, Dy, and Er could enable relative abundances of LREE and HREE to be assessed, no features associated unambiguously with HREEs such as Ho, Dy and Er absorptions at ~640, ~1,193, and ~650 nm were observed (e.g., Adams, 1965; Antonovich et al., 2007). Subsequent discussions thus focus on four prominent Nd absorptions centered at ~583, ~744, ~802, and ~871 nm that do not overlap significantly with other absorptions (Clark, 1995; Turner et al., 2014).

In order to relate properties of Nd absorption features to sample mineralogies and REE grades, background features relating to the main rock-forming mineralogy must first be removed. Simple ratios between the reflectance at absorption wavelengths and the reflectance at reference wavelengths cannot be used because of the highly nonunique shapes of the background spectra. Nd absorption features in all samples were therefore isolated using a continuum removal approach (Clark and Roush, 1984), where background spectra were estimated by fitting a third-order polynomial to spectra either side of the absorption features. The following continuum end points were used to isolate the ~583, ~744, ~802, and ~871 nm absorptions from the combined effects of other spectral components respectively: 550 and 610, 710 and 770, 760 and 850, and 850 and 910 nm. The following properties were then estimated by fitting Gaussian curves to each background-subtracted Nd absorption feature: the central position of the absorption feature, i.e., peak position; full-width half at maximum; and absorption depth, i.e., peak height. Although Gaussian curves are unlikely to represent the true form of absorption features, they render fitting procedures internally consistent and reproducible (Clark and Roush, 1984). The area of each absorption feature was also calculated by subtracting areas under measured spectra from areas under background spectra. Finally, in order compare absorption feature areas between different samples, all Nd absorption areas were normalized to the mean reflectance within each wavelength interval.

The effect of REE mineralogy on spectral properties

Nd absorption features are located at the same wavelengths in samples with different REE mineralogies (Table 6). The mean central positions of absorption features within the four wavelength intervals investigated are as follows: 550 to 610 nm (n = 23), 583.0 ± 1.2 (1σ) nm; 710 to 780 nm (n = 22), 744.4 ± 1.3 (1σ) nm; 770 to 850 nm (n = 32), 801.8 ± 1.4 (1σ) nm; and 850 to 900 nm (n = 17), 870.9± 2.7 (1σ) nm. Deviation of absorption positions from mean absorption positions within each wavelength interval generally increase with decreased absorption depth, indicating that variability in calculated absorption locations is primarily related to analytical and processing errors and not to sample mineralogy. Our findings are thus consistent with previous studies that attribute Nd absorption features to mineral-independent electronic processes (Clark, 1995; Turner et al., 2014). However, subtle changes in the structure of Nd absorption features between different sample mineralogies may nevertheless reflect changes in bonding environments that relate to REE mineralogy.

Ancylite-bearing samples appear to show prominent shoulders on either side of absorption maxima at 583 to 584 nm, which are also located at higher wavelengths than in bastnäsite- and monazite-dominated samples (581–582 nm; Table 6). Absorptions in apatite-dominated sample CR-18 are shifted to slightly higher wavelengths with respect to the other samples considered in this section; this trend does not appear to be reproduced in other apatite-dominated samples. The dominance of a single absorption centered at 870 to 871 nm rather than a doublet with absorptions centered on ~864 and ~871 to 874 nm may distinguish apatite from other key REE-bearing minerals, though the unambiguous detection of phosphates (i.e., apatite and monazite) is best achieved at thermal IR wavelengths (e.g., CR-15, Fig. 11). While representing potentially useful discriminators of mineralogy, fine structures of REE absorption features are likely to only be reproducible in REE-rich samples measured under laboratory conditions; these spectral minutiae are extremely difficult to resolve using remote sensing.

The effect of REE grade on spectral properties

Nd concentration correlates positively with Nd absorption depth across most samples (Fig. 12; Table 6). However, high abundances of magnetite mask Nd absorption features in some cases (e.g., CR-06 and CR-08). For absorptions centered at ~583, ~744, ~802, and ~871 nm r^2 values are as follows: 0.492, 0.674, 0.721 and 0.867. Sample CR-04 (Bayan Obo, Barite stage) is excluded from these fits because the surface from which spectroscopic data were collected is not representative of the bulk mineralogy. However, correlations between Nd concentration and Nd absorption area are generally stronger than those with Nd absorption depth: r^2 = 0.718, 0.733, 0.744, and 0.805 for absorptions centered at ~583, ~744, ~802, and ~871 nm, respectively (Fig. 12; Table 6).

Although the correlation between Nd concentration and absorption area is strongest for the ~871-nm absorption (r^2 = 0.805), few significant absorptions were identified at this wavelength, and the best fit line is very strongly weighted by the three high Nd samples. Nd absorption areas for absorptions centered at ~744 and ~802 nm are therefore the most robust spectral proxies for Nd content. Using absorption areas rather than absorption depths as a measure of sample Nd content has the advantage of bypassing the addition of further errors during Gaussian peak fitting. Relationships between REE grade and spectral features are nevertheless subject to substantial uncertainty that is reflected in the scatter around best fit lines (Fig. 12). Causes for this scatter are difficult to isolate and may incorporate the following: sample heterogeneity, errors in whole-rock analyses, errors in spectroscopic analyses, and errors in continuum removal procedures. Furthermore, we do not account for grain size despite the strong effect it has on both the absolute reflectance of materials and the depth of absorption bands (Clark, 1995). Grain size can vary by orders of magnitude within the field of view of single ASD measurements (e.g., Fig. 3A) and the effects of grain size and composition cannot be separated with the current dataset. Nevertheless, Nd absorption features are readily identifiable in the samples from Bayan Obo (CR-02), Kangankunde (CR-16), and Mountain Pass (CR-36) that have the highest Nd concentrations measured in this study (Nd >30,000 ppm; Table 6). These represent high-grade REE deposits.

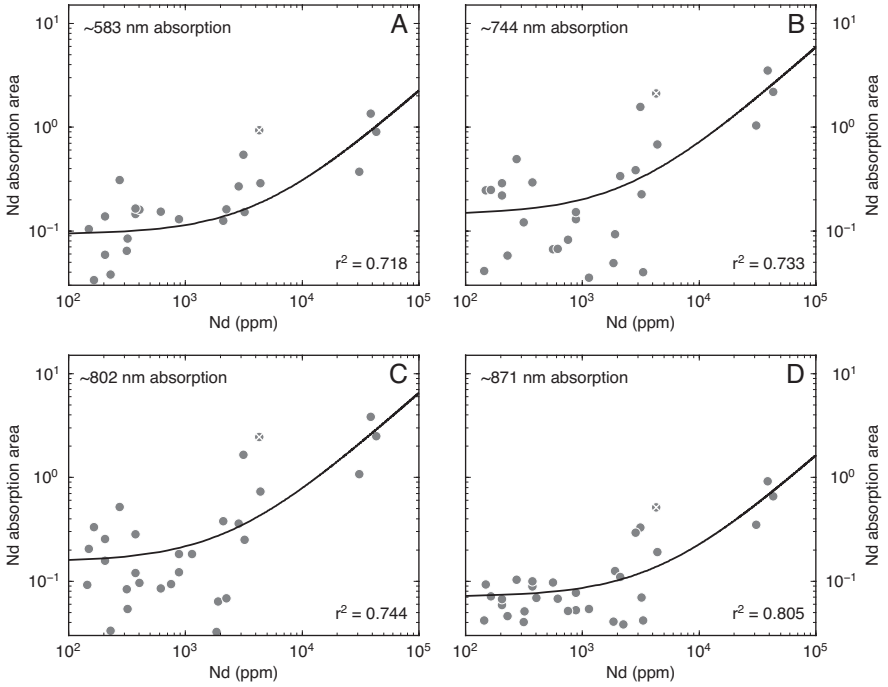

Fig. 12. Plots showing correlations between whole-rock Nd content and Nd absorption areas for four prominent Nd features centered at (A) ~583 nm, (B) ~744 nm, (C) ~802 nm, and (D) ~871 nm. Black lines show the results of linear regressions through the dataset, for which r^2 values are shown in the bottom right of each plot. The data point with the white cross was excluded from the regression because the surface from which spectral data were collected is not representative of the bulk mineralogy.

Detecting REEs Using Remote Sensing

Spectral convolution: REE detectability by multispectral and hyperspectral sensors

Laboratory spectroscopy has a high spectral resolution at wavelengths relevant for detecting Nd (500–900 nm). In order to determine whether REE absorption features could be detected by remote sensing, laboratory spectra were spectrally convolved (i.e., resampled) in order to simulate acquisition by a number of different multispectral and hyperspectral instruments. Multispectral sensors measure relatively few (<20), broadly spaced, discontinuous spectral bands (Kramer, 2002), whereas hyperspectral sensors are defined by their high number (>100) of narrow, contiguous bands that generate continuous spectra (Goetz et al., 1985). Four sensors were selected to encompass a range of well-known current and planned space- and airborne platforms: ASTER, Landsat-8 Operational Land Imager (OLI), EnMAP, and AVIRIS.

The multispectral ASTER instrument onboard Terra, the flagship satellite of the Earth Observing System (EOS) launched in 1999 and operated by the National Aeronautics and Space Administration (NASA), is the most widely used satellite for geologic mapping. ASTER operates in three bands at VNIR wavelengths with a ground resolution of 15 m, six bands at SWIR wavelengths with a ground resolution of 30 m, as well as in five bands at thermal IR wavelengths with a ground resolution of 90 m. The spectral response functions of the ASTER instrument at VNIR-SWIR are provided at http://asterweb.jpl.nasa.gov/characteristics.asp. The multispectral Landsat-8 OLI platform, which is part of the Landsat Program that is jointly managed by NASA and the U.S. Geological Survey, images eight bands at VNIR-SWIR wavelengths, with a ground resolution of 15 m. The spectral response functions for Landsat-8 OLI are provided at http://landsat.gsfc.nasa.gov/?p=5779.

The launch of the German EnMAP hyperspectral satellite is planned for 2018 (Stuffler et al., 2007). EnMAP will carry two sensors capable of detecting 244 bands with a spectral resolution of 5 nm at VNIR wavelengths and 12 nm at SWIR wavelengths (Guanter et al., 2015). The ground resolution will be 30 m. Measured spectral response functions are not yet available for EnMAP, so synthetic spectral response

functions were approximated from expected band centers and FWHM provided on the project website (www.enmap.org/sites/default/files/pdf/Table_EnMAP_Specs.pdf). AVIRIS is an airborne hyperspectral instrument developed by NASA's Jet Propulsion Laboratory (JPL) that has 224 contiguous spectral bands with wavelengths from 400 to 2,500 nm and a spatial resolution ranging from 4 to 18 m, depending on which aircraft it is flown. Spectral response functions for AVIRIS are provided at https://directory.eoportal.org/web/eoportal/airborne-sensors/aviris. AVIRIS is taken to be representative of typical airborne hyperspectral sensors, sharing similar characteristics with other systems such as HyMap®, though we note that some systems such as CASI can achieve higher spatial resolutions (Black et al., 2014).

Convolved reflectance values L at a given band i using the following equation:

$$L_i = \frac{\int L_s(\lambda) r_i(\lambda) \delta\lambda}{\int r_i(\lambda) \delta\lambda},$$

where $L_s(\lambda)$ is the reflectance at band i and wavelength λ, $r_i(\lambda)$ is the spectral response functions of band i and wavelength λ, over the wavelength interval of the sample $\delta\lambda$.

Convolved spectra from sample CR-35, which shows appreciable Nd absorption features, indicate that neither ASTER nor Landsat-8 OLI have sufficient spectral resolutions to distinguish narrow REE features, despite the location of bands at relevant VNIR wavelengths (Fig. 13A). In contrast with the observations of Rowan and Mars (2003) from Mountain Pass, the depression in average reflectance at 700 to 900 nm is insufficient to discern the presence of REEs. Furthermore, the background spectra of many samples in this region are also strongly affected by Fe absorptions at these wavelengths. Nevertheless, a significant advantage of ASTER for geologic mapping over the Landsat-8 OLI platform is the location of bands at >2,200 nm that enable the CO_3 absorption feature centered at ~2,300 nm to be discerned. Data from some

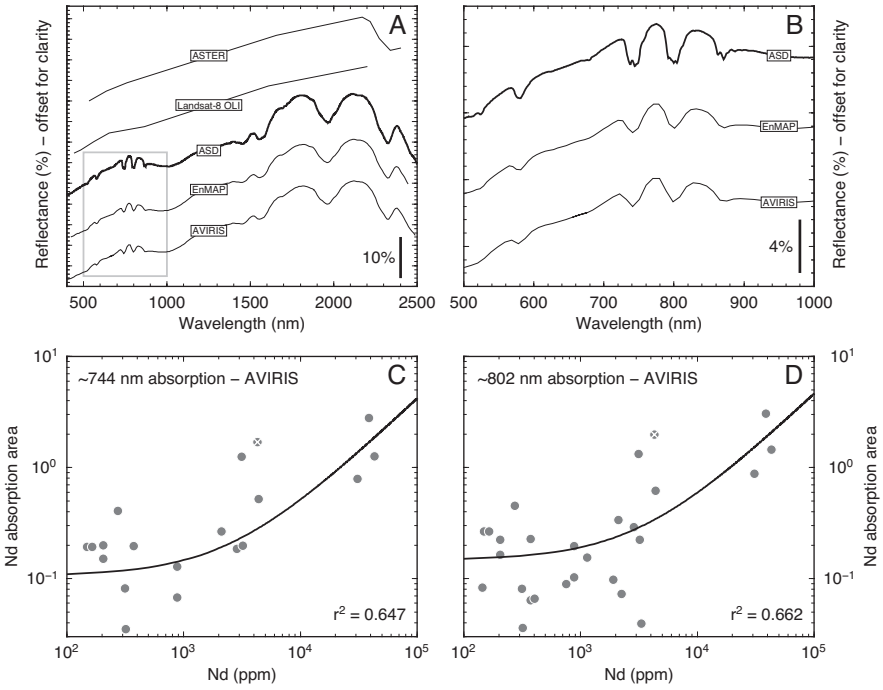

Fig. 13. A. Plot showing the effect of convolving (i.e., resampling) an ASD spectrum to the spectral response functions of a range of multispectral (ASTER and Landsat-8 OLI) and hyperspectral (EnMAP and AVIRIS) instruments. While most spectral information is lost in the convolved ASTER and Landsat-8 OLI spectra, much information is retained in the convolved EnMAP and AVIRIS spectra. B. Zoomed in region of plot (A), showing how the coarse structure of the four largest Nd absorption features is retained following spectral convolution. Fine features, such as the multiple absorptions within the main absorptions centered at ~744 nm, ~802 nm, and ~871 nm are not retained in the convolved data. C. and D. Plots showing the correlations between Nd absorption area in spectra convolved to the AVIRIS spectral response function and whole-rock Nd content for absorptions centered at (C) ~744 nm and (D) ~802 nm.

multispectral instruments are thus capable of identifying and delimiting carbonatites but are unable to provide useful information about their REE contents (Rowan and Mars, 2003; Mars and Rowan, 2011).

In contrast, the spectral resolutions of AVIRIS and EnMAP are sufficient to resolve four prominent Nd absorptions between 550 and 900 nm (Fig. 13A, B). Although the coarser spectral resolution of remote sensing instruments with respect to the ASD (~7 vs. 3–6 nm) results in smoothing of absorptions, individual absorption features remain clear and distinct. However, the spectral resolution of convolved data is insufficient to fit Gaussian curves to background-subtracted Nd features in a consistent manner. Nevertheless, relationships between the area of Nd absorption features centered at both ~744 and ~802 nm, and REE grade remain strong (Fig. 13C, D). EnMAP and AVIRIS thus have the necessary characteristics to detect Nd at economically relevant grades in range of geologic samples.

REE detectability as a function of signal-to-noise ratio

While EnMAP and AVIRIS have sufficient spectral resolutions to detect Nd in REE-rich samples, it is important to assess whether the Nd absorptions are detectable at realistically attainable signal-to-noise ratios. EnMAP spectra are expected to reach signal-to-noise ratios of ~500:1 at 495 nm and ~150:1 at 2,200 nm (www.enmap.org/sites/default/files/pdf/Table_EnMAP_Specs.pdf), though signal-to-noise ratios could be significantly lower during routine operations. Signal-to-noise ratios of AVIRIS spectra have improved significantly since the system's introduction in 1989, and can now reach in excess of 1000:1 at VNIR wavelengths and 500:1 at SWIR wavelengths under optimum conditions (Green et al., 1998; Veraverbeke et al., 2014). In order to investigate the relationship between Nd detectability and spectral signal-to-noise ratios, varying amounts of noise were added to convolved spectra using the method of Bioucas-Dias and Nascimento (2008) in order to generate a suite of spectra with signal-to-noise ratios spanning the range 10 to 500:1.

The effects of adding synthetic noise to convolved spectra are summarized in Figure 14, illustrating how the areas of Nd absorptions centered on ~744 and ~802 nm deviate from the areas calculated for convolved ASD when various amounts of synthetic noise are added. Data are shown for samples CR-16 and CR-49 that are moderately and highly enriched in REEs, respectively. On average, differences in Nd absorption area between ASD and synthetic noisy spectra (Δ) increase as signal-to-noise ratio decreases: below a signal-to-noise ratio of ~250:1, Δ increases at an increasing rate with decreasing signal-to-noise ratio.

At a signal-to-noise ratio of 250:1, Δ values for absorptions centered at ~744 and ~802 nm are ~20% for CR-16 and ~10% for CR-49. The lower Δ values for CR-49 are consistent with the greater abundance of REE minerals in this sample. The Δ values for spectra convolved to the AVIRIS spectral response functions are generally slightly lower than Δ values for spectra convolved to the EnMAP spectral response functions because of the higher spectral resolution of the AVIRIS system. Relative errors in Nd absorption areas are thus likely to be 10 to 20% at signal-to-noise ratios of ~250:1 when imaging REE-rich materials (Nd >30,000 ppm).

As the signal-to-noise ratio of convolved spectra decreases below ~250:1, the strength of correlations between Nd absorption area and Nd content decreases for absorptions centered at both ~744 and ~802 nm (Fig. 14C, D). REE detection will thus be most robust in datasets with signal-to-noise ratios in excess of ~250:1, though detection at lower signal-to-noise ratios may be possible.

Atmospheric inferences

While multispectral imaging bands are generally placed at wavelengths that avoid atmospheric absorption features (i.e., within "atmospheric windows"), hyperspectral instruments collect continuous spectra that encompass numerous atmospheric absorptions (Goetz, 2009). Hyperspectral datasets therefore require careful correction for atmospheric absorption effects generated by the presence of various species, including H_2O, O_3, CO_2, O_2 and CH_4, before they can be interpreted (e.g., Gao et al., 1993, 2009). In order to assess the likely impact of atmospheric interferences on the imaging of REE deposits, we used the MODTRAN® radiative transfer model. This simulates atmospheric conditions relevant to hyperspectral remote sensing along the coastal strips of Greenland, a likely target for remote sensing campaigns (Berk et al., 1998, 2005). The model was parameterized to simulate a 50° solar elevation angle, a sensor with nadir viewing of a target at sea level and a subarctic atmospheric profile with a maritime atmospheric profile. The results of MODTRAN® simulations are shown in Figure 15, where atmospheric transmission is plotted as a function of wavelength in order to illustrate absorption features generated by a number of important atmospheric gases and aerosols.

The largest atmospheric features are ~200-nm-wide H_2O absorptions centered at ~1,400 and ~1,900 nm that block all transmission at these wavelengths; no geologic information can be recovered at ~1,300 to 1,500 or ~1,800 to 2,000 nm. Substantial H_2O absorptions (transmission >0.4) also occur at 950, 1,150, and 2,500 nm that degrade geologic interpretations (Fig. 15). Although the major atmospheric absorptions occur at wavelengths greater than main Nd absorptions, smaller atmospheric features occur within 580- to 870-nm range. Specifically, modest H_2O absorptions centered at ~720 and 820 nm have the potential to complicate the identification of Nd absorption features centered at ~744 and ~802 nm. A narrow but deep O_3 absorption feature 770 nm may also interfere with the identification of absorptions at ~744 and ~802 nm, and a broad O_3 absorption centered at ~590 nm may affect the ability to resolve absorptions centered at ~583 nm. Even though the precise nature of atmospheric corrections required will vary from campaign to campaign this simplistic treatment demonstrates that there is significant atmospheric transmission at the wavelengths relevant to the identification of Nd. Thus, if high-quality atmospheric corrections are applied to datasets with high signal-to-noise ratios, Nd features should remain detectable, though ground calibration may also be required to sufficiently reduce radiative transfer atmospheric residuals.

Spatial resolution: Outcrop versus pixel sizes

Having established that Nd should be detectable at high grades by hyperspectral instruments under optimal conditions, it is

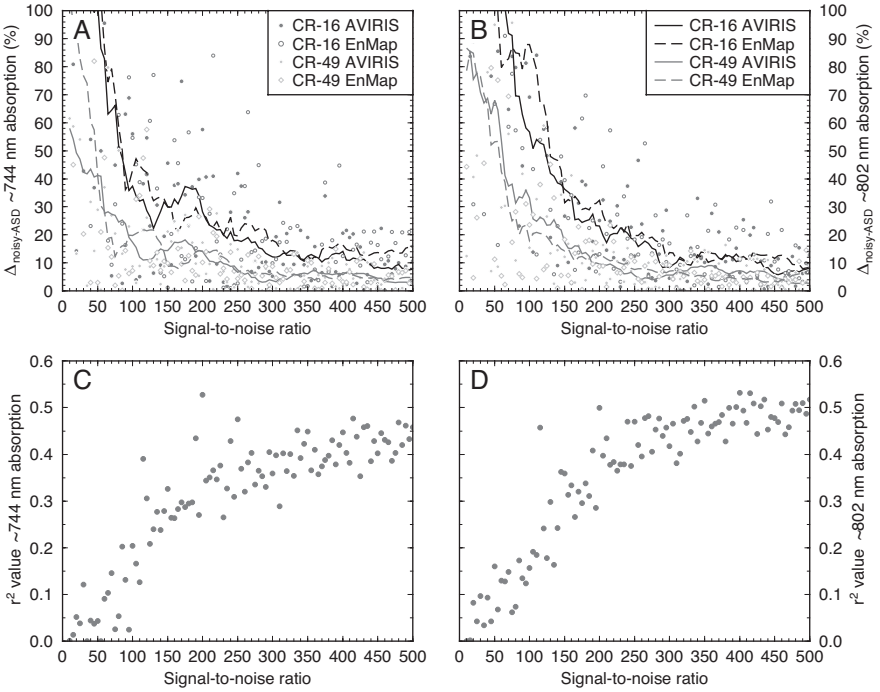

Fig. 14. A. and B. Plots showing how the area of absorption features in convolved spectra diverge from the area of absorption features measured by ASD as varying amounts of synthetic noise are added. The absolute difference between noisy convolved spectra and ASD spectra is expressed in % and given the notation $\Delta_{noisy\text{-}ASD}$. The effects of adding noise are shown for a moderately REE rich sample (CR-16) and a very REE rich sample (CR-49). The relationship between spectra signal-to-noise ratio and $\Delta_{noisy\text{-}ASD}$ are shown for the ~744 nm and ~802 nm absorptions in (A) and (B), respectively. Solid and dashed lines show the smoothed variation of $\Delta_{noisy\text{-}ASD}$ with signal-to-noise ratio for data convolved to the AVIRIS and EnMAP spectral response functions, respectively. C. and D. Plots illustrating how adding varying amounts of synthetic noise to spectra convolved to the AVIRIS spectral response function degrades correlations between Nd absorption area and whole-rock Nd content for absorptions centered at (C) ~744 nm and (D) ~802 nm.

important to assess whether their spatial resolution is sufficient to detect zones of REE mineralization. Although some REE deposits, such as the Sulphide Queen Orebody at Mountain Pass and Bayan Obo outcrop on hundreds of meter length scales (Castor, 2008; Smith et al., 2015), most REE occurrences are meter-scale dikes and veins (Mitchell, 2005). It is therefore likely that the outcropping portions of most REE deposits will be too small to be detected using satellite-based platforms: EnMAP is expected to have a spatial resolution of 30 m at VNIR wavelengths. Airborne platforms can achieve the meter-scale spatial resolutions required: up to ~4 and ~0.5 m for AVIRIS and CASI, respectively (Kruse, 2012; Black et al., 2014), and hence represent a much better tool for REE mapping. Perhaps the greatest opportunity for REE remote sensing would involve the deployment of hyperspectral instruments on unmanned aerial vehicles. While still at early stages of development, unmanned aerial vehicles could enable hyperspectral mapping to be carried out at the centimeter scale (Hugenholtz, 2012; Colomina and Molina, 2014), making it possible to map Nd grade across whole deposits. Indeed, the feasibility of such fine-scale mapping has already been demonstrated using ground-based hyperspectral imaging of monazite enrichments in the Fen complex (Boesche et al., 2015).

Applications

Our results indicate that direct detection of REEs by hyperspectral imaging will be best suited to high-grade deposits, such as carbonatites that contain discrete REE minerals. It would also be applicable to other high-grade igneous and metamorphic (Steenkampskraal-type monazite) and hydrothermal deposits. However, given the general relationship between Nd absorption depth and abundance (Fig. 12), it will be more difficult to make the technique sufficiently robust for

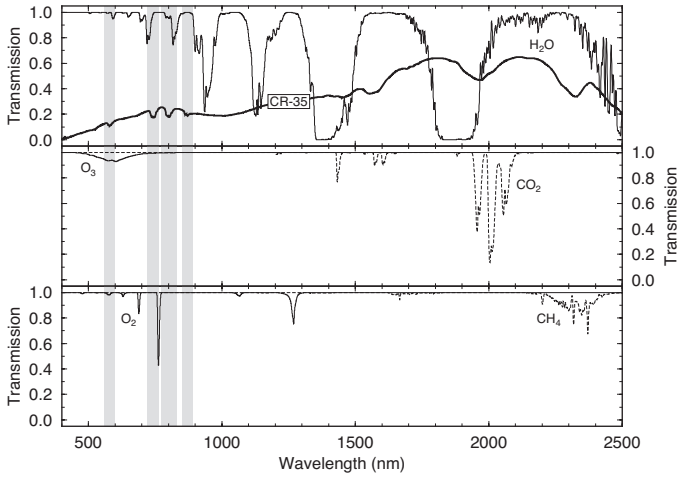

Fig. 15. Plot summarizing the transmission of major atmospheric gases and aerosols at VNIR-SWIR wavelengths simulated, using the MODTRAN radiative transfer model (Berk et al., 1998, 2005). The model was parameterized to simulate a 50° solar elevation angle, a sensor with nadir viewing of a target at sea level, and the subarctic atmospheric profile with a maritime aerosol model; indicative of the likely conditions in Greenland. A typical REE-rich sample spectrum is shown for reference. Although atmospheric absorption features are present at the wavelengths relevant to REE detection, none reduce transmission to zero, as occurs at higher wavelengths.

identifying lower grade REE deposits, such as those currently of interest for their higher proportions of mid and heavy REEs, in either carbonatitic or silicate systems. Although the technique could detect Nd in the eudialyte-bearing kakortokite tested here, further development is necessary to correlate Nd absorption features with the lower Nd concentrations characteristic of nepheline syenites (Wall, 2014). The same holds true for apatite-bearing deposits where whole-rock REE concentrations will be below levels where correlations between spectral properties and Nd content become clear: apatite typically contains only up to 1 or 2 wt % ΣREO.

Nevertheless, hyperspectral remote sensing is potentially superior to radiometric surveys, a traditional REE exploration tool in which radioactivity from U and Th serve as pathfinders to REE-rich rocks. However, U and Th are penalty elements and an ideal REE deposit has high REE but low U and Th. Hyperspectral imaging can target REEs directly and help find deposits low in radioactive elements.

Nd is a LREE, and the main driver for the REE market owing to its use in high-strength permanent magnets, but there is also a current need to find new sources of HREEs (Hatch, 2012): using Nd as a pathfinder element unfortunately makes the technique inapplicable to xenotime-(Y) deposits, such as Lofdal (Namibia) and Browns Range (Australia) because xenotime-(Y) contains very low Nd contents. At Lofdal, however, there are also LREE minerals in addition to xenotime-(Y), so direct hyperspectral imaging of LREEs might be a guide to HREE-rich dikes and surrounding mineralization. Hyperspectral imaging has been applied to exploration at Lofdal but only for the detection of carbonate, not as a direct indicator of REE content (Swinden and Siegfried, 2011; Do Cabo, 2014). Nepheline syenite deposits are also often cited as HREE deposits. While alkaline rocks tend to contain minerals with higher HREE/LREE ratios than typical carbonatite deposits (e.g., eudialyte), HREE minerals are generally scarce and whole-rock Nd concentrations remain appreciable with respect to HREE concentrations. Nd could thus still be used in the exploration of these deposits if problems associated with of detecting low Nd concentrations can be overcome. While there is potential for detecting HREEs by reflectance spectroscopy (e.g., Dy, Ho, and Er; Adams, 1965; Antonovich et al., 2007), we did not identify these elements in our LREE-dominated samples. In any case, published reference spectra for HREE-rich materials are sparse and obtaining such spectra thus represents a key future objective in the development of REE remote sensing.

Conclusions

Nd absorption features, which are the strongest LREE absorption features at VNIR-SWIR wavelengths, have been identified in reflectance spectra collected from a suite of predominantly carbonatitic samples with variable REE contents. Absorption features centered at wavelengths of ~583, ~744, ~802, and ~871 nm were detected by laboratory reflectance spectroscopy in samples with Nd concentrations >1,000 ppm. Nd absorption features are dominantly elemental in nature and do not change significantly as a function of host mineralogy at the FWHM of an ASD spectroradiometer. Continuum removal was performed using a third-order polynomial fit around the wavelength brackets of each Nd absorption

feature; this allowed for the subtraction of the background spectrum which isolated the Nd absorption feature(s) and suppressed the spectral variability associated with changes in sample composition and mineralogy. Nd absorption features depth and area correlate positively with whole-rock Nd content, though correlations between Nd concentration and Nd absorption area are generally more robust. Absorptions centered at wavelengths of ~744 and ~802 nm give the most reliable fits (r^2 ~0.7). Nd absorption features in VNIR reflectance spectra thus represent a crude proxy for whole-rock Nd content under laboratory conditions.

Convolving laboratory reflectance spectra to the spectral response functions of various remote sensing instruments demonstrates that, while multispectral platforms lack the spectral resolution to resolve Nd absorption features at geologically relevant concentrations, hyperspectral platforms such as AVIRIS and EnMAP have the spectral resolution needed to detect narrow Nd absorptions. Correlations between whole-rock Nd content and Nd absorption areas are moderately strong following spectral convolution (r^2 ~0.6). The addition of synthetic noise to convolved spectra indicates that spectral signal-to-noise ratios of at least ~250:1 are required for relationships between Nd grade and spectral properties to remain robust, i.e., Nd features will only be resolvable in high-quality datasets. Fortunately, the results of simple atmospheric modeling confirm that atmospheric transmission mostly remains above 0.8 within the crucial 500- to 900-nm wavelength interval within which Nd may be detected. A final consideration of the spatial resolution of different hyperspectral systems shows that, while satellite-based instruments currently lack the spatial resolution to detect the meter-scale REE enrichments that occur within carbonatites, many airborne platforms will not suffer from the same limitations. With high-quality datasets (signal-to-noise >250:1) and well-constrained atmospheric models it should be possible to image Nd in high-grade, carbonatite-hosted REE deposits (Nd ~30,000 ppm) regardless of REE host mineralogy using currently available technology. While our proposed technique is dependent on the presence of Nd, and may be unsuitable for detecting some HREE-rich deposits, it offers a key advantage over radiometric surveys allowing the detection of REEs to be isolated from the detection of radioactive penalty elements. Mounting hyperspectral sensors on unmanned aerial vehicles offers the exiting possibility of being able to map REE grade across whole deposits at resolutions as fine as a few centimeters in the near future.

Acknowledgments

We thank Jon Russill and Adrian Finch from SRK Consulting (UK) Ltd. and the University of St. Andrews, respectively, for providing samples. Alan Woolley and David Smith helped with the loan of samples from the Natural History Museum in London. Dan Pemberton and Rob Theodore helped with the loan of samples from the Harker Collection at the University of Cambridge. Chris MacLellan provided invaluable guidance with the collection of spectroscopic data at the Natural Environment Research Council Field Spectroscopy Facility at the University of Edinburgh. Nick Marsh at the University of Leicester carried out the XRF analyses on our highly challenging sample suite. We also thank Rob Clark, Jason Day, and Iris Buisman at the University of Cambridge for their assistance with sample preparation, SEM imaging, and EDX analyses. Todd Hoefen and Lyle Mars provided detailed and highly constructive reviews that significantly improved the quality of the manuscript. Finally, we thank Larry Meinert for his efficient editorial handling.

DAN and the project as a whole were supported by funds from the University of Cambridge Higher Education Innovation Funding (HEIF) allocation, as part of the effort to establish a new Innovation Centre for the Environment located at the British Antarctic Survey (BAS). MB was supported by a Natural Environment Research Council (NERC) Research Studentship (NE/K50094X/1).

REFERENCES

Adams, J.W., 1965, The visible region absorption spectra of rare earth minerals: American Mineralogist, v. 50, p. 356–366.

Andersen, T., 1988, Evolution of peralkaline calcite carbonatite magma in the Fen complex, southeast Norway: Lithos, v. 22, p. 99–112.

Antonovich, V.P., Stoyanova, I.V., Chivireva, N.A., Timukhin, E.V., Zinchenko, V.F., and Efryushina, N.P., 2007, Identification and quantitative determination of some inorganic lanthanide compounds by diffuse reflectance spectroscopy: Journal of Analytical Chemistry, v. 62, p. 238–244.

Bailey, J.C., Gwozdz, R., Rose-Hansen, J., and Sørensen, H., 2001, Geochemical overview of the Ilímaussaq alkaline complex, South Greenland: Geology of Greenland Survey Bulletin, v. 190, p. 35–53.

Basu, N.K., and Mayila, A., 1986, Petrographic and chemical characteristics of the Panda Hill carbonatite complex, Tanzania: Journal of African Earth Sciences, v. 5, p. 589–598.

Bedini, E., 2009, Mapping lithology of the Sarfartoq carbonatite complex, southern West Greenland, using HyMap imaging spectrometer data: Remote Sensing of Environment, v. 113, p. 1208–1219.

Berk, A., Bernstein, L.S., Anderson, G.P., Acharya, P.K., Robertson, D.C., Chetwynd, J.H., and Adler-Golden, S.M., 1998, MODTRAN cloud and multiple scattering upgrades with application to AVIRIS: Remote Sensing of Environment, v. 65, p. 367–375.

Berk, A. et al., 2005, MODTRAN5: A reformulated atmospheric band model with auxiliary species and practical multiple scattering options: Proceedings of SPIE, v. 5655, p. 88–95.

Bioucas-Dias, J.M., and Nascimento, J.M.P., 2008, Hyperspectral subspace identification: IEEE Transactions on Geoscience and Remote Sensing, v. 46, p. 2435–2445.

Black, M., Fleming, A., Riley, T.R., Ferrier, G., Fretwell, P., McFee, J., Achal, S., and Diaz, A.U., 2014, On the atmospheric correction of Antarctic airborne hyperspectral data: Remote Sensing, v. 6, p. 4498–4514.

Boesche, N., Rogass, C., Lubitz, C., Brell, M., Herrmann, S., Mielke, C., Tonn, S., Appelt, O., Altenberger, U., and Kaufmann, H., 2015, Hyperspectral REE (rare earth element) mapping of outcrops—applications for neodymium detection: Remote Sensing, v. 7, p. 5160–5186.

Bradshaw, C., 1988, A petrographic, structural and geochemical study of the alkaline igneous rocks of the Motzfeldt centre, south Greenland: Durham, UK, Durham University, 401 p.

Brooker, R.A., and Kjarsgaard, B.A., 2011, Silicate-carbonate liquid immiscibility and phase relations in the system SiO_2-Na_2O-Al_2O_3-CaO-CO_2 at 0.1-2.5 GPa with applications to carbonatite genesis: Journal of Petrology, v. 52, p. 1281–1305.

Broom-Fendley, S., Styles, M.T., Appleton, J.D., Gunn, G., and Wall, F., 2016, Evidence for dissolution-reprecipitation of apatite and preferential LREE mobility in carbonatite-derived late-stage hydrothermal processes: American Mineralogist, v. 101, p. 596–611, http://www.minsocam.org/msa/ammin/toc/2016/index.html?issue_number=03.

Do Cabo, V.N., 2014, Geological, mineralogical and geochemical characterisation of the heavy rare earth-rich carbonatites at Lofdal, Namibia: Exeter, UK, University of Exeter, 548 p.

Campbell, L.S., and Henderson, P., 1997, Apatite paralgenesis in the Bayan Obo REE-Nb-Fe ore deposit: Lithos, v. 42, p. 89–103.

Castor, S.B., 2008, The Mountain Pass rare-earth carbonatite and associated ultrapotassic rocks, California: Canadian Mineralogist, v. 46, p. 779–806.

Chakhmouradian, A.R., and Zaitsev, A.N., 2012, Rare earth mineralization in igneous rocks: Sources and processes: Elements, v. 8, p. 347–353.

Christensen, P.R., Bandfield, J.L., Hamilton, V.E., Howard, D.A., Lane, M.D., Piatek, J.L., Ruff, S.W., and Stefanov, W.L., 2000, A thermal emission spectral library of rock-forming minerals: Journal of Geophysical Research, v. 105, p. 9735–9739.

Clark, R.N., 1995, Reflectance spectra: Rock physics and phase relations. A handbook of physical constants: American Geophysical Union Reference Shelf 3, p. 178–188.

Clark, R.N., and Roush, T.L., 1984, Reflectance spectroscopy: Quantitative analysis techniques for remote sensing applications: Journal of Geophysical Research, Solid Earth, v. 89, p. 6329–6340.

Clark, R.N., Swayze, G., Wise, R., Livo, E., Hoefen, T., Kokaly, R., and Sutley, S.J.J., 2007, U.S. Geological Survey Digital Spectral Library splib06a: U.S. Geological Survey, Digital Data Series 231, http://speclab.cr.usgs.gov/spectral.lib06.

Colomina, I., and Molina, P., 2014, Unmanned aerial systems for photogrammetry and remote sensing: A review: International Society for Photogrammetry and Remote Sensing, ISPRS Journal of Photogrammetry and Remote Sensing, v. 92, p. 79–97.

Dawson, J.B., and Hinton, R.W., 2003, Trace-element content and partitioning in calcite, dolomite and apatite in carbonatite, Phalaborwa, South Africa: Mineralogical Magazine, v. 67, p. 921–930.

Dieke, G.H., 1970, Spectra and energy levels of rare earth ions in crystals: American Journal of Physics, v. 38, p. 399.

Drew, L.J.J., Qingrun, M., and Weijun, S., 1990, The Bayan Obo iron-rare-earth-niobium deposits, Inner Mongolia, China: Lithos, v. 26, p. 43–65.

Eby, G.N., Lloyd, F.E., and Woolley, A.R., 2009, Geochemistry and petrogenesis of the Fort Portal, Uganda, extrusive carbonatite: Lithos, v. 113, p. 785–800.

Erdosh, G., 1979, The Ontario carbonatite province and its phosphate potential: Economic Geology, v. 74, p. 331–338.

Eriksson, S.C., 1989, Phalaborwa: A saga of magmatism, metasomatism and miscibility, *in* Bell, K., ed., Carbonatites, genesis and evolution: London, Unwin Hyman, p. 221–254.

Ferguson, J., 1970, The differentiation of agpaitic magmas: The Ilímaussaq intrusion, South Greenland: Canadian Mineralogist, v. 10, p. 335–394.

Fitton, J.G., and Upton, B.G.J., 1987, Alkaline igneous rocks: Oxford, Blackwell, p. 558–559.

Freestone, I.C., and Hamilton, D.L., 1980, The role of liquid immiscibility in the genesis of carbonatites—an experimental study: Contributions to Mineralogy and Petrology, v. 73, p. 105–117.

Gaffey, S.J., 1985, Reflectance spectroscopy in the visible and near-infrared (0.35–2.55 um): Applications in carbonate petrology: Geology, v. 13, p. 270–273.

Gao, B.C., Heidebrecht, K.B., and Goetz, A.F.H., 1993, Derivation of scaled surface reflectances from AVIRIS data: Remote Sensing of Environment, v. 178, p. 165–178.

Gao, B.C., Montes, M.J., Davis, C.O., and Goetz, A.F.H., 2009, Atmospheric correction algorithms for hyperspectral remote sensing data of land and ocean: Remote Sensing of Environment, v. 113, p. S17–S24.

Garson, M.S.S., 1965, Carbonatites of southern Malawi: Bulletin of the Geological Survey of Malawi, v. 15, p. 1–128.

Gittins, J., 1989, The origin and evolution of carbonatite magmas, *in* Bell, K., ed., Carbonatites, genesis and evolution: London, Unwin Hyman, p. 580–600.

Goetz, A.F.H., 2009, Three decades of hyperspectral remote sensing of the Earth: A personal view: Remote Sensing of Environment, v. 113, p. S5–S16.

Goetz, A.F.H., Vane, G., Solomon, J.E., and Rock, B.N., 1985, Imaging spectrometry for Earth remote sensing: Science, v. 228, p. 1147–1153.

Görller-Walrand, C., and Binnemans, K., 1998, Spectral intensities of f-f transitions, *in* Schneidner, K.A.G., and Eyring, L., eds., Handbook on the Physics and Chemistry of Rare Earths: Amsterdam, Elsevier, p. 101–264.

Green, R.O. et al., 1998, Imaging spectroscopy and the Airborne Visible/Infrared Imaging Spectrometer (AVIRIS): Remote Sensing of Environment, v. 65, p. 227–248.

Guanter, L. et al., 2015, The EnMAP spaceborne imaging spectroscopy mission for Earth observation: Remote Sensing, v. 7, p. 8830–8857.

Harmer, R.E., and Gittins, J., 1998, The case for primary, mantle-derived carbonatite magma: Journal of Petrology, v. 39, p. 1895–1903.

Hatch, G.P., 2012, Dynamics in the global market for rare earths: Elements, v. 8, p. 341–346.

Hook, S.J., and Kahle, A.B., 1996, The micro Fourier transform interferometer (μFTIR)—a new field spectrometer for acquisition of infrared data of natural surfaces: Remote Sensing of Environment, v. 56, p. 172–181.

Hook, S.J., Karlstrom, K.E., Miller, C.F., and McCaffrey, K.J.W., 1994, Mapping the Piute Mountains, California, with thermal infrared multispectral scanner (TIMS) images: Journal of Geophysical Research, v. 99, p. 15605–15622.

Hornig-Kjarsgaard, I., 1998, Rare earth elements in Sövitic carbonatites and their mineral phases: Journal of Petrology, v. 39, p. 2105–2121.

Huang, Y.-M., Hawkesworth, C.J., van Calsteren, P., and McDermott, F., 1995, Geochemical characteristics and origin of the Jacupiranga carbonatites, Brazil: Chemical Geology, v. 119, p. 79–99.

Hugenholtz, C., 2012, Small unmanned aircraft systems for remote sensing and earth science research: EOS, v. 93, p. 24–25.

Jones, A.P., and Larsen, L.M., 1985, Geochemistry and REE minerals of nepheline syenites from the Motzfeldt centre, south Greenland: American Mineralogist, v. 70, p. 1087–1100.

Kahle, A.B., and Alley, R.E., 1992, Separation of temperature and emittance in remotely sensed radiance measurements: Remote Sensing of Environment, v. 111, p. 107–111.

Kerr, A., Rafuse, H., Sparkes, G., Hinchey, J., and Sandeman, H., 2011, Visible/infrared spectroscopy (VIRS) as a research tool in economic geology: Background and pilot studies from Newfoundland and Labrador: Geological Survey of Canada Report 11-1, p. 145–166.

Korb, A.R., Dybwad, P., Wadsworth, W.J., and Salisbury, J.W., 1996, Portable Fourier transform infrared spectroradiometer for field measurements of radiance and emissivity.: Applied Optics, v. 35, p. 1679–1692.

Kramer, H.J., 2002, Observation of the earth and its environment: Survey of missions and sensors: Berlin Heidelberg, Springer-Verlag.

Kruse, F.A., 2012, Mapping surface mineralogy using imaging spectrometry: Geomorphology, v. 137, p. 41–56.

Le Bas, M.J., Le Maître, R.W., Streckeisen, A., and Zanettin, B., 1986, A chemical classification of volcanic rocks based on the total alkali-silica diagram: Journal of Petrology, v. 27, p. 745–750.

Le Maître, R.W., 2002, Igneous rocks: A classification and glossary of terms: Cambridge, Cambridge University Press.

Liu, G., 2005, Electronic energy level structure, *in* Hull, R., Parisi, J., Osgood, R.M., Warlimont, H., Liu, G., and Jacquier, B.,eds., Spectroscopic properties of rare earths in optical materials: Berlin, Springer, p. 1–94.

Lottermoser, B.G., 1990, Rare-earth element mineralisation within the Mt.Weld carbonatite laterite, Western Australia: Lithos, v. 24, p. 151–167.

Mariano, A.N., 1989, Nature of economic mineralisation in carbonatites and related rocks, *in* K.Bell, ed., Carbonatites, genesis and evolution: London, Unwin Hyman, p. 149–176.

Mars, J.C., and Rowan, L.C., 2011, ASTER spectral analysis and lithologic mapping of the Khanneshin carbonatite volcano, Afghanistan: Geosphere, v. 7, p. 276–289.

McCormick, G.R., and Le Bas, M.J., 1996, Phlogopite crystallization in carbonatitic magmas from Uganda: Canadian Mineralogist, v. 34, p. 469–478.

McCreath, J.A., Finch, A.A., Herd, D.A., and Armour-Brown, A., 2013, Geochemistry of pyrochlore minerals from the Motzfeldt center, south Greenland: The mineralogy of a syenite-hosted Ta, Nb deposit: American Mineralogist, v. 98, p. 426–438.

Mitchell, R.H., 2005, Carbonatites and carbonatites and carbonatites: Canadian Mineralogist, v. 43, p. 2049–2068.

——2015, Primary and secondary niobium mineral deposits associated with carbonatites: Ore Geology Reviews, v. 64, p. 626–641.

Nicodemus, F.E., 1965, Reflectance nomenclature and directional reflectance and emissivity: Applied Optics, v. 7, p. 767–775.

Ninomiya, Y., Fu, B., and Cudahy, T.J., 2005, Detecting lithology with advanced spaceborne thermal emission and reflection radiometer (ASTER) multispectral thermal infrared "radiance-at-sensor" data: Remote Sensing of Environment, v. 99, p. 127–139.

Olson, J.C., Shawe, D.R., Pray, L.C., and Sharp, W..N., 1954, Rare-earth mineral deposits of the Mountain Pass district, San Bernardino County, California.: Science, v. 119, p. 325–326.

Oppenheimer, C., 1998, Satellite observation of active carbonatite volcanism at Ol Doinyo Lengai, Tanzania: International Journal of Remote Sensing, v. 19, p. 55–64.

Rankin, A.H., 1977, Fluid-inclusion evidence for the formation conditions of apatite from the Tororo carbonatite complex of eastern Uganda: Mineralogical Magazine, v. 41, p. 155–164.

Ribeiro Da Costa, I., Rodrigues, P.C.R., Barriga, F.J.A.S., Rona, P.A., Nunes, C.D., and Vaz, P.D., 2013, Colourless aegirine in metamorphic rocks from Bayan Obo (Inner Mongolia): Lack of charge transfer transitions as possible explanation: European Journal of Mineralogy, v. 25, p. 987–993.

Rowan, L.C., and Mars, J.C., 2003, Lithologic mapping in the Mountain Pass, California area using advanced spaceborne thermal emission and reflection radiometer (ASTER) data: Remote Sensing of Environment, v. 84, p. 350–366.

Rowan, L.C., Kingston, M.J., and Crowley, J.K., 1986, Spectral reflectance of carbonatites and related alkalic igneous rocks: Selected samples from four North American localities: Economic Geology, v. 81, p. 857–871.

Rowan, L.C., Bowers, T.L., Crowley, J.K., Anton-Pacheco, C., Gumiel, P., and Kingston, M.J., 1995, Analysis of Airborne Visible-Infrared Imaging Spectrometer (AVIRIS) data of the Iron Hill, Colorado, carbonatite-alkalic igneous complex: Economic Geology, v. 90, p. 1966–1982.

Simonetti, A., and Bell, K., 1994, Isotopic and geochemical investigation of the Chilwa Island carbonatite complex, Malawi: Evidence for a depleted mantle source region, liquid immiscibility, and open-system behaviour: Journal of Petrology, v. 35, p. 1597–1621.

Smith, M.O., Adams, J.B., and Johnson, P.E., 1985, Quantitative determination of mineral types and abundances from reflectance spectra using principal components analysis: Journal of Geophysical Research, v. 90, p. C797–C804.

Smith, M.P., Henderson, P., and Campbell, L.S., 2000, Fractionation of the REE during hydrothermal processes: Constraints from the Bayan Obo Fe-REE-Nb deposit, Inner Mongolia, China: Geochimica et Cosmochimica Acta, v. 64, p. 3141–3160.

Smith, M.P., Campbell, L.S., and Kynicky, J., 2015, A review of the genesis of the world-class Bayan Obo Fe-REE-Nb deposits, Inner Mongolia, China: Multistage processes and outstanding questions: Ore Geology Reviews, v. 64, p. 459–476.

Stuffler, T. et al., 2007, The EnMAP hyperspectral imager—an advanced optical payload for future applications in Earth observation programmes: Acta Astronautica, v. 61, p. 115–120.

Swinden, H.S., and Siegfried, P., 2011, Amended 43-101 technical report on the rare earth element occurrences in the Lofdal carbonatite complex, Kunene region, Khorixas district, Namibia: Halifax, Swinden Geoscience Consultants Ltd., 210 p.

Tappe, S., Foley, S.F., Stracke, A., Romer, R.L., Kjarsgaard, B.A., Heaman, L.M., and Joyce, N., 2007, Craton reactivation on the Labrador Sea margins: $^{40}Ar/^{39}Ar$ age and Sr-Nd-Hf-Pb isotope constraints from alkaline and carbonatite intrusives: Earth and Planetary Science Letters, v. 256, p. 433–454.

Tappe, S., Steenfelt, A., Heaman, L.M., and Simonetti, A., 2009, The newly discovered Jurassic Tikiusaaq carbonatite-aillikite occurrence, West Greenland, and some remarks on carbonatite-kimberlite relationships: Lithos, v. 112, p. 385–399.

Ting, W., Rankin, A.H., and Woolley, A.R., 1994, Petrogenetic significance of solid carbonate inclusions in apatite of the Sukulu carbonatite, Uganda: Lithos, v. 31, p. 177–187.

Turner, D.J., Rivard, B., and Groat, L.A., 2014, Visible and short-wave infrared reflectance spectroscopy of REE fluorocarbonates: American Mineralogist, v. 99, p. 1335–1346.

Vartiainen, H., and Paarma, H., 1979, Geological characteristics of the Sokli carbonatite complex, Finland: Economic Geology, v. 74, p. 1296–1306.

Veraverbeke, S., Stavros, E.N., and Hook, S.J., 2014, Assessing fire severity using imaging spectroscopy data from the Airborne Visible/Infrared Imaging Spectrometer (AVIRIS) and comparison with multispectral capabilities: Remote Sensing of Environment, v. 154, p. 153–163.

Wall, F., 2014, Rare earth elements, *in* Gunn, G., ed., Critical metals handbook: Oxford, John Wiley and Sons, p. 312–339.

Wall, F., and Mariano, A.N., 1996, Rare earth minerals in carbonatites: A discussion centered on the Kangankunde carbonatite, Malawi, *in* Jones, A.P., Wall, F., and Williams, C.T., eds., Rare earth minerals: Chemistry, origin and ore deposits: London, Chapman and Hall, p. 193–225.

Wall, F., and Zaitsev, A.N., 2004, Rare earth minerals in Kola carbonatites, *in* Wall, F., and Zaitsev, A.N., eds., Phosphorites and carbonatites from mantle to mine: The key example of the Kola alkaline province: Mineralogical Society Series 10, p. 341–373.

Wallace, M.E., and Green, D.H., 1988, An experimental determination of primary carbonatite magma composition: Nature, v. 335, p. 343–346.

Williams, C.E., 1952, Carbonatite structure: Tororo Hills, eastern Uganda: Geological Magazine, v. 89, p. 286.

Woolley, A.R., and Kempe, D.R.C., 1989, Carbonatites: Nomenclature, average chemical compositions, and element distribution, *in* Bell, K., ed., Carbonatites, genesis and evolution: London, Unwin Hyman, p. 1–14.

Woolley, A.R., and Kjarsgaard, B.A., 2008, Paragenetic types of carbonatite as indicated by the diversity and relative abundances of associated silicate rocks: Evidence from a global database: Canadian Mineralogist, v. 46, p. 741–752.

Woolley, A.R., Barr, M.W.C., Din, V.K., Jones, G.C., Wall, F., and Williams, C.T., 1991, Extrusive carbonatites from the Uyaynah area, United Arab Emirates: Journal of Petrology, v. 32, p. 1143–1167.

Yang, K.F., Fan, H.R., Santosh, M., Hu, F.F., and Wang, K.Y., 2011, Mesoproterozoic carbonatitic magmatism in the Bayan Obo deposit, Inner Mongolia, North China: Constraints for the mechanism of super accumulation of rare earth elements: Ore Geology Reviews, v. 40, p. 122–131.

Zaitsev, A.N., Demeny, A., Sindern, S., and Wall, F., 2002, Burbankite group minerals and their alteration in rare earth carbonatites—source of elements and fluids (evidence from C-O and Sr-Nd isotopic data): Lithos, v. 62, p. 15–33.

APPENDIX

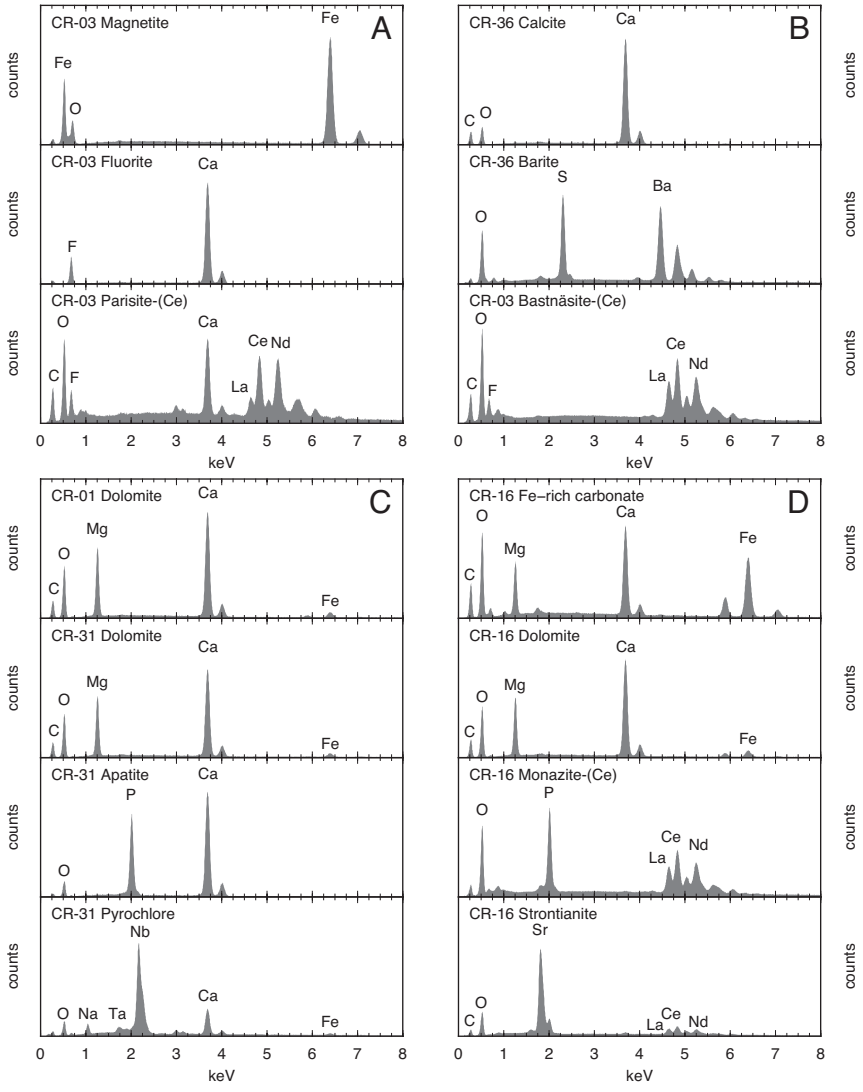

Fig. A1. Characteristic energy dispersive X-ray (EDX) spectra collected from a range of rock-forming and REE minerals. Peaks used for mineral identification are labeled according to element.

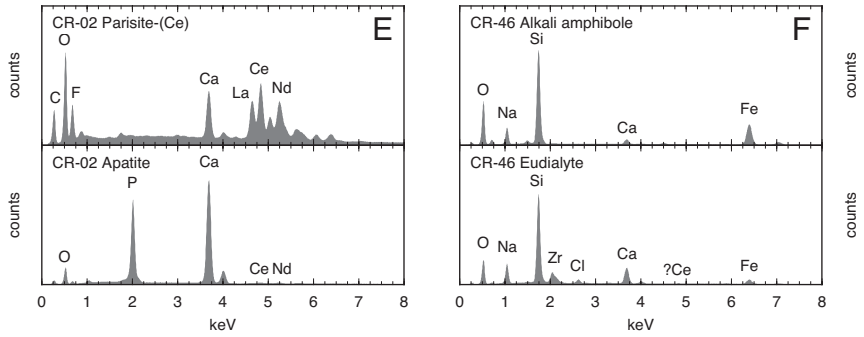

Fig. A1. *(Cont.)*

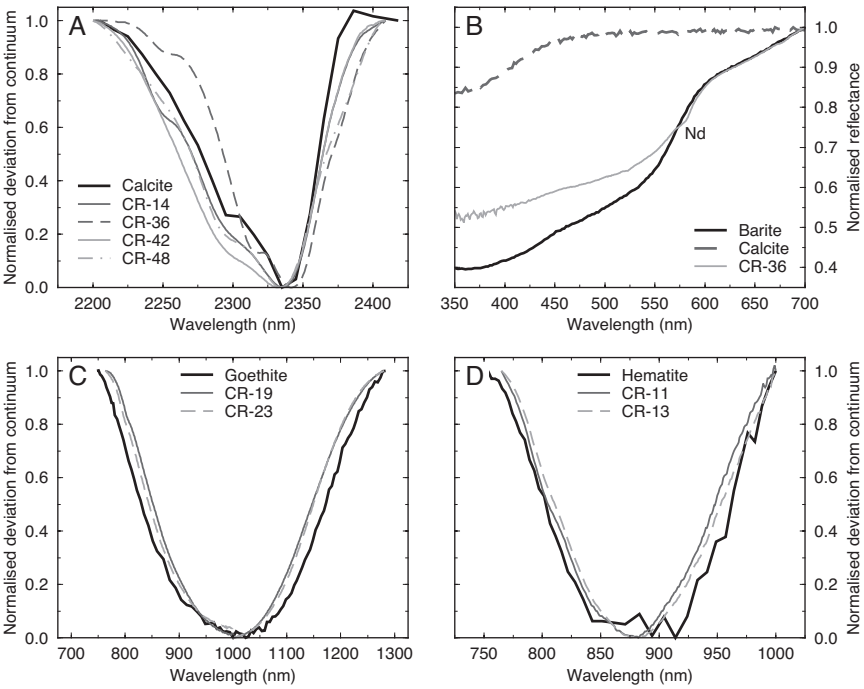

Fig. A2. A. Normalized continuum-removed spectra of CO_3 absorptions in a range of carbonate-rich samples compared with a calcite reference spectrum (Clark et al., 2007). All spectra show reflectance minima at ~2,330 nm. B. Normalized spectra of barite-rich, calcite-bearing CR-36 from Mountain Pass compared with barite and calcite reference spectra (Clark et al., 2007). The location of inflection points in the CR-36 spectrum are consistent with barite dominating the spectral signal, not calcite. A small additional absorption at ~583 nm can be attributed to Nd. C. Normalized continuum-removed spectra showing Fe absorptions in CR-19 and CR-23 from Kaiserstuhl and Songwe compared with a reference goethite spectrum (Clark et al., 2007). D. Normalized continuum-removed spectra showing Fe absorptions in CR-11 and CR-13 from Motzfeldt compared with a reference hematite spectrum (Clark et al., 2007).

The Cryosphere Discuss., doi:10.5194/tc-2016-56, 2016
Manuscript under review for journal The Cryosphere
Published: 7 March 2016

The Cryosphere Discussions
Open Access
EGU

A fully automated methodology for differentiating rock from snow, clouds and sea in Antarctica from Landsat imagery: A new rock outcrop map and area estimation for the entire Antarctic continent

Alex Burton-Johnson[1]*, Martin Black[1,2], Peter T. Fretwell[1] and Joseph Kaluza-Gilbert[3]

[1] British Antarctic Survey, Cambridge, CB3 OET, UK
[2] Department of Geography, Environment and Earth Sciences, University of Hull, Hull, HU6 7RX, UK
[3] School of Geography, Earth and Environmental Sciences, University of Birmingham, Birmingham, B15 2TT, UK

Correspondence to: Alex Burton-Johnson (alerto@bas.ac.uk)

Abstract. Differentiating exposed rock from snow and ice is a particular problem in Antarctica where extensive cloud cover and widespread shaded regions lead to classification errors. The existing rock outcrop dataset has significant georeferencing issues including overestimation and generalisation of rock exposure areas. The most commonly used method for automated rock and snow differentiation, the Normalised Difference Snow Index (NDSI), has difficulty differentiating rock and snow in Antarctica due to misclassification of shaded pixels and cannot differentiate illuminated rock from clouds. This study presents a new method for identifying rock exposures using Landsat 8 data. This is the first fully automated methodology for snow and rock differentiation that excludes areas of snow (both illuminated and shaded), clouds and liquid water whilst identifying both sunlit and shaded rock, achieving higher and more consistent accuracies than alternative data and methods such as the NDSI. The new methodology has been applied to the whole Antarctic continent (north of 82°40' S) using Landsat 8 data to produce a new rock outcrop dataset for Antarctica. The new data (merged with existing data south of 82°40' S) reveals that exposed rock forms 0.18% of the total land area of Antarctica; half of previous estimates.

1 Introduction

Differentiating areas of snow and exposed rock in Antarctica is important in a variety of contexts, including mapping, navigation, glaciological, geological and geomorphological research, and monitoring changes in the ice sheet and its response to climate change. The only existing continent-wide geospatial dataset for exposed rock in Antarctica is available from the Scientific Committee on Antarctic Research (SCAR) Antarctic Digital Database (ADD) website, www.add.scar.org. This data (the ADD rock outcrop dataset) has been derived through manual identification and digitization of published topographic maps. This data comes from a variety of sources and variety of scales and accuracies, so the quality of the dataset is regionally inconsistent and has no quality assessment associated with it (in contrast to the automated identification method presented here for which accuracies and error sources have been determined). Although extensively used (over 2500 downloads of the rock dataset in the last 3 years) the data suffers from poor georeferencing, frequent misclassification of shaded snow as rock, as

The Cryosphere Discuss., doi:10.5194/tc-2016-56, 2016
Manuscript under review for journal The Cryosphere
Published: 7 March 2016

well as overestimating and generalising areas of rock exposure. Additionally as satellite derived coastlines and digital elevation models become available, the inconsistency and inaccuracy of the present cartographically derived ADD rock outcrop dataset becomes difficult to resolve with these new data sources. There is therefore an urgent need to improve the consistency georeferencing and accuracy of rock outcrop data for Antarctica.

In several temperate regions methods have been formulated to automatically identify exposed rock outcrop from satellite imagery (e.g. Racoviteanu *et al.* 2010, Dozier 1989, Hall *et al.* 1995, Paul *et al.* 2002, Paul *et al.* 2009, Bolch *et al.* 2010, Zhu & Woodcock 2012, Zhu *et al.* 2015), but the methods have never been applied to Antarctica. The most commonly used existing method for delineating snow cover and rock outcrop is the Normalised Difference Snow Index (NDSI, Hall *et al.* 1995, Dozier 1989). The NDSI was developed following other indices, such as the Normalised Difference Vegetation Index (NDVI, Tucker 1986, Tucker 1979), initially for application to MODIS and Landsat satellite imagery. The NDSI is calculated according to equation (1) (modified for Landsat 8 data) where Landsat 8 band 3 equates to spectral wavelengths of 0.53 to 0.59 µm (the green band) and Landsat 8 band 6 equates to spectral wavelengths of 1.57 to 1.65 µm (the short wavelength infrared band, SWIR 1):

$$NDSI = \frac{Landsat\ 8\ band\ 3 - Landsat\ 8\ band\ 6}{Landsat\ 8\ band\ 3 + Landsat\ 8\ band\ 6} \quad (1)$$

Equation (1) works on the basis that snow reflects visible wavelengths more strongly than middle-infrared wavelengths whilst rock displays a slightly higher reflectance for middle infrared wavelengths than visible wavelengths (Fig. 1) and so a threshold value can be determined for the NDSI of an image differentiating pixels of snow and rock (typically in the range 0.25 to 0.45 - Hall *et al.*, 1995). One problem for application of the thresholded NDSI technique to automated snow and rock differentiation is that the optimal threshold value must be determined for each individual image being analysed or even within the same image due to changes in illumination or fresh snow cover across the image's area (Burns and Nolin, 2014). It is often the case that the optimal threshold is manually determined on each scene by comparison to reference data, however this becomes a problem when large numbers of images need to be analysed or reference data is not available.

Although the application of the NDSI has been successful at lower latitudes (e.g. Burns & Nolin 2014) where vertically illuminated imagery is available, high solar elevation angles in Antarctica lead to exclusion of shaded rock. This issue of shaded rock is greater in Antarctica where unavoidably low sun angle results in large percentages of the outcrop being in shadow. The problem has been addressed for glacier mapping at lower latitudes by thresholding the Landsat blue band (in addition to an NDSI or alternative band ratio threshold) due to the higher reflectance of shaded snow than shaded rock in blue wavelengths (Arendt et al., 2012; Bishop et al., 2004; Paul et al., 2007; Paul and Kääb, 2005).

Unavoidable cloud cover in some Antarctic images, especially on the Antarctic Peninsula, leads to the classification of clouds as rock exposure by the NDSI technique (Fig. 2) as the two are indiscernible using this methodology. Any effective dataset of rock outcrop in Antarctica would have to ensure that clouds are not misrepresented.

A further problem for automated rock identification at lower latitudes is debris cover on glaciers which is indiscernible in multispectral imagery from exposed rock (Paul et al., 2004). This is accentuated by the melting and ablation of low latitude

The Cryosphere Discuss., doi:10.5194/tc-2016-56, 2016
Manuscript under review for journal The Cryosphere
Published: 7 March 2016

glaciers (Stokes et al., 2007) and is intensified by large amount of debris from frost shattering and freeze thaw activity (Fig. 3a and 3b). However Antarctic glaciers are rarely debris covered due the prevailing climatic conditions where constant sub-freezing conditions result in a lack of ablation (Fig. 3c and 3d) . The limited number of positive degree days and the lack of a day/night cycle at polar latitudes reduces freeze thaw activity meaning that less frost shattering takes place. Most Antarctic glaciers and ice streams are marine terminating and relatively few have active ablation zones (with the exception of a small percentage on the northern and eastern Antarctic Peninsula. The result is that most Antarctic glaciers are largely debris-free, removing this limitation from our study.

Here we present a new technique for fully automated rock outcrop identification using freely available Landsat satellite data. The method is a composite technique combining separate algorithms that divide the image into cloud, liquid water, shaded snow and sunlit snow and shaded and sunlit rock exposures. We test the method against manually digitised polygons, the existing ADD rock outcrop dataset and the NDSI to validate and compare its accuracy.

We apply the new methodology to the entire landmass of Antarctica, (>12,000,000 km^2) using Landsat 8 data over all regions of the continent that contain rock outcrop. The resulting dataset represents an improvement over the previous dataset (ADD), providing consistent and accurate estimation of the amount and location of rock outcrop in Antarctica.

2. New Methodology

2.1 Input data

To produce a rock outcrop map for the entire Antarctic continent requires a freely available georeferenced multiband dataset. The dataset must cover high latitudes; be recently acquired; be of a high enough resolution to identify individual outcrops and geomorphological features; and individual images must have a large enough extent for manual selection of suitable tiles for the entire continent. On this basis, the Landsat 8 multispectral satellite data was chosen for analysis. Landsat 8 is the latest and continuing satellite mission for multispectral global data acquisition launched by NASA and the United States Geological Survey (Roy et al., 2014). The satellite's sensors record 8 electromagnetic bands (0.43 to 2.29 µm wavelengths) at 30m resolution, plus a panchromatic band (0.50 to 0.68 µm) at 15m resolution and two thermal infrared bands (TIRS 1 and 2, 10.60 to 12.51 µm) acquired at 100m resolution and resampled to 30m.

For the production of an Antarctic-wide rock outcrop map, tiles were selected that were acquired during the Austral summer and display strong illumination and minimal cloud cover. Of particular importance was to exclude tiles with extensive cumulus or stratocumulus cloud where shadows within and below the cloud layer can be indiscernible from illuminated rock exposure. A total of 249 Landsat 8 tiles meeting these requirements were identified using the USGS Earth Explorer website (earthexplorer.usgs.gov). Details of the tiles used are provided as supplementary material.

In addition to the raw data, pre-processed tiles (170 km North-South by 183 km East-West) corrected for top of atmosphere reflectance, surface reflectance and brightness temperature are freely available for download (espa.cr.usgs.gov). However, the calculation of surface reflectance values in Antarctica is problematic due to a lack of adequate atmospheric correction models

The Cryosphere Discuss., doi:10.5194/tc-2016-56, 2016
Manuscript under review for journal The Cryosphere
Published: 7 March 2016

for the continent, limited *in situ* atmospheric data and inadequate quality elevation data (Black et al., 2014). This renders the surface reflectance corrected data unsuitable and so top of atmosphere reflectance and brightness temperature corrected products were used instead for this study.

2.2 Methodology

The new methodology identifies areas of sunlit and shaded rock through two separate workflows and then merges both outputs to produce the final dataset. Within both procedures a series of masks are produced to identify areas of exposed outcrop and to exclude areas of snow, cloud and liquid water. At each stage band ratios were used in preference to threshold values for individual bands to allow application of a single set of threshold values to a large dataset. These two procedures are detailed below and a flowchart for executing this process shown in Fig. 4. The complete methodology was automated within ArcPy (Zandbergen, 2013). The script is included in the supplementary material.

Procedure A. Sunlit Rock:

A.1. Sunlit rock identification: the NDSI

Although the NDSI is unable to identify shaded rock and often misclassifies clouds as rock outcrop, it remains the best method for identifying regions of exposed sunlit rock. Consequently, it is the primary input for this methodology with a threshold value of <0.75 being used to identify pixels of sunlit rock outcrop and confidently exclude pixels of snow (Fig. 5a).

A.2. Cloud mask: TIRS / Blue and TIRS1 Threshold

One of the main problems of rock outcrop identification in Antarctica is that sunlit rock and clouds are indiscernible using the NDSI alone (Fig. 5a). Consequently we have derived a mask for sunlit snow and clouds using the thermal infrared band (TIRS1, 10.60 to 11.19 μm) and the blue band. Using a ratio of these bands, clouds and sunlit snow give low values as they are cold but have high blue reflectance (Fig. 5b). In contrast, pixels of sunlit and shaded rock are warmer when associated with high blue reflectance or colder when associated with low blue reflectance, resulting in high to moderate ratio values. However, shaded snow and liquid water also give high to moderate values. A TIRS/blue threshold value of >0.4 is most effective in selecting cloud free pixels and excluding pixels of sunlit snow and cloud to produce an accurate final product, although some sunlit rock pixels are also discarded (Fig. 5b). To aid this cloud masking further an absolute TIRS1 threshold of >2550 is also applied as <1% of sunlit rock pixels have lower TIRS1 values whilst 10% of cloud pixels and 5% of sunlit and shaded snow pixels do have lower values (Fig. 5c).

A.3. Liquid water mask: NDWI and coastline

The most widely applied approach for the identification of liquid water in multispectral imagery is the Normalised Difference Water Index (NDWI, McFeeters 1996). Modified for Landsat 8 data with Landsat 8 band 3 equating to spectral wavelengths

The Cryosphere Discuss., doi:10.5194/tc-2016-56, 2016
Manuscript under review for journal The Cryosphere
Published: 7 March 2016

of 0.53 to 0.59 µm (the green band) and Landsat 8 band 5 equating to spectral wavelengths of 0.85 to 0.88 µm (the near infrared band, NIR) the NDWI is calculated using equation (2):

$$NDWI = \frac{Landsat\ 8\ band\ 3 - Landsat\ 8\ band\ 5}{Landsat\ 8\ band\ 3 + Landsat\ 8\ band\ 5} \quad (2)$$

A liquid water mask is applied to both the sunlit and shaded rock identification procedures, and so the same threshold value of <0.45 is used for both (Fig. 5d). Unfortunately, due to the presence of calved ice and suspended glacial debris in Antarctic coastal seawater, a large overlap in NDWI values exists between pixels of sea and shaded rock exposure (Fig. 5d). To aid this step the manually derived coastline of Antarctica (available from www.add.scar.org) was also used as a mask for excluding liquid water and sea ice.

Procedure B. Shaded Rock:

B.1. Shaded rock identification: Blue threshold

Even in the shade, snow is more reflective at blue wavelengths than shaded rock. Consequently by determining the blue intensity values for a pixels representing rock and snow a threshold value of <2500 was found to successfully identify pixels containing shaded rock exposure.

B.2. Liquid water mask: NDWI and coastline

Although a blue wavelength threshold successfully differentiates shaded snow and rock, liquid water is also misclassified as rock. Thus, the NDWI and coastline mask applied to the sunlit rock data are also applied to the shaded rock data (again using the NDWI threshold value of <0.45, Fig. 5d). This step also aids exclusion of shaded snow pixels as 25% of their values are discarded by the NDWI threshold (Fig. 5d).

Procedure C. Applying the masks and merging the datasets

Pixels that were identified as rock by the NDSI mask and not identified as cloud or water represent sunlit rock outcrops. Similarly, pixels with blue band intensities below the threshold for shaded rock that aren't subsequently identified as liquid water by the NDWI threshold represent shaded rock exposures. Merging these two outputs produced the rock outcrop map for each tile. The output of each tile was then reprojected to the same coordinate system and the results of all tiles mosaicked together for the entire continent. As most areas were covered by multiple Landsat tiles, any pixels identified as rock exposure by any of the overlying tiles was included as exposed rock in the final dataset. Finally, this dataset was merged with the existing ADD rock outcrop dataset for areas not covered by the LANDSAT 8 imagery (Fig. 6).

The Cryosphere Discuss., doi:10.5194/tc-2016-56, 2016
Manuscript under review for journal The Cryosphere
Published: 7 March 2016

3. Results

3.1 Accuracy Assessment

To quantify the accuracy of the new methodology and its limitations, the extent of rock exposure was manually delineated using ten 10x10 km images (110,889 pixels each, Fig. 7). Images were selected from distal locations across the continent (Fig. 8), covering a range in geology, geomorphology and latitude. Areas of rock outcrop were manually identified by three operators. One tile (Ryder Bay, Fig. 7a) was traced by all operators; operator variability for pixel identification (rock or non-rock) was ±0.27% (one standard deviation).

The manually derived land cover was compared with the existing ADD rock outcrop dataset, the new automated method and the optimum NDSI-determined output for each image. Optimum NDSI threshold values (maximum values for pixels identified as rock) were taken as those with the lowest total quantity disagreement (abundance accuracy) and allocation disagreement (location accuracy) (Pontius Jr&Millones 2011). As shown by Fig. 9, optimum NDSI threshold values are highly variable. For well illuminated images without any cloud cover (Fig. 7b to 7f), NDSI threshold values of 0.6 or 0.7 are optimal. Images of extensive shade achieve more accurate results at higher NDSI threshold values (0.8, Fig. 7g) allowing identification of shaded rock. In contrast, images with extensive cloud require lower values (0.3 to 0.5, Fig. 7a, h and i) so as not to include the cloud as misidentified rock outcrop pixels. For mixed images (Fig. 7j) with shaded and illuminated rock with minor cloud cover, 0.7 remained the optimal threshold value.

Well illuminated, cloud free images produce similar accuracies for the NDSI techniques and the new method (Fig. 7b to 7f), with low commission or omission disagreements (Fig. 10a). However, the required determination of an optimal NDSI threshold value renders this alternative methodology more involved than that used for our new dataset;, when using the optimal threshold value the NDSI technique omits areas of rock in shaded images as well as both shaded or sunlit rock in cloudy images, leading to high and variable omission disagreements (Fig. 10b).

The ADD rock outcrop dataset produces variable accuracies. In Ryder Bay (Fig. 7a) the map has been recently been updated using manual delineation from very high resolution aerial photography and so has high accuracy with low omission and commission disagreement, similar to the new dataset. However, it is important to stress that areas of high resolution delineation are limited in the ADD rock outcrop dataset. The ADD rock outcrop dataset is more accurate than the NDSI technique in shaded images (Fig. 7g and 7j), but highly generalised and poorly georeferenced outcrop extents in other tiles (Fig. 7e and 7h) produce high and highly variable disagreements (Fig. 10), particularly in commission.

The new methodology performed poorest in images with limited areas of rock outcrop (e.g. Fig. 7h, 0.1% rock), although shade, clouds and mixed pixels of snow and rock in Fig. 7h make even manual pixel identification difficult. There are omission disagreements in shaded images (Fig. 7g and 7j) although these are much lower than for the alternative techniques (a mean of 15% for all images compared to 38% for the NDSI technique and 30 % for the ADD rock outcrop dataset, Fig. 10b). Clouds were successfully masked and do not contribute to the commission disagreement (Fig. 7h, i and j). The quality assessment shows higher accuracies for the new method (a mean of 85 ±8% of identified rock pixels being correct for all ten images

The Cryosphere Discuss., doi:10.5194/tc-2016-56, 2016
Manuscript under review for journal The Cryosphere
Published: 7 March 2016

compared with 62 ±32% or 70 ±14% for the NDSI technique and ADD rock outcrop dataset respectively) with lower and much more consistent commission and omission disagreements than the alternative NDSI or ADD rock outcrop datasets (Fig. 10b).

4. Discussion

This is the first fully automated methodology for the differentiation of snow and rock in Antarctica, from which a new outcrop map of the entire Antarctic continent has been produced at higher and more consistent accuracies than existing data and techniques (85 ±8% mean correct pixel identification for the new method compared to 62 ±32% or 70 ±14% for the NDSI and ADD data respectively, Fig. 10). The new dataset is available online via the SCAR ADD website (www.add.scar.org) and from this article's supplementary material.

Despite the poorer accuracy of the ADD rock outcrop dataset (70% mean for correct pixel identification compared to 85% for the new dataset), due to the methodology by which it was derived, certain features are better represented. This includes South Georgia and the South Orkney Islands where a lack of cloud-free imagery in the late Austral summer (when the outcrops aren't covered by snow) prevents automated outcrop identification. Consequently, rock outcrop extents in these areas are derived from the existing ADD dataset rather than remotes sensing imagery in addition to outcrops south of 82°40' S (Fig. 6).

It is important when using the new Landsat 8 rock outcrop map to consider seasonal variability in snow cover and that most outcrops were derived from multiple tiles from different years and different months of the Austral summer. Consequently, the map may not be representative of current conditions and may not consistently represent maximum outcrop extent across the continent.

4.1 Limitations

Using the new methodology we have produced a revised map of rock outcrops in Antarctica. Landsat 8 does not provide coverage south of 82°40' S so the existing ADD rock outcrop dataset was clipped to latitudes greater than this and merged with the new automatically derived data to produce the final dataset. There are two further limitations to the new methodology:

1. Because an overlap exists between the NDWI values of shaded rock and liquid water (Fig. 5d), some pixels of coastal seawater not masked by the ADD coastline have been misidentified as exposed rock. This is particularly problematic for pixels adjacent to seawater rich in calved ice and glacial debris (Fig. 11a). These pixels are spectrally identical to shaded rock and thus cannot be excluded automatically from the data. Consequently they were manually removed from the final dataset, although some of these misidentified pixels may still be present.

2. Even though spectral properties have been chosen that distinguish rock pixels from those of snow, clouds or sea, some overlap exists where pixels remain ambiguous (Fig. 5). Consequently, to allow automated analysis over such a large area mildly conservative threshold values were chosen. For example, the NDSI threshold for sunlit rock set at the 95th percentile rather than the complete range exhibited by sunlit outcrops as this excludes any overlap with the range of NDSI values for

The Cryosphere Discuss., doi:10.5194/tc-2016-56, 2016
Manuscript under review for journal The Cryosphere
Published: 7 March 2016

sunlit snow (Fig. 5a). This results in the exclusion of some pixels of exposed rock that are spectrally similar to clouds and snow (e.g. Fig. 11b).

3. Due to the 100m spatial resolution of the TIRS band, small outcrops around the continent (especially those less than 60m or 2 pixels across) are often excluded by the new technique and may be better represented in the ADD rock outcrop dataset.

4.2 Total outcrop area

We calculate (using an Equal Area projection) that the existing ADD rock outcrop dataset has 44,900 km^2 area of rock outcrop, equivalent to 0.37% of the total land area of Antarctica (12,188,650 km^2). In contrast the new data has a 21,745 km^{2}total area of rock outcrop, equivalent to 0.18% of the continent's land area and 48% of the previous estimate. This is a significant decrease and highlights an overestimation in the current predictions of rock outcrop extent in Antarctica.

4.3 Applications and future developments

The new Landsat 8 rock outcrop map will provide a revised and accurate base dataset for future topographical, glaciological, geological and geomorphological mapping. A number of satellite programs collecting new high resolution colour images are currently under development or planned for launch, including Digitalglobe's Worldview-3 satellite, NASA's HyspIRI satellite, European Space Agency's Sentinel program and the continuing Landsat data acquisition; these new datasets will allow further application of this technique at higher resolutions and consequently higher accuracies, allowing future improvement of the datasets broader applications. Application of the new technique to these alternative datasets would however require modification of the threshold values for each mask in the procedure.

5. Conclusions

A new map of exposed rock outcrop has been developed for the Antarctic continent. The new map was achieved via a fully automated methodology employing Landsat 8 multispectral imagery. The new methodology uses the NDSI technique to identify sunlit rock exposure and low blue intensities for shaded rock, and then applies separate masks to remove incorrectly classified pixels of cloud, snow and liquid water. This is the first automated methodology for rock outcrop identification in Antarctica, and achieves higher and more consistent accuracies than the existing dataset or what can be achieved using the alternative automated technique (the NDSI). Assessing the accuracy of these alternative techniques and datasets across a range of images gives a mean value for correct pixel identification of 85 ±8% for the new method compared to 62 ±32% or 70 ±14% for the NDSI technique and existing ADD rock outcrop dataset respectively, The new map, supplemented by existing data for latitudes south of 82°40' S (the limit of Landsat 8 coverage), reveals that rock outcrop forms 0.18% of the total land area of Antarctica, 48% of the previous estimate.

The Cryosphere Discuss., doi:10.5194/tc-2016-56, 2016
Manuscript under review for journal The Cryosphere
Published: 7 March 2016

Acknowledgements

This study is part of the British Antarctic Survey Polar Science for Planet Earth programme, funded by the Natural Environment Research Council.

References

Arendt, A., Bolch, T., Cogley, J. G., Gardner, A., Hagen, J.-O., Hock, R., Kaser, G., Pfeffer, W. T., Moholdt, G., Paul, F. and others: Randolph glacier inventory [v2. 0]: A dataset of global glacier outlines. Global land ice measurements from space, boulder Colorado, USA, 2012.

Baldridge, A. M., Hook, S. J., Grove, C. I. and Rivera, G.: The ASTER spectral library version 2.0, Remote Sens. Environ., 113(4), 711–715, 2009.

Bishop, M. P., Olsenholler, J. A., Shroder, J. F., Barry, R. G., Raup, B. H., Bush, A. B., Copland, L., Dwyer, J. L., Fountain, A. G., Haeberli, W. and others: Global Land Ice Measurements from Space (GLIMS): remote sensing and GIS investigations of the Earth's cryosphere, Geocarto Int., 19(2), 57–84, 2004.

Black, M., Fleming, A., Riley, T., Ferrier, G., Fretwell, P., McFee, J., Achal, S. and Diaz, A. U.: On the Atmospheric Correction of Antarctic Airborne Hyperspectral Data, Remote Sens., 6(5), 4498–4514, 2014.

Bolch, T., Menounos, B. and Wheate, R.: Landsat-based inventory of glaciers in western Canada, 1985–2005, Remote Sens. Environ., 114(1), 127–137, 2010.

Burns, P. and Nolin, A.: Using atmospherically-corrected Landsat imagery to measure glacier area change in the Cordillera Blanca, Peru from 1987 to 2010, Remote Sens. Environ., 140, 165–178, 2014.

Dozier, J.: Spectral signature of alpine snow cover from the Landsat Thematic Mapper, Remote Sens. Environ., 28, 9–22, 1989.

Hall, D. K., Riggs, G. A. and Salomonson, V. V.: Development of methods for mapping global snow cover using moderate resolution imaging spectroradiometer data, Remote Sens. Environ., 54(2), 127–140, 1995.

McFeeters, S. K.: The use of the Normalized Difference Water Index (NDWI) in the delineation of open water features, Int. J. Remote Sens., 17(7), 1425–1432, 1996.

Paul, F. and Kääb, A.: Perspectives on the production of a glacier inventory from multispectral satellite data in Arctic Canada: Cumberland Peninsula, Baffin Island, Ann. Glaciol., 42(1), 59–66, 2005.

Paul, F., Kääb, A., Maisch, M., Kellenberger, T. and Haeberli, W.: The new remote-sensing-derived Swiss glacier inventory: I. Methods, Ann. Glaciol., 34(1), 355–361, 2002.

Paul, F., Huggel, C. and Kääb, A.: Combining satellite multispectral image data and a digital elevation model for mapping debris-covered glaciers, Remote Sens. Environ., 89(4), 510–518, 2004.

Paul, F., Kääb, A. and Haeberli, W.: Recent glacier changes in the Alps observed by satellite: Consequences for future monitoring strategies, Glob. Planet. Change, 56(1), 111–122, 2007.

Paul, F., Barry, R. G., Cogley, J. G., Frey, H., Haeberli, W., Ohmura, A., Ommanney, C. S. L., Raup, B., Rivera, A. and Zemp, M.: Recommendations for the compilation of glacier inventory data from digital sources, Ann. Glaciol., 50(53), 119–126, 2009.

Pontius Jr, R. G. and Millones, M.: Death to Kappa: birth of quantity disagreement and allocation disagreement for accuracy assessment, Int. J. Remote Sens., 32(15), 4407–4429, 2011.

Racoviteanu, A. E., Paul, F., Raup, B., Khalsa, S. J. S. and Armstrong, R.: Challenges and recommendations in mapping of glacier parameters from space: results of the 2008 Global Land Ice Measurements from Space (GLIMS) workshop, Boulder, Colorado, USA, Ann. Glaciol., 50(53), 53–69, 2010.

Roy, D. P., Wulder, M. A., Loveland, T. R., Woodcock, C. E., Allen, R. G., Anderson, M. C., Helder, D., Irons, J. R., Johnson, D. M., Kennedy, R. and others: Landsat-8: Science and product vision for terrestrial global change research, Remote Sens. Environ., 145, 154–172, 2014.

Stokes, C. R., Popovnin, V., Aleynikov, A., Gurney, S. D. and Shahgedanova, M.: Recent glacier retreat in the Caucasus Mountains, Russia, and associated increase in supraglacial debris cover and supra-/proglacial lake development, Ann. Glaciol., 46(1), 195–203, 2007.

Tucker, C. J.: Red and photographic infrared linear combinations for monitoring vegetation, Remote Sens. Environ., 8(2), 127–150, 1979.

Tucker, C. J.: Cover Maximum normalized difference vegetation index images for sub-Saharan Africa for 1983-1985, Int. J. Remote Sens., 7(11), 1383–1384, 1986.

Zandbergen, P. A.: Python scripting for ArcGIS., 2013.

Zhu, Z. and Woodcock, C. E.: Object-based cloud and cloud shadow detection in Landsat imagery, Remote Sens. Environ., 118, 83–94, 2012.

Zhu, Z., Wang, S. and Woodcock, C. E.: Improvement and expansion of the Fmask algorithm: cloud, cloud shadow, and snow detection for Landsats 4–7, 8, and Sentinel 2 images, Remote Sens. Environ., 159, 269–277, 2015.

Acknowledgements

This study is part of the British Antarctic Survey Polar Science for Planet Earth programme, funded by the Natural Environment Research Council.

The Cryosphere Discuss., doi:10.5194/tc-2016-56, 2016
Manuscript under review for journal The Cryosphere
Published: 7 March 2016

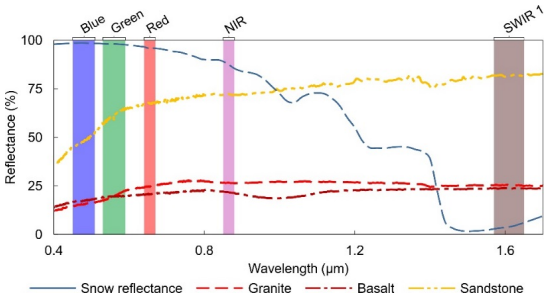

Fig. 1. Spectral reflectance data for snow and rock (granite, basalt and sandstone) from the ASTER Spectral Library v1.2 (Baldridge et al., 2009). Designations of spectral regions as defined by the Landsat 8 bands: Blue – Band 2, 0.45 – 0.51 µm; Green – Band 3, 0.53 – 0.59 µm; Red – Band 4, 0.64 – 0.67 µm; NIR, Near Infrared – Band 5, 0.85 – 0.88 µm; SWIR 1, Short Wave Infrared – Band 6, 1.57 – 1.65 µm.

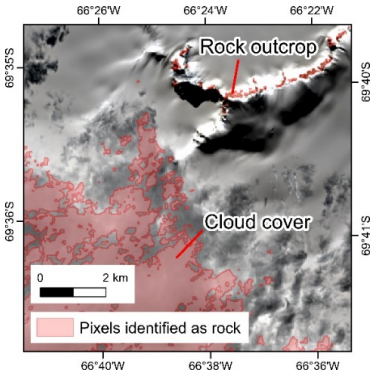

Fig. 2. Illustration of the misclassification of cloud cover as rock pixels when using the NDSI technique. An NDSI threshold of 0.6 was used to identify the rock outcrops, but at this threshold much of the cloud cover is also included.

The Cryosphere Discuss., doi:10.5194/tc-2016-56, 2016
Manuscript under review for journal The Cryosphere
Published: 7 March 2016

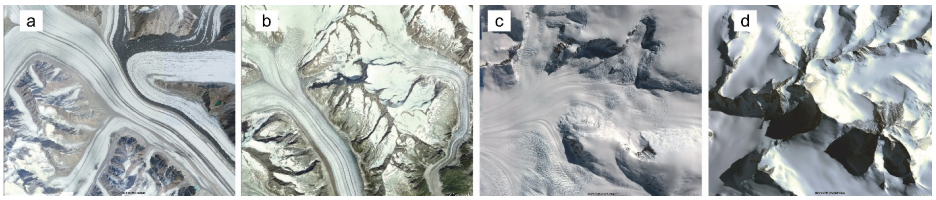

Fig. 3. Comparison of debris cover for glaciers at low latitudes (3a, Karakoram Range (35°N), and 3b, Jungfrau Range, Alps (46°N)) with those of Antarctica (3c, Antarctic Peninsula (66°S), and 3d, Transantarctic Mountains (72°S)). Note the lack of surface moraine and the deep shadows in 3e and 3d, typical of Antarctic glaciers where a lack of day-night cycle and year-round low temperatures restricts freeze thaw action and the permanently low sun angles result in deep shadows in remotely sensed imagery.

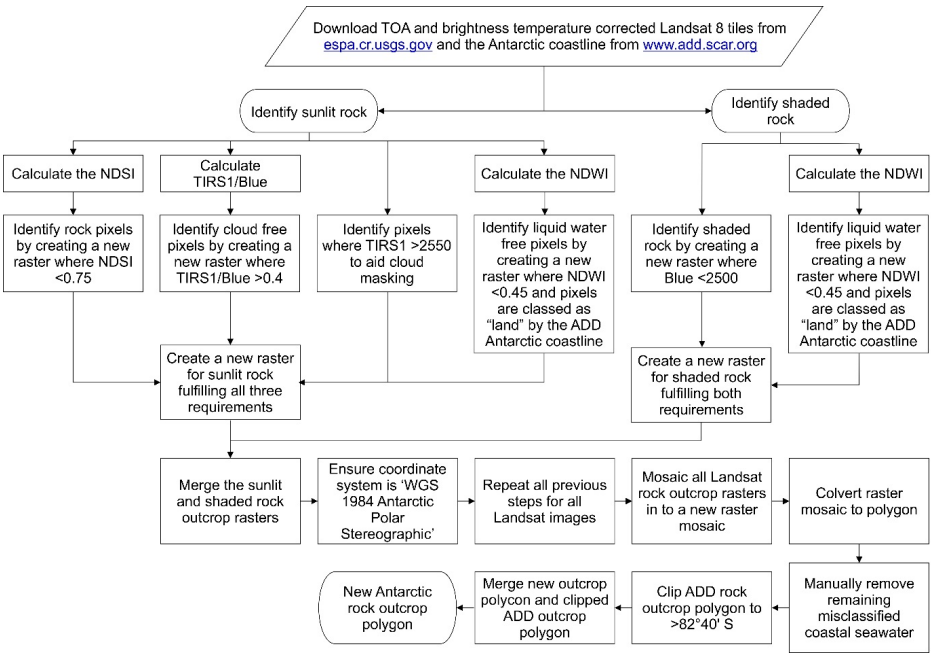

Fig. 4. Flowchart for the automated identification of rock outcrops in Antarctica using the new methodology.

The Cryosphere Discuss., doi:10.5194/tc-2016-56, 2016
Manuscript under review for journal The Cryosphere
Published: 7 March 2016

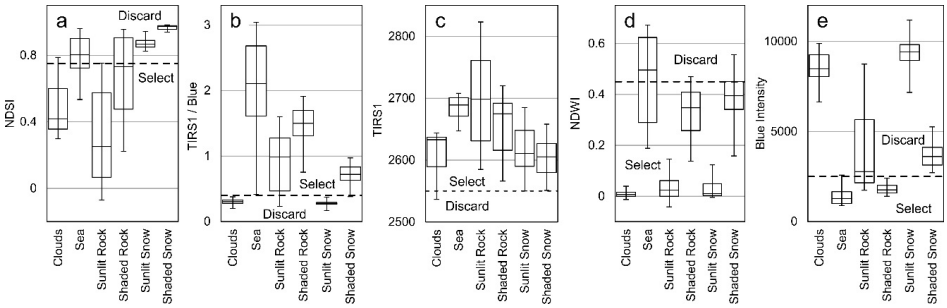

Fig. 5. Box plots of extracted pixel values from three Landsat 8 tiles illustrating the different spectral properties of clouds (*n* = 871), sea (*n* = 3277), sunlit rock (*n* = 1158), shaded rock (*n* = 1224), sunlit snow (*n* = 1293) and shaded snow (*n* = 918). Boxes indicate the 2nd and 3rd quartiles and median values. Whiskers indicate the 5th and 95th percentile. Dashed lines indicate the chosen threshold values for the automated rock outcrop extraction and the values to be selected or discarded.

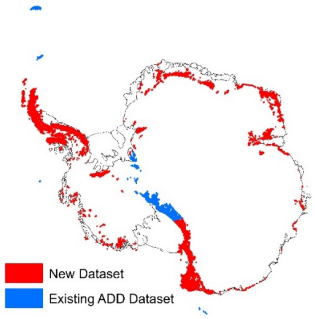

Fig. 6. Rock exposure map of Antarctica showing the data sources for the new dataset. Outcrops shown in red were derived using the new remote sensing methodology and outcrops in blue were derived from the existing ADD rock outcrop dataset to supplement areas south of 82°40' S (not covered by Landsat 8) or islands lacking suitable cloud free images. Areas of rock exposure are exaggerated for illustration.

The Cryosphere Discuss., doi:10.5194/tc-2016-56, 2016
Manuscript under review for journal The Cryosphere
Published: 7 March 2016

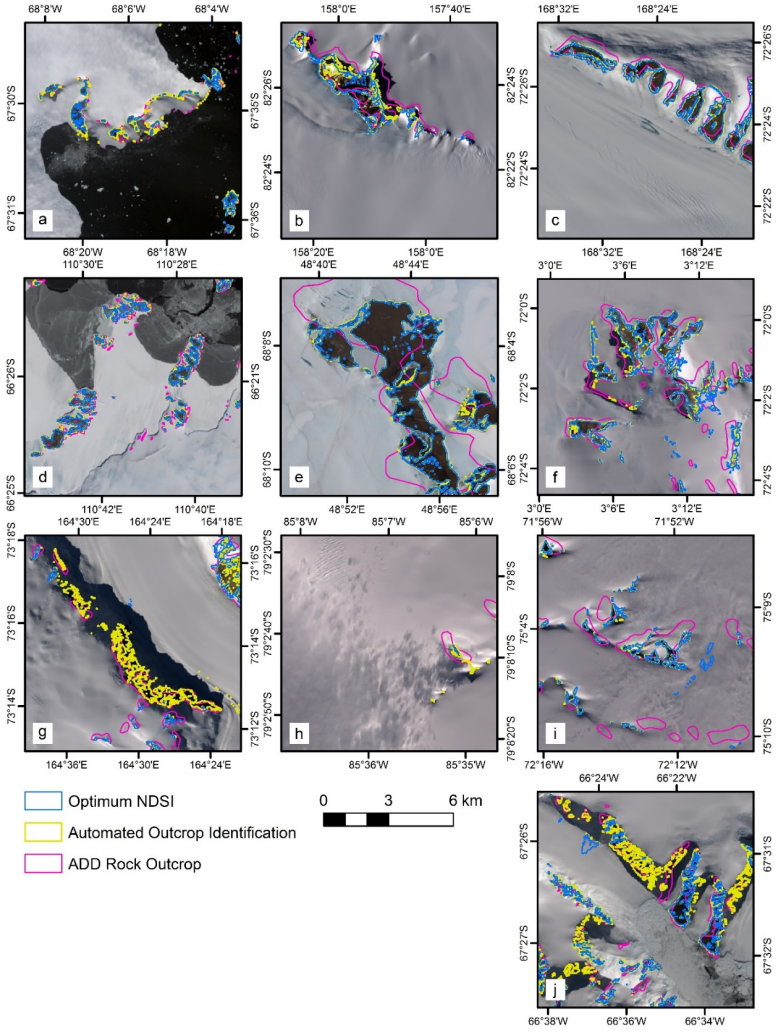

Fig. 7. Images used for the quality assessment overlain by the tree alternative methodologies and datasets: Pixels extracted using optimum NDSI thresholds for each image; pixels extracted using the new methodology presented here; and the extents of the current ADD rock outcrop map.

The Cryosphere Discuss., doi:10.5194/tc-2016-56, 2016
Manuscript under review for journal The Cryosphere
Published: 7 March 2016

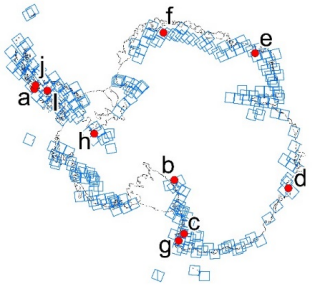

Fig. 8. Locations of the 249 Landsat 8 tiles (blue squares) used to identify rock outcrop in Antarctica and the locations (a to j) of the 10x10 km images used for the quality assessment in Fig. 5.

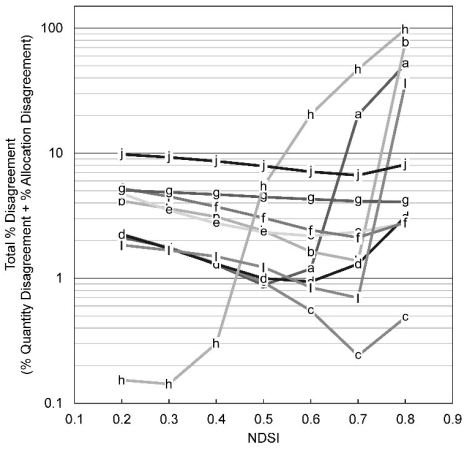

Fig. 9. Total quantity and allocation disagreement values (Pontius Jr and Millones, 2011) for pixels extracted from the images in Fig. 5 using the NDSI threshold technique.

The Cryosphere Discuss., doi:10.5194/tc-2016-56, 2016
Manuscript under review for journal The Cryosphere
Published: 7 March 2016

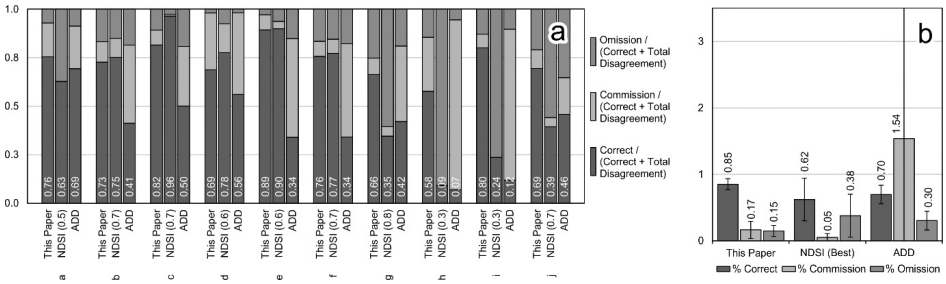

Fig. 10. (a) 100% normalised accuracy assessment data for correctly classified pixels and pixels of omission and commission disagreements for the images in Fig. 5. Optimal NDSI values used are shown in brackets. (b) Overall accuracy assessment data for the three alternative datasets. Error bars shown at 1SD.

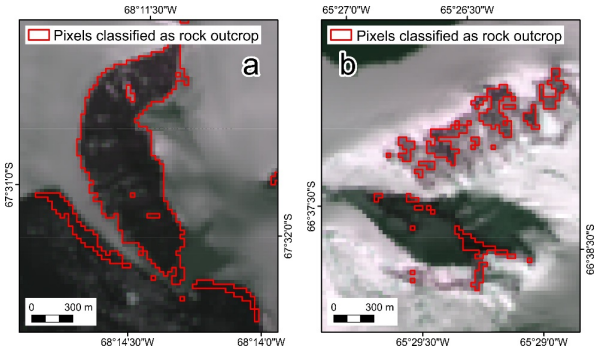

Fig. 11. Limitations of the new methodology. (a) Seawater near calving ice classified as rock (later removed manually). (b) An illustration of conservative outcrop extent estimation using the new technique.

Appendix B: Electron microprobe analysis

Sample J13.19.10

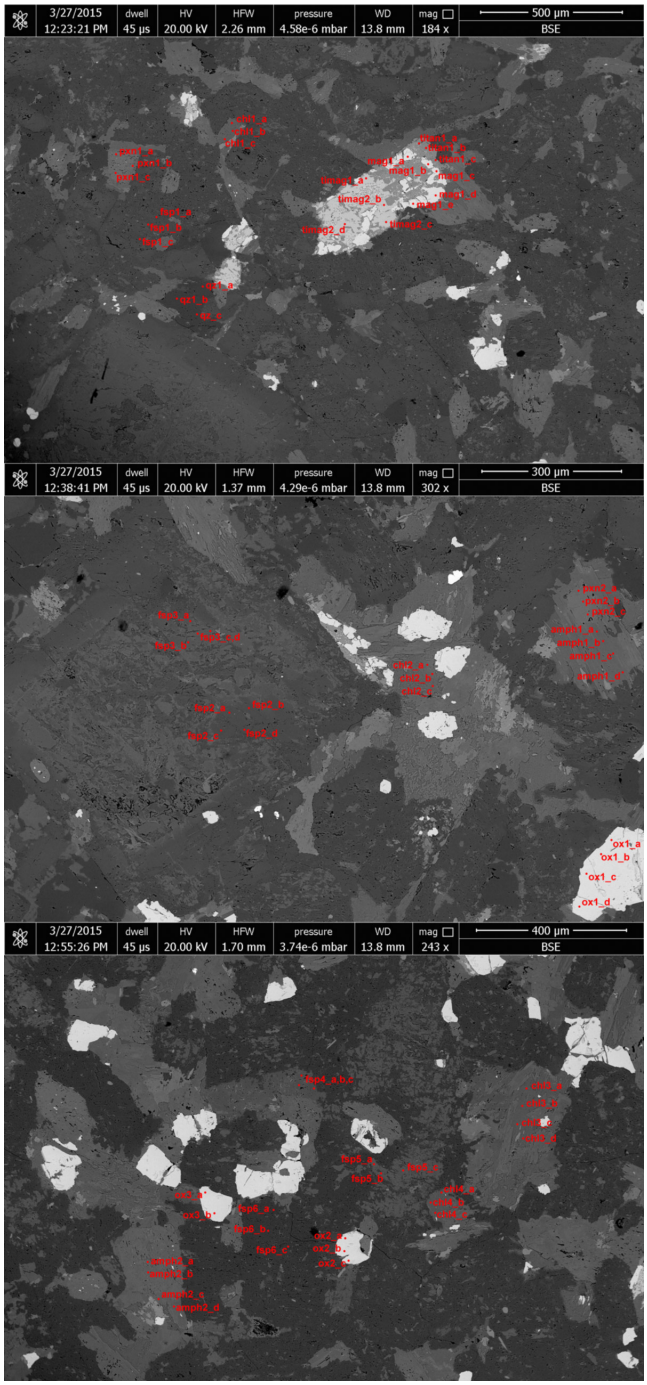

Electron microprobe analysis (EMPA) points for sample J13.19.10.

ID	SiO2	TiO2	Al2O3	FeO	MnO	MgO	CaO	Na2O	K2O	P2O5	F	Total	mineral id
amph1_a	55.75	0.19	1.02	8.18	0.24	19.35	12.43	0.21	0.09	0.01	0.19	97.73	amphibole actinolite
amph1_b	54.79	0.31	1.57	8.63	0.40	18.83	12.03	0.25	0.11	0.00	0.11	97.05	amphibole actinolite
amph1_c	54.35	0.43	2.13	8.73	0.37	18.92	11.69	0.35	0.16	0.02	0.30	97.46	amphibole actinolite
amph1_d	54.49	0.26	2.05	9.31	0.58	18.94	10.60	0.42	0.09	0.02	0.15	96.98	amphibole actinolite
amph2_a	52.70	0.18	3.00	15.02	0.45	13.94	12.22	0.35	0.10	0.01	0.00	97.95	amphibole actinolite
amph2_b	52.64	0.18	3.35	12.25	0.57	15.82	12.40	0.37	0.10	0.01	0.02	97.71	amphibole actinolite
amph2_c	53.14	0.15	3.02	11.55	0.35	16.10	12.54	0.27	0.11	0.02	0.00	97.36	amphibole actinolite
amph2_d	55.10	0.16	1.73	10.81	0.89	17.22	10.97	0.34	0.03	0.02	0.01	97.35	amphibole actinolite
chl1_a	28.27	0.02	18.28	21.37	0.39	18.43	0.07	0.03	0.04	0.00	0.08	86.97	Mg-Fe chlorite
chl1_b	27.17	0.03	19.24	20.77	0.40	19.06	0.06	0.00	0.00	0.08	0.03	86.86	Mg-Fe chlorite
chl1_c	27.49	0.05	18.91	20.70	0.35	18.86	0.14	0.03	0.02	0.03	0.00	86.59	Mg-Fe chlorite
chl2_a	27.75	0.01	18.41	22.43	0.30	18.00	0.28	0.03	0.03	0.03	0.04	87.32	Mg-Fe chlorite
chl2_b	26.63	0.01	19.06	21.81	0.35	19.05	0.07	0.02	0.00	0.02	0.06	87.09	Mg-Fe chlorite
chl2_c	27.07	0.00	18.55	22.57	0.28	17.88	0.09	0.02	0.03	0.04	0.01	86.53	Mg-Fe chlorite
chl3_a	27.64	0.06	19.09	20.99	0.36	18.80	0.07	0.03	0.03	0.05	0.06	87.18	Mg-Fe chlorite
chl3_b	28.00	0.02	18.83	21.64	0.37	18.40	0.19	0.05	0.04	0.05	0.11	87.70	Mg-Fe chlorite
chl3_c	29.10	0.03	18.25	20.59	0.31	18.59	0.59	0.04	0.05	0.05	0.00	87.59	Mg-Fe chlorite
chl3_d	27.68	0.06	18.93	21.20	0.36	18.28	0.10	0.02	0.02	0.05	0.06	86.76	Mg-Fe chlorite
chl4_a	27.92	0.00	18.16	21.84	0.29	17.88	0.12	0.03	0.02	0.08	0.00	86.35	Mg-Fe chlorite
chl4_b	28.02	0.01	18.59	21.46	0.43	18.00	0.09	0.00	0.02	0.04	0.00	86.66	Mg-Fe chlorite
chl4_c	27.80	0.04	18.88	21.14	0.30	18.24	0.09	0.03	0.02	0.05	0.00	86.58	Mg-Fe chlorite
fsp1_a	62.85	0.02	22.87	0.17		0.00	4.55	8.87	0.27			99.60	plagioclase oligoclase
fsp1_b	61.25	0.01	23.68	0.09		0.02	5.23	8.28	0.29			98.84	plagioclase oligoclase
fsp1_c	62.44	0.02	23.21	0.21		0.00	4.88	8.66	0.13			99.55	plagioclase oligoclase
fsp2_a	57.80	0.01	26.12	0.20		0.00	8.31	6.78	0.14			99.35	plagioclase labradorite
fsp2_b	58.25	0.00	26.03	0.18		0.00	8.25	6.79	0.26			99.78	plagioclase labradorite
fsp2_c	59.47	0.03	25.10	0.16		0.01	7.03	7.51	0.39			99.70	plagioclase labradorite
fsp2_d	58.58	0.01	25.60	0.28		0.00	7.57	7.14	0.23			99.41	plagioclase labradorite
fsp3_a	50.30	0.02	29.37	0.26		0.00	14.60	3.55	0.29			98.40	plagioclase bytownite
fsp3_b	47.53	0.02	32.86	0.30		0.00	16.20	2.18	0.08			99.17	plagioclase bytownite
fsp3_c	46.37	0.02	33.49	0.37		0.01	17.28	1.66	0.10			99.31	plagioclase bytownite
fsp3_d	57.99	0.02	26.43	0.13		0.01	8.55	6.62	0.12			99.87	plagioclase labradorite
fsp4_a	64.58	0.00	18.02	0.12		0.04	0.05	0.56	15.96			99.33	K-feldspar orthoclase
fsp4_b	64.89	0.00	18.21	0.16		0.00	0.02	0.65	15.95			99.89	K-feldspar orthoclase
fsp4_c	64.97	0.00	17.87	0.12		0.00	0.02	0.62	15.89			99.48	K-feldspar orthoclase
fsp5_a	43.59	0.05	23.09	1.36		0.00	26.61	0.05	0.01			94.76	?plagioclase anorthite
fsp5_b	46.43	0.02	23.18	0.43		0.00	23.74	1.42	0.02			95.25	?plagioclase anorthite
fsp5_c	44.69	0.03	23.45	0.40		0.00	25.58	0.46	0.01			94.62	?plagioclase anorthite
fsp6_a	68.54	0.01	19.61	0.12		0.01	0.38	11.38	0.03			100.09	plagioclase albite
fsp6_b	67.24	0.00	20.01	0.07		0.03	1.07	10.87	0.06			99.35	plagioclase albite
fsp6_c	66.47	0.00	19.70	0.06		0.03	1.05	10.65	0.07			98.02	plagioclase albite
mag1_a	0.03	0.47		91.97	0.00	0.00						92.51	magnetite
mag1_b	0.02	0.44		92.56	0.04	0.00						93.11	magnetite
mag1_c	0.02	0.58		92.17	0.00	0.00						92.77	magnetite
mag1_d	0.08	0.28		91.84	0.03	0.00						92.25	magnetite
mag1_e	0.00	0.43		92.53	0.04	0.01						93.07	magnetite
ox1_a	0.02	0.04		92.46	0.01	0.01						92.57	magnetite
ox1_b	0.01	0.06		93.62	0.13	0.00						93.83	magnetite
ox1_c	0.03	0.07		93.43	0.00	0.02						93.56	magnetite
ox1_d	0.00	0.02		92.89	0.01	0.00						92.93	magnetite
ox2_a	0.01	0.06		92.48	0.07	0.03						92.67	magnetite
ox2_b	0.01	0.06		92.94	0.04	0.00						93.05	magnetite
ox2_c	0.01	0.04		92.78	0.01	0.00						92.84	magnetite
ox3_a	0.03	0.04		92.88	0.00	0.02						93.01	magnetite
ox3_b	0.01	0.04		92.33	0.00	0.00						92.40	magnetite
pxn1_a	53.28	0.04	0.25	8.96	0.79	12.86	23.66	0.19	0.00	0.02		100.07	pyroxene augite
pxn1_b	54.92	0.03	1.15	11.04	0.31	16.57	12.99	0.13	0.03	0.05		97.24	pyroxene pigeonite
pxn1_c	53.60	0.00	0.22	8.30	0.39	13.07	25.04	0.11	0.01	0.00		100.79	pyroxene augite
pxn2_a	53.61	0.08	0.34	6.18	0.30	15.50	23.26	0.28	0.01	0.01		99.59	pyroxene augite
pxn2_b	52.37	0.14	0.76	9.39	0.41	13.70	22.12	0.45	0.01	0.01		99.50	pyroxene augite
pxn2_c	52.66	0.05	0.77	8.98	0.58	13.98	22.26	0.41	0.00	0.00		99.84	pyroxene augite

ID	SiO2	TiO2	Al2O3	FeO	MnO	MgO	CaO	Na2O	K2O	P2O5	F	Total	mineral id
qz1_a	100.52	0.07	0.04	0.10		0.01	0.03	0.00	0.01			100.78	quartz
qz1_b	100.48	0.04	0.03	0.07		0.00	0.06	0.00	0.01			100.69	quartz
qz1_c	100.11	0.05	0.12	0.08		0.01	0.05	0.00	0.01			100.44	quartz
timag1_a	0.01	49.68		44.65	5.97	0.21						100.60	ilmenite
timag1_b	0.00	43.05		49.29	5.27	0.21						97.84	ilmenite
timag1_c	0.01	50.04		44.87	5.64	0.18						100.80	ilmenite
timag1_d	0.01	50.99		44.41	5.21	0.14						100.76	ilmenite
titan1_a	28.49	38.77	0.92	3.30	0.32	0.00	26.22	0.00	0.00	0.10	0.14	98.27	titanite
titan1_b	29.79	38.42	0.98	2.10	0.13	0.00	27.28	0.01	0.00	0.04	0.09	98.83	titanite
titan1_c	21.52	42.68	0.69	14.04	1.54	0.06	18.67	0.00	0.00	0.04	0.00	99.24	titanite

Sample J13.22.5

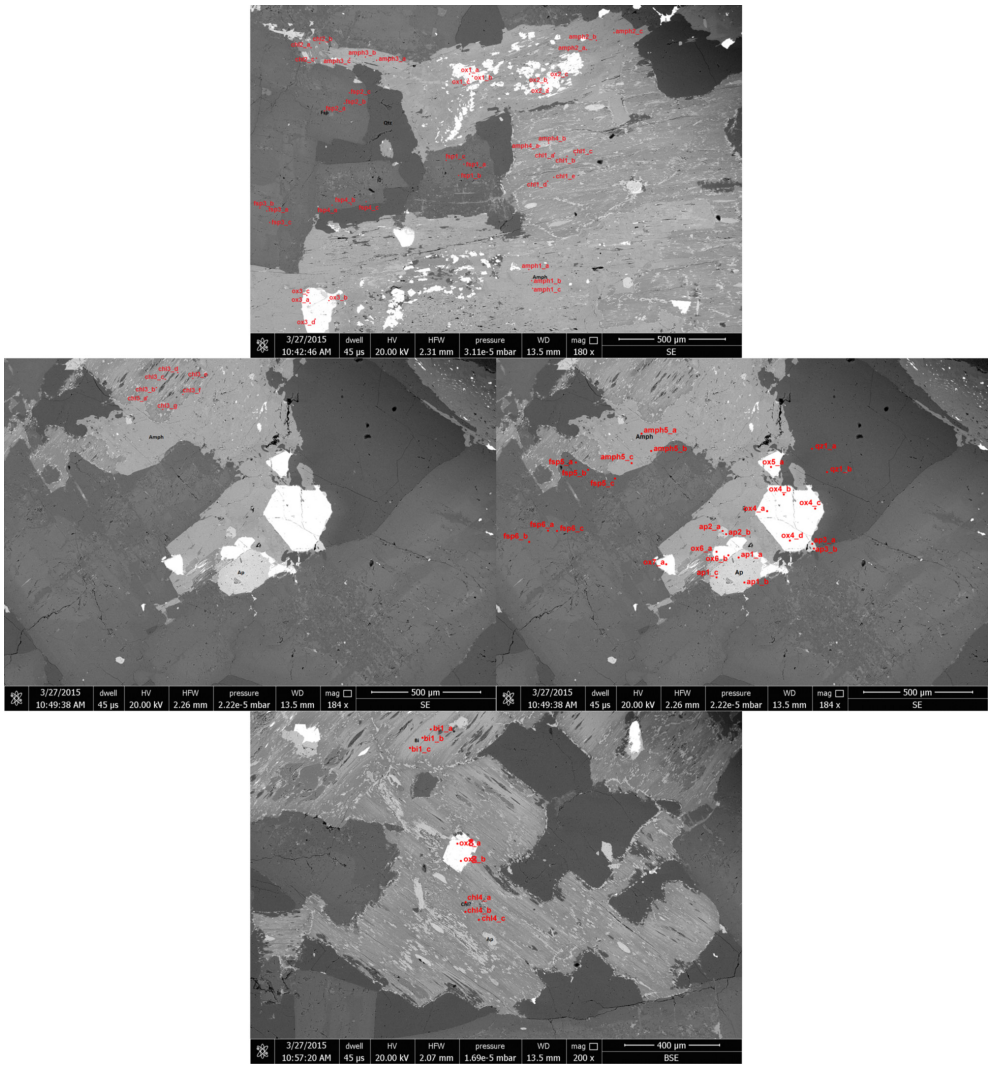

Electron microprobe analysis (EMPA) points for sample J13.22.5.

ID	SiO2	TiO2	Al2O3	FeO	MnO	MgO	CaO	Na2O	K2O	P2O5	F	Total	mineral id
amph1_a	48.33	1.26	5.15	16.22	0.54	13.38	10.60	1.07	0.53	0.02	0.24	97.39	magnesio hornblende amphibole
amph1_b	49.86	0.99	4.43	15.32	0.53	14.05	10.77	0.94	0.39	0.00	0.25	97.56	magnesio hornblende amphibole
amph1_c	48.82	1.15	4.98	15.81	0.49	13.35	10.81	1.14	0.51	0.04	0.03	97.22	magnesio hornblende amphibole
amph2_a	52.77	0.26	2.51	15.26	0.95	15.54	10.08	0.34	0.16	0.02	0.00	97.95	magnesio hornblende amphibole
amph2_b	50.54	0.69	4.16	14.04	0.49	14.51	11.64	0.62	0.34	0.02	0.17	97.25	magnesio hornblende amphibole
amph2_c	49.01	1.02	5.19	15.53	0.43	13.91	10.74	1.05	0.47	0.00	0.23	97.56	magnesio hornblende amphibole
amph3_a	49.34	0.70	4.52	16.44	0.52	13.32	10.73	1.02	0.42	0.02	0.15	97.19	magnesio hornblende amphibole
amph3_b	49.26	0.96	4.69	16.01	0.55	13.38	11.18	0.87	0.45	0.00	0.14	97.60	magnesio hornblende amphibole
amph3_c	47.84	1.25	5.42	16.66	0.51	12.45	11.20	0.92	0.56	0.00	0.15	96.95	magnesio hornblende amphibole
amph4_a	36.43	0.41	17.95	17.45		0.14	22.21	0.00	0.00			94.60	mixed
amph4_b	36.61	1.93	16.52	17.38		0.28	22.34	0.05	0.01			95.12	mixed
amph5_a	48.83	0.97	4.83	15.76	0.47	13.79	10.83	1.16	0.44	0.00	0.24	97.38	magnesio hornblende amphibole
amph5_b	48.89	1.06	4.98	15.57	0.51	13.69	10.84	1.07	0.51	0.02	0.17	97.31	magnesio hornblende amphibole
amph5_c	47.98	1.20	5.62	15.94	0.38	13.07	10.83	1.21	0.61	0.01	0.12	97.04	magnesio hornblende amphibole
ap1_a	0.15		0.01	0.37		0.00	53.86	0.06	0.02	41.65	7.13	103.26	apatite
ap1_b	0.17		0.01	0.07		0.00	54.01	0.05	0.01	42.01	6.97	103.31	apatite
ap1_c	0.09		0.00	0.15		0.00	54.23	0.02	0.00	42.56	7.42	104.49	apatite
ap2_a	0.11		0.00	0.35		0.00	54.12	0.01	0.01	42.33	6.45	103.39	apatite
ap2_b	0.14		0.02	0.48		0.00	53.98	0.05	0.03	42.60	5.84	103.17	apatite
ap3_a	0.31		0.00	0.30		0.00	54.25	0.00	0.00	42.56	5.68	103.10	apatite
ap3_b	0.15		0.01	0.19		0.00	53.89	0.01	0.00	42.11	6.24	102.64	apatite
bi1_a	36.77	4.43	12.95	20.22	0.40	11.07	0.12	0.14	8.94	0.01	0.28	95.31	Ti-rich biotite
bi1_b	36.04	4.23	12.98	20.20	0.33	10.68	0.10	0.12	8.50	0.02	0.22	93.44	Ti-rich biotite
bi1_c	35.84	4.03	13.26	20.90	0.43	11.13	0.17	0.16	8.30	0.03	0.16	94.40	Ti-rich biotite
chl1_a	28.45	0.16	16.73	25.47	0.55	16.03	0.16	0.02	0.01	0.08	0.00	87.67	Mg-Fe chlorite
chl1_b	28.05	0.16	16.99	24.38	0.70	16.59	0.17	0.05	0.05	0.06	0.06	87.26	Mg-Fe chlorite
chl1_c	28.34	0.14	17.09	23.66	0.55	17.49	0.17	0.01	0.02	0.11	0.07	87.63	Mg-Fe chlorite
chl1_d	27.82	0.14	17.14	24.24	0.63	17.40	0.16	0.05	0.03	0.09	0.12	87.82	Mg-Fe chlorite
chl1_e	27.72	0.09	17.73	24.32	0.64	17.66	0.15	0.05	0.00	0.09	0.00	88.46	Mg-Fe chlorite
chl2_a	27.59	0.10	18.20	21.48	0.56	18.09	0.12	0.04	0.04	0.04	0.15	86.40	Mg-Fe chlorite
chl2_b	27.47	0.03	19.01	20.94	0.57	18.91	0.14	0.06	0.06	0.07	0.03	87.29	Mg-Fe chlorite
chl2_c	27.18	0.07	18.62	21.85	0.61	18.06	0.10	0.07	0.07	0.06	0.07	86.76	Mg-Fe chlorite
chl3_a	29.05	0.35	16.17	24.51	0.58	16.26	0.15	0.03	0.38	0.08	0.07	87.62	Mg-Fe chlorite
chl3_b	30.35	1.46	15.45	24.66	0.49	15.03	0.21	0.05	1.75	0.07	0.12	89.65	Mg-Fe chlorite
chl3_c	32.31	4.49	14.27	22.05	0.42	12.55	1.54	0.11	3.51	0.17	0.22	91.64	Mg-Fe chlorite
chl3_d	30.92	2.62	14.92	23.49	0.46	14.47	0.40	0.10	1.93	0.14	0.11	89.55	Mg-Fe chlorite
chl3_e	30.25	0.53	15.08	25.43	0.44	14.72	0.35	0.03	0.50	0.15	0.09	87.58	Mg-Fe chlorite
chl3_f	30.58	1.79	14.65	24.47	0.49	14.75	0.68	0.07	1.21	0.19	0.05	88.95	Mg-Fe chlorite
chl3_g	28.40	0.18	16.93	24.57	0.54	17.17	0.17	0.08	0.10	0.07	0.07	88.27	Mg-Fe chlorite
chl4_a	28.67	0.59	16.33	23.07	0.53	17.18	0.37	0.00	0.23	0.02	0.10	87.10	Mg-Fe chlorite
chl4_b	28.06	0.69	16.47	24.64	0.52	17.34	1.64	0.00	0.05	0.07	0.04	89.53	Mg-Fe chlorite
chl4_c	28.40	0.16	16.94	23.79	0.58	17.52	0.09	0.03	0.14	0.04	0.04	87.75	Mg-Fe chlorite
fsp1_a	59.93	0.02	25.04	0.16		0.00	6.89	7.64	0.31			99.99	plagioclase andesine
fsp1_b	60.52	0.02	24.80	0.21		0.00	6.59	7.59	0.32			100.04	plagioclase andesine
fsp1_c	57.84	0.03	26.49	0.16		0.00	8.48	6.60	0.19			99.79	plagioclase andesine
fsp2_a	56.57	0.03	26.79	0.11		0.00	9.05	6.30	0.14			98.99	plagioclase andesine
fsp2_b	58.45	0.02	25.60	0.17		0.00	7.65	7.18	0.26			99.32	plagioclase andesine
fsp2_c	58.56	0.03	25.79	0.22		0.00	7.94	6.97	0.21			99.72	plagioclase andesine
fsp3_a	54.66	0.04	28.16	0.21		0.00	10.60	5.27	0.14			99.07	plagioclase labradorite
fsp3_b	54.88	0.04	28.01	0.18		0.00	10.75	5.39	0.17			99.41	plagioclase labradorite
fsp3_c	54.93	0.04	28.10	0.22		0.01	10.41	5.50	0.14			99.35	plagioclase labradorite
fsp4_a	60.61	0.01	24.00	0.15		0.00	6.19	7.97	0.30			99.22	plagioclase andesine
fsp4_b	60.05	0.00	24.75	0.20		0.03	5.73	7.86	0.59			99.20	plagioclase andesine
fsp4_c	61.54	0.01	24.12	0.14		0.00	5.59	8.25	0.23			99.88	plagioclase andesine
fsp5_a	60.93	0.03	23.70	0.28		0.01	5.49	8.43	0.37			99.25	plagioclase andesine
fsp5_b	61.72	0.02	23.45	0.28		0.02	5.05	8.65	0.30			99.49	plagioclase andesine
fsp5_c	61.88	0.01	23.00	0.20		0.01	4.90	8.57	0.25			98.81	plagioclase andesine
fsp6_a	54.90	0.04	27.59	0.23		0.00	10.19	5.72	0.18			98.85	plagioclase labradorite
fsp6_b	53.65	0.06	28.46	0.29		0.00	11.37	5.01	0.14			98.97	plagioclase labradorite
fsp6_c	55.50	0.03	27.56	0.17		0.01	9.77	5.81	0.15			99.01	plagioclase labradorite
ox1_a	1.99	0.75		90.63	0.04	0.06						93.51	magnetite
ox1_b	0.40	0.01		87.63	0.01	0.55						88.67	magnetite
ox1_c	2.52	1.37		88.73	0.07	0.09						92.84	magnetite
ox2_a	0.45	0.56		92.66	0.07	0.01						93.80	magnetite
ox2_b	6.09	2.19		82.77	0.05	1.87						92.99	magnetite
ox2_c	1.72	0.44		91.05	0.01	0.15						93.43	magnetite
ox3_a	0.03	82.51		15.63	0.52	0.00						98.81	rutile
ox3_b	0.07	34.63		60.04	0.73	0.08						95.60	ilmenite
ox3_c	0.03	1.51		90.54	0.65	0.02						93.27	magnetite
ox3_d	0.02	0.71		92.13	0.21	0.00						93.47	magnetite
ox4_a	0.13	0.46		91.90	0.19	0.04						92.96	magnetite
ox4_b	0.04	0.22		92.60	0.12	0.00						93.26	magnetite
ox4_c	0.04	0.30		92.61	0.09	0.00						93.28	magnetite
ox4_d	0.03	1.69		90.90	0.48	0.01						93.41	magnetite
ox5_a	0.04	0.28		92.45	0.03	0.01						93.13	magnetite
ox6_a	0.03	0.98		91.61	0.27	0.00						93.15	magnetite
ox6_b	1.36	1.29		89.91	0.07	0.00						92.87	magnetite
ox7_a	0.02	1.45		90.52	0.80	0.02						93.18	magnetite
ox8_a	0.02	0.55		92.04	0.11	0.01						93.24	magnetite
ox8_b	0.03	5.40		86.76	0.11	0.00						92.79	magnetite
qz1_a	100.18	0.05	0.02	0.02		0.01	0.00	0.02	0.00			100.30	quartz

Sample J13.22.10

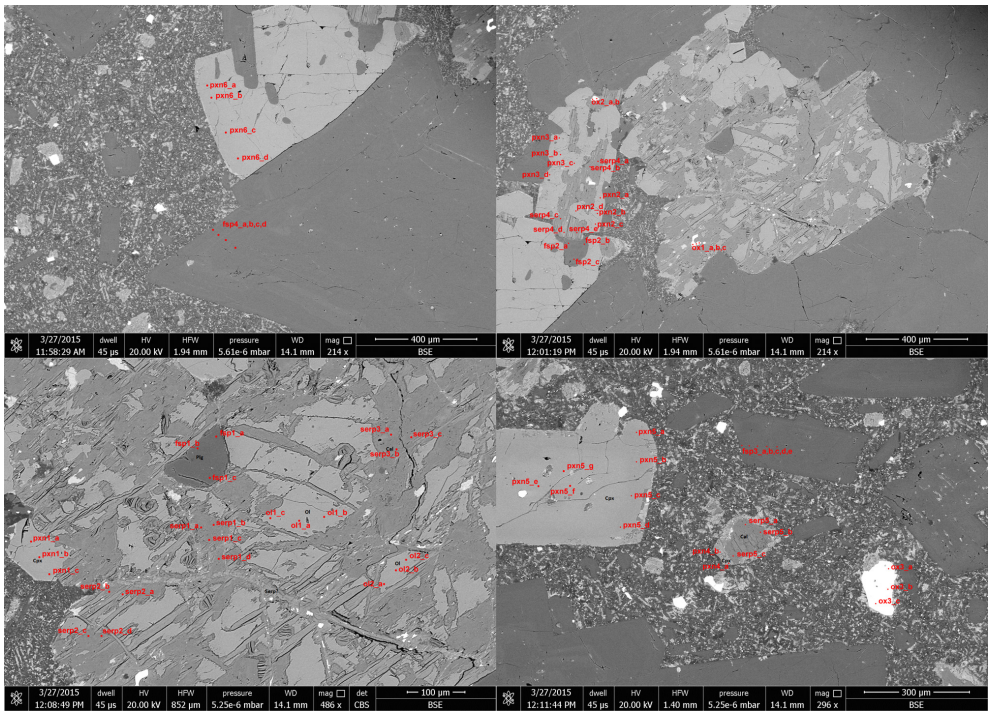

Electron microprobe analysis (EMPA) points for sample J13.22.10.

ID	SiO2	TiO2	Al2O3	FeO	MnO	MgO	CaO	Na2O	K2O	P2O5	F	Total	mineral id
fsp1_a	52.37	0.06	28.84	0.96		0.15	12.86	4.00	0.27			99.51	plagioclase labradorite
fsp1_b	52.97	0.07	28.80	0.95		0.13	12.27	4.21	0.38			99.77	plagioclase labradorite
fsp1_c	53.17	0.06	28.46	1.05		0.12	12.50	4.56	0.36			100.28	plagioclase labradorite
fsp2_a	52.45	0.05	28.36	1.03		0.08	12.02	4.23	0.44			98.66	plagioclase labradorite
fsp2_b	51.78	0.05	29.00	0.97		0.10	12.98	3.74	0.31			98.93	plagioclase labradorite
fsp2_c	51.72	0.06	29.09	0.92		0.12	13.06	3.77	0.21			98.96	plagioclase labradorite
fsp3_a	53.07	0.06	28.59	0.85		0.09	12.20	4.45	0.35			99.67	plagioclase labradorite
fsp3_b	53.01	0.09	28.31	0.91		0.12	12.11	4.45	0.34			99.35	plagioclase labradorite
fsp3_c	51.31	0.04	29.72	0.89		0.10	13.22	3.60	0.26			99.16	plagioclase labradorite
fsp3_d	52.03	0.06	29.16	0.82		0.17	12.90	3.97	0.32			99.43	plagioclase labradorite
fsp3_e	50.72	0.05	30.15	0.88		0.10	13.68	3.63	0.24			99.47	plagioclase labradorite
fsp4_a	52.34	0.06	28.54	0.83		0.16	12.10	4.43	0.36			98.82	plagioclase labradorite
fsp4_b	51.32	0.06	29.11	0.81		0.11	12.73	4.05	0.31			98.49	plagioclase labradorite
fsp4_c	49.02	0.04	30.52	0.90		0.12	14.58	2.84	0.21			98.24	plagioclase labradorite
fsp4_d	51.36	0.06	29.08	0.83		0.14	12.87	3.96	0.27			98.59	plagioclase labradorite
ol1_a	53.27	0.32	1.11	18.86	0.45	23.90	2.04			0.00		100.00	pyroxene pigeonite
ol1_b	53.60	0.31	1.05	18.94	0.50	23.84	2.09			0.00		100.44	pyroxene pigeonite
ol1_c	52.86	0.37	1.27	18.13	0.41	23.62	2.16			0.01		98.95	pyroxene pigeonite
ol2_a	53.11	0.38	1.34	18.80	0.51	24.20	2.22			0.01		100.65	pyroxene pigeonite
ol2_b	52.94	0.34	1.34	18.53	0.57	23.70	2.11			0.01		99.69	pyroxene pigeonite
ol2_c	53.18	0.38	1.28	18.49	0.54	23.66	2.10			0.00		99.81	pyroxene pigeonite
ox1_a	0.84	0.75		88.25	0.15	0.08						90.38	magnetite
ox1_b	0.86	0.63		89.38	0.16	0.06						91.37	magnetite
ox1_c	0.88	0.46		87.99	0.12	0.02						89.71	magnetite
ox2_a	0.84	1.00		87.64	0.25	0.03						90.14	magnetite
ox2_b	0.90	0.66		88.51	0.13	0.03						90.50	magnetite
ox3_a	0.12	13.15		74.24	0.87	0.10						89.09	titanomagnetite
ox3_b	0.10	13.39		74.00	0.38	0.11						88.97	titanomagnetite
ox3_c	0.12	12.81		74.48	0.44	0.11						88.64	titanomagnetite
pxn1_a	50.73	0.72	2.98	10.96	0.33	15.14	19.21	0.32	0.01	0.04		100.70	pyroxene augite
pxn1_b	50.67	0.74	2.42	10.84	0.33	14.49	18.91	0.32	0.00	0.04		98.99	pyroxene augite
pxn1_c	50.84	0.65	1.96	10.51	0.27	15.18	18.26	0.30	0.00	0.01		97.98	pyroxene augite
pxn2_a	50.88	0.72	2.05	10.85	0.44	15.07	18.79	0.29	0.00	0.00		99.17	pyroxene augite
pxn2_b	51.23	0.73	2.05	11.31	0.27	15.27	18.44	0.30	0.01	0.03		99.68	pyroxene augite
pxn2_c	50.82	0.73	2.00	11.05	0.47	15.32	18.68	0.26	0.00	0.00		99.34	pyroxene augite
pxn2_d	51.23	0.71	1.77	11.21	0.39	14.93	18.53	0.30	0.00	0.00		99.14	pyroxene augite
pxn3_a	51.19	0.74	2.04	11.09	0.39	15.34	18.50	0.27	0.02	0.06		99.64	pyroxene augite
pxn3_b	50.33	0.79	3.22	11.09	0.24	14.30	19.32	0.25	0.01	0.00		99.75	pyroxene augite
pxn3_c	51.48	0.64	1.99	11.26	0.26	15.03	18.48	0.25	0.00	0.00		99.43	pyroxene augite
pxn3_d	50.79	0.54	1.85	11.12	0.33	15.39	18.47	0.31	0.00	0.01		98.93	pyroxene augite
pxn4_a	49.61	0.84	2.95	11.17	0.31	14.98	17.72	0.29	0.00	0.00		97.95	pyroxene augite
pxn4_b	50.21	0.72	2.80	12.78	0.42	15.88	16.10	0.30	0.01	0.00		99.35	pyroxene augite
pxn5_a	51.33	0.57	2.09	9.85	0.35	15.85	18.64	0.26	0.00	0.03		99.07	pyroxene augite
pxn5_b	51.21	0.60	2.37	10.26	0.46	16.23	17.46	0.23	0.01	0.06		99.05	pyroxene augite
pxn5_c	50.73	0.62	2.49	10.12	0.25	15.75	18.72	0.21	0.00	0.00		99.05	pyroxene augite
pxn5_d	51.23	0.51	2.12	10.23	0.33	16.13	18.33	0.25	0.02	0.00		99.22	pyroxene augite
pxn5_e	50.97	0.57	1.88	11.71	0.30	15.12	18.20	0.27	0.01	0.00		99.14	pyroxene augite
pxn5_f	50.55	0.85	2.15	11.54	0.30	14.68	18.04	0.34	0.01	0.00		98.57	pyroxene augite
pxn5_g	50.23	0.82	2.47	12.26	0.45	14.97	17.85	0.25	0.01	0.05		99.44	pyroxene augite
pxn6_a	51.07	0.57	2.26	9.78	0.29	15.55	18.61	0.29	0.01	0.02		98.52	pyroxene augite
pxn6_b	51.21	0.58	2.14	9.92	0.27	15.65	18.45	0.26	0.00	0.00		98.74	pyroxene augite
pxn6_c	50.61	0.54	2.39	10.29	0.29	15.59	19.01	0.22	0.00	0.03		99.09	pyroxene augite
pxn6_d	51.15	0.55	1.91	10.01	0.44	16.08	18.37	0.25	0.00	0.03		98.84	pyroxene augite
serp1_a	3.75	0.16	0.29	2.24	0.49	1.47	51.40	0.01	0.00	0.02	0.13	59.96	calcite
serp1_b	10.38	0.00	3.92	8.67	0.32	5.26	36.83	0.03	0.10	0.01	0.00	65.53	calcite
serp1_c	0.60	0.00	0.24	2.88	0.25	0.18	54.19	0.01	0.00	0.03	0.08	58.47	calcite
serp1_d	1.52	0.16	0.16	1.49	1.94	1.61	51.69	0.08	0.02	0.05	0.09	58.80	calcite
serp2_a	5.06	0.02	2.03	4.77		2.97	45.45	0.03	0.02			60.35	calcite
serp2_b	4.59	0.03	0.79	2.84		2.05	48.82	0.00	0.02			59.16	calcite
serp2_c	5.90	0.03	2.11	4.94		2.97	45.11	0.04	0.04			61.14	calcite
serp2_d	3.03	0.01	1.10	2.68		1.48	50.34	0.00	0.03			58.67	calcite
serp3_a	2.72	0.14	0.28	1.54		1.15	51.51	0.02	0.01			57.36	calcite

ID	SiO2	TiO2	Al2O3	FeO	MnO	MgO	CaO	Na2O	K2O	P2O5	F	Total	mineral id
serp3_b	13.82	0.04	4.89	10.84		6.88	31.31	0.12	0.14			68.03	calcite
serp3_c	1.24	0.00	0.33	1.17		0.69	53.36	0.00	0.01			56.79	calcite
serp3_d	0.98	0.00	0.25	0.84		0.35	54.21	0.00	0.00			56.64	calcite
serp4_a	2.80	0.06	0.36	1.81	1.32	1.74	49.94	0.00	0.00	0.03	0.00	58.07	calcite
serp4_b	4.32	0.02	0.36	2.22	0.43	1.81	50.18	0.00	0.01	0.02	0.00	59.37	calcite
serp4_c	0.25	0.00	0.01	0.40	0.38	0.04	55.87	0.00	0.00	0.00	0.00	56.96	calcite
serp4_d	51.18	0.40	2.25	18.36	0.48	23.25	2.39	0.08	0.06	0.02	0.01	98.49	pyroxene pigeonite
serp4_e	3.01	0.12	0.66	2.16	0.72	1.33	49.81	0.04	0.01	0.01	0.00	57.87	calcite
serp5_a	5.15	0.21	0.86	3.00	0.77	2.23	46.23	0.06	0.03	0.03	0.07	58.63	calcite
serp5_b	3.06	0.31	0.68	2.17	0.97	1.26	49.32	0.11	0.06	0.03	0.11	58.09	calcite
serp5_c	6.30	0.41	0.38	2.80	0.79	2.60	47.49	0.00	0.02	0.03	0.08	60.90	calcite

Sample J13.21.10

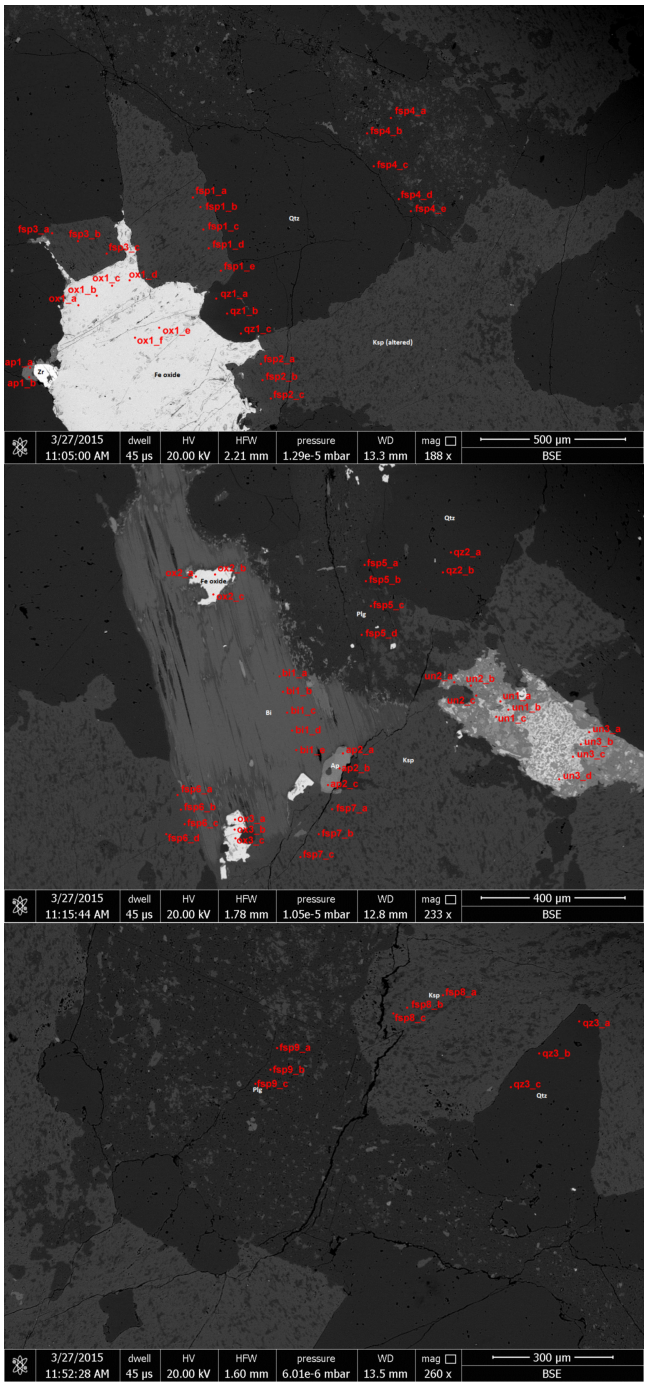

Electron microprobe analysis (EMPA) points for sample J13.21.10.

ID	SiO2	TiO2	Al2O3	FeO	MnO	MgO	CaO	Na2O	K2O	P2O5	F	Total	mineral_id
ap1_a	0.13		0.00	0.06		0.00	54.54	0.04	0.00	41.98	7.84	104.62	apatite
ap1_b	0.11		0.00	0.10		0.00	55.16	0.04	0.03	41.93	8.18	105.57	apatite
ap2_a	1.13		0.00	0.25		0.00	53.00	0.09	0.02	40.48	6.79	101.76	apatite
ap2_b	1.13		0.01	0.12		0.00	53.16	0.07	0.01	39.95	6.02	100.47	apatite
ap2_c	0.77		0.00	0.11		0.00	53.40	0.09	0.00	40.44	7.60	102.43	apatite
bi1_a	38.45	4.36	12.70	14.47	0.22	15.67	0.22	0.12	9.69	0.00	1.26	97.16	biotite
bi1_b	38.35	4.38	12.95	14.64	0.16	15.43	0.26	0.11	9.60	0.01	1.20	97.10	biotite
bi1_c	38.57	4.18	12.91	14.56	0.23	15.72	0.03	0.07	10.03	0.00	1.27	97.56	biotite
bi1_d	38.34	4.48	12.70	14.50	0.20	15.86	0.00	0.14	9.90	0.01	1.41	97.53	biotite
bi1_e	38.74	3.75	12.75	14.16	0.21	16.04	0.03	0.07	9.86	0.01	1.33	96.95	biotite
fsp1_a	70.15	0.00	15.57	0.06		0.01	0.07	1.67	12.21			99.74	mixed mineral
fsp1_b	64.97	0.00	18.11	0.10		0.02	0.05	0.99	15.41			99.66	microcline K-feldspar
fsp1_c	65.40	0.00	17.94	0.03		0.00	0.02	0.69	16.09			100.17	microcline K-feldspar
fsp1_d	64.21	0.02	17.94	0.38		0.00	0.01	0.37	16.53			99.45	microcline K-feldspar
fsp1_e	64.76	0.01	18.44	0.09		0.00	0.05	0.64	16.20			100.17	microcline K-feldspar
fsp2_a	64.90	0.00	17.99	0.15		0.00	0.01	0.86	15.98			99.89	orthoclase K-feldspar
fsp2_b	64.86	0.00	18.13	0.14		0.00	0.04	0.82	15.73			99.72	orthoclase K-feldspar
fsp2_c	64.97	0.00	18.00	0.08		0.03	0.07	1.79	14.58			99.52	orthoclase K-feldspar
fsp3_a	64.78	0.00	18.17	0.08		0.00	0.00	0.54	16.26			99.83	orthoclase K-feldspar
fsp3_b	65.27	0.01	18.43	0.15		0.00	0.04	1.09	15.65			100.63	orthoclase K-feldspar
fsp3_c	65.11	0.00	18.17	0.18		0.03	0.06	0.56	16.14			100.23	orthoclase K-feldspar
fsp4_a	68.38	0.00	19.34	0.00		0.00	0.34	11.21	0.03			99.30	plagioclase albite
fsp4_b	58.58	0.00	21.28	0.04		0.00	11.38	6.94	0.04			98.26	plagioclase andesine
fsp4_c	100.93	0.02	0.01	0.03		0.01	0.00	0.01	0.00			100.99	quartz
fsp4_d	100.61	0.02	0.01	0.00		0.00	0.02	0.02	0.01			100.68	quartz
fsp4_e	100.56	0.02	0.00	0.00		0.02	0.01	0.00	0.00			100.60	quartz
fsp5_a	100.99	0.01	0.01	0.00		0.01	0.02	0.03	0.00			101.07	quartz
fsp5_b	77.80	0.00	12.78	0.04		0.02	0.52	7.75	0.07			99.00	mixed mineral
fsp5_c	65.77	0.01	21.17	0.18		0.00	2.45	9.94	0.16			99.68	plagioclase albite
fsp5_d	66.19	0.00	20.36	0.07		0.00	1.60	10.55	0.09			98.86	plagioclase albite
fsp6_a	65.11	0.01	18.18	0.21		0.01	0.05	0.90	15.78			100.25	orthoclase K-feldspar
fsp6_b	65.60	0.00	18.58	0.21		0.00	0.03	2.20	13.76			100.38	K-feldspar
fsp6_c	65.63	0.00	18.28	0.16		0.00	0.03	2.10	14.19			100.41	K-feldspar
fsp6_d	65.67	0.01	18.46	0.12		0.00	0.09	2.23	13.82			100.40	K-feldspar
fsp7_a	64.83	0.00	18.20	0.03		0.03	0.04	0.53	16.38			100.05	orthoclase K-feldspar
fsp7_b	64.62	0.00	18.12	0.07		0.01	0.01	0.78	16.19			99.81	orthoclase K-feldspar
fsp7_c	65.04	0.00	18.40	0.40		0.00	0.26	4.83	10.10			99.04	K-feldspar
fsp8_a	64.77	0.00	18.08	0.09		0.00	0.02	0.52	16.52			100.00	orthoclase K-feldspar
fsp8_b	64.56	0.00	18.13	0.03		0.02	0.08	0.83	15.92			99.57	orthoclase K-feldspar
fsp8_c	64.58	0.00	18.28	0.03		0.02	0.05	0.42	16.64			100.00	orthoclase K-feldspar
fsp9_a	68.67	0.01	19.83	0.00		0.00	0.40	11.37	0.06			100.34	plagioclase albite
fsp9_b	61.69	0.00	23.87	0.46		0.08	0.30	8.44	3.41			98.26	sanidine
fsp9_c	67.59	0.01	20.37	0.03		0.02	0.48	10.86	0.38			99.75	sanidine
ox1_a	0.02	0.07		93.12	0.18	0.02						93.47	magnetite
ox1_b	0.05	2.39		89.92	0.18	0.05						92.59	magnetite
ox1_c	0.01	0.11		93.00	0.18	0.01						93.35	magnetite
ox1_d	0.02	0.09		93.30	0.24	0.03						93.68	magnetite
ox1_e	0.05	3.80		89.06	0.11	0.02						93.10	magnetite
ox1_f	0.06	0.42		92.60	0.14	0.04						93.27	magnetite
ox2_a	0.00	0.07		93.37	0.07	0.02						93.62	magnetite
ox2_b	0.01	0.53		93.09	0.03	0.00						93.72	magnetite
ox2_c	0.02	0.17		93.22	0.03	0.01						93.47	magnetite
ox3_a	0.02	0.12		93.20	0.08	0.00						93.42	magnetite
ox3_b	0.03	0.11		93.67	0.00	0.00						93.82	magnetite
ox3_c	0.04	0.07		93.41	0.05	0.00						93.60	magnetite
qz1_a	100.81	0.01	0.05	0.14		0.00	0.01	0.00	0.00			101.03	quartz
qz1_b	100.97	0.02	0.01	0.05		0.03	0.00	0.03	0.00			101.11	quartz
qz1_c	101.00	0.01	0.00	0.17		0.01	0.00	0.00	0.00			101.19	quartz
qz2_a	100.92	0.02	0.03	0.05		0.00	0.00	0.03	0.01			101.06	quartz
qz2_b	100.41	0.01	0.01	0.00		0.02	0.00	0.00	0.01			100.46	quartz
qz3_a	100.69	0.04	0.00	0.00		0.00	0.01	0.01	0.02			100.77	quartz

ID	SiO2	TiO2	Al2O3	FeO	MnO	MgO	CaO	Na2O	K2O	P2O5	F	Total	mineral_id
qz3_b	100.69	0.00	0.02	0.00		0.02	0.02	0.00	0.01			100.77	quartz
qz3_c	100.51	0.01	0.01	0.04		0.00	0.01	0.00	0.00			100.58	quartz
un1_a	0.03	40.12	0.00	52.09	3.11	0.01	0.43	0.07	0.02	0.00	0.00	95.88	ulvospinel
un1_b	0.02	48.26	0.00	44.56	1.67	0.04	0.25	0.03	0.01	0.00	0.01	94.86	ulvospinel
un1_c	0.04	73.48	0.00	24.84	0.34	0.00	0.17	0.01	0.01	0.00	0.02	98.92	ulvospinel
un2_a	30.32	35.80	1.99	1.50	0.06	0.00	27.85	0.07	0.11	0.01	0.70	98.40	titanite
un2_b	30.32	34.79	3.37	1.13	0.02	0.00	28.42	0.02	0.05	0.23	0.67	99.02	titanite
un2_c	26.66	37.51	1.54	8.54	0.24	0.08	24.74	0.05	0.02	0.01	0.46	99.86	titanite
un3_a	0.03	59.01	0.00	34.88	5.36	0.09	0.14	0.00	0.01	0.00	0.00	99.53	ulvospinel
un3_b	0.01	47.60	0.00	42.79	9.95	0.13	0.19	0.03	0.02	0.00	0.03	100.74	ulvospinel
un3_c	11.03	45.51	0.52	26.39	7.48	0.09	9.45	0.03	0.01	0.15	0.20	100.87	titanite
un3_d	1.22	12.82	0.72	81.47	0.33	0.83	0.08	0.01	0.00	0.00	0.00	97.48	titanomagnetite